

AN INCLUSIVE SEARCH FOR NEW
LONG-LIVED PARTICLES AT THE LARGE
HADRON COLLIDER IN $\sqrt{s} = 13$ TeV DATA

JOSHUA ROBERT HARDENBROOK

A DISSERTATION
PRESENTED TO THE FACULTY
OF PRINCETON UNIVERSITY
IN CANDIDACY FOR THE DEGREE
OF DOCTOR OF PHILOSOPHY

RECOMMENDED FOR ACCEPTANCE
BY THE DEPARTMENT OF
PHYSICS
ADVISOR: CHRISTOPHER G. TULLY

JUNE 2017

© Copyright by Joshua Robert Hardenbrook, 2017.

All rights reserved.

Abstract

A search for long-lived particles was performed with data corresponding to an integrated luminosity of 2.6 fb^{-1} collected at a center-of-mass energy of 13 TeV by the CMS experiment in 2015. The analysis exploits two customized topological trigger algorithms and an offline displaced-jet tagging algorithm. The multiplicity of displaced jets is used to search for the presence of a signal with a proper lifetime between 1 mm and 1000 mm. Pair-produced long-lived decays to four-jet final states, with cross sections larger than 1.2 fb are excluded for a proper lifetime of 50 mm. For pair-produced long-lived decays to two b quarks and two leptons with equal decay rates between lepton flavors, cross sections larger than 2.5 fb are excluded for proper lifetimes between 70 mm and 100 mm. As a mass exclusion bound, pair-produced long-lived R-parity violating top squarks lighter than 550–1130 GeV are excluded depending on their lifetime and decay mode. This mass exclusion bound is currently the most stringent bound available for top squark proper lifetimes greater than 3 mm.

Acknowledgements

My time as a PhD student and the time leading up to this research was shaped by many and it is important to me to take the time to express my gratitude for those who personally and academically made this work possible.

Advisor

I would like to first acknowledge my advisor Chris Tully. He has guided my PhD experience by directing me towards projects where I could succeed. I thank him for always making himself available and for making me feel supported and welcome within the Princeton group. I owe much of my success and happiness as a PhD student to the intellectual freedom he gave me to explore my ideas. I have always felt, and continue to feel, that Chris values my happiness and success as a person above all else. Chris is an exemplary physicist and role model who leaves me continually humbled by our interactions. Princeton is lucky to have him as a teacher and researcher.

Mentors

I was fortunate to have the pleasure of working with Maurizio Pierini for more than 7 years, a period from when I was an undergraduate at Caltech till my last days at CERN. Maurizio worked with me through the details of the analysis from its conception to the final approval. Week by week, and espresso by espresso, we pushed the analysis through the final approval process. I'd like to thank Maurizio for being my advocate. When data samples were delayed in production, he would reach out to management on our behalf. When I applied for fellowships, he was always willing to write a recommendation. He is an esteemed colleague, a mentor and a friend. I wish him the best.

Toyoko Orimoto began mentoring me when I was an undergraduate at Caltech performing a search for diphoton search with Yousi Ma. During my first visit to CERN,

she was kind enough to invite myself and fellow hungry students to her apartment in Servette for vegan dinners. She made me feel a part of the CERN and high energy physics community. I express my gratitude for the time she spend editing my NSF Fellowship proposal and graduate school applications. Toyoko always actively kept me in her thoughts. She would nominate me for talks and forward job opportunities. I am proud to have seen her attain a professorship position at Northeastern. Her students will inevitably know the same nurturing, caring, and intelligent physicist I have had the joy of working with. I value her friendship and am excited to see her continued success as a professor.

Princeton

When I first arrived to CERN and joined the Princeton Group, I will remember Halil Saka for picking me up from the Geneva airport. I'd like to thank him for some of the most intense and enjoyable discussions I had at CERN. He is at his best acting as my my de facto table partner at conferences. When I think of Halil I think futbol, Clubhouse nachos, and trying to calculate longitudinal impact parameters from track variables by hand. Halil is a one of a kind physicist.

I also had the pleasure of working with Andrzej Zuranski. The theoretical community had significant interest in what he had done, especially the inclusive nature of the search. I was drawn to continue his search after he graduated and used the triggers and variables of his analysis as a starting point for improvement at 13 TeV. The documentation and discussions with Andrzej were integral to the decisions made in the early stages of the analysis. I thank him for enabling me to perform this study.

Thank you Phil Hebda for pushing me to learn French. His performance as the 1 km leg in the CERN relay will not be forgotten. Go ΔF ! His dedication to his work and his hobbies are admirable.

Additionally, I would like to thank Xiaohang Quan for aiding my initial work on the diphoton triggers, Paul Lujan for useful discussion on long lived monte carlo

generation, and Dan Marlow for serving as my second reader for this work. Many thanks to Ted Laird and Edmund Berry for their advice and wisdom on navigating CERN, CMS, and Princeton.

In addition to my colleagues in within the CMS group I would like to thank Professors Mariangela Lisanti and Joshua Shaveitz for serving on my thesis committee.

My time at Princeton would not have been the same without my close physics department friends in the 2012 cohort. Our preliminary exams were a formative time in my life and I know it would not have been the same without you. Aitor Lewkowycz you are an impressive theorist and I look forward to following your career. I fondly remember the time you came to visit me at CERN. Zachary Sethna, your love of problem solving, reading, and politics continues to keep me sharp. The Z-bar will forever live on in the minds of those who enjoyed your generosity and welcoming demeanor. Joaquin Turiaci, you are incredibly patient and insightful. Many of the finer points in this thesis are the product of our discussions. Great men are born on September 27th. Aaron Levy, I respect your detailed approach to problem solving. I will remember you best for our work on QFT problem sets together and arguing with Zach about politics. You were a like minded personality during an important time of my life, thank you for being my friend. Dave Zajac, you are a machine. I will not forget our early morning gym work outs spent discussing prelim problems. I admire your dedication to your lab and respect your ability as an experimental physicist. Keep on climbing. I could not possibly leave out KL Moscato who provided a much needed outlet for me from physics to talk about dance and yoga. Thank you for your hospitality and your listening ear. You are tough as nails and I'm excited for you moving on from ARB. Mattia you are hilarious and keep me laughing, please never change.

CERN

I would like to thank Daniele Del Re, Slava Valouev, and Oliver Muchmuller for serving as the Exotica group conveners on this analysis. Additionally, I thank Ted Kolberg and Wells Wulsin for serving as the long-lived subgroup conveners. I appreciate the time spent by Luca Scodellaro, Kevin Stenson, Matt Walker, and Bora Isildak as the ARC members of the analysis. Many thanks to fellow CERN affiliates who helped me along the way including: Zeynep Demiragli, Mia Tosi, Matt Strassler, Steve Mrenna, Juliette Alimena, Jamie Antonelli, Bingxuan Liu, Luca Pernie, Emanuele Di Marco, Josh Bendavid, Nadir Daci, and many more.

I also had the great pleasure of living with *two of the best* roommates I could have asked for. Brad Axen and Russell Smith, you were the Americans I needed in my life. Thank you for the adventures, the tribulations, the laughter, and the numerous catastrophes that we endured at Avenue de Sécheron 7, 5ème étage. I am happy to see both of you move on from Geneva and restart your lives in the US. I want to smile and cry every time I think about that apartment. You are both bright, good natured physicists. Thank you for being my friends.

Caltech

I began my work on the CMS experiment with the Caltech group working with Harvey Newman and Maria Spiropulu. I am forever grateful for the impact this had on my trajectory in science. Harvey and Maria have always been nurturing and encouraging in my pursuit of doing research. I admire Harvey's love of science and his commitment to advocating in Washington DC for fundamental science. My first summer, a Caltech senior, Andy Yen, taught me the basics of experimental physics and how to work with ROOT. I want to thank him for remaining a friend and advising me on career decisions while he manages his successful startup: Proton Mail. I must also express my gratitude to Yousi Ma for answering day to day questions and advising me through the graduate school process. Yousi is a patient and kind person as well as a scientist. I was lucky to have him as a mentor. Thank you Chris Rogan for

counseling me on academic life and for some of the most educational discussions on particle physics I had in my time as a student. I consider you both a role model friend and physicist. I found inspiration in your research and am proud to have known you personally. I would additionally like to thank members of the Caltech group who supported me in my research: Marat Gataullin, Vladamir Litvin, Vladlen Timciuc, and Yong Yang.

Family and Friends

Mom and Dad, you have always stood behind my pursuit to go to college and graduate school. Thank you for constant words of encouragement and financial support. You've raised me to be who I am today and I can never repay the sacrifices you've made to get me here.

I also want to thank those friends who have supported me from afar: Thompson and Kristina Heavey, Adam Khan, Arda Antikacioglu, Paul Fleiner, Barbara Gao, Kevin Shaprio, Helen Jing, and Colin Ho. I always knew when I came back to the US you had a place for me to stay and reminisce. Good friends are hard to find, but easy to keep.

A special thank you goes out to Arda. Through the toughest times and the best of times you have always been on the other side of the phone to break it down. Our friendship is a high priority in my life and I wish you the best. You are always near to my thoughts. This ones for you.

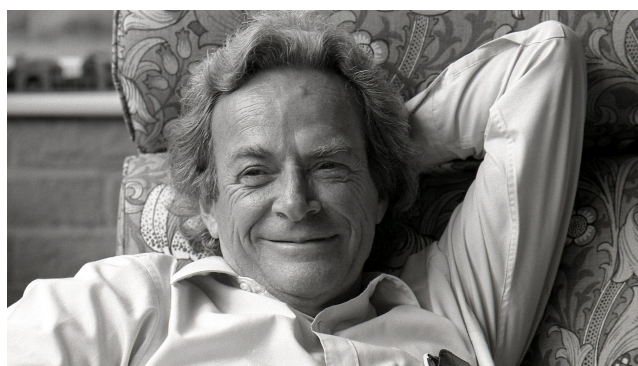
Summary

While my PhD has had it's share of difficult and isolating times, I have had the pleasure and the privilege of being surrounded by a revolving door of smart and engaging personalities at both Princeton and CERN. Physics would not have been the same to me without you in it.

I would like to end with a quote from an interview with Richard P. Feynman. I turn to this quote for inspiration in difficult times to be reminded myself why I do physics. Thank you for your words. They are a reminder to keep my mind open to the world not as I see it, but as it chooses to reveal itself.

“People say to me: are you looking for the ultimate laws of physics? No, I’m not. I’m just looking to find out more about the world and if it turns out there is a simple ultimate law that explains everything—so be it. That would be very nice to discover. If it turns out its like an onion with millions of layers and we’re just sick and tired of looking at the layers. Then that’s the way it is. But whatever way it comes out its nature that’s there and she’s going to come out the way she is. Therefore when we go to investigate it, we shouldn’t pre-decide what we want to find out besides to find out more about it. You see – one thing is, I can live with doubt, and uncertainty and not knowing. I think its much more interesting to live not knowing than to have answers that might be wrong. I have approximate answers and possible beliefs, and different degrees of certainty about different things, but I’m not absolutely sure of anything and there are many things I don’t know anything about. But I don’t have to know an answer. I don’t have to. I don’t feel frightened by not knowing things.”

—Richard P. Feynman



This material is based upon work supported by the National Science Foundation Graduate Research Fellowship under Grant No. DGE-1656466. Any opinion, findings, and conclusions or recommendations expressed in this material are those of the authors(s) and do not necessarily reflect the views of the National Science Foundation.

To Arda,
my brother,
may no distance ever alter our friendship.

Contents

Abstract	iii
Acknowledgements	iv
1 Introduction	1
2 Theory	9
2.1 Introduction	9
2.1.1 Quantum Field Theory	10
2.1.2 Symmetries	15
2.1.3 The Standard Model Lagrangian	24
2.1.4 Maxwell's Laws	34
2.1.5 Feynman Diagrams	38
2.1.6 Radiative Corrections and Renormalization	45
2.2 Supersymmetry (SUSY)	50
2.2.1 The Miraculous Cancelation	57
2.2.2 The Minimally Supersymmetric Standard Model	60
2.3 Long-lived Signatures	64
2.3.1 Standard Model Particles with Long Lifetimes	64
2.3.2 Split SUSY and Naturalness at the LHC	67
3 Simulation and Collider Physics	69
3.1 Introduction	69

3.2	From Matrix Elements to Cross Sections	70
3.3	Parton Model of Hadron Collisions	75
3.4	Kinematic Conventions for Collider Physics	77
3.5	Showering	81
3.6	Hadronization	84
3.7	Hadron Decay	89
3.8	Jet Clustering	90
4	The Compact Muon Solenoid Experiment	93
4.1	CERN Laboratory and the LHC	97
4.1.1	The Large Hadron Collider	99
4.2	Superconducting Solenoid	102
4.3	Electromagnetic Calorimeter (ECAL)	105
4.4	Hadronic Calorimeter (HCAL)	109
4.5	Tracking Layers	112
4.6	Muon Spectrometer	116
4.7	Trigger System	120
4.7.1	Level 1 (L1) Trigger	123
4.7.2	High Level Trigger (HLT)	124
5	Studies of Displaced Jet Tagging Variables	127
5.1	Introduction	127
5.2	Displaced Jet Samples	131
5.3	Displaced Jet Tagging Variables	132
5.3.1	Impact Parameter Information	132
5.3.2	Calo Jet Information	141
6	Displaced Jet Analysis	143
6.1	Introduction	143

6.2	Datasets and simulated samples	144
6.3	Event selection	145
6.4	An inclusive displaced-jet tagger	146
6.4.1	Tagging Variable Cut Optimization	151
6.5	Background prediction	153
6.5.1	Signal region removal correction	156
6.5.2	Tag probability cross validation	157
6.5.3	Signal injection tests	163
6.6	Systematic uncertainties	166
6.6.1	Background systematic uncertainties	166
6.6.2	Signal systematic uncertainties	167
6.7	Results and interpretation	172
7	Conclusions	189
	Bibliography	190

Chapter 1

Introduction

“The first principle is that you must not fool yourself – and that you are the easiest person to fool.”

– Richard P. Feynman

When convincing ourselves of something new, to make assertions with confidence, we must be cautious. Personally, this means avoiding believing I know something, when I do not understand the underlying assumptions or the importance of a conclusion. Using some theorem or an algorithm by name without knowing its origins or how it is implemented, while perhaps inevitable for practical purposes, is at best precarious and at worst dishonest. Rather, knowledge drawn by connecting a path of fundamental assumptions/principles with the necessary corollaries, and arriving at an ultimate conclusion affords a security in one’s results.

fortunate for those wish to take this bottom-up approach to its ultimate and earthly end, history’s scientific heroes have developed a field of study for the foundational principles of the physical world. The study of high energy particle physics, while limited in its applicable scope, allows one to make connected steps from core postulates of nature, to the experimental observations inside of high energy experiments. In this same way, this thesis is an effort to build up an intellectually continuous

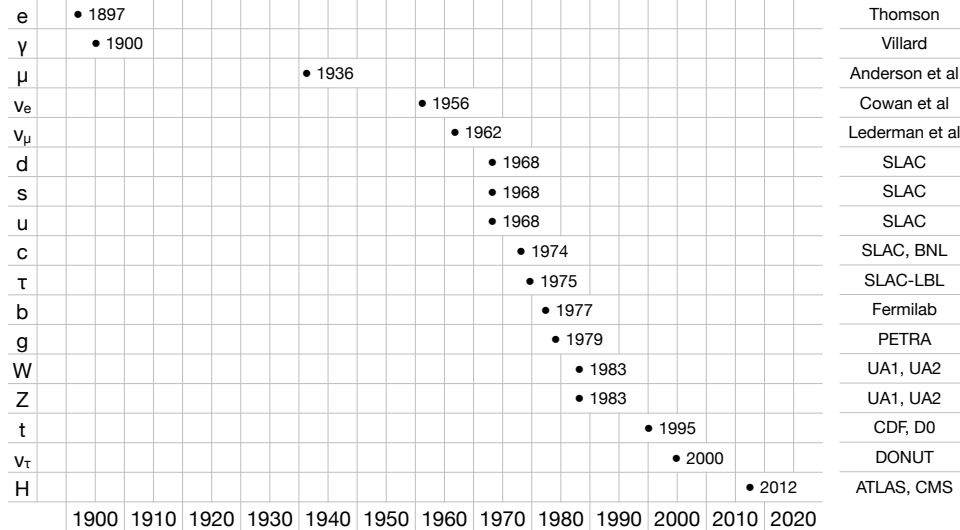


Figure 1.1: The discovery of the standard model particle content through time. [67]

(albeit coarse) discussion on how to make quantitative statements about fundamental physics by utilizing the massively complex experiments found at the Large Hadron Collider (LHC).

In pursuit of a theory of fundamental interactions, the Standard Model of particle physics, has performed miraculously well within its scope. As of the July 4, 2012 discovery of the Higgs Boson, the complete particle content of the theory has been discovered (Figure 1.1). Precision electroweak measurements have held up to calculations to 14 significant figures [36]. These measurements are more precise than correctly measuring the distance between the earth and the moon (3.8×10^8 meters) within the width of a human hair (1.7×10^{-5} meters).

However, the Standard Model is not a theory capable of describing everything, it rather functions as a tool to discover new fundamental physics. By consistently incorporating what we understand into a single theory, we can search for more complete physics by looking for deviations from the model in nature.

Here I list a series of outstanding questions within the Standard Model, while not complete, can sufficiently motivate the need to search for beyond the standard model

(BSM) physics. I group questions into two categories. The first set of questions are forward looking and ask how will known phenomenon be incorporated into an extension of the Standard Model.

- **Gravity:** How will the Standard Model which describes the weak, strong, and electromagnetic force be extended into a theory of quantum gravity?
- **The Hierarchy Problem:** How can the Higgs mass be so small compared to the size of the leading one loop contributions to the mass? How can the vacuum energy of the universe be nearly zero when calculations yield values that are 100 orders of magnitude larger?
- **Neutrino Masses:** How will an extended theory generate the masses of neutrinos which are known to be non-zero from neutrino oscillation experiments?
- **Dark Matter:** How will the abundance of dark matter observed in the universe be described?
- **Stability of the Vacuum:** Given the mass of the Higgs, the universe's vacuum is meta-stable. How has the vacuum not decayed? What physics, if any, would resolve this meta-stability?
- **UV Completeness:** The Standard Model is interpreted as the low energy effective theory of a larger theory. What physics will complete the theory at high energies? Will the gauge coupling strengths unify at high energies?

The second set of questions asks why does the Standard Model take its specific form. Are there deeper principles that explain why? Or will we ultimately need to accept these ideas without a simpler explanation?

- **Gauge Theory:** Why does the Standard Model have the gauge group $SU(3) \times SU(2) \times U(1)$? Does the universe accept a more complete symmetry group that is then broken into these components?

Summary of CMS SUSY Results* in SMS framework

ICHEP 2014

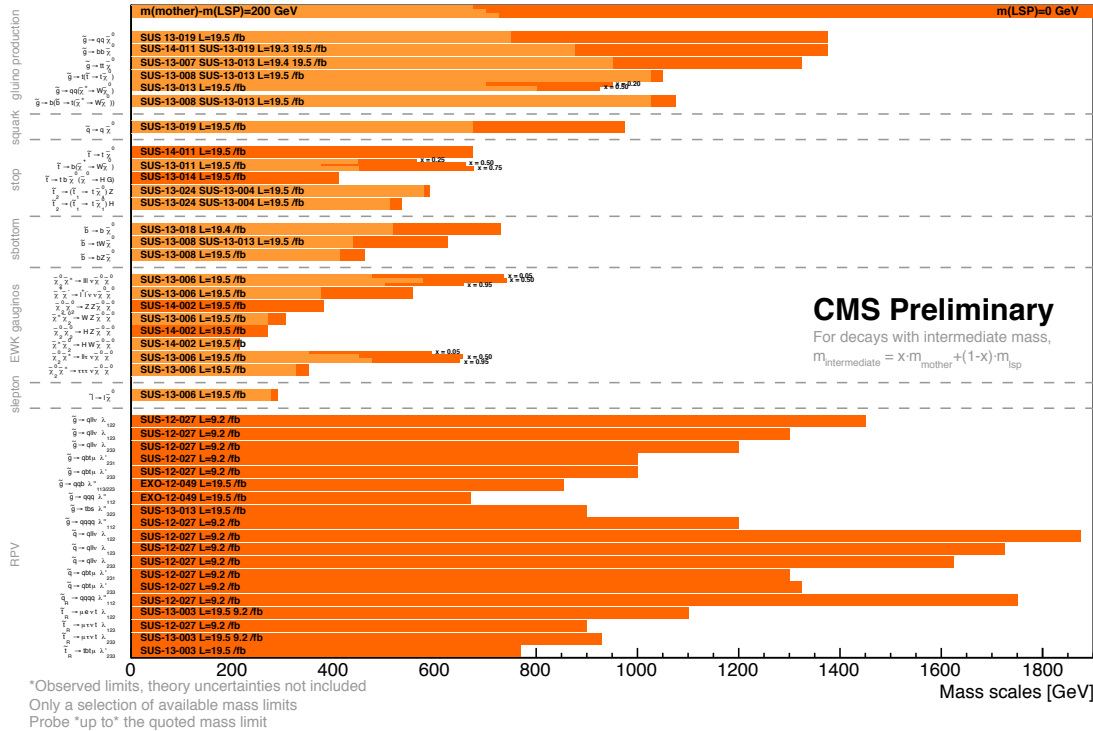


Figure 1.2: A summary of mass exclusions for supersymmetric models in 7 + 8 TeV data by the CMS experiment.

- **Space-time and Particle Content:** Why are there three families of particles and 3+1 space-time dimensions? Is space-time an emergent phenomenon? Are there extra dimensions which explain the weakness of the gravitational force?
- **Naturalness:** Are the free parameters of our theory natural? That is, are small values of free parameters an artifact of new physics yet to be incorporated or are the observed values coincidental?
- **Strong CP Problem:** Why is there no evidence of the term $\theta \epsilon_{\mu\nu\rho\sigma} F^{\rho\sigma} F_{\mu\nu}$ in the Standard Model Lagrangian ($\theta < 10^{-10}$)?

So what then are the candidates for BSM physics? A multitude of full and simplified models are tested in hopes of observing statistically significant deviations from the Standard Model (Figures 1.2 and 1.3) in 7, 8, and 13 TeV data by both the ATLAS

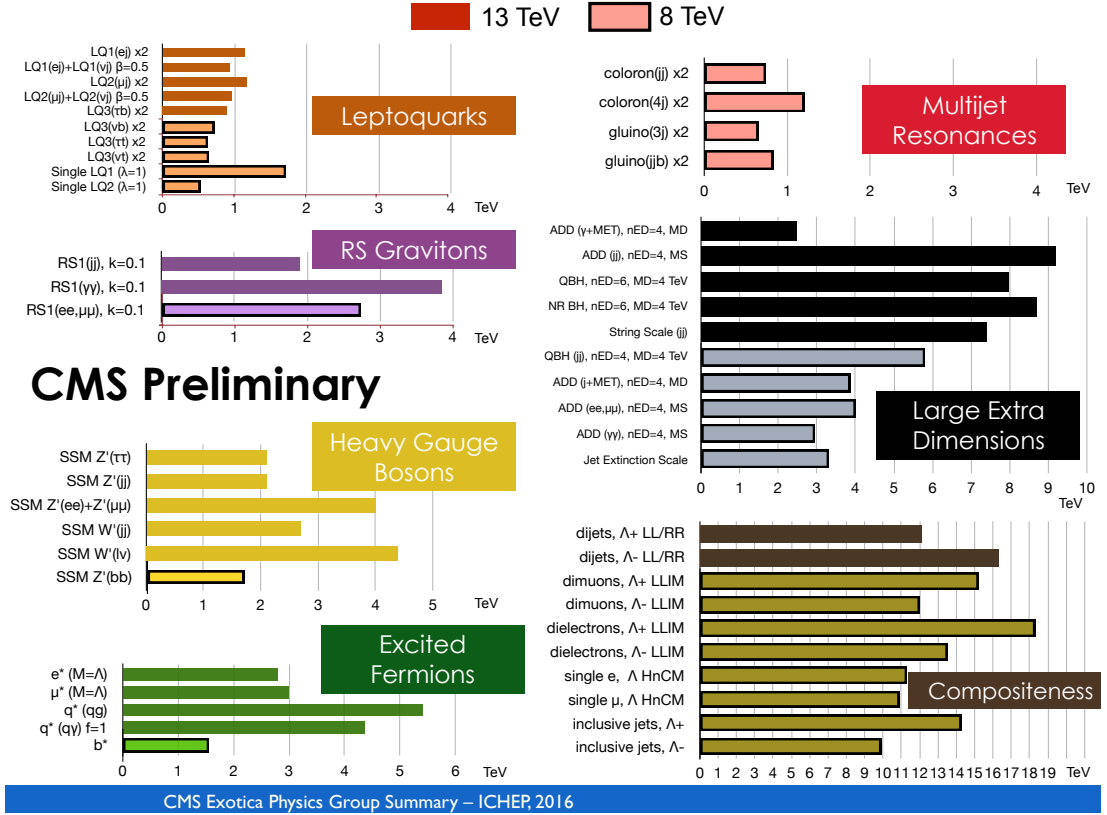


Figure 1.3: A summary of mass exclusions for exotic models in 8 + 13 TeV data by the CMS experiment.

and CMS experiments at the LHC. Searches for models containing the most theoretically motivated signatures (jets and missing energy, two leptons, two jets, missing energy, among many others) have significantly narrowed the remaining parameter space where BSM physics could be hiding.

The most popular answer to many of the questions posed above is Supersymmetry (SUSY), a new symmetry of space time, that would imply heavy super partners to Standard Model particles whose masses are heavier, but still explorable at the LHC. The expectation of discovering SUSY at the LHC has been largely motivated by the naturalness of the theory. For a given model of Supersymmetry the mass of the Standard Model Higgs boson is sensitive to the high energy scale where SUSY exists (m_{SUSY}), its mass, of order the electroweak scale, ($m_h \approx m_{EW} \ll m_{\text{SUSY}}$)

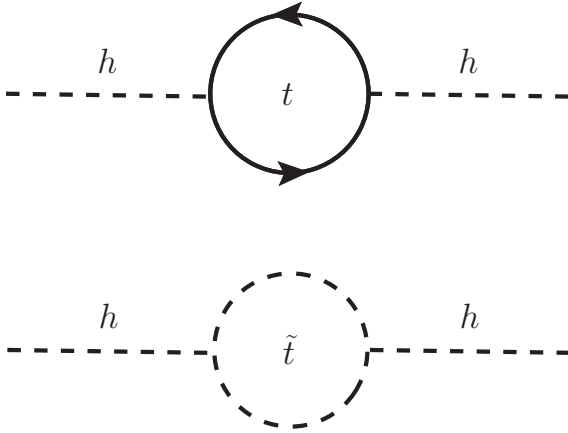


Figure 1.4: (top) The 1 loop contribution to the Higgs mass induced by a fermionic top loop. (bottom) The one loop correction to the Higgs mass due to a scalar stop loop.

would need to be tuned to order $m_{EW}^2/m_{\text{SUSY}}^2$. To avoid fine-tuning, we would like $m_h^2 \approx m_{\text{SUSY}}^2 \implies m_{\text{SUSY}} \leq 1 \text{ TeV}$. More specifically, knowing $m_H \approx 125 \text{ GeV}$ we expect light SUSY partners (in particular, light top quark partners) less than 1 TeV to stabilize the quadratic divergences of 1 loop corrections to the Higgs mass (Figure 1.4). The naturalness of a theory, has long been a guiding principle of model building extensions to the Standard Model, but unfortunately these scalar partners, despite considerable effort, have not yet been discovered.

As the parameter space of possible BSM physics continues to narrow and the kinematic gains from increasing the collider energy are no longer available, we must thoughtfully consider where we might have missed something. If new physics exists at the TeV scale and is still probable at the LHC, why is it yet to reveal itself? One such possibility is that the new physics is long lived.

A fundamental assumption of non-specific analyses is that the new physics will be prompt. That is to say, the BSM particles, when produced, will decay a distance from the original collision too small to detect. In these scenarios, there is a reconstructable vertex where the collision took place, and the final state particles will arrive at the detector face at predictable angles. In the case of long-lived physics, the BSM particles

will travel measurable distances in the detector before decaying. The resulting BSM decays will unlikely have a primary collision vertex and the final state particles may arrive at glancing angles to the detector face. In these cases, it has been shown standard particle identification techniques are inefficient and in many cases completely veto long-lived signatures. If nature exhibited long-lived BSM behavior, prompt searches would unintentionally clean it from their signal regions at early stages in the data processing.

The theoretical motivations for long-lived particles arise in a variety of scenarios including, but not limited to:

- Split Supersymmetry [9, 32, 8, 10, 37]
- Twin Higgs Models [26]
- WIMP Baryogenesis [27]
- Hidden Valley Models and Higgs Portal Processes [35]
- R-Parity Violating SUSY [33]

This search was designed from the initial data collection algorithms to the final background prediction to be as inclusive as possible to all displaced signatures. Prompt analyses have been shown to have strong sensitivity to signatures with proper lifetimes less than 1 mm. Accordingly, this analysis is tuned to target complementary lifetimes greater than 1 mm. Essential to this study is the definition of a displaced jet tag, which does not rely on commonly utilized physics objects, but rather is constructed from the geometry of globally reconstructed charged particle tracks matched to separately reconstructed clusters of calorimeter energy. The result is an object with strong background rejection (1 in 2000 false positives) with sensitivity to electrons, jets, and taus in any combination. The simplicity of the construction also exhibits sensitivity to exotic BSM jets without narrowing the scope of the analysis.

This document is organized beginning from the fundamental theory that describes the Standard Model (Chapter 2). The underlying framework of quantum field theory is built up from classical equations of motion and the structure of the Standard Model is described in some detail. The theory is then connected with the methods of simulation and physics necessary to evolve the initial scattering amplitudes to the final state showering in Chapter 3. After a discussion of the individual sub-detectors of the experiment in Chapter 4, Chapter 5 will outline the studies leading to definition of the displaced jet tag. Chapter 6 will describe the analysis and summarize the results of the search as found in the public document [2] and presented at Moriond 2017 [39] and Aspen 2017 [6]. Conclusions will be drawn in Chapter 7.

Chapter 2

Theory

2.1 Introduction

It is the goal of this section to succinctly derive some of the principal aspects of the Standard Model of particle physics and discuss the fundamental assumptions that give structure to the theory. Starting from classical physics how do we build up to an interacting theory of quantum theory of fields with the particle content of the Standard Model? What are the guiding principles of this model? And importantly what pieces of the theory have been put in by hand to agree to experiment?

First, we will describe the Lagrangian formulation of classical mechanics. From here we introduce, classical field theory and the fundamental quantization of quantum mechanics to arrive at quantum field theory (QFT). By way of Lagrangian symmetries in a QFT, we will elaborate on gauge theories and how local gauge symmetries give rise to the interactions mediating the fundamental forces. We will review spontaneous electroweak symmetry breaking (EWSB) and the tools used to calculate scattering amplitudes. Ultimately, we will discuss radiative corrections, renormalization and Supersymmetry as an extension of the Standard Model.

2.1.1 Quantum Field Theory

Lagrangian Mechanics

In Lagrangian mechanics, the time evolution of some generalized coordinate q can be determined via the fundamental principle of minimal action for $\delta S = 0$ where $S = \int dt L$. Where the Lagrangian L is difference between the kinetic and potential energy $T - V$.

$$S[q(t)] = \int_{t_1}^{t_2} L\left(q, \frac{dq}{dt}, t\right) dt$$

where S is a functional of the time dependent generalized coordinate $q(t)$. Letting $\dot{q} = \frac{dq}{dt}$ The equations of motion are derived by varying S

$$\delta S = \int_{t_0}^{t_1} \left[\frac{\partial L}{\partial \dot{q}} \delta \dot{q} + \frac{\partial L}{\partial q} \delta q \right] dt$$

Note that $\delta \dot{q} = \delta \frac{dq}{dt} = \frac{d(\delta q)}{dt}$. Integrate the first term by parts, and require that δq vanish at the boundaries:

$$\int_{t_0}^{t_1} \left[-\frac{d}{dt} \left(\frac{\partial L}{\partial \dot{q}} \right) \delta q + \frac{\partial L}{\partial q} \delta q \right] dt = \delta S = 0$$

by the principle of minimal action we have arrived at the Euler equations of motion:

$$\frac{d}{dt} \left(\frac{\partial L}{\partial \dot{q}} \right) = \frac{\partial L}{\partial q}$$

For a generic Lagrangian with potential energy term $V(q)$, $L = \frac{1}{2}m_q \dot{q}^2 - V(q)$ we obtain the classical equation of motion as a differential equation $m\ddot{q} = -dV/dq$ that is $F = -dV/dq$.

Classical Field Theory

In comparison with classical mechanics, which deals with finitely many general coordinates q_i , classical field theory deals with an infinite number of degrees of freedom $\phi_i(\vec{x}, t)$ with a degree of freedom for each spatial coordinate \vec{x} , t and index i . For simplicity we use a single index μ for the four space-time dimensions and utilize the Einstein summation convention where repeated indices are summed over $x_i x_i \equiv \sum_i x_i x_i$. The corresponding action can be written in terms of a lagrangian density $\mathcal{L}(\phi, \partial_\mu \phi)$ [65]

$$S = \int dt L = \int d^3x \int dt \mathcal{L}(\phi, \partial_\mu \phi) = \int dx^4 \mathcal{L}(\phi, \partial_\mu \phi)$$

Similarly, we arrive at classical Euler-Lagrange equations of motion:

$$\partial_\mu \left(\frac{\partial \mathcal{L}}{\partial (\partial_\mu \phi)} \right) = \frac{\partial \mathcal{L}}{\partial \phi}$$

We now consider the simple free Lagrangian density for a real scalar field ϕ :

$$\mathcal{L} = \frac{1}{2}(\partial_\mu \phi)^2 - \frac{1}{2}m^2\phi^2 = \frac{1}{2}(\partial_t^2 - \nabla^2)\phi - \frac{1}{2}m^2\phi^2$$

we have achieved a relativistically invariance for free as all indices are contracted. To see this, consider a Lorentz transformation Λ on the kinetic term. The transformation induces $\phi(x) \rightarrow \phi'(x) = \phi(\Lambda^{-1}x) = \phi(y)$. The transformation is Λ as we actively rotate the coordinate system rather than rotating the field.

$$\partial^\mu \partial_\mu = \eta_{\mu\nu} \partial^\nu \partial^\mu \rightarrow_\Lambda \eta_{\mu\nu} (\Lambda^{-1})^\mu{}_\rho (\Lambda^{-1})^\nu{}_\sigma \partial^\rho \partial^\sigma = \eta_{\rho\sigma} \partial^\rho \partial^\sigma = \partial_\mu \partial^\mu$$

where we have used invariance of the spacetime metric under Lorentz transformations. As the action integrates over all space time, the change of variable from $x \rightarrow y$ is

inconsequential and yield the same equations of motion. Applying the Euler-Lagrange equation we arrive at the classical relativistically invariant Klein-Gordon equation.

$$(\partial^2 + m^2)\phi = 0$$

taking the Fourier transform of state ϕ :

$$\phi(\vec{x}, t) = \int \frac{d^3 p}{(2\pi)^3} e^{i\vec{p}\cdot\vec{x}} \phi(\vec{p}, t)$$

Where the $(2\pi)^3$ is a normalization convention on the field. Applying the Klein Gordon equation

$$(\partial^2 + m^2)\phi(\vec{p}, t) = (\partial_t^2 + \vec{p}^2 + m^2)\phi(\vec{p}, t) = 0$$

In this form, we recognize that this is just the equation of motion for a harmonic oscillator, $\partial_t^2\phi = -\omega^2\phi$ with energy $\omega^2 = (\vec{p})^2 + m^2$.

The Canonical Quantization

Quantum mechanics consists of four fundamental postulates. Here we enumerate the postulates and their classical counter parts [58]:

1. **Particle State:** In classical mechanics, a the state of a particle is determined by two variables $x(t)$ and $p(t)$. In quantum mechanics, the state is a vector $|\psi\rangle$ in a Hilbert space \mathcal{H} .
2. **Dynamic Variables :** Classically, all dynamical variables are a function only $x(t)$ and $p(t)$. In quantum mechanics, classical variables represented as a function of x and p are instead represented by Hermitian operators X and P that satisfy the commutation relation $[X, P] = XP - PX = i/\hbar$.

- 3. Measurement:** Classically, the particle state is unaffected by measurement and strictly deterministic based on the values of x and p . Quantum mechanically, a particle in a state $|\psi\rangle$ when measured will yield an eigenvalue ω of the operator Ω with probability $|\langle\omega|\psi\rangle|^2$. After measurement, the particle state is in the corresponding eigenvector $|\omega\rangle$.
- 4. Time Evolution:** Classically, p and x change with time according to Hamilton's (or Lagrangian) equations of motion. Quantum mechanics asserts the state vector evolves with time according to the Schrödinger equation: $i\hbar\frac{d}{dt}|\psi(t)\rangle = H|\psi(t)\rangle$. Where H is the Hamiltonian with classical p and q replaced by the corresponding quantum mechanical operators.

The canonical quantization arises because the position and momentum operators no longer commute (postulate 2). This is the source of the famous Heisenberg uncertainty principle that there are no simultaneously measurable states of p and q .

If we consider the quantum harmonic oscillator with Hamiltonian:

$$H = \frac{p^2}{2} + \frac{1}{2}\omega^2 q^2$$

and define the creation (a^\dagger) and annihilation (a) operators

$$a = \sqrt{\frac{\omega}{2}}q + \frac{1}{\sqrt{2\omega}}p \text{ and } a^\dagger = \sqrt{\frac{\omega}{2}}q - \frac{1}{\sqrt{2\omega}}p$$

we can re-write the position and momentum operators in terms of these operators:

$$q = \frac{1}{\sqrt{2\omega}}(a + a^\dagger) \text{ and } p = -i\frac{\omega}{2}(a - a^\dagger)$$

substituting into the Hamiltonian we find a simple solution after applying the commutation relation $[p, q] = -i$ (using units where $\hbar = 1$):

$$H = \left(a^\dagger a + \frac{1}{2} \right) \omega$$

Consequently the operations $[H, a]|E\rangle = (E - \omega)a|E\rangle$ and $[H, a^\dagger]|E\rangle = (E + \omega)a^\dagger|E\rangle$ show that the operators raise and lower the energy of the harmonic oscillator in multiples of ω . The energy levels are quantized (i.e. restricted) to integer units of ω . a and a^\dagger are also referred to as ladder operators, as they raise and lower the energy state by 1 unit of ω with a non zero ground state energy $\omega/2$.

We can build a quantum field by promoting the coordinate q to a field ϕ in the same way as the classical field theory. This step is often referred to by a misleading name: “the second quantization”, however there is only a single quantization in the theory (the quantum quantization). We now write the solution to the Klein-Gordon equation as an infinite sum of creation and annihilation operators that create or destroy a particle with energy $\omega_p^2 = p^2 + m^2$ designated by its four-momentum p . Taking the Fourier transform:

$$\phi(\vec{x}, t) = \int \frac{d^3 p}{\sqrt{2\omega_p}} [a_p e^{ipx} + a_p^\dagger e^{-ipx}]$$

Quantum fields allow us to account for the observed phenomenon that particles are created and destroyed. Physical law is stated in terms of fields with infinite degrees of freedom that describe particles as excitations at points in space time. Ultimately, this will allow us to describe interactions occurring through virtual particles that are created and destroyed, but never observed. These kinematically unconstrained effects are a departure from the typical study of quantum systems with finite degrees of freedom.

Although the above result only applies for a real scalar field (spin 0), the corresponding fermionic field (spin- $\frac{1}{2}$) field can be found similarly starting from the Dirac equation but now includes spinors. Written in momentum space

$$\psi = \sum_s \int \frac{d^3k}{(2\pi)^3 2E_p} [u(s, p) a_{s,p} e^{-ikx} + v(s, p) a_{s,p}^\dagger e^{ikx}]$$

$$\bar{\psi} = \sum_s \int \frac{d^3k}{(2\pi)^3 2E_p} [\bar{v}(s, p) a_{s,p} e^{-ikx} + \bar{u}(s, p) a_{s,p}^\dagger e^{ikx}]$$

where the sum is taken over spin polarizations s and u, v, \bar{u}, \bar{v} are dirac four-spinors which satisfy the completeness relationships with

$$\sum_s u\bar{u} = p^\mu \gamma_\mu + m$$

$$\sum_s v\bar{v} = p^\mu \gamma_\mu - m$$

Here, the gamma matrices γ^μ satisfy the anti-commutation relationships $\{\gamma^\mu, \gamma^\nu\} = \gamma^\mu \gamma^\nu + \gamma^\nu \gamma^\mu = 2\eta^{\mu\nu}$. The creation and annihilation operators now create states with a spin and momentum.

2.1.2 Symmetries

Noether's Theorem

The importance and the consequences of symmetries cannot be understated in physics. The invariance of the action (equivalently the equations of motion) under linear translations of the coordinates gives rise to conservation of momentum. Similarly, rotations of the coordinate space yields the conservation of angular momentum. This is a consequence of Noether's theorem, that every continuous symmetry of the action has a corresponding conservation law.

To be concrete, let us consider an action that is invariant under some field transformation $\phi \rightarrow \phi + \delta\phi$. If we consider a gauge transformation $\phi \rightarrow e^{i\beta}\phi$ then the

infinitesimal transformation is $\delta\phi = i\beta\phi$, here we assume the principle of minimal action ($\delta S = 0$) under this variation. This is the same as $\delta\mathcal{L}$ up to surface terms in the action integral.

$$\delta\mathcal{L} = \left[\frac{\partial\mathcal{L}}{\partial\phi}\delta\phi + \frac{\delta\mathcal{L}}{\partial_\mu(\partial_\mu\phi)}\delta(\partial_\mu\phi) \right] = i\beta \left[\frac{\partial\mathcal{L}}{\partial\phi}\phi + \frac{\partial\mathcal{L}}{\partial(\partial_\mu\phi)}(\partial_\mu\phi) \right]$$

We further require that the solution satisfying the Euler-Lagrange equations, and exchange the first term:

$$= i\beta \left[\partial_\mu \left[\frac{\partial\mathcal{L}}{\partial(\partial_\mu\phi)} \right] \phi + \frac{\partial\mathcal{L}}{\partial_\mu\phi}(\partial_\mu\phi) \right] = i\beta \left[\partial_\mu \left[\frac{\partial\mathcal{L}}{\partial(\partial_\mu\phi)}\phi \right] \right] = \partial_\mu \left[\frac{\partial\mathcal{L}}{\partial(\partial_\mu\phi)} \right] = \partial_\mu j^\mu$$

Where j^μ is the conserved current corresponding to the continuous symmetry. Accordingly minimal action tells us $\delta\mathcal{L} = 0 = \partial_\mu j^\mu$. Now consider the consequences for fermionic Lagrangian:

$$\mathcal{L} = \bar{\psi}(i\gamma^\mu\partial_\mu - m)\psi$$

the corresponding current is $j^\mu = i\bar{\psi}\gamma^\mu\psi = (\rho, \vec{j})$ where ρ is charge density and \vec{j} is electric current. When we expand the index and $\partial_\mu = (\frac{d}{dt}, \vec{\nabla})$ we obtain the continuity equation:

$$\frac{d\rho}{dt} + \nabla \cdot \vec{j} = 0$$

This corresponds to the conservation of charge. The change in the charge density of the system is equal to the outflowing current. It is critical to the study of particle physics that we understand the consequences of symmetries of the Lagrangian under such transformations. The following sub-section will discuss the concept of symmetry in finer detail.

Symmetry Groups and Algebras [41]

Describing symmetry mathematically requires the definition of groups. The study of groups is known as group theory and it is a subfield of abstract algebra. A group is an algebraic structure that consists of a set G (eg. Integers) and a pairwise operation (eg. multiplication) $a \cdot b = c$ where $a, b, c \in G$. The group must also contain an identity $i \in G$ (ex. 1) such that $i \cdot g = g$ for all $g \in G$. All elements $g \in G$ must have an inverse $g^{-1} \in G$ such that $g \cdot g^{-1} = g^{-1}g = i$. The operation must additionally satisfy associativity $(a \cdot b) \cdot c = a \cdot (b \cdot c)$. The group does not necessarily need to be commute $a \cdot b = b \cdot a$, a common example in physics is matrix multiplication. $M_{ij}N_{jk} \neq N_{ij}M_{jk}$ for all matrices M and N .

We can check the group of rotations $SO(3)$ (read special orthogonal group of dimension 3) about the origin in euclidian \mathbb{R}^3 under composition for group like properties. Clearly the composition of two rotations is another rotation, the inverse rotation is just rotating backward, and the identity is performing no rotation at all. The rotations can be represented by 3 by 3 matrices with real number valued element, determinant ± 1 , and inverses equal to their transpose $g^{-1} = g^T$. The group $SU(2) \cong SO(3)/\mathbb{Z}_2$, that is, $SU(2)$ is a double covering of $SO(3)$ corresponding to a redundancy of 2 elements $SU(2)$ for each element of $SO(3)$.

A lie group is a continuous group with a multiplicative law that is a differentiable function of the parameters. linear combinations of generator elements:

$$e^{-i\beta^i T^i} = U_G(\vec{\beta})$$

where the T^i are the generator elements. For instance, we can build rotations in 3 dimensional space using the dimension 2 representation by exponentiating the Pauli

spin matrices $\vec{\sigma} = (\sigma_1, \sigma_2, \sigma_3)$ with a conventional (1/2) normalization:

$$L_1 = \frac{\sigma_1}{2} = \frac{1}{2} \begin{pmatrix} 0 & 1 \\ 1 & 0 \end{pmatrix} \quad L_2 = \frac{\sigma_2}{2} = \frac{1}{2} \begin{pmatrix} 0 & -i \\ i & 0 \end{pmatrix} \quad L_3 = \frac{\sigma_3}{2} = \frac{1}{2} \begin{pmatrix} 1 & 0 \\ 0 & -1 \end{pmatrix}$$

A lie algebra of a group G is defined by the commutation relations of its generators T^i , specifically:

$$[T^i, T^j] = T^i T^j - T^j T^i = i c_{ijk} T^k$$

where c_{ijk} are the structure constants of the algebra. The algebra is abelian if and only if all $c_{ijk} = 0$. Otherwise, by construction the c_{ijk} must be anti-symmetric in any of the two indices.

The Poincaré symmetry group $SO(3, 1)$ (Lorentz transformations + translations) is the source of the most fundamental conservation laws and the statistics of the quantum fields. A transformation of the space-time coordinate x^μ takes the form:

$$x^\mu \rightarrow \Lambda^\mu{}_\nu x^\nu + a^\mu$$

where $\Lambda^\mu{}_\nu$ is a transformation from the Lorentz group $SO(3, 1)$ (boosts and rotations) and a_μ is a translation consisting of single 4-vector $\mathbb{R}^{3,1}$.

The generators of the Poincaré group can be enumerated as generalized angular momentum operators: $M_{\mu\nu} = i(x_\mu \partial_\nu - x_\nu \partial_\mu)$ with the commutation relations:

$$[M_{\mu\nu}, M_{\rho\sigma}] = -i(\eta_{\mu\rho} M_{\nu\sigma} - \eta_{\nu\sigma} M_{\mu\rho} + \eta_{\nu\sigma} M_{\mu\rho} - \eta_{\mu\rho} M_{\nu\sigma})$$

However, by decomposing the operators into rotations and boosts these relations become much simpler. Define:

$$J_i = \frac{1}{2}\epsilon_{ijk}M_{jk} \text{ and } P_i = i\partial_i \text{ and } K_i = M_{0i}$$

Where J and P are the familiar angular and linear momentum operators. The K_i correspond to rapidity boosts. With this notation, we can derive more easily digested commutation relations:

$$\begin{aligned} [J_i, J_j] &= i\epsilon_{ijk}J_k & [P_0, J_j] &= 0 \\ [P_i, J_j] &= i\epsilon_{ijk}P_k & [P_0, K_i] &= iP_i \\ [P_i, K_j] &= iP_0\delta_{ij} \end{aligned}$$

For a given lie algebra, the dimension of the representation of the group is physically related to the quadratic Casimir. For a given concrete representation L_n for a n dimensional representation, the quadratic Casimir C_2 can be written as:

$$L_n^2 = C_2(L_n)I \text{ and for example in } SO(3) \quad J^2 = j(j+1)I$$

where I is the identity. In $SO(2)$ the j representation has dimension $n = 2j + 1$ with quadratic Casimir $j(j+1)$. For $j = 0$ we have $n = 1$ where the rotation is trivial and $J^2 = 1$. For $j = 1/2$, $J^2 = \frac{3}{4}$ and $n = 2$. The Lorentz group can further be decomposed into $SO(3, 1) \cong SU(2) \times SU(2)$ where $SU(2)$ is the group of matrices with determinant ± 1 where the inverses are the conjugate transpose: $g^{-1} = (g^T)^*$. The fundamental fields in the Standard Model Lagrangian are characterized by the four corresponding combinations of $SU(2)$ representations. The $(0,0)$ representation of $SU(2) \times SU(2)$ corresponds to scalar spin 0 fields ϕ . The two chiral representations $(\frac{1}{2}, 0)$ and $(0, \frac{1}{2})$ correspond to fermionic matter fields $\psi, \bar{\psi}$. The $(\frac{1}{2}, \frac{1}{2})$ representation

corresponds to the fundamental vector boson fields W_μ^i, B_μ, G_μ^i and the fields after EWSB. $W_\mu^\pm, Z_\mu^0, A_\mu, G_\mu^i$.

There are three fundamental gauge groups which govern the Standard Model which also arise as symmetries in unrelated systems. The first group, $U(1)$, governing electric hyper charge is simply unitary 1×1 matrices i.e. complex numbers. The second group in context of rotations in Euclidian space is $SU(2)$ governing the weak force. The group is generated by the Pauli spin matrices plus the identity with structure constants $c_{ijk} = \epsilon_{ijk}$. The final group $SU(3)$, the strong force gauge group, is similar in structure to $SU(2)$ and is generated by the eight Gell-Man matrices (λ_i for $i = 1 \dots 8$) and the identity matrix. The Gell-Mann matrices are the three dimensional analogues to the Pauli spin matrices. Each matrix is traceless and satisfies the commutation relations with anti-symmetric structure constants f_{ijk} .

Consider a field transformation $\phi_a \rightarrow \phi'_a$ under some lie algebra with generators L_i such that the transformation is $U_g(\beta)$. In the Heisenberg picture of quantum mechanics where operators evolve but the states remain fixed:

$$\begin{aligned}\langle O' \rangle &= \langle \phi | U_g^{-1}(\beta) O U_g(\beta) | \phi \rangle \\ \implies O' &= U_g^{-1}(\beta) O U_g(\beta)\end{aligned}$$

we obtain a transformed quantum field:

$$\phi'_a = e^{-i\vec{\beta} \cdot \vec{T}} \phi_a e^{i\vec{\beta} \cdot \vec{T}}$$

the exponentials can be expanded as nested commutators

$$\phi'_a = \phi_a - i[\vec{\beta} \cdot \vec{T}, \phi_a] + \frac{(-i)^2}{2} [\vec{\beta} \cdot \vec{\tau}, [\vec{\beta} \cdot \vec{T}, \phi_a]] + O(\beta^2)$$

If L^i is the concrete representation of T^i . applying the commutation relation $[T^i, \phi_a] = -L_{ab}^i \phi_b$ gives the field transformation law in terms of the representation:

$$\phi'_a = \left(e^{i\vec{\beta} \cdot \vec{L}} \right)_{ab} \phi_b$$

Similarly the conjugate field ϕ_a^\dagger transforms in the adjoint representation:

$$\phi_a^\dagger = \left(e^{-i\vec{\beta} \cdot \vec{L}} \right)_{ab} \phi_b^\dagger$$

Local Gauge Invariance and the Covariant Derivative [53]

What if we promote the Lagrangian symmetry of fields under the Standard Model gauge symmetries to a local symmetry? The symmetry is local with a value dependent on the position in space-time x^μ . For example, a local $U(1)$ gauge symmetry would transform the field ψ as:

$$\psi(x) \rightarrow e^{i\alpha(x)} \psi(x)$$

If we then consider a direction derivative in the direction n^μ as defined:

$$n^\mu \partial_\mu \psi(x) = \lim_{\epsilon \rightarrow 0} \frac{\psi(x + \epsilon n) - \psi(x)}{\epsilon}$$

This is not going to have a simple transformation law, since the two states are not at the same point in space time. We need a connection $U(x, y)$ the derivative transformations simply. Taking the directional derivative:

$$n^\mu \partial_\mu \psi(x) = \lim_{\epsilon \rightarrow 0} \frac{1}{\epsilon} (\psi(x + \epsilon n) - U(x + \epsilon n, x) \psi(x))$$

where $U(x, y)$ is our connection and transforms as:

$$U(x, y) \rightarrow e^{i\alpha(x)} U(x, y) e^{-i\alpha(y)}$$

such that when we apply the transformation to the directional derivative we obtain:

$$n^\mu \partial_\mu \psi(x) = \lim_{\epsilon \rightarrow 0} \frac{1}{\epsilon} e^{i\alpha(x+n\epsilon)} (\psi(x + \epsilon n) - U(x + \epsilon n, x) \psi(x))$$

Now lets expand the transformation for an infinitesimal ϵ :

$$\begin{aligned} U(x + \epsilon n, x) &\approx U(x, x) + c\epsilon n^\mu A_\mu(x) + O(\epsilon^2) \\ &= 1 + c\epsilon n^\mu A_\mu(x) + O(\epsilon^2) \end{aligned}$$

The connection between x and itself was trivial and we have specified an arbitrary (while suggestive) constant $c = ie$. If we would then like to see how this field A_μ transforms we need to check the $U(x, y)$ transformation:

$$\begin{aligned} e^{i\alpha(x)} U(x + \epsilon n, x) e^{-i\alpha(y)} &= (1 + i\alpha(x + n\epsilon))(1 - ie\epsilon n^\mu A_\mu)(1 - i\alpha(x)) \\ &= 1 + i\alpha(x + n\epsilon) - ie\epsilon n^\mu A_\mu - i\alpha(x) \end{aligned}$$

comparing this to the expansion of $U(x + \epsilon n, x)$ we see:

$$\begin{aligned} 1 + ie\epsilon n^\mu A_\mu(x) &\rightarrow 1 + i\alpha(x + n^\mu \epsilon) - ie\epsilon n^\mu A_\mu(x) - i\alpha(x) \\ A_\mu(x) &\rightarrow \left[\frac{\alpha(x + n^\mu \epsilon) + \alpha(x)}{en^\mu \epsilon} + A_\mu(x) \right] \\ A_\mu(x) &\rightarrow \left[A_\mu(x) - \frac{1}{n^\mu} \frac{1}{e} \partial_\mu \alpha(x) \right] \end{aligned}$$

If we pick the axes such that $n^\mu = 1$ then we have the transformation law for the gauge field: $A_\mu(x) \rightarrow A_\mu(x) - \frac{1}{e} \partial_\mu \alpha(x)$.

Now that we understand how the field component must transform under a gauge transformation, apply a $U(1)$ gauge transformation $U(\alpha)$ to a field. It should be understood that α is now local.

$$\psi' = U(\alpha)\psi = (e^{i\alpha})\psi \text{ and } \mathcal{L}' = U(\alpha)\psi\partial^\mu(U(\alpha)\psi)$$

because the transformation is local, the derivative will act on the transformation and an extra term is generated:

$$\partial^\mu(U(\alpha)\psi) = U(\alpha)\partial^\mu\psi + (\partial^\mu U(\alpha))\psi$$

This term is not gauge invariant as the transformation appears explicitly. To account for this, we introduce a substitution for $\partial^\mu \rightarrow D^\mu$ which will allow us to preserve gauge invariance

$$\partial^\mu \rightarrow D^\mu = \partial^\mu + igA^\mu$$

Checking the transformation law for $\partial^\mu\psi \rightarrow D^\mu\psi$ with the necessary A^μ transformation included

$$\begin{aligned} (\partial^\mu + igA^\mu)\psi &\rightarrow \left(\partial^\mu + ig(A^\mu + \frac{1}{g}\partial^\mu\alpha) \right) (e^{-i\alpha}\psi) \\ &= e^{-i\alpha}\partial^\mu\psi + igA^\mu e^{-i\alpha}\psi - i\partial^\mu\alpha e^{-i\alpha}\psi + i\partial^\mu\alpha e^{-i\alpha}\psi \\ &= e^{-i\alpha}(\partial^\mu + igA^\mu)\psi \\ &= U(\alpha)D^\mu\psi \end{aligned}$$

For non-abelian gauge groups, the introduction of the covariant derivative will enforce local gauge symmetry of the Lagrangian, but require modified substitutions

$$A^{\mu,i} \rightarrow A^{\mu,i} - c_{ijk}\alpha_j A^{\mu,k} - \frac{1}{g}\partial^\mu\alpha_i L^i$$

$$\partial^\mu \rightarrow D^\mu = \partial^\mu + igA_{\mu,i}L_i$$

where c_{ijk} are the structure constants, A_i are the gauge bosons for the transformation, and L_i are the concrete representations of the generators.

The consequence of promoting the partial derivatives to gauge symmetry preserving covariant derivatives yields new terms in the Lagrangian

$$i\bar{\psi}\partial_\mu\gamma^\mu\psi \rightarrow i\bar{\psi}\partial_\mu\gamma^\mu\psi - e\bar{\psi}A_\mu\gamma^\mu\bar{\psi}$$

New gauge interactions with the matter fields have arisen. The force's symmetry group and the invariance of the Lagrangian naturally induce the force's interactions with matter. Symmetries always always have important consequences to a theory. The following section will expand in detail the variety of terms in the Standard Model Lagrangian.

2.1.3 The Standard Model Lagrangian

The Standard model of particle physics is a quantum field theory of 3+1 dimensional spacetime governed by a Lagrangian with four sectors and three local gauge symmetries developed to describe and study the physics of fundamental particles in the physical, observable universe.

The Standard Model Lagrangian has three types of fundamental fields: spin-0 (scalar boson), spin-1/2 (dirac fermion), and spin 1 (vector boson). Any theory describing

Table 2.1: Standard Model particle representations under the symmetry groups $SU(2)$ and $SU(3)$ respectively n_2 and n_3 . Also listed is associated electroweak hyper charge Y as well as the electric charge Q

	q_L	l_L	u_R	d_R	e_R	ν_R	ϕ
n_3	3	1	3	3	1	1	1
n_2	2	2	1	1	1	1	2
$Y_{U(1)}$	1/6	-1/2	2/3	-1/3	-1	0	1/2
$Q = Y + T_L^3$	2/3	-1	2/3	-1/3	-1	0	0

Table 2.2: The fundamental fields types contained in the SM Lagrangian [66]

Field	Lagrangian Term	Field Dim. [Mass]
Scalar Field	$(1/2)(\partial_\mu \phi)(\partial^\mu \phi)$	$[\phi] = M^2$
Dirac Field	$\bar{\psi}M\psi$	$[\psi] = M^{3/2}$
Field Stress Tensor	$-(1/4)F_{\mu\nu}F^{\mu\nu}$	$[F_{\mu\nu}] = M^2$
Vector Field	$F_{\mu\nu} = \partial_\mu A_\nu - \partial_\nu A_\mu$	$[A_\mu] = M$

Table 2.3: The types of terms included in the Standard Model Lagrangian [66]

Coupling Type	Lagrangian Term	Coupling Dim [Mass]
Scalar Coupling w/ Gauge Bosons	$\tilde{g}A_\mu A^\mu \phi$	$[\tilde{g}] = M$
	$gA_\mu(\partial^\mu \phi)\phi$	$[g] = 1$
Scalar self-couplings	$\tilde{g}\phi^3$	$[\tilde{g}] = M$
	$g\phi^4$	$[g] = 1$
Gauge Coupling	$g\bar{\psi}\gamma_\mu \psi A^\mu$	$[g] = 1$
Triple Gauge Coupling	$A_\mu A^\mu \partial_\nu A^\nu$	$[g] = 1$
Quartic Gauge Coupling	$g^2(A_\mu A^\nu)^2$	$[g] = 1$
Yukawa Coupling	$g\bar{\psi}\psi\phi$	$[g] = 1$

Table 2.4: The 19 free parameters of the Standard Model with values as dictated by experimental observation

Category	Name	Parameter	Remarks
Lepton Masses	Electron, Tau, and Mu	m_e, m_μ, m_τ	$m_l = (\lambda_l \nu)/2$
Fermion Masses	Up, Charm, Top Down, Strange, Bottom	m_u, m_c, m_t m_d, m_s, m_b	
CKM Matrix	Mass-Flavor Mixing Angles CP Violating Phase	$\theta_{12}, \theta_{23}, \theta_{13}$ δ	
Higgs Parameters	Vacuum Expectation Value Higgs Mass	ν m_h	$\nu = \mu/\sqrt{\lambda}$ $m_h^2 = -2\mu^2$
Force Strength	Gauge Couplings	g, g', g_s	$\alpha, \alpha_w, \alpha_s$
CP Violating Terms	Vaccum QCD Angle	θ_{QCD}	unobserved

gravity would also include a unique spin-2 particle mediating gravity known as the graviton. A supersymmetric theory of gravity would also include a particle of spin-3/2, a supersymmetric partner of the graviton known as the gravitino. The complete field content of the theory is listed in Table 2.2 with the associated mass dimensions of the fields. Dimensional analysis tells us the mass dimension of the Lagrangian is 4 as dictated by the action being unitless. Requiring mass dimension 4 of each term (by dimensional analysis) and requiring that all indices are contracted (Lorentz invariance) is highly constraining to the types of terms within the Lagrangian. The types of interactions (after EWSB) are listed in Table 2.3.

It is important to understand the principal components of the theory, so we can separate the aspects which are emergent from the underlying assumptions and those which are put in by hand. Here we list principal aspects of the theory.

1. **Relativistic Theory:** The Lagrangian must be invariant under Lorentz transformations as well as rotations and translations in 3+1 dimensional spacetime.
2. **Matter:** There are three families of fermionic particles consisting of an up-type quark with an associated down-type quark and a lepton with an associated neutrino.
3. **Fundamental Charges:** Each particle transforms as a multiplet of the gauge symmetries as dictated in Table 2.1. This determines how the 3 forces interact with matter.
4. **Gauge Symmetry:** The fundamental action must be invariant under local gauge transformations.
5. **Free Parameters:** The Lagrangian includes 19 free parameters which set the experimentally observed fermion masses, interaction strengths, mass-flavor mixing, the vacuum potential and the possible charge parity symmetry violating terms in the strong sector (Table 2.4).

6. Renormalizable: All terms of the Standard Model have been shown to be renormalizable. This also means there are no terms with mass dimension greater than 4. Higher dimension terms have dimensions of inverse mass and are irrelevant until experiments are made capable of probing near the energy scale Λ where the Standard Model theory breaks down.

The simplicity of the governing assumptions and naturalness of free parameters are certainly an ambition of any theory of fundamental particle physics, but a more aesthetically pleasing theory is not necessarily the ultimate goal. The Standard Model, is a tool towards finding a more complete theory. The theory admits incompleteness in its formulation (eg. the exclusion of gravity), but achieves incredible experimental verification [36] of theoretical predictions [7] accurate to 14 decimal places where the theory is tested.

The Standard Model Lagrangian can be grouped into four sectors written in a simplified form where the individual terms have not been expanded and EWSB has yet not occurred:

$$\begin{aligned}\mathcal{L}_{SM} &= \mathcal{L}_{Gauge} + \mathcal{L}_{Fermion} + \mathcal{L}_{Higgs} + \mathcal{L}_{Yukawa} \\ &= \left(-\frac{1}{4} F_{\mu\nu} F^{\mu\nu} \right) + (\bar{\psi} i \gamma^\mu \partial_\mu \psi) + \left(\frac{1}{2} (\partial_\mu \phi)^2 + V(\phi) \right) + (\bar{\psi}_i y_{ij} \psi_j \phi)\end{aligned}$$

In our discussion, we will expand each sector in terms of the field content and point out free parameters of the theory where they have been included.

Gauge Sector

The gauge sector consists of the field stress energy tensor of the 3 corresponding types of gauge bosons: G^i (gluons of the color force), W^i (W 's of the weak force) and B (of the weak hyper charge). Here the index i enumerates their multiplicity. There are 8 gluons, 3 W 's and a single B . Ultimately, we will arrive have 8 gluons, W^\pm , Z^0 ,

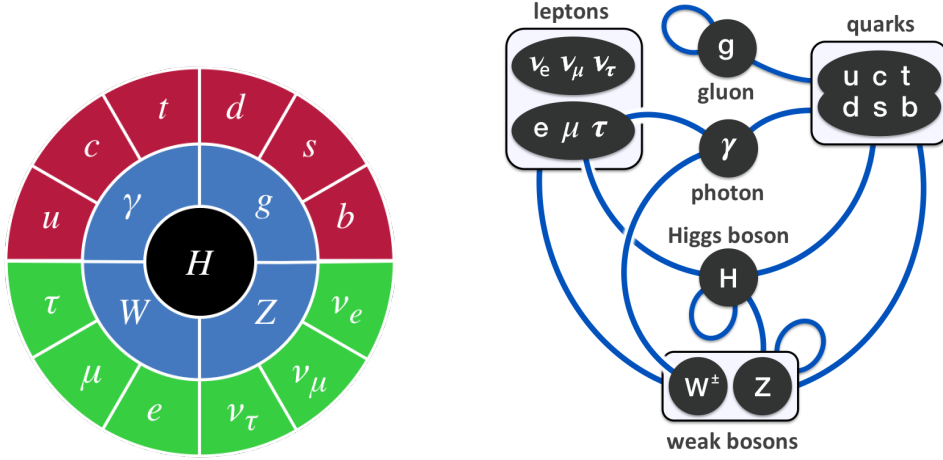


Figure 2.1: (left) A representation of the particle content of the Standard Model. The inner circle is the unique scalar Higgs field. The next ring consists of the gauge bosons. The outer ring are the fermionic fields broken into quarks and leptons. (right) Lines drawn between particles show the fundamental interaction terms in the theory. Higher order effects can generate interactions not shown here (such as $h \rightarrow \gamma\gamma$ which is generated through a top quark loop).

and the photon A after the $SU(2) \times U(1)$ symmetry is spontaneously broken and the scalar field ϕ takes on a new vacuum state. The strong color force remains unbroken.

Although not exclusive to this sector, the gauge transformations add three free parameters to the theory corresponding to the gauge coupling strengths: g, g' , and g_s .

$$\mathcal{L}_{Gauge} = -\frac{1}{4}F_{\mu\nu}^i F^{\mu\nu i} = -\frac{1}{4}G_{\mu\nu}^i G^{\mu\nu i} - \frac{1}{4}W_{\mu\nu}^i W^{\mu\nu i} - \frac{1}{4}B_{\mu\nu} B^{\mu\nu} \quad (2.1)$$

where the double scripts correspond to the commutation relations for the gauge group algebra:

$$X_{\mu\nu} = [D_\mu X_\nu, D_\nu X_\mu]$$

$$[\partial_\mu X_\nu, \partial_\nu X_\mu] = \partial_\mu X_\nu - \partial_\nu X_\mu - g f_{ijk} X_\mu^j X_\nu^k$$

where g is the coupling constant, the D_μ terms correspond to the covariant derivative and the f_{ijk} are the corresponding structure constants for the non-abelian groups that arise from the non commuting generators of the algebra. The B_μ has no structure constants, the W^i of $SU(2)$ have $f_{ijk} = \epsilon_{ijk}$ and the $SU(3)$ has f_{ijk} determined by 8 Gell-mann λ_i generators. After EWSB, when these terms are written in the mass eigenstates of the theory, this sector generates self-interactions between gauge bosons such as the triple and quartic gauge couplings as shown in Table 2.3.

Fermion Sector

The fermion sector consists of the kinetic energy terms for each quark (up and down types) and leptons (lepton, neutrinos) in the Standard Model. The left handed quarks transform as an $SU(2)$ doublet:

$$q_{m\alpha}^L = \begin{pmatrix} u_{m\alpha} \\ d_{m\alpha} \end{pmatrix}^L \quad \text{and} \quad l_m^L = \begin{pmatrix} \nu_m \\ e_m^- \end{pmatrix}^L \quad (2.2)$$

where the subscript m denotes the family (1st, 2nd and 3rd generation) and α denotes the color charge (red, green, and blue). As the $SU(2)_L$ symmetry only acts on the left handed fermions we further separate the fermion sector into left and right components:

$$\begin{aligned} \mathcal{L}_{fermion,L} &= \bar{q}_{mL} i\gamma^\mu D_\mu q_{mL} + \bar{l}_{mL} i\gamma^\mu D_\mu l_{mL} \\ \mathcal{L}_{fermion,R} &= \bar{u}_{mR} i\gamma^\mu D_\mu u_{mR} + \bar{d}_{mR} i\gamma^\mu D_\mu d_{mR} + \bar{e}_{mR} i\gamma^\mu D_\mu e_{mR} + \bar{\nu}_{mR} i\gamma^\mu D_\mu \nu_{mR} \end{aligned}$$

Yukawa Sector

The Yukawa sector consists of couplings between the matter fields and the scalar field ϕ .

$$\mathcal{L}_{Yukawa} = - \sum_{m,n=1}^3 \left[y_{mn}^u \bar{q}_{mL} \tilde{\phi} u_{nR} + y_{mn}^d \bar{q}_{mL} \phi d_{nR} + y_{mn}^e \bar{l}_{mL} \phi e_{nR} \right] + (h.c)$$

The sum is taken over families n, m . The single scalar field ϕ is written in two ways: $\phi = (\phi^+, \phi^0)$ and ϕ after a $SU(2)$ gauge transformation $\tilde{\phi} = i\tau^2 \phi^\dagger = \epsilon \phi^\dagger = (\phi^\dagger, -\phi^-)$.

These terms need to be included such that we will later be able to generate mass terms for the up type quarks during EWSB. The reason we would not be able to write these terms is they would violate weak hyper charge gauge invariance. Similarly, we can not write explicit mass terms $\bar{u}_L m u_R + (h.c.)$ since the left and right particles have different hyper charge. To be concrete calculate the total hyper charge:

$$\bar{q}_{mL} \phi u_{nR} \implies Y = -\frac{1}{6} + \frac{1}{2} + \frac{2}{3} = 1 \neq 0$$

Whereas $\tilde{\phi}$ will transform in the adjoint representation:

$$\bar{q}_{mL} \tilde{\phi} u_{nR} \implies Y = -\frac{1}{6} - \frac{1}{2} + \frac{2}{3} = 0$$

The Yukawa sector contains a large number of the free parameters in the Standard Model (13 of 19). The individual masses of each fermion and lepton are generated by the y_{ij} terms which are set to agree with experimental values (9 free parameters). These parameters also set the coupling of the corresponding interaction strength with the Higgs boson after electroweak symmetry breaking.

The Yukawa couplings also implicitly include parameters characterizing the mismatch mixing between the quark flavor and mass eigenstates that occurs after EWSB (4 parameters). Had the mass flavor states been aligned, we would not need

the two family indices to be able to generate mass terms after EWSB. The mixing is characterized by the 3×3 unitary Cabibbo-Kobayashi-Maskawa (CKM) matrix V^{CKM} . The convention is chosen that flavor states u^I for up type quarks are aligned with the mass states u with the down type quarks rotated by the transformation $d_i^I = V_{ij}^{CKM} d_j$. From the unitarity condition, the matrix can be parameterized in 4 parameters: three mixing angles $\theta_{12}, \theta_{23}, \theta_{13}$ and a CP violating phase δ :

$$\begin{aligned} \begin{pmatrix} d^I \\ s^I \\ b^I \end{pmatrix} &= \begin{pmatrix} V_{ud} & V_{us} & V_{ub} \\ V_{cd} & V_{cs} & V_{cb} \\ V_{td} & V_{ts} & V_{tb} \end{pmatrix} \begin{pmatrix} d \\ s \\ b \end{pmatrix} \\ &= \begin{pmatrix} c_{12}c_{13} & s_{12}c_{13} & s_{13}e^{-i\delta} \\ -s_{12}c_{23} - c_{12}s_{23}s_{13}e^{i\delta} & c_{12}c_{23} - s_{12}s_{23}s_{13}e^{i\delta} & s_{23}c_{13} \\ s_{12}s_{23} - c_{12}c_{23}s_{13}e^{i\delta} & -c_{12}s_{23} - s_{12}c_{23}s_{13}e^{-\delta} & c_{23}c_{13} \end{pmatrix} \begin{pmatrix} d \\ s \\ b \end{pmatrix} \end{aligned}$$

where $c_{ij} = \cos \theta_{ij}$ and $s_{ij} = \sin \theta_{ij}$. It is important to note a similar matrix exists for leptons and is used for the study of neutrino oscillations known as the Pontecorvo-Maki-Nakagawa-Sakata (PMNS) matrix but is assumed to be 1 in the Standard Model.

Higgs Sector and Electroweak Symmetry Breaking

The Higgs sector consists of terms related to the single scalar field ϕ that transforms as a doublet of $SU(2)$ as $\phi = (\phi^+, \phi^0)$ and $\phi^\dagger = (\phi^-, (\phi^0)^\dagger)$ noting that $\phi^\dagger \phi = \phi^+ \phi^- + (\phi^0)^\dagger \phi^0$

$$\mathcal{L}_{higgs} = (D^\mu \phi)^\dagger (D_\mu \phi) + \mu^2 \phi^\dagger \phi + \lambda (\phi^\dagger \phi)^2 \quad (2.3)$$

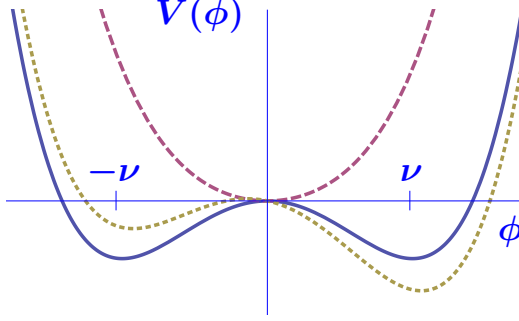


Figure 2.2: Shape of the ϕ potential varying the values of μ^2

This sector contains only two free parameters: μ and λ . The two parameters set the minimum and stability of the vacuum of the theory and set the masses of the fermions and gauge bosons after EWSB.

This sector determines the shape of the vacuum potential and is essential to the stability of the vacuum. We require that $\lambda > 0$ such that the potential is bounded from below, however μ^2 can be arbitrary. If $\mu^2 > 0$ we would have a minimum at $\phi = 0$ and $\langle \phi \rangle = 0$. If $\mu^2 < 0$ the theory becomes unstable at $\phi = 0$ with alternate stable vacuum.

As the field ϕ is a complex scalar field we can parameterize the field in terms of real scalar fields ϕ_1 and ϕ_2 :

$$\phi = \frac{1}{\sqrt{2}}(\phi_1 + i\phi_2) \text{ and } \phi^\dagger = \frac{1}{\sqrt{2}}(\phi_1 - i\phi_2)$$

Given this parameterization, the potential becomes:

$$V(\phi) = \frac{1}{2}\mu^2(\phi_1^2 + \phi_2^2) + \frac{\lambda}{4}(\phi_1^2 + \phi_2^2)^2$$

letting $x = \phi_1^2 + \phi_2^2$ and minimizing $\frac{\partial V}{\partial x} = 0$ we find $x_{min} = \nu$ where $\nu^2 = \mu^2/\lambda$. As the vacuum is stable the theory will move to this minimum (Figure 2.2). Expanding around the new vacuum $\phi'_1 = \nu + \phi_1$ and $\phi'_2 = \phi_2$ we obtain the new vacuum potential

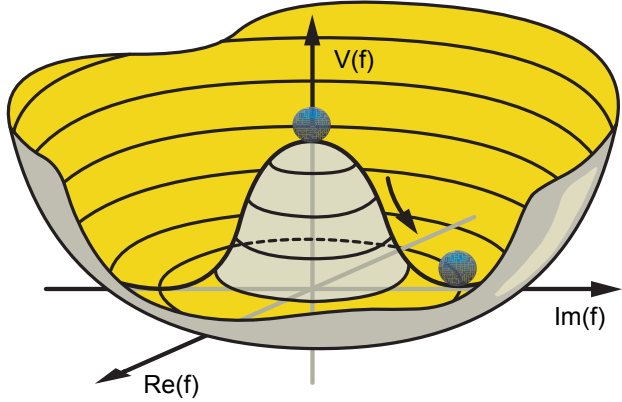


Figure 2.3: The Higgs potential exhibiting spontaneously broken symmetry, where the expected vacuum expectation value has moved from the 0 of the theory to ν in the broken theory

terms relative to the unbroken theory:

$$V_{\text{new}} = \frac{-\mu^2}{4\lambda} - \mu^2(\phi_1^2) + \lambda\nu\phi_1(\phi_1^2 + \phi_2^2) + \frac{\lambda}{4}(\phi_1^2 + \phi_2^2)^2$$

The first of these terms is a cosmological constant and does not affect the dynamics of the theory. However, such a constant would be relevant gravitational theories where gravity couples to energy. The Higgs Boson, h . the final piece of the Standard Model to be discovered is the excited mode about this new vacuum $\phi = (\nu + h(x), 0)$. The second term is the mass term for the Higgs field. The third and fourth correspond to the cubic and quadratic self interactions.

If we consider the kinetic term for the field ϕ at the now broken vacuum $\langle\phi\rangle = (0, \nu)$ in the gauged theory we find:

$$(D^\mu\phi)^\dagger(D_\mu\phi) = \frac{1}{\sqrt{2}} \begin{pmatrix} 0 & \nu \end{pmatrix} \left| \partial_\mu + ig\frac{\tau}{2} \cdot W_\mu + i\frac{g'}{2}B_\mu \right|^2 \frac{1}{\sqrt{2}} \begin{pmatrix} 0 \\ \nu \end{pmatrix}$$

Considering the weak gauge term:

$$\tau \cdot W = \begin{pmatrix} W_{\mu,3} & W_{\mu,1} - iW_{\mu,2} \\ W_{\mu,1} + iW_{\mu,2} & -W_{\mu,3} \end{pmatrix}$$

adding in the diagonal B_μ terms and taking the square (ignoring the derivative terms):

$$(D^\mu \phi)^\dagger (D_\mu \phi) \supset \frac{\nu^2}{8} [g^2(W_1^2 + W_2^2) + (g'B_\mu - gW_{\mu,3})^2]$$

Now if we perform a redefinition of the gauge fields into mass eigenstates we arrive at a clean expression:

$$\begin{aligned} W_\mu^\pm &= \frac{1}{\sqrt{2}}(W_{\mu,1} \pm iW_{\mu,2}) \\ A_\mu &= \frac{1}{\sqrt{g^2 + (g')^2}}(g'W_{\mu,3} + gB_\mu) = \sin \theta_W W_\mu^3 + \cos \theta_W B_\mu \\ Z_\mu &= \frac{1}{\sqrt{g^2 + (g')^2}}(g'B_\mu - gW_{\mu,3}) = \sin \theta_W B_\mu - \cos \theta_W W_\mu^3 \end{aligned}$$

Here we have defined the electroweak mixing angle θ_W in terms of a right triangle with legs g and g' . With this substitution:

$$\begin{aligned} (D^\mu \phi)^\dagger (D_\mu \phi) &\supset \frac{\nu^2 g^2}{4} W_\mu^- W_\mu^+ + \frac{(g + g')\nu^2}{8} Z_\mu^2 + (0 \times A_\mu^2) \\ &= \frac{1}{2} m_W^2 W_\mu^- W_\mu^+ + \frac{1}{2} m_Z^2 Z_\mu^2 + (0 \times A_\mu^2) \end{aligned}$$

EWSB has generated the mass terms for the gauge bosons! $m_{W^\pm} = \frac{\nu g}{\sqrt{2}} = 80.385$ [GeV], $m_Z = \frac{\nu}{2} \sqrt{g + g'} = \frac{m_W}{\cos \theta_W} = 91.1876$ [GeV] and the massless photon A_μ .

2.1.4 Maxwell's Laws

After EWSB we can perform a sanity check by deducing the well studied equations governing electrodynamics from the QFT description. Keeping only the terms that

contain the field A_μ :

$$\mathcal{L}_{EM} = -\frac{1}{4}F_{\mu\nu}F^{\mu\nu} - ie\bar{\psi}\gamma^\mu A_\mu\psi \text{ for } F_{\mu\nu} = \partial_\mu A_\nu - \partial_\nu A_\mu$$

where by definition $F_{\mu\nu} = \partial_\mu A_\nu - \partial_\nu A_\mu$. Applying the left side of Euler-Lagrange we find:

$$\partial_\mu \left(\frac{\partial \mathcal{L}}{\partial(\partial_\mu A_\nu)} \right) = -\frac{1}{2}\partial_\mu \left[\left(\frac{\partial}{\partial(\partial_\mu A_\nu)} F_{\mu\nu} \right) F^{\mu\nu} \right] = -\partial_\mu F^{\mu\nu}$$

The other term is simply $\frac{\partial \mathcal{L}}{\partial A_\mu} = -ie\bar{\psi}\gamma^\mu\psi = -J^\mu = -(\rho, \vec{J})$. Where ρ is charge density and \vec{J} is current. This yields our first equation:

$$\partial_\nu F^{\nu\mu} = J^\mu \tag{2.4}$$

recognizing the field stress tensor is antisymmetric we can apply a partial derivative and contract with the indices of the 4 dimensions anti-symmetric symbol to obtain:

$$\epsilon_{\theta\rho\mu\nu} \partial_\rho F_{\mu\nu} = 0 \tag{2.5}$$

Using these two laws we first see that the electric and magnetic field, E and B , can be defined in terms of the field stress tensor

$$F_{0i} = \partial_0 A_i - \partial_i A_0 = -\frac{\partial A}{\partial t} - \nabla\Phi = E$$

As for the magnetic field B_i :

$$\epsilon_{ijk}B^k = \epsilon_{ijk}\epsilon_{klm}\partial_l A_m = \epsilon_{kij}\epsilon_{klm}\partial_l A_m = (\delta_{il}\delta_{jm} - \delta_{im}\delta_{jl})\partial_l A_m = \partial_i A_j - \partial_j A_i = F_{ij}$$

From the first current law we immediately obtain two of Maxwell's laws:

$$\partial_i F^{0i} = J^0 \implies \nabla \cdot E = \rho$$

and for the second we separate the sum between space and time-like components:

$$\partial_i F^{ji} + \partial_0 F^{j0} = J^j$$

$$\epsilon_{jik} \partial_i B_k - \partial_0 E^j = J^j$$

$$\nabla \times B - \frac{\partial E}{\partial t} = \vec{J}$$

The remaining two laws come from manipulations of the antisymmetry of the field stress tensor:

$$0 = \epsilon_{0ijk} \partial_i F^{jk} = \epsilon_{0ijk} \partial_i \epsilon_{0kl} B_l = \epsilon_{jk0i} \epsilon_{jkl0} \partial_i B_l = -\delta_{il} \partial_i B_l$$

$$\implies \nabla \cdot B = 0$$

The time component of the field stress tensor in the last equation in terms of E and B yields

$$\epsilon_{\mu\nu 0\sigma} \partial_\nu F^{0\sigma} + \epsilon_{\mu\nu i\sigma} \partial_\nu F^{i\sigma} = 0 \text{ for } i = 1, 2, 3$$

$$\epsilon_{0\sigma\mu\nu} \partial_\nu E^\sigma + \epsilon_{\mu\nu i\sigma} \epsilon_{0i\sigma k} \partial_\nu B_k = 0 \text{ where } k \neq 0$$

The first term is $\nabla \times \vec{E}$. Separately expanding the second term by permuting the ϵ indices

$$\begin{aligned}
& \epsilon_{i\sigma\mu\nu} \epsilon_{i\sigma k0} \partial_\nu B_k \text{ where } k \neq 0 \\
& = (\delta_{uk} \delta_{\nu 0} - \delta_{\mu 0} \delta_{\nu k}) \partial_\nu B_k \\
& = \partial_0 B_\nu - \partial_k B_k \\
& = \frac{\partial \vec{B}}{\partial t} - \nabla \cdot \vec{B} \\
& = \frac{\partial \vec{B}}{\partial t}
\end{aligned}$$

The last line used $\nabla \cdot \vec{B} = 0$. Combining the two terms:

$$\nabla \times \vec{E} + \frac{\partial \vec{B}}{\partial t} = 0$$

We should not forget that the assumptions that led us to these equations. Firstly, the existence of the field stress tensor. We obtained this by writing the most general Lorentz invariant and gauge invariant Lagrangian possible. Additionally, we made geometric arguments about the continuity in the derivative under the local $U(1)$ gauge symmetry in the Lagrangian to obtain the interaction term between the gauge boson and the electron ψ . Everything we understand from the study of electromagnetism naturally arises from the Standard Model Lagrangian. This even includes the curiosity of electromagnetism that when the theory is written in terms of vector and scalar potential the equations remain unchanged under a gauge transformation. However, in a gauge theory this is the fundamental principle rather than a consequence of the form of Maxwell's equations. I feel compelled to note that this is amazing.

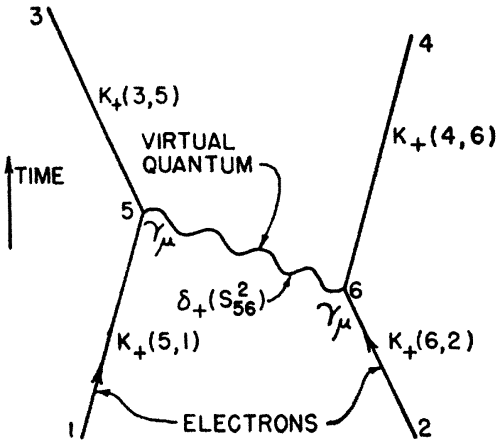


Figure 2.4: The Feynman diagram for describing t-channel scattering of two electrons through the exchange of a virtual photon. This particular figure was the example used in Feynman's original paper describing the pictorial representation of calculating matrix elements.

2.1.5 Feynman Diagrams

Historically, the outcome of a scattering event in a quantum field theory was tedious to calculate. One of Feynman's greatest contributions to the field of particle physics was an organizational tool to group and quickly calculate terms in the perturbative expansion of the action [31]. The diagrams, Feynman diagrams (Figure 2.4), take the form of a directed graph of lines and vertices providing a representation the components needed in a scattering calculation calculation. This treatment is intuitive to work with and incredibly information dense minimal effort to construct. In this section we will derive principal aspects of how scattering events can be represented leaving the subtleties to the references [53, 61].

We write down a simple scalar quantum field theory with a single scalar field ϕ and a ϕ^3 interaction term:

$$\mathcal{L} = \mathcal{L}_0 + \mathcal{L}_{int} = \frac{1}{2}(\partial_\mu\phi)(\partial^\mu\phi) + m^2\phi^2 - \frac{\kappa}{3!}\phi^3$$

In the Schrödinger picture of quantum mechanics the states $|\psi\rangle$ evolve in time according to the Hamiltonian $H_S = H_0 + H_{int}$. The component H_0 is the free particle component and $H_{int} = -\mathcal{L}_{int}$ is the interacting component. The quantum state obeys the Schrödinger equation:

$$i\frac{d}{dt}|\psi\rangle = H_S|\psi\rangle$$

This gives we obtain the solution $|\psi(t, x)\rangle = U(t, 0)|\psi(0, x)\rangle$ where we define the time evolution operator $U(t, t_0) = \exp(-iH_S(t - t_0))$. The observables are constant in time and the expected value of some operator (in our case the quantum field ϕ) on a state at time t can be written:

$$\langle\phi(t, x)\rangle = \langle x, t_0 | e^{iH_S(t-t_0)} \phi(x) e^{-iH_S(t-t_0)} | x, t_0 \rangle$$

In this interpretation of quantum mechanics, we instead absorb the time dependence into the operator, leaving the states constant.

$$\phi(t, x) = e^{iH_S t} \phi(x) e^{-iH_S t}$$

Let us define a new interacting field $\phi_I = e^{iH_0 t} \phi e^{-iH_0 t}$ which evolves with the free Hamiltonian. In the Heisenberg picture, the field can be written in terms of ϕ_I as:

$$\phi(t, x) = e^{iH_S t} e^{-iH_0 t} \phi_I(x) e^{iH_0 t} e^{-iH_S t} = U^\dagger(t) \phi_I U(t)$$

We have defined a unitary operator $U(t) = e^{iH_0t}e^{-iH_S t}$. If we apply a time derivative to $U(t)$ we find:

$$\begin{aligned} i\partial_t U(t) &= -e^{iH_0t}H_0e^{-iH_S t} + e^{iH_0t}H_S e^{-iH_S t} \\ &= e^{iH_0t}H_{int}e^{-iH_S t} \\ &= e^{iH_0t}H_{int}e^{-iH_0t}e^{iH_0t}e^{-iH_S t} \\ &= H_I U(t) = \left(\frac{\kappa}{3!}\phi_I^3\right) U(t) \end{aligned}$$

We have shown the time evolution operator obeys the Schrödinger equation under a Hamiltonian H_I , corresponding to H_{int} in the Heisenberg picture. Solving this equation, we obtain a time evolution operator $U(t) = T \exp(-\int dt iH_I)$. The operator T denotes time ordering of the time integrals for each term in the series expansion of the exponential which will not necessarily commute. Since each $H_I(t)$ will be integrated against its own dummy time variable, the time ordering operator will place $H_I(t)$ terms farther to the left, if they occur later in time. The reason for this time ordering requires detail that can be found in the references [53, 61].

We have succeeded in writing the time evolution operator in terms of the field ϕ_I , which evolves according to the free Hamiltonian where we already have a solution expressed in terms of creation and annihilation operators:

$$\phi_I(\vec{x}, t) = \int \frac{d^4 3}{(2\pi)^3 \sqrt{2E}} [a_p e^{ipx} + a_p^\dagger e^{-ipx}]$$

Now when we would compute the matrix element of $\phi\phi$ scattering, we expand the time evolution operator:

$$\begin{aligned} U(t, 0) &= 1 - i \int_0^t H_I(t') - \frac{1}{2} \int_0^t dt \int_0^{t'} dt' T\{H_I(t)H_I(t')\} \dots \\ &= 1 - i \frac{\kappa}{3!} \int d^4 x \phi^3(x) - \frac{1}{2} \frac{\kappa^2}{3! 3!} \int d^4 x \int d^4 x' T\{\phi^3(x)\phi^3(x')\} \dots \end{aligned}$$

For a matrix element \mathcal{M} if $\kappa < 1$ the theory is perturbative and the first non-zero term will dominate. For $2 \rightarrow 2$ scattering this term will be at order κ^2 and is computed by expanding the fields in terms of the creation and annihilation operators. Since $a|0\rangle = \langle 0|a^\dagger = 0$, the only terms which will contribute will be the terms with equal numbers of creation and annihilation operators coming from the $\phi^3(x)\phi^3(x')$ term.

Rather than expanding all of these fields, we use a result known as Wick's Theorem to convert the time ordered product into a series of pair-wise contractions between the individual fields. A contraction is defined for a field ϕ in terms of its positive and negative frequency components $\phi_I = \phi_I^+ + \phi_I^-$ where the $+$ field contains the annihilation operator, and $-$ the creation operator.

$$\overline{\phi(x)\phi(y)} = [\phi^+(x), \phi^-(y)] \text{ if } x^0 > y^0 \text{ else } [\phi^+(y), \phi^-(x)]$$

Given this definition, we state Wick's theorem as:

$$T[\phi_1(x_1) \dots \phi_N(x_N)] = N [\phi_1(x_1) \dots \phi_N(x_N) + \text{all possible contractions}]$$

Where N is the normal ordering operator which operates on a sequence of creation and annihilation operators by moving all creation operators to the left and annihilation operators to the right. By normally ordering a term in the expansion, we can eliminate all un-contracted terms as they will annihilate the vacuum. In lieu of a proof of Wick's theorem (which can be shown by induction) we can consider the process of taking the original term and moving creation operators to the left using commutation relations. Each time an operator is moved closer to its normal ordered configuration, we pick up a commutator between two elements which enters the expansion as a contraction. In fact, all possible contractions will be produced. When we are left with only normal ordered terms, if a term is not fully contracted the term will annihilate the vacuum

state. Lets enumerate the contractions on a ϕ^4 term:

$$\begin{aligned} & \left(\overbrace{\phi_1 \phi_2 \phi_3 \phi_4} + \overbrace{\phi_1 \phi_2 \phi_3 \phi_4} \right) + \\ & \left(\overbrace{\phi_1 \phi_2 \phi_3 \phi_4} + \overbrace{\phi_1 \phi_2 \phi_3 \phi_4} + \overbrace{\phi_1 \phi_2 \phi_3 \phi_4} \right) \end{aligned}$$

We have not yet considered the initial and final states. The external observable states of the diagram when evaluated on a fully contracted term correspond to an unscattered state. However, we are only interested in cases where the states have scattered. The only contributing terms are those where the number of inner + outer states is equal to the number of uncontracted fields in the inner term. A scalar field operating on the outer states give just a factor of 1 (equivalently a phase in momentum space) times the vacuum Ω . We can think of these terms as contractions between inner and outer states:

$$\langle p_f | \phi = \langle \Omega | \text{ and } \phi | p_i \rangle = | \Omega \rangle$$

To summarize, for a given term in the Lagrangian, if we restrict ourselves to scattered states, we need to have a full contracted term that includes the outer states. If we return to our ϕ^3 theory and attempt to scatter $\phi\phi \rightarrow \phi\phi$ we would need 4 ϕ fields to contract with the outer states. So at lowest order, this means we need a $\phi^3(x)\phi^3(y)$ term where two of the internal fields are contracted between x and y . If we had no contraction between the x and y terms, this would yield one term which would only be connected to a single outer state. If this is the case, the in going states p_1, p_2 would yield final states with momentum p_3 and $p_1 + p_2$, momentum conservation means $p_3 = 0$, so we do not include it in the calculation. It can be shown that all disconnected diagrams will not contribute to \mathcal{M} . An example contributing term

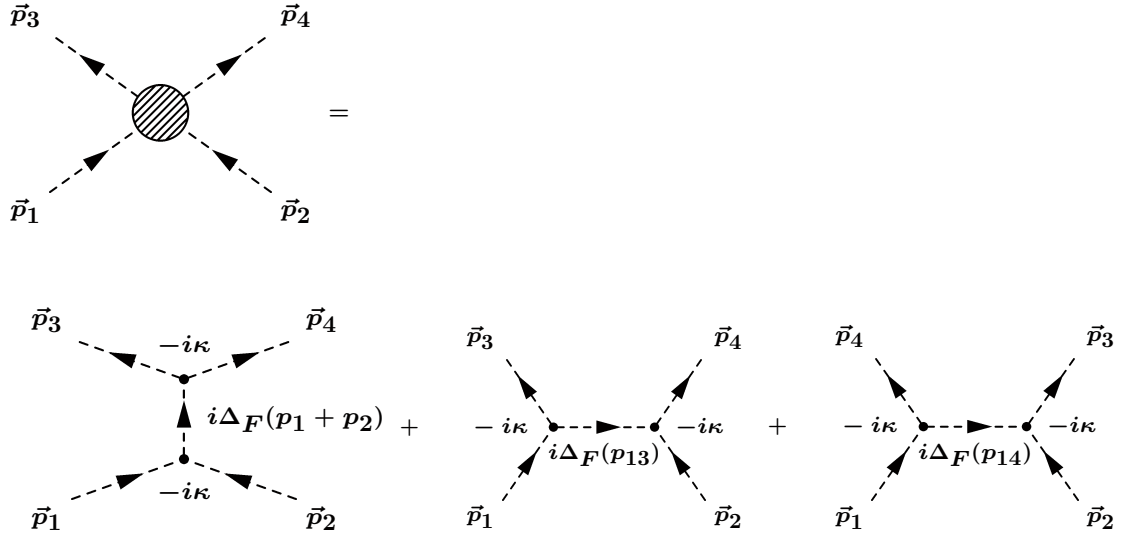


Figure 2.5: The 3 diagrams corresponding to $\phi\phi \rightarrow \phi\phi$ scattering at tree level (leading order). Time is directed vertically.

would look like:

$$\frac{(-i\kappa)^2}{2 * 3! * 3!} \langle p_1 p_2 | \overbrace{\phi(x)}^{} \overbrace{\phi(x)}^{} \overbrace{\phi(x)}^{} \overbrace{\phi(y)}^{} \overbrace{\phi(y)}^{} \overbrace{\phi(y)}^{} | p_3 p_4 \rangle$$

For the first $\phi^3(x)$ term we have $3!$ choices of pairing two fields with a single outer state (and same for the second $\phi^3(y)$). There is an additional factor two for interchanging which outer state contracts with $\phi^3(y)$ or $\phi^3(x)$. Knowing where we were headed, we have already included the combinatorial factor with the coupling constant. With this normalization of the coupling, each non-zero term will include a propagator and a factor $(-i\kappa)^2$. Moving to momentum space, the inner contractions (propagators) correspond to the Greens function of the free Klein-Gordon equation: $[\phi(x), \phi(y)] = i/(p^2 - m^2)$. There are three unique terms. The terms correspond to the three possible ways the outer momentum states can be contracted with the two terms.

$$(-i\kappa)^2 \left(\frac{i}{(p_1 + p_2) - m^2} + \frac{i}{(p_1 - p_3) - m^2} + \frac{i}{(p_1 - p_4) - m^2} \right)$$

This is where the wonderful simplicity of Feynman diagrams enters the picture. The structure of contractions can be represented visually by vertices connected by lines (Figure 2.5). Our ϕ^3 term in the Lagrangian represents a vertex with 3 legs corresponding to the three ϕ fields. The vertex itself introduces the coupling constant (when normalized properly) and the legs are then connected to an outer state or another vertex. The unconnected legs are the contractions with outer states. These legs are physical and are referred to as external lines. The legs connected between vertices are virtual and referred to as internal lines.

Since these products and differences of momentum are common in particle physics we use the conventional Mandelstam variables, which add a reduction in notation. The variables can also be written in terms of the $2 \rightarrow 2$ scattering angle and the center of mass energy of the collision.

$$\begin{aligned}s &= (p_1 + p_2)^2 = 4(p^2 + m^2) = E_{cm}^2 \\ t &= (p_1 - p_3)^2 = -2p^2(1 - \cos\theta) \\ u &= (p_1 - p_4)^2 = -2p^2(1 + \cos\theta)\end{aligned}$$

Here the scattering angle θ is defined as $\hat{p}_i \cdot \hat{p}_f$ in the center of mass frame. Summing the diagrams appropriately named the s , t , and u -channel diagrams, we calculate the un-squared amplitude.

$$\mathcal{M} = (-i\kappa)^2 \left(\frac{i}{s - m^2} + \frac{i}{t - m^2} + \frac{i}{u - m^2} \right)$$

The rate of this process is proportional to $|\mathcal{M}|^2$. The exact way this corresponds to what we observe in the detector is left to the following section.

In practice, one can avoid needing to compute the combinatorics of contractions by simply knowing the terms contained in the theory, and the Feynman “rules” for particular fields (spin-0, spin-1, spin- $\frac{1}{2}$). For a spin-0 field the Feynman rules are:

- Internal lines: $\Delta(p) = \frac{i}{p^2 - m^2 + i\epsilon}$. The epsilon enforces a pole prescription for the integral the corresponds to causal propagation of the virtual quantum.
- Vertices: $-i\kappa$
- Symmetry Factors: Account for possible symmetries in the diagram that would over count the multiplicities of diagrams. These factors are rare except higher order diagrams. Calculations by hand are rarely more than a factor 2.
- Momentum Conservation: Require that four momentum is conserved at each vertex. This condition was enforced by the phases in the quantum fields, but is put in by hand in the diagrams.
- Integrate over any undetermined momentum.

Given an initial and final state, one uses the vertices as building blocks to construct all connected diagrams at the chosen order in the coupling. The rules then dictate the form of the calculation. For the scalar field at tree level (no undetermined momentum) this amounts to a quick calculation. Theories including higher spin fields like fermions and gauge bosons require more complex rules, but are straightforward to calculate from the formulation of the matrix element \mathcal{M} .

2.1.6 Radiative Corrections and Renormalization

The perturbative expansion of the scattering matrix introduces momenta unconstrained by the in-going and out-going momentum and must be integrated out in our calculation of a scattering amplitude (Figure 2.6). By construction these diagrams must be integrated up to infinite energies. This can lead to infinite matrix elements. Such a process is clearly unphysical, as its probability has no proper normalization. The means of interpreting these infinite contributions to a matrix element is known as renormalization. The method of renormalization was a historical triumph

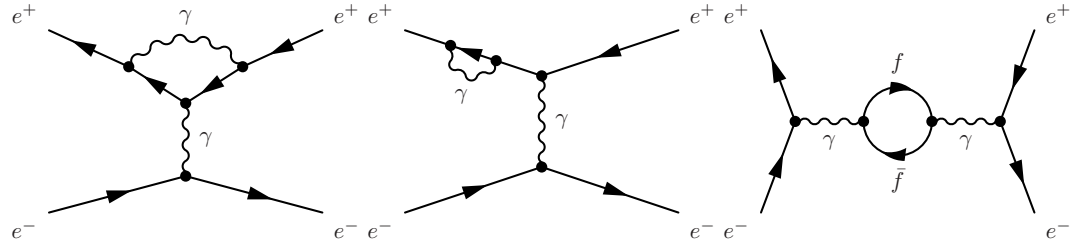


Figure 2.6: Radiative corrections at one loop in electron scattering. Time is directed horizontally. (left) The vertex correction for interaction strength. (middle) The self-energy correction for the electron. (right) The photon self-energy propagator correction.

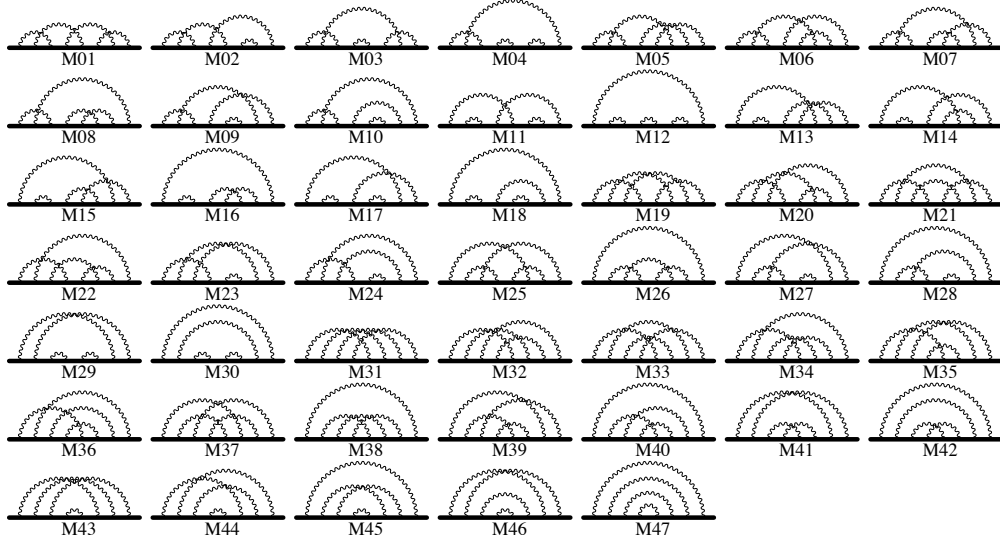


Figure 2.7: Example 8th order self-energy diagrams necessary for precision electroweak experiments [7].

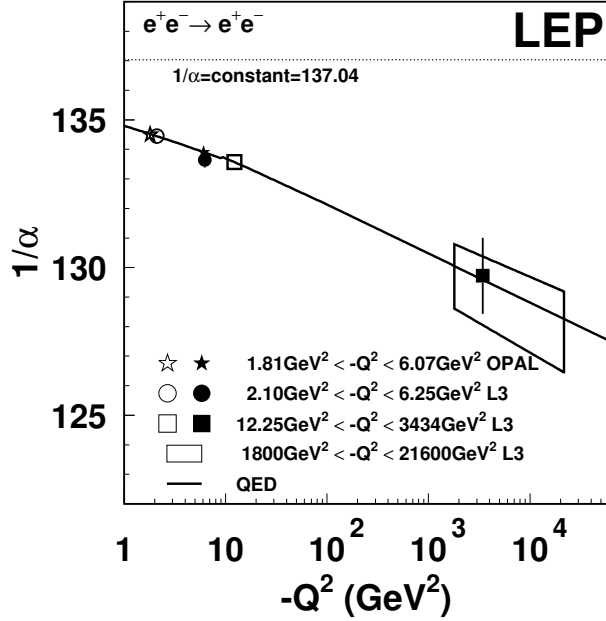


Figure 2.8: The running of the electromagnetic coupling α as a function of the momentum transfer Q^2 .

of quantum field theory as a tool of describing high energy particle physics. In the Wilsonian perspective of renormalization, an effective theory like the Standard Model would only integrate over momentums below some finite energy scale where we expect the theory to no longer valid, the cut off scale Λ . This scale has important consequences for the theory. All dimensionful parameters of the theory will be expressed in terms of Λ times constants which must be tuned against the cutoff. The level to which these constants must be tuned to agree with measured values is known as the “natural”-ness of the theory.

Examples of one loop diagrams are shown in Figure 2.6. These diagrams have important consequences on the experimentally measured values of the parameters of the theory. The first diagram gives a correction to the electroweak coupling strength and the electron magnetic moment. The second and third diagrams induce corrections to the electron and photon propagator, respectively. An important consequence is on parameters of the theory. For instance, values of the coupling strength will effec-

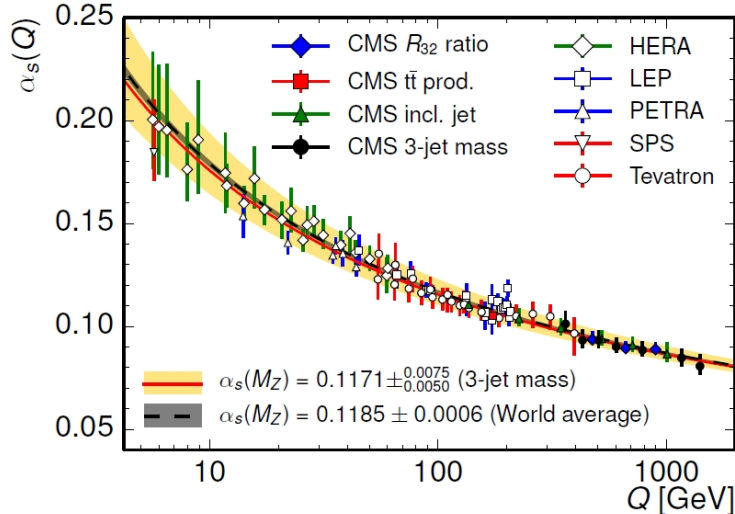


Figure 2.9: The running of the strong coupling constant α_s as a function of the momentum transfer Q .

tively change or “run” with the momentum transfer of the process q^2 . Historically, experiments (Figures 2.8 and 2.9) have confirmed the q^2 dependence of the couplings α_s, α . Additionally, these loops will have contributions from all possible vertices in the Lagrangian, not just the flavors and families included in the in and out going states. Interestingly, the largest uncertainty in precision electroweak theory comes from hadronic loop contributions.

When dimensional analysis is performed on Lagrangian terms with mass dimension greater than 4, say $\frac{g}{5!}\phi^5$ a consequence of the action begin dimensionless is the coupling constant g must have dimension $1/[M]$. As the only mass scale in the theory is Λ , the coupling will scale as $1/(c\Lambda)$ where c is some dimensionless number. When the scales probed by the theory are small compared to cutoff $q^2/\Lambda^2 \rightarrow 0$ these terms are irrelevant in the theory. If the higher dimensional operators existed, we would only see evidence when probing energies $q^2 \sim \Lambda^2$. This would be evidence of new physics to be incorporated and a subsequent increase of the value of Λ to where the new theory would break down.

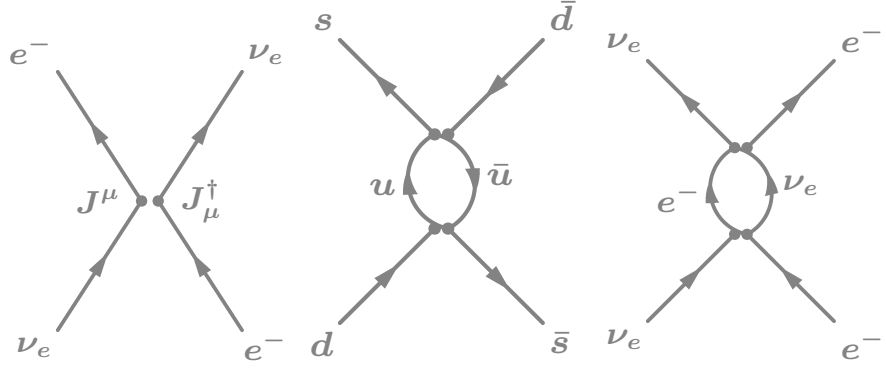


Figure 2.10: (left) The two current four fermi interaction describing electroweak processes. (center and right) Two divergent diagrams with caused by an unconstrained momentum in the inner loop.

As a concrete example, we consider the four point Fermi interaction which models electroweak theory as a contraction of hadronic and leptonic currents

$$\begin{aligned}
 -\mathcal{L} &= \frac{G_F}{\sqrt{2}} J_\mu^\dagger J^\mu \text{ with } J_\mu = J_\mu^l + J_\mu^{had} \\
 J_\mu^l &= \bar{e}^- \gamma_\mu (1 - \gamma^5) \nu_e + \bar{\mu} \gamma_\mu (1 - \gamma^5) \nu_\mu \\
 J_\mu^{had} &= \bar{u} \gamma_\mu (1 - \gamma^5) d'
 \end{aligned}$$

These diagrams are capable of describing a variety of processes correctly at tree level[49]:

- Neutron \$\beta\$ decay: \$n \rightarrow p e^- \bar{\nu}_e\$
- \$\mu, \tau\$ decay: \$\mu^- \rightarrow e^- \bar{\nu}_e \nu_\mu\$ and \$\tau \rightarrow \mu^- \bar{\nu}_\mu \nu_\tau\$
- \$\pi, K\$ decay: \$\pi^+ \rightarrow \mu^+ \nu_\mu\$
- heavy quark decays: \$c \rightarrow s e^+ \nu_e\$ and \$b \rightarrow c \mu^- \bar{\nu}_\mu\$

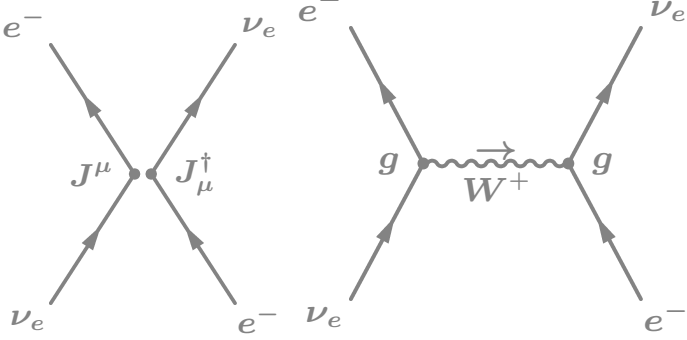


Figure 2.11: The four fermi theory (left) for the weak interaction in terms of currents J^μ is realized in the Standard Model through a three point function including intermediate vector boson propagator (right).

While the model is successful at tree level, the theory has quadratically divergent diagrams $O(\Lambda^2)$ (Figure 2.10) at one loop.

$$\int d^4k \left(\frac{k_\mu \gamma^\mu}{k^2} \right) \left(\frac{k_\mu \gamma^\mu}{k^2} \right) \sim \int dk k \sim \Lambda^2$$

Since a fermion has $[\psi] \sim [M]^{3/2}$ the coupling G_F must have dimension $[M]^{-2}$ and is therefore non-renormalizable. New physics at the electroweak scale was needed to complete the theory in the ultraviolet (UV). Today, we know these diagrams needed an intermediate vector boson (Figure 2.11) to be UV complete. The $[M]^{-2}$ dependence of the G_F was in fact due to the W 's propagating mass:

$$G_F = \frac{\sqrt{2}}{8} \frac{g_W^2}{m_W^2} \text{ with } m_W \approx 80 \text{ GeV and } g_W = 0.65$$

2.2 Supersymmetry (SUSY)

The general discussion of SUSY at the level of experimental particle physics typically begins by positing that SUSY is a symmetry of particles. For every scalar particle, it posits a fermionic partner (and vice versa). This is experimentally relevant to designing searches for new particles. As the super partners of Standard Model particles

have not yet been discovered it stands to reason they must be much heavier than their partners implying Supersymmetry is a broken symmetry. From loop corrections to Standard Model Feynman diagrams, we know that the mass of these partners, should they exist in nature, will determine the level of tuning required in the new theory.

It is less often mentioned that the theory of Supersymmetry posits something about the nature of the space-time. Nature exhibiting Supersymmetry would arise through an expansion of the fundamental coordinates of spacetime to include components that are neither space nor time. In this section, we will discuss the elementary aspects of how Supersymmetry [54] extends the usual quantum field theory discussed previously in this section. The goal is to have a basic understanding of the theory that has served as a major motivation for the Large Hadron Collider.

To begin our discussion, we first need to review Lorentz transformations in terms of $SL(2, \mathbb{C})$ (read special linear group of order 2 with complex entries). This group is convenient for expressing Lorentz transformations of a 4-vector x^μ by considering transformations on $\tilde{x} = x_\mu \sigma^\mu$ where $\sigma^\mu = (1, \vec{\sigma})$ and $\bar{\sigma}^\mu = (1, -\vec{\sigma})$. $\vec{\sigma}$ are the usual Pauli spin matrices. The transformation $\tilde{x} \rightarrow N\tilde{x}N^\dagger$ preserves $\det(\tilde{x}) = x_0^2 - \vec{x}^2$. The map between $\Lambda \in SO(3, 1)$ the Lorentz group transformations and $N \in SL(2, \mathbb{C})$ has a redundancy caused by the 2 to 1 mapping of $N = \pm 1$ to the identity. Explicitly we can write $\Lambda^\mu{}_\nu$ in terms of the transformation N as:

$$\Lambda^\mu{}_\nu = \frac{1}{2} \text{Tr} \left\{ \bar{\sigma}^\mu N \sigma_\nu N^\dagger \right\}$$

The representations of $SL(2, \mathbb{C})$ act on Weyl spinors which have an spinor index $\alpha = 1, 2$ corresponding to the two dimensions of the transformation. The left handed Weyl spinors transform under N as:

$$\psi'_\alpha = N_\alpha{}^\beta \psi_\beta$$

The right handed Weyl spinors transform under the conjugate representation. Indices which transform under the conjugate representation are denoted by a dot $\dot{\alpha}$

$$\bar{\chi}'_{\dot{\alpha}} = N_{\dot{\alpha}}^{*\dot{\beta}} \bar{\chi}_{\dot{\beta}}$$

Just as the momentum operator P^μ and the generalized angular momentum operator $M^{\mu\nu}$ served as the generators of Poincaré lie group algebra, we have new Weyl spinor generators Q_α^A and $\bar{Q}_{\dot{\alpha}}^A$ where $A = 1, \dots, \mathcal{N}$ indexes the number of super symmetries in the theory \mathcal{N} . A theory with \mathcal{N} The Weyl spinors transform under the $SL(2, \mathbb{C})$ generators $\sigma_\alpha^{\mu\nu\beta} = \frac{i}{4}(\sigma^\mu\bar{\sigma}^\nu - \sigma^\nu\bar{\sigma}^\mu)_\alpha{}^\beta$ and $\bar{\sigma}_{\dot{\alpha}}^{\mu\nu\dot{\beta}} = \frac{i}{4}(\bar{\sigma}^\mu\sigma^\nu - \bar{\sigma}^\nu\sigma^\mu)^{\dot{\alpha}}{}^{\dot{\beta}}$ for the conjugate representation

$$Q'_\alpha = \exp\left(\frac{i}{2}\omega_{\mu\nu}\sigma^{\mu\nu}{}_\alpha{}^\beta\right) Q_\beta$$

By comparing the infinitesimal transformation between the Lorentz transformation and the $SL(2\mathbb{C})$ transformation we extract the commutation relations between Q and $M^{\mu\nu}$:

$$[Q_\alpha, M^{\mu\nu}] = (\sigma^{\mu\nu})_\alpha{}^\beta Q_\beta$$

From this we can determine $[Q, P^2] = 0$ which consequently shows us that multiplets of unbroken Supersymmetry are degenerate in mass. Since we have not discovered these partners, we believe Supersymmetry is a broken symmetry. To understand how Q acts on a state, we look at the commutation relations with the z component spin operator J_3 which can be expressed in terms of $M^{\mu\nu}$ as $J_3 = \frac{1}{2}\epsilon_{3ij}M^{ij}$ for $i, j = 1, 2$.

From this, we compute the commutator:

$$\begin{aligned}[Q_\alpha, J_3] &= \frac{1}{2}\epsilon_{3ij}[Q_\alpha, M^{ij}] = \frac{1}{2}\epsilon_{3ij} \left(\frac{i}{4}[\sigma^j, \sigma^i] \right)_\alpha{}^\beta Q_\beta \\ &= -\frac{1}{4}(\epsilon_{3ij}\epsilon_{ji3}\sigma_3)_\alpha{}^\beta Q_\beta = -\frac{1}{2}(\sigma_3)_\alpha{}^\beta Q_\beta\end{aligned}$$

The individual relations for the spinors are $[Q_1, J_3] = -\frac{1}{2}Q_1$ and $[Q_2, J_3] = \frac{1}{2}Q_2$. That is to say, the Supersymmetry generators raise or lower the spin of a particle by 1/2. This is important. The SUSY generators have the effect of interchanging fermionic and bosonic states!

From the structure of the indices we can also determine the anti-commutation relations between the generators up to a constant c which is set to 2.

$$\{Q_\alpha, \bar{Q}_{\dot{\beta}}\} = c(\sigma^\mu)_{\alpha\dot{\beta}}P_\mu = 2(\sigma^\mu)_{\alpha\dot{\beta}}P_\mu$$

here we see the two symmetry transformations together generate a translation in spacetime. This relation is suggestive that we should consider Supersymmetry a symmetry of spacetime. A complete super-Poincaré transformation (Lorentz transformations + translations + Supersymmetry transformations) is written in terms of the generators as:

$$g = \exp(i(\omega^{\mu\nu}M_{\mu\nu} + a^\mu P_\mu + \theta^\alpha Q_\alpha + \bar{\theta}_{\dot{\alpha}}\bar{Q}^{\dot{\alpha}}))$$

where θ^α and $\bar{\theta}_{\dot{\beta}}$ are spinors of anti-commuting Grassmann numbers which square to zero. In this way, θ^α and $\bar{\theta}_{\dot{\beta}}$ are like differential one forms dx that only exist at linear order. When reading supersymmetric Lagrangians, which have explicit dependance on the θ and $\bar{\theta}$ spinors, it is important to understand the suppressed index structure. Although the individual Grassmann components of the spinor square to zero, the

spinor terms will appear at second order as mixed components.

$$\theta\theta = \theta^\alpha\theta_\alpha = \epsilon^{\alpha\beta}\theta_\beta\theta_\alpha = \theta_2\theta_1 - \theta_1\theta_2 = 2\theta_2\theta_1$$

$$\bar{\theta}\bar{\theta} = \bar{\theta}_{\dot{\alpha}}\bar{\theta}^{\dot{\alpha}} = (\theta_{\dot{\alpha}})^*(\theta^{\dot{\alpha}})^* = \theta_1^*\theta_2^* - \theta_2^*\theta_1^* = 2\theta_1^*\theta_2^*$$

The spinor indices between fermionic fields and θ are also suppressed $\theta\psi = \theta^\alpha\psi_\alpha$. Because $\theta_1^2 = \theta_2^2 = 0$, there are no cubed spinor terms of the form $(\theta\theta)\theta\psi$ terms as all terms would be at least order 2 in the components. It is also possible to formulate superspace in terms of Dirac matrices as a single component rather than two, however the majority of literature takes the Weyl spinor approach.

Now that we understand index structure, we can write the most general chiral super field as an expansion in the superspace coordinates as:

$$\Phi(x^\mu, \theta^\alpha, \bar{\theta}^{\dot{\alpha}}) = \varphi(x) + \sqrt{2}\theta\psi(x) + \theta\theta F(x) + i\theta\sigma^\mu\bar{\theta}\partial_\mu\varphi(x) - \frac{i}{\sqrt{2}}(\theta\theta)\partial_\mu\psi(x)\sigma^\mu\bar{\theta}$$

$$- \frac{1}{4}(\theta\theta)(\bar{\theta}\bar{\theta})\partial_\mu\partial^\mu\varphi(x)$$

Here $\sigma^\mu = (1, \vec{\sigma})$. The field has 4 bosonic components (φ and F) and 4 fermionic components (ψ_α i.e. one for each coordinate θ_a and $\bar{\theta}_a$). When a super-translation is applied to the field, the individual coefficients of the super-coordinates will transform into each other. However, it is possible to greatly reduce the terms with a transformation of variables $y^\mu = x^\mu + i\theta\sigma^\mu\bar{\theta}$. In these coordinates, the field appears only as a function of θ .

$$\Phi(y^\mu, \theta^\alpha) = \varphi(y^\mu) + \sqrt{2}\theta\psi(y^\mu) + \theta\theta F(y^\mu)$$

φ represents the scalar components of the theory (squarks, sleptons, the Higgs) and ψ the fermionic fields (quarks, leptons, and higgsinos).

As for vector super-fields, the most general vector super-field expression is much longer:

$$\begin{aligned}
V(x, \theta, \bar{\theta}) = & C(x) + i\theta\chi(x) - i\bar{\theta}\bar{\chi}(x) \\
& + \frac{i}{2}\theta\theta(M(x) + iN(x)) - \frac{i}{2}\bar{\theta}\bar{\theta}(M(x)) \\
& - iN(x) + \theta\sigma^\mu\bar{\theta}V_\mu(x) + i\theta\theta\bar{\theta}\left(-i\bar{\lambda}(x) + \frac{i}{2}\bar{\sigma}^\mu\partial_\mu\chi(x)\right) \\
& - i\bar{\theta}\bar{\theta}\theta\left(i\lambda(x) - \frac{i}{2}\sigma^\mu\partial_\mu\bar{\chi}(x)\right) + \frac{1}{2}(\theta\theta)(\bar{\theta}\bar{\theta})\left(D - \frac{1}{2}\partial_\mu\partial^\mu C\right)
\end{aligned}$$

This field has 8 bosonic components (C, M, N, D, V_μ) and 8 fermionic components ($\chi_\alpha, \lambda_\alpha$). It is possible to build a vector super-field from a chiral field Λ via $i(\Lambda - \Lambda^\dagger)$. With this, we can define a transformation $V \rightarrow V - \frac{i}{2}(\Lambda - \Lambda^\dagger)$ inducing a gauge transformation $V_\mu \rightarrow V_\mu + \partial_\mu(Re[\varphi]) = V_\mu + \partial_\mu\alpha$ that allows us the freedom to gauge away a number of components. In the Wess-Zumino Gauge, the vector field we can set $C = \chi = M = N = 0$ yielding a significantly reduced form:

$$V_{WZ}(x, \phi, \bar{\phi}) = (\theta\sigma^\mu\bar{\theta})V_\mu(x) + (\theta\theta)\bar{\theta}\bar{\lambda}(x) + (\bar{\theta}\bar{\theta})\theta\lambda(x) + \frac{1}{2}(\theta\theta)(\bar{\theta}\bar{\theta})D(x)$$

In this form, V_μ corresponds to the usual Standard Model gauge bosons (γ, W^\pm, Z, g). $\lambda, \bar{\lambda}$ are the gauginos and D is an auxiliary field.

The most generic Lagrangian \mathcal{L} for a chiral super-field is written in terms of the Khaler potential K and the super potential W as

$$\begin{aligned}
K(\Phi, \Phi^\dagger) &= \Phi^\dagger\Phi \\
W(\Phi) &= \alpha + \lambda\Phi + \frac{m}{2}\Phi^2 + \frac{g}{3}\Phi^3 \\
\mathcal{L} &= K|_D + (W|_F + h.c.)
\end{aligned}$$

where we have taken the D auxiliary term of the Kahler potential and the F auxiliary term of the super potential. Expanding the Kahler potential in terms of the components of the most general solution to the chiral super field Φ and collecting the D term (the coefficient of $\theta^2\bar{\theta}^2$):

$$\begin{aligned} K &= K_1 + K_2 + K_3 + K_4 \\ K_1 &= -\frac{1}{4}\bar{\theta}^2\theta^2(\partial_\mu\partial^\mu\varphi^*)\varphi - \frac{1}{4}(\partial_\mu\partial^\mu\varphi)\varphi^* \\ K_2 &= -i\bar{\theta}\bar{\psi}\theta^2(\partial_\mu\psi\sigma^\mu\bar{\theta}) + i\bar{\theta}^2(\theta\sigma^\mu\partial_\mu\bar{\psi})\theta\psi \\ K_3 &= (\theta\sigma^\mu\bar{\theta})(\theta\sigma_\nu\bar{\theta})\partial_\mu\varphi\partial^\nu\varphi \\ K_4 &= \bar{\theta}^2\theta^2|F|^2 \end{aligned}$$

K_1 can be written as a $\frac{1}{2}(\partial_\mu\varphi)(\partial^\mu\varphi^*)$ plus a total derivative which contributes zero in the action. K_4 yields another factor $\frac{1}{2}(\partial_\mu\varphi)(\partial^\mu\varphi^*)$ after contracting the σ terms. K_2 yields the massless Dirac equation $-i\psi\sigma^\mu\partial_\mu\bar{\psi}$ plus a non contributing total derivative. The final constant term $|F|^2$ is relevant to how SUSY is broken. Impressively, the simple expression of the Khaler potential as a product of the most general chiral super-field and its conjugate yields precisely the free kinetic terms for the scalar and fermionic fields.

$$K = (\partial_\mu\varphi)(\partial^\mu\varphi^*) - i\psi\sigma^\mu\partial_\mu\bar{\psi} + |F|^2$$

For the potential terms, the derivatives of the super potential are evaluated in an expansion about $\Psi = \varphi$ where $\frac{\partial W}{\partial \varphi} = \frac{\partial W}{\partial \Phi}|_\varphi$

$$W(\Phi) = W(\varphi) + (\Phi - \varphi)\frac{\partial W}{\partial \varphi} + \frac{1}{2}(\Phi - \varphi)^2\frac{\partial^2 W}{\partial \varphi^2}$$

Evaluating the expansion at its F term:

$$\begin{aligned} W(\varphi)|_F &= 0 \\ (\Phi - \varphi) \frac{\partial W}{\partial \varphi}|_F &= F(m\varphi + g\varphi^2) = -|m\varphi + g\varphi^2|^2 \\ \frac{1}{2}(\Phi - \varphi)^2 \frac{\partial W}{\partial \varphi^2}|_F &= -\frac{1}{2}\psi^2(m + 2g\varphi) \end{aligned}$$

Here we have made use of $-F = \frac{\partial W^*}{\partial \varphi^*}$ which can be obtained from minimal action. From the F component of the Lagrangian $\mathcal{L}_F = |F|^2 + \frac{\partial W}{\partial \varphi}F + \frac{\partial W^*}{\partial \varphi^*}F^*$ we apply the minimal action principle and obtain $\frac{\delta S_F}{\delta F} = 0 \implies F^* + \frac{\partial W}{\partial \varphi} = 0$ (the same is done for F^* . In this form, after adding the Hermitian conjugate of the potential term, the complete Lagrangian reads:

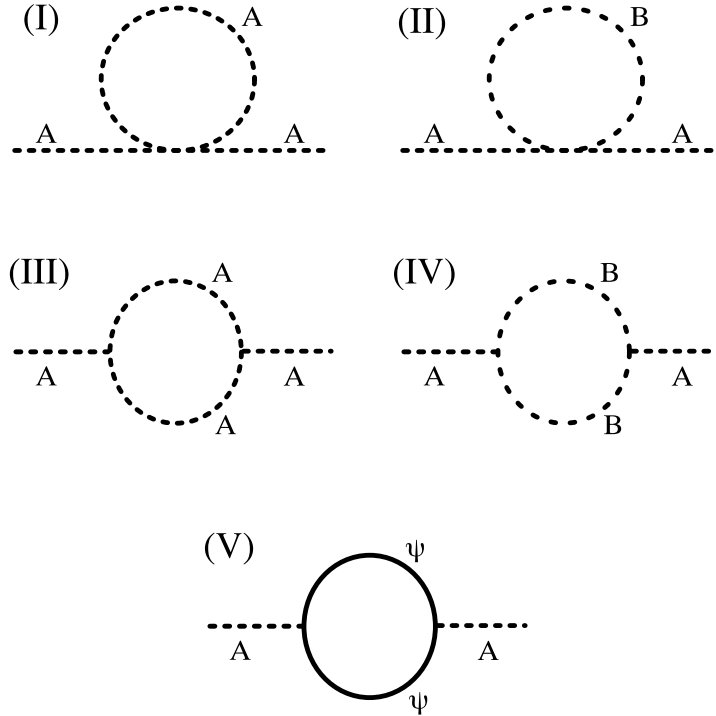
$$\begin{aligned} \mathcal{L} = & (\partial_\mu \varphi)(\partial^\mu \varphi^*) - i\psi \sigma^\mu \partial_\mu \bar{\psi} + |F|^2 \\ & - |m\varphi + g\varphi^2|^2 - \psi^2\left(\frac{m}{2} + g\varphi\right) - \bar{\psi}^2\left(\frac{m}{2} + g\varphi^*\right) + \partial^\mu \varphi \partial_\mu \varphi^* \end{aligned}$$

Now that we have the Lagrangian in terms of the super-field components, we can discuss why this construction is so attractive to the theoretical community.

2.2.1 The Miraculous Cancelation

In this section, we would like to investigate the statement that supersymmetric top quarks partners resolve the quadratic divergences in the Higgs mass corrections at one loop. In Supersymmetry, because the super potential is written only in terms the field Φ the couplings between its scalar and fermionic components are sourced by the same coupling. As fermionic loops inherit a minus sign from fermionic statistics, this opens up the possibility of removing troubling divergences. To check this, we will look at the corrections to the real components of the complex scalar field φ . This is based on material from the reference [54].

Figure 2.12: The five 1 loop diagrams which correct the mass of the scalar particle A at one loop [54].



The complex scalar field can then be expanded in terms of its real components $\varphi = (A + iB)/2$ yielding a Lagrangian $\mathcal{L} = \mathcal{L}_0 + \mathcal{L}_{int}$:

$$\begin{aligned}\mathcal{L}_0 &= \frac{1}{2}\partial^\mu A\partial_\mu A - \frac{1}{2}m^2 A^2 + \frac{1}{2}\partial^\mu B\partial_\mu B - \frac{1}{2}m^2 B^2 + \frac{1}{2}\bar{\psi}(i\gamma^\mu\partial_\mu - m)\psi \\ \mathcal{L}_{int} &= \frac{mg}{\sqrt{2}}A(A^2 + B^2) - \frac{g^2}{4}(A^4 + B^4 + 2A^2B^2) - \frac{g}{\sqrt{2}}\bar{\psi}(A - iB\gamma^5)\psi\end{aligned}$$

From the interaction terms we see there are 2 quartic corrections to the propagating A mass, one from the $(g^2/4)A^4$ term and one from $(g^2/2)A^2B^2$. There are 2 scalar 3-point terms that contribute to the mass correction $(mg/\sqrt{2})A^3$ and $-(mg/\sqrt{2})AB^2$. Finally, and most importantly there is a fermionic loop induced by $-(g\sqrt{2})\bar{\psi}A\psi$ with the same coupling g that will induce a cancellation. These corrections are summarized in Figure 2.12.

Diagrams (I) and (II) have similar form and are quadratically divergent. Adding the two diagrams:

$$4g^2 \int \frac{d^4k}{(2\pi)^4} \frac{1}{k^2 - m^2}$$

Diagram (III) has the same form as diagram (IV) and their contributions sum:

$$4g^2 m^2 \int \frac{d^4k}{(2\pi)^4} \frac{1}{(k^2 - m^2)((k-p)^2 - m^2)}$$

Diagram (V) is more difficult to evaluate due to the gamma matrices in the fermionic loop. Ultimately, the integral expands into 3 terms:

$$\begin{aligned} & - \left(-\frac{ig}{\sqrt{2}} \right) 2 \int \frac{d^4k}{(2\pi)^4} Tr \left\{ \frac{i(\gamma^\mu k_\mu + m)}{k^2 - m^2} \frac{i(\gamma^\mu k_\mu - \gamma^\mu p_\mu + m)}{(k-p)^2 - m^2} \right\} \\ & = -2g^2 \left(\int \frac{d^4k}{(2\pi)^4} \frac{1}{k^2 - m^2} + \int \frac{d^4k}{(2\pi)^4} \frac{1}{(k-p)^2 - m^2} \right) \\ & \quad - 2g^2 \left(\int \frac{d^4k}{(2\pi)^4} \frac{4m^2 - p^2}{(k^2 - m^2)((k-p)^2 - m^2)} \right) \end{aligned}$$

The first term of (V) sums with diagrams (I) and (II) to:

$$2g^2 \int \frac{d^4k}{(2\pi)^4} \frac{1}{k^2 - m^2}$$

The third term of (V) sums with diagrams (II) and (III):

$$-2g^2 \int \frac{d^4k}{(2\pi)^4} \frac{2m^2 - p^2}{(k^2 - m^2)((k-p)^2 - m^2)}$$

The total correction is the sum of these three contributions is

$$2g^2 \left(\int \frac{d^4k}{(2\pi)^4} \frac{1}{k^2 - m^2} - \int \frac{d^4k}{(2\pi)^4} \frac{1}{(k-p)^2 - m^2} + \int \frac{d^4k}{(2\pi)^4} \frac{p^2 - 2m}{(k^2 - m^2)((k-p)^2 - m^2)} \right)$$

The first two terms are quadratically divergent as $\int_{\Lambda} d^4k \frac{1}{k^2} \sim \int_{\Lambda} dk k \sim \Lambda^2$. The third term is logarithmically divergent $\int_{\Lambda} d^4k/k^4 \sim \int_{\Lambda} dk/k \sim \log(\Lambda)$.

If the first two terms were evaluated by dimensional regularization where *all* momenta are integrated in d-dimensions (not just up to the scale Λ) the shift in the second term $k \rightarrow k - p$ would be inconsequential and the two terms would precisely cancel. However, if we take the Wilsonian point of view and impose a strict cut off, the calculation can be performed by integrating the angular component of $k \cdot p$ on the three sphere. The “miracle” of this calculation is that the quadratic components between the first two terms cancel! The formulation of Supersymmetry imposes the same coupling constant for the super-symmetric partners (here A and ψ). For this reason, the quadratic divergences in their mass corrections will precisely cancel. When corrections are integrated to sum up the new physics Λ , say the gravitational scale $M_{pl} \sim 10^{18}$ GeV, the tuning required to keep the Higgs mass small is $\log(\Lambda) \sim 10^1$ rather than 10^{36} ! Supersymmetry structurally preserves historical notions of naturalness.

In general, whether Supersymmetry exists or not, there are likely scalars which couple to the Higgs with top-like couplings to cancel the quadratic divergences. The appeal of Supersymmetry is that these top like couplings come for free in the definition of the top super-field. Unfortunately, the Higgs remains the only fundamental scalar to be discovered at the LHC.

2.2.2 The Minimally Supersymmetric Standard Model

The Minimally Supersymmetric Standard Model (MSSM) is the minimally supersymmetric extension of the Standard Model. This extension is minimal in the sense that it has as few particles as necessary to have a consistent theory and nothing more. As mentioned previously, each Standard Model particle has a supersymmetric partner. The top quark has a stop quark partner and the electron has a selectron

Table 2.5: The chiral super field content of the MSSM. squarks, quarks, leptons, and slepton multiplets have three families as in the standard model. Notably, the MSSM includes a second Higgs doublet to remove non-gauge invariant anomalies.

Superfield	Spin-0 Component	Spin-1/2 Component
Q	left squark ($\tilde{u}_L \tilde{d}_L$)	left quarks (u_L, d_L)
u	right up squark \tilde{u}_R^*	right quark u_R
d	right down squark \tilde{d}_R^*	right down quark u_R
L	left slepton ($\tilde{\nu} \tilde{e}_L$)	left lepton (νe_L)
e	right slepton \tilde{e}_R	right lepton e_R
H_u	up type higgs ($H_u^+ H_u^0$)	up type higgsino ($\tilde{H}_u^+ \tilde{H}_u^0$)
H_d	down type higgs ($H_d^0 H_d^-$)	down type higgsino ($\tilde{H}_d^+ \tilde{H}_d^-$)

Table 2.6: The vector super field content of the MSSM before EWSB. Correspondingly, there are only super partners for the original gauge bosons in the unstable vacuum $\langle \phi \rangle = 0$.

Spin-1/2 Component	Spin-1 Component
gluino \tilde{g}	gluon g
charged winos \tilde{W}^\pm , neutral wino \tilde{W} bino \tilde{B}	charged W^\pm , neutral W B boson

partner. However, when experiments at the LHC design searches for super partners, the numerous particles and names are not as straightforward to understand. Who is the standard model partner of the chargino? Why are there multiple higgses and neutralinos? It is the goal of this sub-section to explain the particle content of the MSSM, specifically the source of many neutralinos, charginos, and additional higgs bosons. This discussion is done in greater detail in the reference [28].

As discussed previously, a supersymmetric model is written in terms of chiral and vector super fields. The MSSM field content is summarized in Tables 2.5 and 2.6. Notably an additional Higgs multiplet has been included with opposite weak hyper charge $Y_{H_d} = -Y_{H_u}$ such that the 1 loop three point gauge anomaly cancels. H_u corresponds to the original Standard Model $SU(2)$ doublet. The three point anomaly

is not gauge invariant due to the higgsinos in the Higgs chiral super field. The second doublet cancels this contribution. When electroweak symmetry breaking occurs, both higgses will take on a vacuum expectation value:

$$\langle H_u \rangle = \frac{1}{\sqrt{2}} \begin{pmatrix} 0 \\ \nu_u \end{pmatrix} \text{ and } \langle H_d \rangle = \frac{1}{\sqrt{2}} \begin{pmatrix} \nu_d \\ 0 \end{pmatrix}$$

where $\nu_u^2 + \nu_d^2 = \nu^2$ the Standard Model vacuum expectation value. Given this relation, we define the quantity $\tan \beta = \frac{\nu_u}{\nu_d}$ in terms of the right triangle with legs ν_u and ν_d . This is a free parameter of the theory and commonly scanned in tests of the MSSM. We believe SUSY is a broken symmetry as the super partners have not been discovered, but there is no consensus on how the symmetry is broken. To separate the discussion of how SUSY is broken and the consequences, certain “soft” terms are added to the Lagrangian with free parameters that are determined by how the symmetry is broken. Specific to the Higgs potential the terms which explicitly break SUSY are $V_{\text{soft}} = m_{H_u}^2 H_u^2 + m_{H_d}^2 H_d^2 + (b H_u H_d + h.c.)$. Combining this with the relevant component of the Higgs potential $\frac{1}{2} \sum_a g_a (\phi^* T^a \phi)^2$ where T^a are the generators of the gauge groups, we obtain the super symmetric Higgs potential:

$$V_{SUSY} = (m_{H_u}^2 + |\mu|^2) H_u^2 + (m_{H_d}^2 + |\mu|^2) H_d^2 + \frac{1}{8} (g_1^2 + g_2^2) (H_u^2 - H_d^2)^2 + \frac{1}{2} g_2^2 |H_u^+ H_d^{0*} + H_u^0 H_d^{-*}|^2 + (b H_u^+ H_d^- - b H_u^0 H_d^0 + h.c.)$$

$$V_{SM} = \frac{1}{2} \mu^2 \phi^2 + \frac{1}{4} \lambda \phi^4$$

From the Standard Model we set $m_Z^2 = (1/4)\nu^2(g_1^2 + g_2^2)$ and $m_W^2 = (1/4)\nu^2 g_2^2$. Expanding about the vacuum expectation values of $\langle H_u^0 \rangle$ and $\langle H_d^0 \rangle$ and diagonalizing the mass matrix, we arrive obtain five Higgs bosons A, h, H^0, H^+, H^- . A is a CP odd Higgs. h is the Standard Model Higgs. H^0 is a heavier CP even Higgs. H^\pm are charged scalars. Counting our degrees of freedom we had two Higgs doublets with

four complex components corresponding to eight degrees of freedom. Two degrees of freedom are lost during EWSB (H_u^+ and H_d^-) leaving six degrees of freedom. These correspond to the five Higgs bosons and the massless Goldstone boson.

As for the neutralinos the masses come from flavor mass mismatch between the binos, winos, and higginos. We list the relevant mass terms:

$$(-\frac{1}{2}M_1\tilde{B}\tilde{B} - \frac{1}{2}M_2\tilde{W}^0\tilde{W}^0 + c.c) + (\mu\tilde{H}^0\tilde{H}_d^0 + c.c.) - \sqrt{2}g\phi_i^*T_{ij}^a\psi_j\lambda^a$$

Where $\psi_j = (\tilde{H}_u^0, \tilde{H}_d^0)$ and $\lambda^a = (\tilde{B}, \tilde{W}^0)$ and T^a are the generators of the relevant gauge group. The mass matrix for the neutralinos is $-(1/2)\psi^T M_{\tilde{\chi}^0} \psi + c.c$:

$$m_{\tilde{\chi}^0} = \begin{pmatrix} M_1 & 0 & -g_1 \frac{\nu_d}{2} & g_1 \frac{\nu_u}{2} \\ 0 & M_2 & g_2 \frac{\nu_d}{2} & -g_2 \frac{\nu_u}{2} \\ -g_1 \frac{\nu_d}{2} & g_2 \frac{\nu_d}{2} & 0 & -\mu \\ g_1 \frac{\nu_u}{2} & -g_2 \frac{\nu_u}{2} & -\mu & 0 \end{pmatrix} \text{ in the basis: } \begin{pmatrix} \tilde{B} \\ \tilde{W}^0 \\ \tilde{H}_u^0 \\ \tilde{H}_d^0 \end{pmatrix}$$

This corresponds to four neutralinos that are combinations of the neutral pieces of the two pieces of the higgino doublets, the bino, and the neutral wino. For the charge mixing the relevant terms are:

$$-M_2\tilde{W}^+\tilde{W}^- - \mu\tilde{H}_u^+\tilde{H}_d^- - g_2\nu_u\tilde{H}_u^+\tilde{W}^- - g_2\nu_d\tilde{W}^+\tilde{H}_d^- + c.c.$$

which amounts to a mass matrix of the form $-\frac{1}{2}\psi^{\pm T} M_{\tilde{\chi}^\pm} \psi^\pm + c.c.$:

$$M_{\tilde{\chi}}^\pm = \begin{pmatrix} 0 & 0 & M_2 & g_2\nu_d \\ 0 & 0 & g_2\nu_u & \mu \\ M_2 & g_2\nu_u & 0 & 0 \\ g_2\nu_d & \mu & 0 & 0 \end{pmatrix} \text{ in the basis: } \begin{pmatrix} \tilde{W}^+ \\ \tilde{H}_u^+ \\ \tilde{W}^- \\ \tilde{H}_d^- \end{pmatrix}$$

The positive charginos are a mixed state of the + wino and the charged up type higgsino. The negative charginos are a mixed state of the + wino and the charged down type higgsino.

2.3 Long-lived Signatures

2.3.1 Standard Model Particles with Long Lifetimes

The Standard Model already includes a variety of common hadrons that can generate displaced vertices (Table 2.7 and Table 2.8). For example, $B^0 \rightarrow J/\psi K^{*0}$ with $K^{*0} \rightarrow K^+ \pi^-$ generates a 4 charge particle vertex. Such a vertex is commonly utilized experimentally in b quark identification (b-tagging). Charge neutral Standard Model particles are of particular interest to identifying single displaced jets outside of the b-tagging lifetime regime. The most relevant states are those decaying to charged particles at a few centimeter proper lifetime, namely: Λ^0 , K_S^0 . These particles would have no charge particle leading to the primary collision vertex and a vertex far outside B meson lifetimes. The most relevant of these processes being:

1. $K_s^0 \rightarrow \pi^+ \pi^-$ 69% of all K_s^0 decays
2. $\Lambda^0 \rightarrow p \pi^-$ 64% of all Λ^0 decays

Jets containing prompt decays as well as long-lived K_s and Λ^0 's will contain tracks with large impact parameters. When a vertex is fit to such a jet, we expect small track multiplicity relative to massive > 50 GeV long-lived particles this analysis targets. Pairs of oppositely signed displaced tracks when vertexed together generate a resonance in the invariant mass distribution as shown in Figure 2.13.

Particles of a characteristic lifetime τ decay with a falling exponential distribution. For reference, a table summarizing the distribution is shown in Table 2.9. As the BSM particles must decay with the detector used to identify them, it is important to note

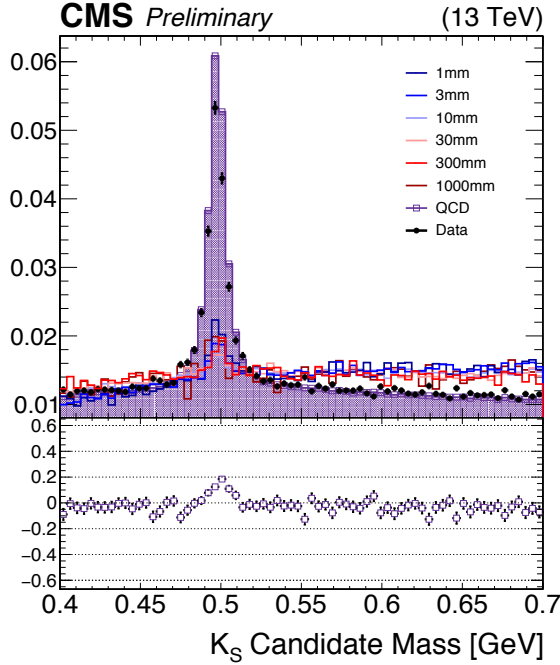


Figure 2.13: The invariant mass of pairs of oppositely charged tracks in data and in simulation. Solid curves correspond to simulated signal models which also contain displaced tracks, but do not share this resonant background as prominently.

Table 2.7: Mesons with proper lifetimes greater than 10^{-2} cm.

Name	Content	Particle	Mass [MeV]	τ_0 [sec]	$c\tau$ [cm]
Pion	ud	π^\pm	139	2.6×10^{-8}	7.8×10^2
Kaon	$u\bar{s}$	K^\pm	497	1.23×10^{-8}	3.7×10^2
K Short	$\frac{1}{\sqrt{2}}(d\bar{s} - s\bar{d})$	K_s^0	497	0.896×10^{-10}	2.68
K Long	$\frac{1}{\sqrt{2}}(d\bar{s} + s\bar{d})$	K_L^0	497	5.1×10^{-8}	1.5×10^3
D	$c\bar{d}$	D^\pm	1869	1×10^{-12}	3.0×10^{-2}
B meson	$u\bar{b}$	B^\pm	5279	1.6×10^{-12}	4.8×10^{-2}
strange B	$s\bar{b}$	B_s^0	5366	1.5×10^{-12}	4.5×10^{-2}
charmed B	$c\bar{b}$	B_c^0	6275	4.5×10^{-13}	1.4×10^{-2}

Table 2.8: Baryons with proper lifetimes greater than 10^{-2} cm.

Name	Content	Particle	Mass [MeV]	τ_0 [s]	$c\tau_0$ [cm]
Lambda	uds	Λ^0	1115	2.6×10^{-10}	7.8
bottom Lambda	udb	Λ_b^0	5620	1.4×10^{-12}	4.2×10^{-2}
Sigma plus	uus	Σ^+	1189	8×10^{-11}	2.4
Sigma minus	dds	Σ^-	1197	1.4×10^{-10}	4.2
Xi zero	uss	Ξ^0	1314	4×10^{-13}	1.2×10^{-2}
Xi minus	dss	Ξ^-	1321	1.6×10^{-10}	4.8
charmed Xi +	usc	Ξ_c^+	2467	4.42×10^{-13}	1.3×10^{-2}
charmed Xi	dsc	Ξ_c^0	2471	1.12×10^{-13}	3.3×10^{-2}
bottom Xi	dsb	Ξ_b^-	5792	1.56×10^{-12}	4.7×10^{-2}
bottom Omega	ssb	Ω_b^-	6054	1.13×10^{-12}	3.3×10^{-2}
Omega minus	sss	Ω^-	1672	8×10^{-11}	2.4

 Table 2.9: The cumulative probability for a particle of lifetime λ to have decayed before a certain distance in units of λ , the proper lifetime. For example, after 0.5λ we expect 39% of long-lived particles with lifetime λ to have decayed.

Distance (λ)	Probability to have decayed
0.01	1%
0.1	9.5%
0.25	22%
0.5	39%
0.75	52%
1	63%
1.5	77%
2	86%
3	95%
5	99.3%

that for proper lifetimes 10 and 100 times the size of the relevant detector (~ 1 m), we would still expect 10% and 1% of decays (respectively) to occur within the sensitive region of the detector.

2.3.2 Split SUSY and Naturalness at the LHC

When motivating Supersymmetry with naturalness, it is important to note that the stability of the Higgs boson mass is not the only fine-tuning problem in particle physics. When the same argument is used to calculate the cosmological constant we arrive at cut off scale $\Lambda \geq m_{SUSY}^4$, where experimentally $\Lambda = 10^{-59}$ TeV⁴. If we use the same SUSY scale $m_{SUSY} = 1$ TeV we have a new fine tuning problem of 10⁶⁰!

As addressed by Arkani-Hamed and Dimopoulos [9], many theoretical approaches have been motivated by a natural explanation for the Higgs mass while separately seeking an explanation of the cosmological constant through some other mechanism. Arkani-Hamed and Dimopoulos propose a reconsideration of naturalness, entertaining the idea that fine tuning could have a role to play in beyond the Standard Model physics. Conceivably, both Λ and m_h fine tuning could be resolved by the same mechanism. This un-natural model was further investigated by Giudice and Romanino [32] and dubbed “Split Supersymmetry”.

Split SUSY assumes a much higher SUSY scale $m_{SUSY}^2 \gg 1$ TeV where all scalars (excluding the Higgs) become very heavy $O(m_{SUSY})$ and the lightest sparticles (higgsinos and gluinos) are kept at the TeV scale by requiring the lightest neutralino to be a good dark matter candidate. Because the scalars are so much heavier, the decay of gluinos through squarks is suppressed. The characteristic signature of split Supersymmetry is thus long-lived gluinos [37]; such processes with long lifetimes are rare in the Standard Model, particularly for particles with mass larger than the m_{EW} .

Following the discovery of the Higgs boson in July 2012, Arkani-Hamed et al. [10] investigated the scalar super-partner mass scale for $m_h \approx 125$ GeV. The most phenomenologically interesting point is the gluino lifetime given by:

$$c\tau_{\tilde{g}} \approx 10^{-5} m \left(\frac{m_{\tilde{q}}}{\text{PeV}} \right)^4 \left(\frac{\text{TeV}}{m_{\tilde{g}}} \right)^5$$

For massive gluinos still within the reach of the $\sqrt{s} = 13$ TeV LHC ($m_{\tilde{g}} \lesssim 3$ TeV) we would probe up to $m_{sq} \simeq 10^4$ TeV if the proper gluino lifetimes is on the order of the relevant detector ($c\tau_{\tilde{g}} < 1$ m).

As the Higgs at 125 GeV has been the only scalar discovered in the LHC's $\sqrt{s} = 7, 8$, and 13 TeV program, the natural SUSY parameter space has become more tightly constrained. If no new scalar super-partners are found soon, less natural scenarios like split SUSY would become even stronger candidates for BSM physics. CMS is well prepared for most, if not all, SUSY final states with prompt decays. Long-lived scenarios allow one to probe significantly higher energy scales if components of the theory are light enough to be probed at the LHC.

Chapter 3

Simulation and Collider Physics

3.1 Introduction

In the previous chapter, we outlined principal aspects and fundamental assumptions of the Standard Model. However, a considerable amount of physics is still required to reach a practical description of what occurs inside of an experiment. The goal of this section is to connect the matrix elements \mathcal{M} from the quantum field theoretic description of the Standard Model to the Monte Carlo simulations. These simulations allow us to test our understanding of a given theory in terms of quantities observable in experimental high energy physics. First, we will discuss how we can compare the matrix amplitudes with the observations in a physical detector. After, we will discuss the considerations that must be made for the fact that LHC collides hadrons rather than fundamental particles. We will discuss the models used to describe physics after the hard scattering occurs where perturbative physics breaks down and calculations from first principles cannot be performed. Generic principles for parton showering and hadronization models will be examined. To conclude, we will discuss common jet clustering algorithms.

3.2 From Matrix Elements to Cross Sections

In high energy experimental particle physics the most studied quantity (in addition to particle quantum numbers and masses) is the cross section σ of the process. This is the rate or equivalently, the probability that a process occurs. It is the proportionality between the number of observed collisions and amount of data collected by the Large Hadron Collider L (the integrated luminosity) expressed simply as:

$$N_{\text{events}} = L \times \sigma$$

Consider a target of particles type A and density ρ_A and aim particles type B with density ρ_B . If the lengths of the bunches of particles are l_A and l_B then the cross section of the processes is defined for a beam with cross-sectional area as:

$$\sigma \equiv \frac{N_{\text{events}}}{\rho_A l_A \rho_B l_B}$$

Inverting this and assuming that we have constant density along the beams length:

$$N_{\text{events}} = \frac{\sigma N_A N_B}{A} = \sigma N_A n_B \quad (3.1)$$

by comparing this with the relation $N_{\text{events}} = L \times \sigma$ above containing luminosity, we see the luminosity is in effect counting the number of colliding particles per unit transverse area of the beams. More incident particles and a more focused beam means more scattered events. In the last equality we have introduced the impact parameter density n_B for the incident B particles.

However, the end results of Feynman diagram calculations yield scattering amplitudes. The amplitudes are probabilities of scattering a given initial state into a given final state, not a cross section. We need to relate the process strength into something concrete experimentally.

First, consider the quantum fields within the beams that are colliding. Start by, setting up two initial wave packets A and B in a limit of definite momentum p_A and p_B and evolve them forward for a very long time with the time evolution operator $\exp(-iHt)$. We would like to link the probability the final state consist of ϕ_1, ϕ_2, \dots . This probability is written [53].

$$\mathcal{P} = |\langle \phi_1 \phi_2 \dots | \phi_A \phi_B \rangle|^2$$

Let the incident wave packets collide along the z-axis, but each with non-trivial transverse displacement b_i . We will take the perspective that A is a target and B is collinear with the target and account for the shift in position with an explicit factor of $\exp(-ib \cdot k_B)$. The properly normalized expression then reads:

$$|\phi_A \phi_B\rangle = \int \frac{d^3 k_A}{\sqrt{2E_A}(2\pi)^3} \int \frac{d^3 k_B}{\sqrt{2E_B}(2\pi)^3} \phi_A(k_A) \phi_B(k_B) e^{-ib \cdot k_B}$$

For a single target A and a beam B with constant impact parameter density $n_B = N_B/A$ we can write the number of events as

$$N_{\text{events}} = \sum_{\text{incident particles } i} \mathcal{P}_i = \int d^2 b n_B(b) \mathcal{P}(b) = n_B \int d^2 b \mathcal{P}(b)$$

Comparing this to Equation 3.1 we can write the cross section as:

$$\sigma = \int d^2 b \mathcal{P}(b)$$

The properly normalized differential cross section for scattering into a the infinitesimal final state momentum element is:

$$d\sigma = \left(\prod_f \frac{d^3 p_f}{(2\pi)^3 2E_f} \right) \int d^2 b \left(\prod_{i=A,B} \int \frac{d^3 k_i}{(2\pi)^3 \sqrt{2E_i}} \phi_i(k_i) \int \frac{d^3 \bar{k}_i}{(2\pi)^3 \sqrt{2\bar{E}_i}} \phi_i^*(\bar{k}_i) \right) \\ \times e^{ib \cdot (\bar{k}_S - k_B)} |\langle \{p_f\} | \{k_i\} \rangle|^2$$

We have six dummy integrals to do in \bar{k} over the three momenta of particle A and B so count our delta functions. The $d^2 b$ integral gives two delta functions in the transverse momentum $(2\pi)^2 \delta^2(k_B^\perp - \bar{k}_B^\perp)$. We have eight delta functions from the matrix element enforcing that the process to conserve energy and momentum $\delta^4(k_A + k_B - \sum p_f)$ and in the complex conjugate with the dummy variable \bar{k} : $\delta^4(\bar{k}_A + \bar{k}_B - \sum p_f)$. Performing the transverse integrals in \bar{k}_B sets $\bar{k}_B^T = k_B^T$ which in combination with the \bar{k} delta functions yields $\bar{k}_A^T = k_A^T$. The remaining 2 integrals in z require some properties of delta functions:

$$\int d\bar{k}_A^z d\bar{k}_B^z \delta(\bar{k}_A^z + \bar{k}_B^z - \sum p_f^z) \delta(\bar{E}_A + \bar{E}_B - \sum E_f)$$

We can integrate the first B integral interpreting \bar{k}_B^z as a function of \bar{k}_A^z and writing the barred energy terms in the momentums and masses:

$$\int d\bar{k}_A^z \delta \left(\sqrt{\bar{k}_A^2 + m_A^2} + \sqrt{\bar{k}_B^2 + m_B^2} - \sum E_f \right)$$

We now need to use the property that $\delta[f(x)] = \sum_i (\delta(x_i)/|f'(x_i)|)$ where x_i are the zeros of the function $f(x)$. Note that given our parameterization from the first delta

function $\partial_{\bar{k}_A^z}(\bar{k}_B^2) = -2\bar{k}_B^z$.

$$\begin{aligned} & \int d\bar{k}_A^z \left(\frac{1}{2} \frac{2\bar{k}_A}{\sqrt{\bar{k}_A^2 + m_A^2}} - \frac{1}{2} \frac{2\bar{k}_B}{\sqrt{\bar{k}_B^2 + m_B^2}} \right)^{-1} \delta(\bar{E}_A + \bar{E}_B - \sum E_f) \\ &= \int d\bar{k}_A^z \frac{1}{\frac{\bar{k}_A}{E_A} - \frac{\bar{k}_B}{E_B}} \delta(\bar{E}_A + \bar{E}_B - \sum E_f) = \frac{1}{\beta_A - \beta_B} \end{aligned}$$

The six remaining integrals in k_A and k_B remain:

$$\begin{aligned} d\sigma = & \left(\prod_f \frac{d^3 p_f}{(2\pi)^3 2E_f} \right) \frac{|\mathcal{M}|^2}{2E_A 2E_B |\beta_A - \beta_B|} \int \frac{d^3 k_A}{(2\pi)^3 \sqrt{2E_i}} |\phi_A(k_A)|^2 \\ & \times \int \frac{d^3 k_B}{(2\pi)^3 \sqrt{2E_i}} |\phi_B(k_B)|^2 \delta^4(k_A + k_B - \sum p_f) \end{aligned}$$

To proceed further, we must consider the quality of measurements made by particle detectors. Real detectors cannot measure arbitrarily small spreads in the momentums $k_A + k_B$. The measurements made in a realistic experimental setup are not sensitive to the spread of momentum in the initial wave packets ϕ_A and ϕ_B . Given this, we can take the central value $k_A + k_B = p_A + p_B$ to be a good approximation for the delta function. With this approximation, we can move the delta function outside the integral and perform the integrals using the unit normalization condition of the two fields ϕ_i :

$$d\sigma = \left(\prod_f \frac{d^3 p_f}{(2\pi)^3 2E_f} \right) \frac{|\mathcal{M}|^2}{2E_A 2E_B |\beta_A - \beta_B|} (2\pi)^4 \delta^4(p_A + p_B - \sum p_f) \quad (3.2)$$

Let's consider the simple case of $2 \rightarrow 2$ scattering and use the energy delta function of the 4 remaining delta functions to compute integral over the final state. To do so, we go to the center of mass frame where $|p_1| = |p_2| = P$, $\vec{p}_1 = -\vec{p}_2$, $E_{cm} = 2P$. We

first integrate p_2 to enforce 3-momentum conservation

$$\int \left(\frac{d^3 p_1}{(2\pi)^3 2E_1} \right) \left(\frac{d^3 p_2}{(2\pi)^3 2E_2} \right) (2\pi)^4 \delta^4(P - \sum p_f)$$

now switching to a spherical integral with a Jacobian $p_1^2 dp_1 d\Omega$ where $d\Omega$ is and infinitesimal solid angle.

$$\int \frac{dp_1 p_1^2 d\Omega}{(2\pi)^3 (2\pi)^3 2E_1 2E_2} (2\pi) \delta(E_{cm} - E_1 - E_2)$$

using the same delta function identity as before:

$$\begin{aligned} \int d\Omega \frac{p_1^2}{(2\pi)^2 2E_1 2E_2} \left(\frac{p_1}{E_1} + \frac{p_2}{E_2} \right)^{-1} &= \int d\Omega \frac{p_1^2}{(2\pi)^2 2E_1 2E_2} \left(\frac{E_1 E_2}{p_1(E_1 + E_2)} \right) \\ &= \int d\Omega \frac{p_1}{16\pi^2 E_{cm}} \end{aligned}$$

Combining the result for the final state integral with Equation 3.2:

$$\left(\frac{d\sigma}{d\Omega} \right)_{CM} = \frac{1}{2E_A 2E_B |\beta_A - \beta_B|} \frac{p_1}{16\pi^2 E_{cm}} |\mathcal{M}|^2$$

Now if we assume the masses of the four particles are the same (or negligible at the energies involved) and substitute $\beta = p/E$:

$$\left(\frac{d\sigma}{d\Omega} \right)_{CM} = \frac{|\mathcal{M}|^2}{64\pi^2 E_{cm}^2}$$

This is the relation between the rate at which a detector will observe a $2 \rightarrow 2$ process proportional to the matrix element derived from the Feynman diagrams governing the process. Integrating over a solid angle gives the number of scattered events per unit integrated luminosity collected by the experiment.

3.3 Parton Model of Hadron Collisions

For hadronic collisions like that of the LHC the fundamental scattering process is not between the individual hadrons, but rather the hadron's inner structure: the quarks and gluons. Unlike a lepton collider, where the full four vector p^μ can be controlled by the collider, the energy in a hadron-hadron scattering process is probabilistic in nature. The individual partons have some unknown fraction of the proton energy in each collision [29].

The cross section for a process for two hadrons with four momentum P_1 and P_2 can be written:

$$\sigma(P_1, P_2) = \sum_{i,j} \int dx_1 dx_2 f_i(x_1, \mu) f_j(x_2, \mu) \hat{\sigma}_{ij}(p_1, p_2, \alpha_S(\mu), Q) \quad (3.3)$$

where the momentum of the partons participating in the hard interaction are $p_i = x_i P_i$ $i = 1, 2$. The scale of the hard scattering is denoted by Q . For example, $Q = m_W$ for W boson production. The f_i are the quark or gluon distributions within the protons. These are the parton distribution function (PDFs). The short distance cross section $\hat{\sigma}$ can be calculated as a perturbative series in the asymptotically small running QCD coupling α_S . The factorization scale μ is an arbitrary parameter that is chosen as the boundary between the long and short distance interaction physics. The boundary at μ separates the soft emitted partons that should be considered part of the hadron and the partons emitted at large transverse momentum that should be considered part of the hard process. In general, it is chosen such that that $\mu = Q$.

The ratio of $\sqrt{\hat{s}}$ of the hard process relative to the proton \sqrt{s} can be written in terms of the variable $\tau = x_1 x_2$ as:

$$\frac{s}{\hat{s}} = \frac{(p_1 + p_2)^2}{(x_1 p_1 + x_2 p_2)^2} = \frac{2p_1 \cdot p_2}{2x_1 x_2 p_1 \cdot p_2} = \frac{1}{x_1 x_2} = \frac{1}{\tau}$$

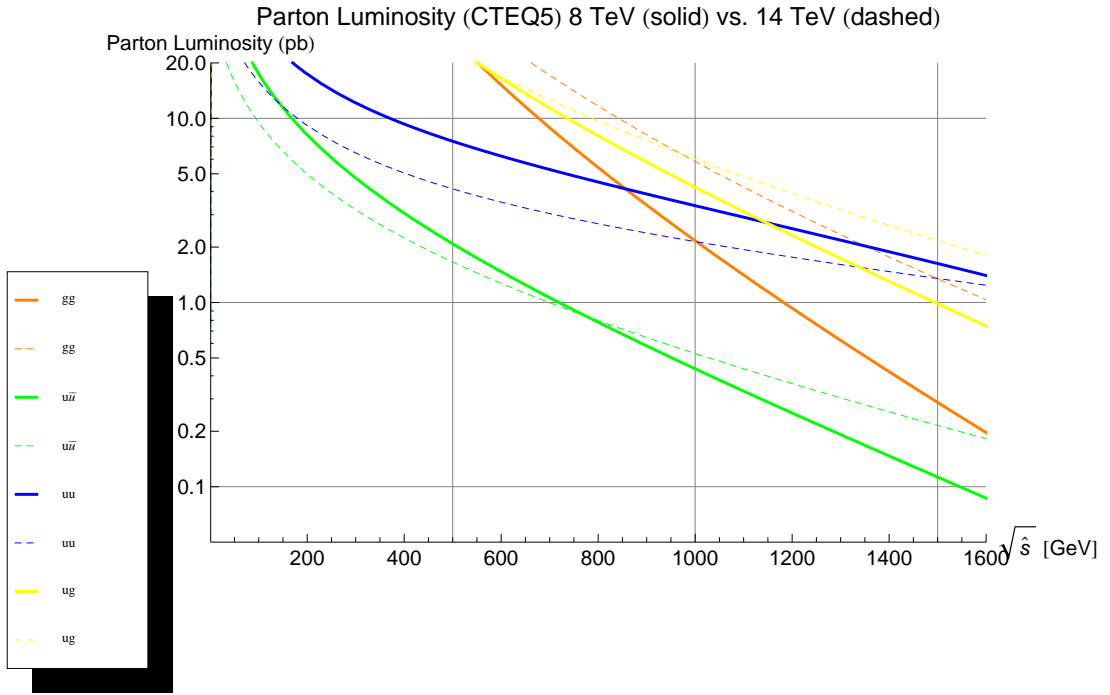


Figure 3.1: Contours of the parton luminosity function derived from CTEQ5 parton distribution functions for $\sqrt{s} = 8$ TeV and $\sqrt{s} = 14$ TeV. Contours are separated by collisions the individual partons in the collision.

Now let us calculate the total cross section σ_{TOT} in terms of two factors: (i) parton luminosity L_{ij} for two individual partons i and j and (ii) the corresponding cross sections σ_{ij} . We assume that the cross section $\hat{\sigma}$ is only a function of \hat{s} , (a property that holds true for many processes, but not in general). Let τ_0 be the minimum τ at which the process can occur.

$$\begin{aligned}\sigma_{TOT} &= \sum_{i,j} \sigma_{ij} L_{ij} = \sum_{i,j} \int_{\tau_0}^1 \frac{dL_{ij}}{d\tau}(1) \hat{\sigma}_{ij} d\tau \\ &= \sum_{i,h} \int_{\tau_0}^1 \frac{dL_{ij}}{d\tau} d\tau \left(\frac{\hat{s}}{s\tau} \right) \hat{\sigma}_{ij} = \sum_{i,j} \int_{\tau_0}^1 \frac{d\tau}{\tau} \left(\frac{1}{s} \frac{dL_{ij}}{d\tau} \right) (\hat{s} \hat{\sigma}_{ij})\end{aligned}$$

Here the center term is referred to as the parton luminosity function and contains the parton distribution functions with some extra accounting for the parton types to

avoid double counting:

$$\tau \frac{dL_{ij}}{d\tau} = \frac{1}{1 + \delta_{ij}} \int_0^1 dx_1 dx_2 \times [(x_1 f_i(x_1, \mu^2) x_2 f_j(x_2, \mu^2)) + (1 \leftrightarrow 2)] \delta(\tau - x_1 x_2)$$

3.4 Kinematic Conventions for Collider Physics

Due to the cylindrical symmetry of the detector it is preferable to make a change from a cartesian parameterization of energy and momentum to a rotationally-symmetric parameterization about the collision access. Furthermore, since the center of mass frame between the two colliding particles is generally moving relative to the lab frame, we would like parameterization of our problem which is invariant under longitudinal boosts. First, we will motivate using hyperbolic functions of rapidity to parameterize energy and momentum. Lets recall the hyperbolic trigonometric functions:

$$\cosh(x) = \frac{e^x + e^{-x}}{2}, \quad \sinh(x) = \frac{e^x - e^{-x}}{2}, \quad \text{and} \quad \tanh^{-1} x = \ln \left(\sqrt{\frac{1+x}{1-x}} \right)$$

combining \cosh and \tanh^{-1} conveniently gives the relativistic γ factor for $x = \beta$:

$$\cosh(\tanh^{-1} x) = \frac{1}{2} \left(\sqrt{\frac{1+x}{1-x}} + \sqrt{\frac{1-x}{1+x}} \right) = \frac{1}{2} \left(\frac{(1+x) + (1-x)}{\sqrt{1-x^2}} \right) = \frac{1}{\sqrt{1-x^2}}$$

and similarly derived:

$$\sinh(\tanh^{-1} x) = \frac{x}{\sqrt{1-x^2}} = x\gamma(x)$$

Defining $w = \tanh^{-1}(\beta)$ conveniently defines energy and momentum as:

$$E = \gamma m = m \cosh w$$

$$|p| = \gamma m \beta = m \sinh w$$

Now lets re-write a Lorentz boost γ along the z-axis in terms of w :

$$E' = \gamma(E - \beta p_z) = E \cosh w - p_z \sinh w$$

$$p'_z = \gamma(p_z - \beta E) = p_z \cosh w - E \sinh w$$

If instead we set $w = y \equiv \tanh^{-1}(\beta_z^*)$ where β_z^* is the boost required to reach the frame where the particle is moving only transversely to the beam line p_μ^* . We can then reach the lab frame by performing the transformation from the $*$ frame. First lets write the four vector in the $*$ frame

$$p_\mu^* = (E, p_x, p_y, 0) = (\sqrt{p_T^2 + m^2}, p_T \sin \phi, p_T \cos \phi, 0)$$

$$\rightarrow p_\mu^{lab} = (m_T \cosh y, p_T \sin \phi, p_T \cos \phi, m_T \sinh y)$$

where $m_T = \sqrt{m^2 + p_T^2}$, $p_T = \sqrt{p_x^2 + p_y^2}$, and y is the definition of rapidity generally used in particle physics. In the limit of light masses relative to the transverse energy of a collision, as is generally the case for collisions at the Large Hadron Collider:

$$p^\mu = p_T(\cosh y, \sin \phi, \cos \phi, \sinh y)$$

From the experimental perspective, what is most important about this definition is that there is a simple geometric relation between pseudorapidity and the angle of the particle relative to the beam line. To see this, we go back to the definition of rapidity and take $\beta \rightarrow 1$ or equivalently $|p| = E$:

$$y = \tanh^{-1}(\beta_z^*) = \ln \left(\sqrt{\frac{1 + \beta_z^*}{1 - \beta_z^*}} \right) \approx_{\beta \rightarrow 1} \ln \left(\sqrt{\frac{1 + p_z/|p|}{1 - p_z/|p|}} \right)$$

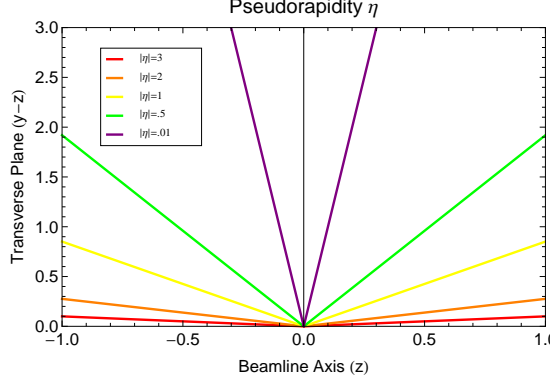


Figure 3.2: Lines of constant pseudorapidity in the z-y plane

Now if we consider the angle with the beam line in the lab frame θ we use a half angle trigonometric identity.

$$1 + \cos \theta = 1 + \frac{p_z}{|p|} = 2 \cos^2(\theta/2)$$

$$1 - \cos \theta = 1 - \frac{p_z}{|p|} = 2 \sin^2(\theta/2)$$

combining this with the approximation with massless limit of y we obtain pseudorapidity η :

$$\eta = \ln \left(\sqrt{\frac{\cos^2(\theta/2)}{\sin^2(\theta/2)}} \right) = -\ln \left(\tan \frac{\theta}{2} \right)$$

The energies of particles at the LHC are typically negligible in mass relative to their energies and the approximation $\eta \approx y$ is accurate. This has a number of useful applications. First, differences in rapidity are invariant under longitudinal Lorentz boosts along the beam axis which can be seen by applying the transformation in terms of γ factors to $y_1 - y_2$. Given this relation, pseudorapidity provides an intuitive geometric interpretation as the angle from the beam axis. The ray extending directly transverse from the collision point is $\eta = 0$ with symmetric values $\pm|\eta|$ to either side

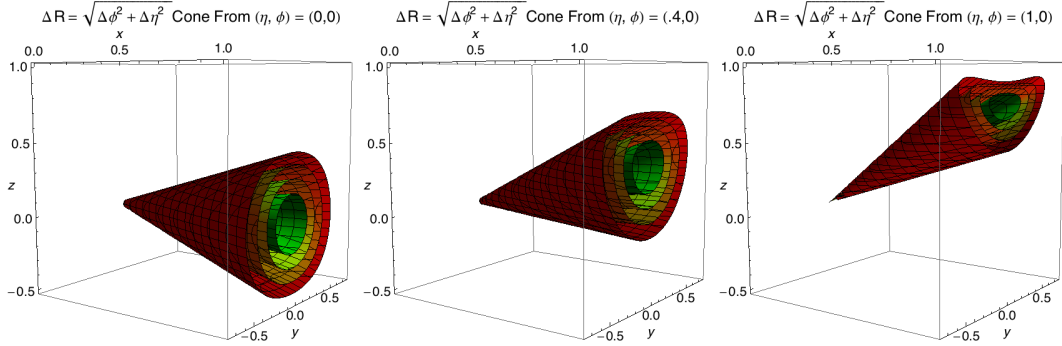


Figure 3.3: Contours of constant ΔR from $(\eta_0, \phi_0) = 0, 0$

of this ray along the z-axis Figure 3.2.

$$\Delta R = \sqrt{(\Delta\phi)^2 + (\Delta\eta)^2}$$

Fixed values of ΔR form a solid angle “cone” extending from the interaction point outward. This can be seen by using our definition of η to convert from cylindrical coordinates to (x, y, z) and the distance relative to the point (η_0, ϕ_0) . Here the angle θ can be related to (x, y, z) by examining the ray extended from the origin to any point along a circle with radius $r = x^2 + y^2$.

$$\cos \theta = \frac{z}{x^2 + y^2} \implies \theta = \cos^{-1} \frac{z}{x^2 + y^2}$$

substituting this into our definition of pseudorapidity $\eta = -\ln(\tan \theta/2)$ we obtain η in terms of x, y, z . For the angle ϕ , $\tan \phi = y/x \implies \phi = \tan^{-1}(y/x)$. We can now express the equation for ΔR below and the contours of Figure 3.3.

$$\Delta R = \sqrt{(\phi_0 - \tan^{-1}(y/x))^2 + \left(\eta_0 + \log \left(\tan \frac{\cos^{-1}(z/\sqrt{x^2 + y^2})}{2} \right) \right)^2}$$

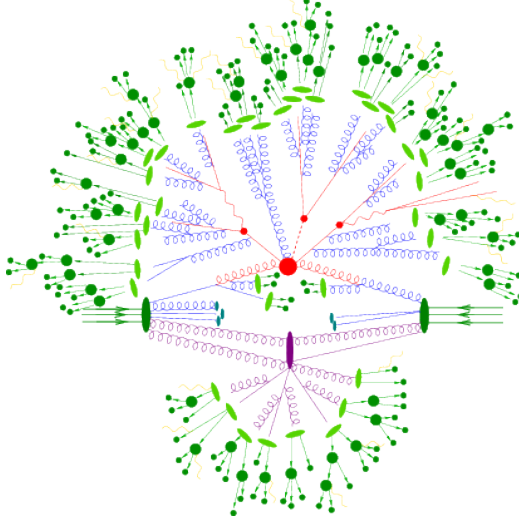


Figure 3.4: A graphic depiction of the showering and hadronization process. The incoming protons can be seen as the two sets of three incoming arrows representing the proton quark content.

3.5 Showering

After the initial hard process is simulated, even if performed at high orders in perturbation theory, we have not described the large multiplicity and variety of particles which result from the showering of free quarks (Fig. 3.4). We might even take for granted that high energy proton collisions yield collimated showers of hadrons we more commonly refer to as *jets*. In certain conformal theories the hadronization steps more closely resemble shells [38].

As the collisions are made between hadrons, the dominant fraction of the total cross section is governed by the dynamics of QCD. The strength of QCD is set by the strong coupling $\alpha_s(q^2)$ where the q^2 dependence arises from loop corrections to the tree level Feynman diagram vertices. [66]

$$\alpha_s(q^2) = \frac{12\pi}{(33 - 2n_f) \ln(q^2/\Lambda_{QCD}^2)} \quad (3.4)$$

Here n_f is the number of flavors of participating fermions in the interaction and $\Lambda_{QCD} = 0.1 - 0.3$. Here we notice two important features. As q^2 becomes large, the interaction becomes asymptotically weak and the physics is perturbative. As $q^2 \rightarrow \Lambda_{QCD}$ the theory is strongly coupled ($\alpha > 1$) and a perturbative approach leaves higher order terms that cannot be neglected [29].

We need a method to evolve the high energy states to some low energy cut off where the physics is clearly non-perturbative. This scale is typically taken to be on the order of momentum transfer $t^2 = 1 \text{ GeV}^2$. This provides a natural division of labor for generating physics events between the perturbative hard scattering, the approximately perturbative showering, and the non-perturbative physics of hadronization. The terms fragmentation and hadronization are often used interchangeably to describe the non-perturbative of this division. However, in certain contexts, hadronization can refer to the both the parton showering as well as hadron formation.

In experimental high energy particle physics the term Monte Carlo (MC) is used as a short hand for simulated physics samples, however the MC method of generating these samples means something specific. The MC method of generating parton branching is stated as: given some virtual mass scale t_1 and momentum fraction x_1 generate (t_2, x_2) after one step in the branching evolution. To perform this step-wise evolution of the parton branching we need the shower evolution equations [59].

Consider the branching of a particle a : $a \rightarrow bc$ with a momentum scale Q^2 . We denote energy and momentum fraction imparted to particle b as z such that particle c receives $1-z$. We introduce the momentum transfer variable (reminiscent of Equation 3.4) $t = \ln(Q^2/\Lambda^2)$. The differential probability for the particle a to branch is given:

$$d\mathcal{P}_a = \sum_{b,c} \frac{\alpha_{abc}}{2\pi} P_{a \rightarrow bc}(z) dt dz$$

where the sum is over all possible branchings and α is the appropriate coupling (α_{EM}, α_S) for the branching evaluated at the appropriate scale. We enumerate the kernels that map the momentum fraction from splitting to the possible states after branching:

$$\begin{aligned} P_{q \rightarrow qg}(z) &= C_F \frac{1+z^2}{1-z} & P_{q \rightarrow q\gamma}(z) &= e_q^2 \frac{1+z^2}{1-z} \\ P_{g \rightarrow gg}(z) &= N_C \frac{(1-z)(1-z)^2}{z(1-z)} & P_{l \rightarrow l\gamma}(z) &= e_l^2 \frac{1+z^2}{1-z} \\ P_{g \rightarrow q\bar{q}}(z) &= T_R(z^2 + (1-z)^2) \end{aligned}$$

where $C_F = 4/3$ is a color factor, N_C is the number of colors in QCD, $T_R = n_f/2$ is half the number of allowed $q\bar{q}$ flavors. e_i^2 is the charge squared of the quark or lepton.

Let us define an integral over the probability distribution for some fixed t between the minimally allowable momentum fraction z_- and the maximum z_+ as:

$$\mathcal{I}_{a \rightarrow bc}(t) = \int_{z_-(t)}^{z_+(t)} dz \frac{\alpha_{abc}}{2\pi} P_{a \rightarrow bc}(z)$$

From this we can find the total probability of branching as a sum over the possible branching states $p_{\text{branch}} = \sum_{bc} \mathcal{I}_{bc}(t)$. If we consider the probability of no branching occurring $(1 - p_{\text{branch}})$ in some finite interval (t, t_0) as the product of differential time steps δt , probability exponentiates:

$$\begin{aligned} \mathcal{P}_{\text{no-branch}}^a(t_0, t) &= \prod_{\delta t \in (t, t_0)} (1 - p_{\text{branch}}) \approx \lim_{N \rightarrow \infty} \sum_{k=0}^N \frac{N!}{(N-k)!k!} 1^{N-k} (-p_{\text{branch}})^k \\ &= \sum_{k=0}^{\infty} \frac{1}{k!} (-p_{\text{branch}})^k = \exp(-p_{\text{branch}}) \end{aligned}$$

Such that the total probability of not branching within a given t interval is given by:

$$\mathcal{P}_{\text{no-branch}}^a(t_0, t) = \exp \left(- \int_{t_0}^t dt' \sum_{b,c} \mathcal{I}_{a \rightarrow bc}(t') \right) = S_a(t)$$

Where we have introduced the notation $S_a(t)$ for what is referred to as the Sudakov form factor [63]. With this single parameterization we can write the probability of not branching as a ratio of $S_a(t)$ functions (since the ratio of exponentials will just alter the integral bounds):

$$\mathcal{P}(t_2, t_1) = \frac{S_a(t_2)}{S_a(t_1)}$$

Note here that t is not time, but rather serves a proxy for time, where the final state showering occurs from an initial t_{\max} set by the hard scattering and progressively becomes smaller through the branching process.

The MC process generates a random number \mathcal{P} and solves for t_2 in terms of t_1 . The process is then applied to the newly branched particles b and c . If t_2 is smaller than the scale set for hadronization, then the showering process terminates. Eventually from the monotonicity of t_i the cascade terminates and the generation process is handed off to hadronization.

3.6 Hadronization

When the quark model, a.k.a. the eight-fold way, was originally introduced in 1961, it was a large simplification of the space of observed particles. Each combination of possible light quarks was observed in nature (the third generation had not yet been discovered). Despite experimental efforts, a single “bare” quark was never observed. Today, we understand that it is the inherent nature of the strong force that prevents light quarks from being liberated from their hadronic bound states. As an interesting

side note, the discovery of the top quark, whose width is larger than Λ_{QCD} , will decay before hadronization takes place. In this section, we briefly discuss the way MC simulation models the non-perturbative confinement of quarks.

When we leave the showering process, we are left with a large number of virtual particles on the order of the cutoff t_{\min} . Although this parameter is unrelated to the hadronization process, an ideal hadronization model would use the chosen value of t_{\min} to compensate for effects of having a hard cutoff value for the showering. As t_{\min} is increased, there are fewer particles that are increasingly off-shell. These virtual particles should be able to hadronize, however, the favored values of t_{\min} to begin the hadronization step tend to be a few times the scale of hadronization $\Lambda_{QCD} \approx 0.1 - 0.3$ GeV. This is suggestive that the extensions of perturbation theory are more reliable than models of hadronization [29].

It is important to state that there are only models of hadronization and no calculations from first principles. Even lattice QCD calculations which are made on euclidean space times fail for processes which are inherently Minkowskian such as hadron formation. Two main categories of hadronization models exist. The string model which transforms virtual particles directly into hadrons and the cluster model which uses an intermediate clustering step before the conversion to hadrons [16].

The string model, the most well known of which is the Lund String Model [5], relies on an assumption of linear confinement. One expects a linear potential $V(r) = \kappa r$ at long distances, where the string constant $\kappa \approx 1$ GeV/fm ≈ 0.2 GeV 2 . In general, there is an additional coulomb potential at shorter distances (Figure 3.5). The Lund model assumes that this term is negligible in hadron formation.

One motivation for the linear confinement comes from the linear relationship between the spin of mesons J and their m^2 (Figure 3.6). To explain why, lets consider a spinning rod of mass constant density σ and length $2R$. Such a rod, like the string

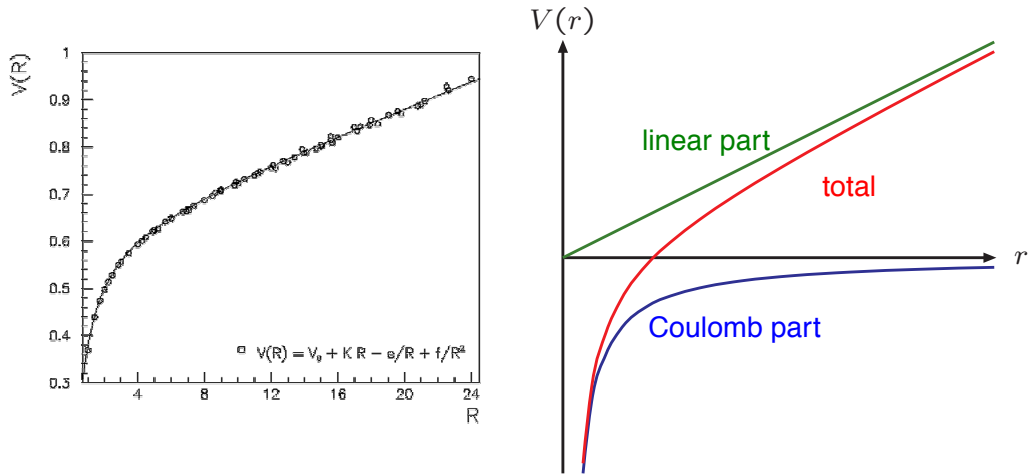


Figure 3.5: The static quark anti-quark potential as measured from lattice QCD calculations. An additional f/R^2 term is included to account for known artifacts from performing the measurement on a lattice. The linearity at large R in units of fm is clearly visible.

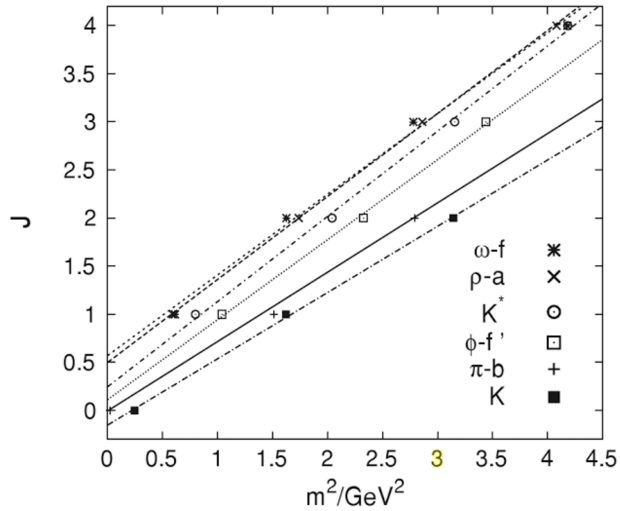


Figure 3.6: When the spin of mesons are plotted against their mass squared a linear relationship is found with nearly the same scaling. These lines are known as Regge trajectories.

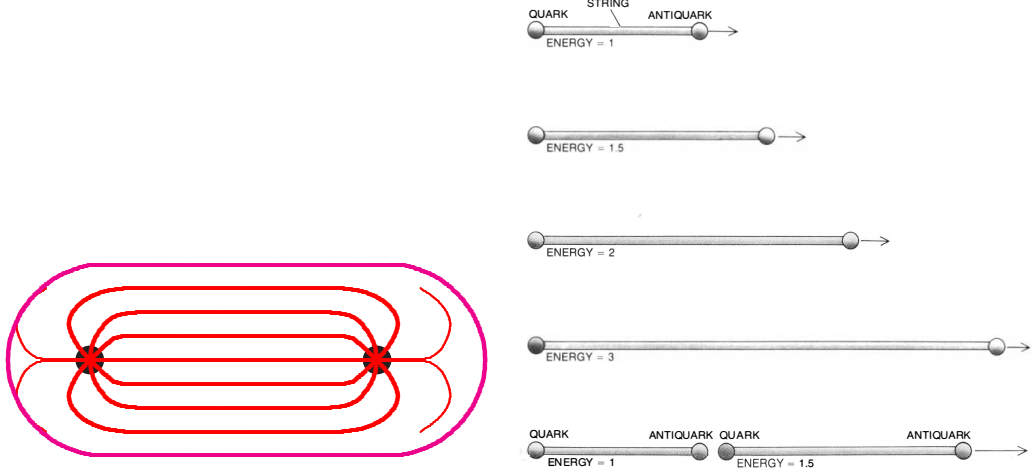


Figure 3.7: The flux between a quark and anti-quark (left) A simple model of quarks as the ends of a string. As an attempt is made to separate the two quarks, the string breaks producing two new ends i.e. quarks (right) [51]

has linearly scaling energy with length. Calculate the total energy: total energy as:

$$m = E = 2 \int_0^R \gamma(r) \sigma dr = 2 \int_0^R \frac{\sigma dr}{\sqrt{1 - \frac{r^2}{R^2}}} = \pi \sigma R$$

Calculating the angular momentum

$$J = 2 \int_0^R r \beta \gamma(r) \sigma dr = 2 \int_0^R \frac{\sigma r \beta}{\sqrt{1 - \beta^2(r)}} = \frac{2}{R} \int_0^R \frac{\sigma r^2}{\sqrt{1 - \frac{r^2}{R^2}}} = \frac{1}{2} \pi \sigma R^2$$

by comparison we see that $J = \frac{1}{2\pi\sigma} m^2 = \alpha m^2$. From experimental data this constant, α , is found to be $\alpha = 0.9$ GeV/fm. This relationship was also found to be accurate in static calculations of the quark anti-quark potential in lattice QCD as shown in Figure 3.5. The string model of hadronization should not be confused with the strings of “string theory”, where strings serve as the fundamental objects. The linear confinement of QCD is best visualized as a color flux tube being stretched between a quark and anti-quark (Figure 3.7). These flux lines are similar to those of the equipotential lines between a positive and negative electric charge but with a

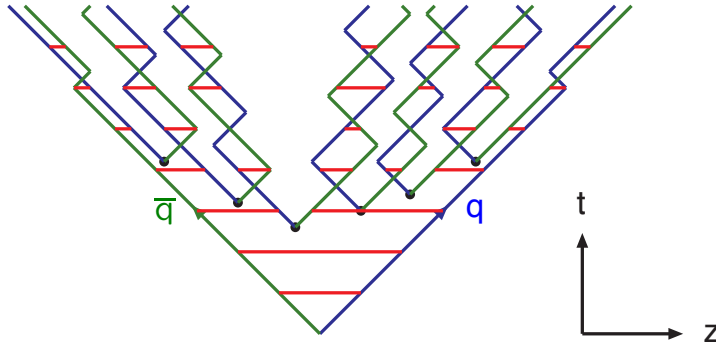


Figure 3.8: The 1+1 dimensional propagation of the hadronization process beginning from a quark anti-quark pair.

characteristic r dependence rather than $1/r$. As the two quarks are increasingly separated in space, the flux tube is stretched maintaining constant energy per unit length κ . The Lorentz covariant and causal description of this energy flow uses a massless one-dimensional string that parameterizes the axis of a cylindrically symmetric flux tube. In the simple case of quark anti-quark production in the (Figure 3.8), the two quarks separate from each other along the z-axis and the potential energy stored in the string increases. When the potential energy is large enough, the string can break via the production of a new quark anti-quark pair. These breaks typically occur between 1 and 5 fm in the rest frame of the pair, however in the lab frame these processes are highly length contracted. After the break, widening regions of no flux arise. By the end of the process, the string has been broken into many segments through the creation of $q\bar{q}$ pairs. Hadrons are formed by a quark from one break and the anti-quark of an adjacent break [16]. The energy-momentum picture is derived from the space-time picture through the string tension as:

$$\left| \frac{dE}{dz} \right| = \left| \frac{dp_z}{dz} \right| = \left| \frac{dE}{dt} \right| = \left| \frac{dp_z}{dt} \right| = \kappa$$

This is to say that the hadron has energy equal to the string constant times the separation in space between the two quarks and momentum equal to the string constant

times the separation in time. By requiring the hadrons to be formed on shell, the constituent pair of breaks that build a hadron are correspondingly causally separated i.e. space-like.

$$m_T^2 = E^2 - p_z^2 = \kappa((\Delta t)^2 - (\Delta z)^2) > 0$$

This also means that as the hadron propagates, the kinks in the hadron pair will always occur with the same separation (the bound rectangles in Figure 3.8 will always have the same area). This corresponds the hadron remaining on shell.

Note that the incredibly dense and active environment of hadronic collisions could lead to significant collective effects which are not considered in current hadronization models. Such effects are studied in high energy lead collisions where the environment is significantly more dense.

3.7 Hadron Decay

Once we have the final hadron picture, the hadrons must be decayed into particles which are stable on the length scales of the detector. That is, the final particles that are measured by the experiment. It might seem simple that the generators could use known branching ratios from the extensive Particle Data Group tables on particle decays [52], however, this information is often incomplete. The least documented decay modes are excited multiplets including heavy quarks (bottom and charm) [16].

One important choice that must be made for different generators is which hadrons to include in their simulation. Generally, all simulators include the lightest pseudo scalar, vector, scalar, even and odd charge conjugation pseudo vector and tensor multiplets of light mesons. These decisions must be made carefully as in certain models the exclusion of any members of a given multiplet cause unphysical rates of isospin violation. Decisions are also made on which decay channels to include.

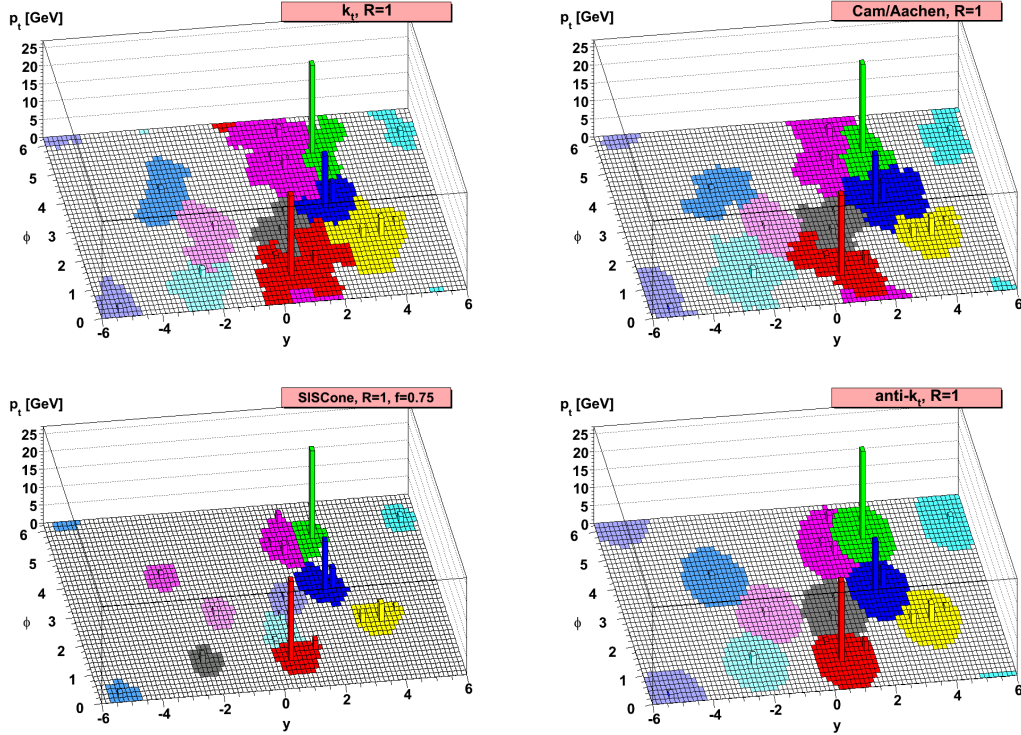


Figure 3.9: Comparisons made between varied clustering algorithms when many soft “ghost” entities are added to exaggerate the effect soft radiation has on the boundary of clustering algorithms for the same event.

Historically the kinematics of hadron decay were done with simple Breit-Wigner smearing of the hadron mass, nowadays more sophisticated matrix element methods exist for tau leptons (TAUOLA [40]) and certain hadron decays (EvtGen [50]). Significant work has been done to model the decays of B-mesons which serves the b physics community search in the search for rare B mesons decays and $B^0 - \bar{B}^0$ mixing.

3.8 Jet Clustering

Once the showering and hadronization have constructed the final state particles we need a way of clustering the numerous deposits or particles in the final state simulation as well as in data. While in simulation one can trace the hadrons back through their branching tree to their mother particle from the hard interaction, data has no such

information. This problem necessitates a fast algorithm that takes as input energy deposits in the detector and outputs clusters with kinematic properties representative of the hard scattering process quarks and gluons.

Any desirable clustering algorithm should be collinear and infrared safe. Such an algorithm is insensitive to the soft and collinear radiation that could alter the boundaries of clustered deposits. The most commonly utilized clustering algorithm is anti- k_t [17] which takes a size parameter R . The resultant four momentum of the cluster is given by the four-momentum sum of the individual deposits.

To cluster jets the inclusive algorithm defines two distances, d_{ij} , the distance between two recombining entities i and j , and d_{iB} , the distance from the entity to the beam.

$$d_{ij} = \min(k_{ti}^{2p}, k_{tj}^{2p}) \frac{\Delta_{ij}^2}{R^2} \text{ with } \Delta_{ij}^2 = (y_i - y_j)^2 + (\phi_i - \phi_j)^2$$

$$d_{iB} = k_{ti}^{2p}$$

Here Δ_{ij} is the typical definition of $(\Delta R)^2$ (not to be confused with the algorithm size parameter R) using rapidity y . The value k_{ti} is the transverse momentum of the i^{th} entity and ϕ is the azimuthal angle. The parameter p allows one to vary the relative strength of the momentum against the geometrical distances in the clustering. For $p = 1$ this is the k_t algorithm, for $p = 0$ this is the Cambridge/Aachen algorithm, and for $p = -1$ this is the anti- k_t algorithm.

The algorithm proceeds by identifying the smallest of the two distances for two recombining entities. When the $\min(d_{ij}, d_{iB}) = d_{ij}$ the two entities are combined. If the minimum is d_{iB} then i is a jet and its removed from the list of entities. Afterwards, distances are recalculated and the procedure is repeated until all entities have been removed from the list.

From the definition of the distances we first see two entities will not be combined unless they are within the size parameter. If we locally consider two entities within the size parameter, the distance is entirely determined by the higher momentum entity, with no dependence on the softer entity. This means the distance between a hard and soft entity will be much smaller than a similarly separated soft and soft combination. Thus, the clustering process tends to cluster soft entities with hard entities first. When a hard entity has no hard neighbors it will simply accumulate all of the soft entities nearby within the size parameter leading to a conical jet. If only two hard entities are within $2R$ of each other the two will be conical with a boundary determined by the ratio $\Delta_{1b}/k_{t1} = \Delta_{2b}/k_{t2}$. If two jets within $2R$ have the same momentum then the boundary will be a straight line. Jets with significantly different momentum will induce a crescent shaped boundary.

By injecting soft radiation into an event and plotting the boundaries of the clustering, (Figure 3.9) one can see the strong insensitivity of the algorithm to soft radiation and the correspondingly conical resultant jets.

Chapter 4

The Compact Muon Solenoid Experiment

As discussed in Chapter 2 we cannot make direct measurements of the hard scattering process at experiments. Instead, detectors are built to indirectly probe the hard scattering by measuring the energy and momenta of the final state particles. By relying on known interactions of Standard Model particles with detector materials, strong probabilistic statements can be made about the flavor of particles in a given collision. By building a hermetic detector and integrating the various sub-detectors, one obtains a wholistic view of the collision. This includes the momentum of particles which escape the detector, such as stable dark matter or neutrinos. This chapter will discuss each sub-detector, the particles it is designed to identify, and the underlying physics which allows the individual measurements to be made.

The experiment is made up of nearly 5000 particle physicists, engineers, computer scientists, and technicians from around 200 institutes and universities over more than 40 countries. Although the experiment is incredibly diverse culturally, the experiment is dominated by men (Table 4.1). In the year 2014 there were 4119 Males and 863 females for an overall gender ratio of 4.77 men to every female and equivalently 17.3%

Table 4.1: CMS Gender Demographics by Age as of 2014. Age groups are separated by age range. Columns represented the fraction of the total CMS.

Age Range	% of Men (M)	% of Women (W)	M/W
< 25	12.6%	19.4%	3.1
25-29	20.0%	24.0%	4.0
30-34	12.8%	15.0%	4.2
35-39	9.7 %	8.4%	5.0
40-44	8.5%	8.3 %	4.9
45-49	8.3%	7.2 %	5.5
50-54	8.5%	7.0%	5.8
55-59	6.6%	5.0%	6.3
60-64	5.2%	2.6%	9.8
65-69	3.8%	2.1%	8.7
>69	4.1%	0.6%	34

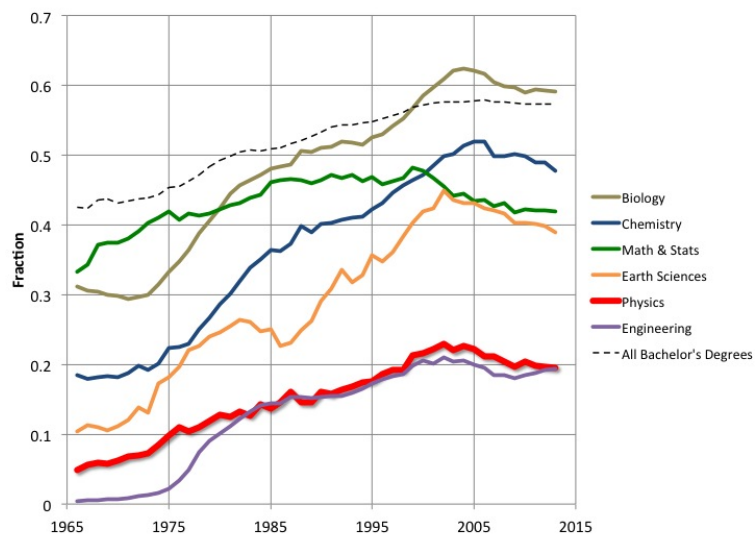


Figure 4.1: The fraction of degrees in science, technology, engineering, and math disciplines [60].

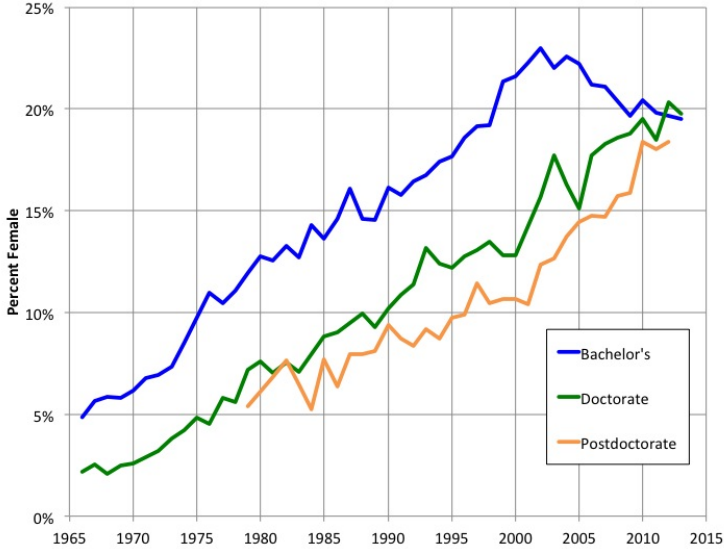


Figure 4.2: The fraction of physics degrees by type earned by women [60].

of the collaboration. 45% (58%) of all men (women) in the experiment are under the age of 35. These ratios however are not restricted to this experiment but common in American Physics programs. About 20% of STEM majors are female 4.1 and 17-20% of Physics degrees earned in 2013 were female 4.2. As the fraction of female physics majors bachelors has flattened, the continued growth in PhD and postdoctorate work appears to be coming from other fields. Although growth would be slow to reach equity, the rate of female participating is growing for graduate level research.

The Compact Muon Solenoid (CMS) Detector (Figures 4.3 and 4.4) is a general-purpose detector consisting of an all silicon tracker, a precision electromagnetic calorimeter (ECAL), a hadron calorimeter (HCAL), a 4 T superconducting solenoid and muon chambers. The solenoid deflects charged particles whose paths are traced in the tracker, making it possible to reconstruct the particle's momentum. The two calorimeters reconstruct the energy of and identify photons, electrons and hadronic jets. The detector has cylindrical symmetry about the interaction point where the proton beams collide. By maintaining near full coverage of the interaction point, it is

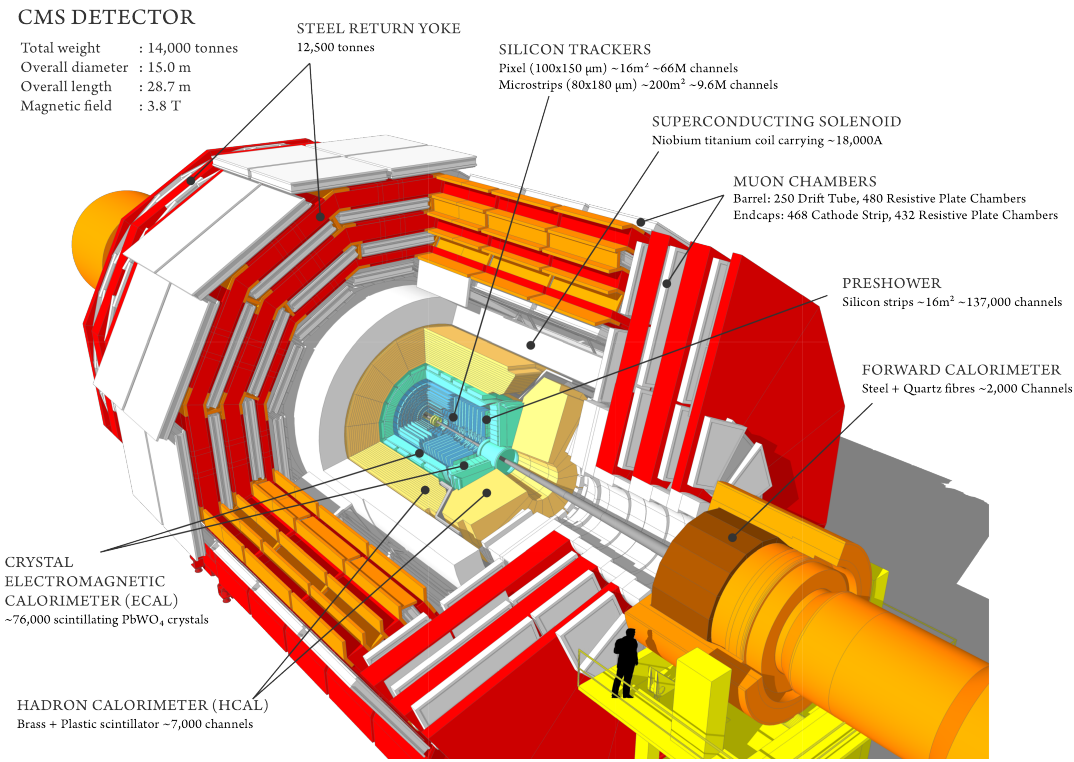


Figure 4.3: The CMS Detector with inner components exposed and a person for scale.

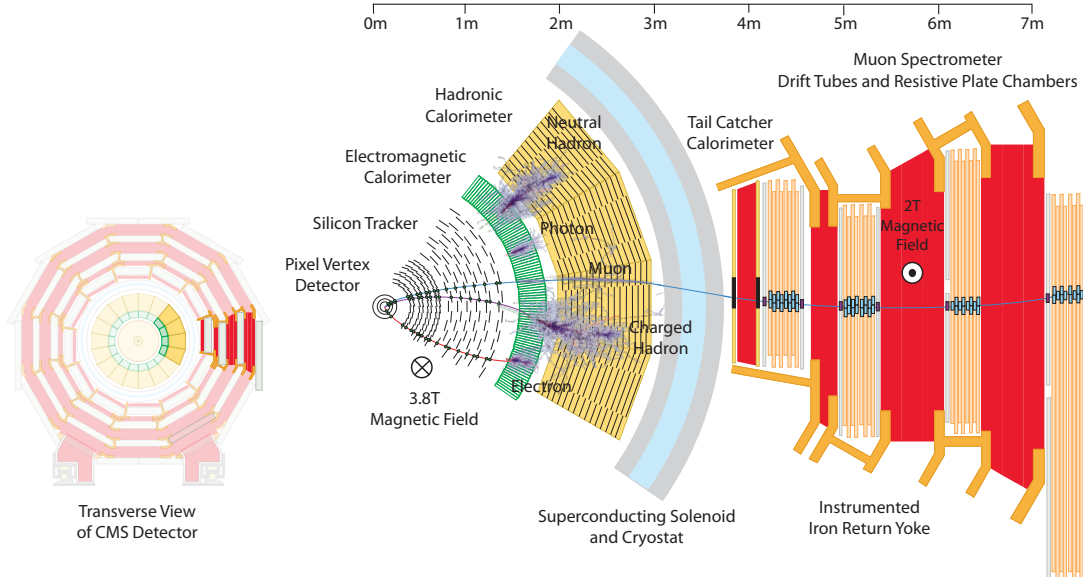


Figure 4.4: A slice of the CMS detector showing particle interactions with the various sub-detectors.

possible to detect signatures such as neutrinos or other weakly interacting particles as missing energy.

4.1 CERN Laboratory and the LHC

CERN Laboratory is located on the border between Switzerland and France where the local language is French. Accordingly, the lab name is an acronym in french “Conseil Européen pour la Recherche Nucléaire” or in English, “European Council for Nuclear Research”. Founded in 1954 as a collaborative project across 12 countries in Western Europe, the project has grown to 22 member states in 2017. The name is derived from the study fundamental physics, which at the time was nuclear physics.

The lab consists of numerous experiments studying fundamental physics [25], the largest of which are related to the Large Hadron Collider which delivers proton-proton (as well as lead-lead) collisions to four experiments: ATLAS, CMS, ALICE, and LHCb. Non-LHC experiments often utilize pieces of the accelerator complex like the Super Proton Synchrotron (SPS) and the Proton Synchrotron (PS) to perform experiments where a single accelerator beam collides with a fixed target. There are groups which study anti-matter and experiments investigating cosmic rays.

Although the United States is large contributor of technology and person power, they are currently not a member state of CERN. There is no provision that requires member states to be European (Israel is currently a member state). One will also not find an official statement by the US or CERN as to why such a large contributor to the experiment is not a member. While the US is not excluded from participation in the experiment, it does pose significant barriers for American scientists trying to obtain positions at CERN. While I consider these decisions largely political in nature, I consider it worthwhile to look at the financial commitments member states make and what comparable US contributions would look like if the contributions were similar.

Table 4.2: A summary of the GDP, CERN lab contribution, and the ratio between GDP and the absolute contribution by country

Country	GDP	Abs (Rel) Cont.	(Cont/GDP) $\times 10^{-7}$
Germany	\$3.36T	231M CHF (20.5%)	6.8 CHF/USD
France	\$2.24T	170M CHF (15.1%)	7.5 CHF/USD
UK	\$2.86T	161M CHF (14.3%)	5.6 CHF/USD
Italy	\$1.82T	125M CHF (11.1%)	6.9 CHF/USD
Spain	\$1.19T	88M CHF (7.82%)	7.4 CHF/USD
USA	\$18.03T	-	-

Table 4.3: Differences in Absolute NNI vs GDP for the year 2015. Countries are ordered by absolute contribution size from highest to lowest.

Country	GDP [USD]	NNI [USD]	NNI/GDP	NNI/Capita
Germany	3.36T	3.31T	0.99	40.6k
France	2.24T	2.27T	1.01	34.4k
UK	2.86T	2.33T	0.81	35.8k
Italy	1.82T	1.84T	1.01	30.3k
Spain	1.19T	1.33T	1.12	28.6k
USA	18.03T	15.67	0.87	48.7k

The CERN operating budget provided by the individual member states (Table 4.3) The total budget for CERN in 2015 was 1127 Million Swiss Francs [48]. The USD/CHF exchange rate as of January 1, 2016 was 0.994 and 0.999 as of December 31, 2015. Countries contributing less than 5% are excluded from the list (Switzerland contributes 3.87%). The average contribution from the top 5 countries which comprise 68.8% of the operating budget is 0.068 million Swiss franc per billion USD of gross domestic product. For the United States, a comparable contribution (1224 Million USD) would be larger than the 2015 operating budget. If contributions were renormalized such that the total budget were fixed, the United States would be funding more than half of the lab's operations.

The contributions although nearly scaling linearly with GDP are defined by the CERN financial committee in terms of a related economic indicator NNI [23] [24]. The scale for each countries contribution is set by:

“Using the arithmetic average of three years of Net National Income values until year before last year and applying the corresponding annual average exchange rate for each year”

The NNI is calculated as the Net National Product (NNP) less Indirect taxes. Indirect taxes are taxes which are collected by an intermediary from the person bearing the ultimate burden of the tax (sales tax, value added tax, ect). The Net National Product is the Gross National Product (GNP) less depreciation, the decrease in value of assets or the allocation of the costs of an asset to a later period in which the asset is used. The GNP was once a more common measure of economic activity than GDP, and is closely related. GNP is equal to GDP plus the income earned by residents from overseas investment and less the income earned within the domestic economy by overseas residents. We thus write NNI as a function of GDP:

$$\begin{aligned} \text{NNI} = & \text{GDP} + (\text{Resident income from overseas investment}) \\ & - (\text{Depreciation}) - (\text{Indirect taxes}) - (\text{Domestic income by overseas residents}) \end{aligned}$$

The Net National Income (NNI) is listed for the top contributors for the year 2015 in Table 4.3. Net national income is defined as the net national product minus indirect taxes. For most countries, GDP/NNI is nearly 1, the exceptions being the UK and Spain. Had the contributions been scaled by GDP, the UK would be paying significantly more and Spain somewhat less. Spain, to have a GDP/NNI ratio greater than 1 must have significant component of income earned by residents from oversea investment.

4.1.1 The Large Hadron Collider

The Large Hadron Collider (LHC) is a 27 kilometer ring 100m underneath the border of Geneva, Switzerland and France (Figure 4.5). It is the largest and most

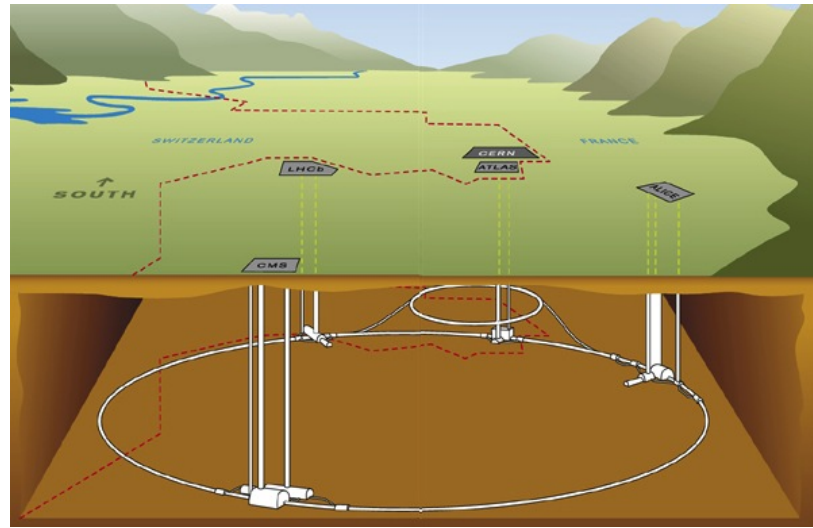


Figure 4.5: The LHC tunnel installed on the border of Geneva, Switzerland and France. The experiments are distributed along the circumference of the ring.

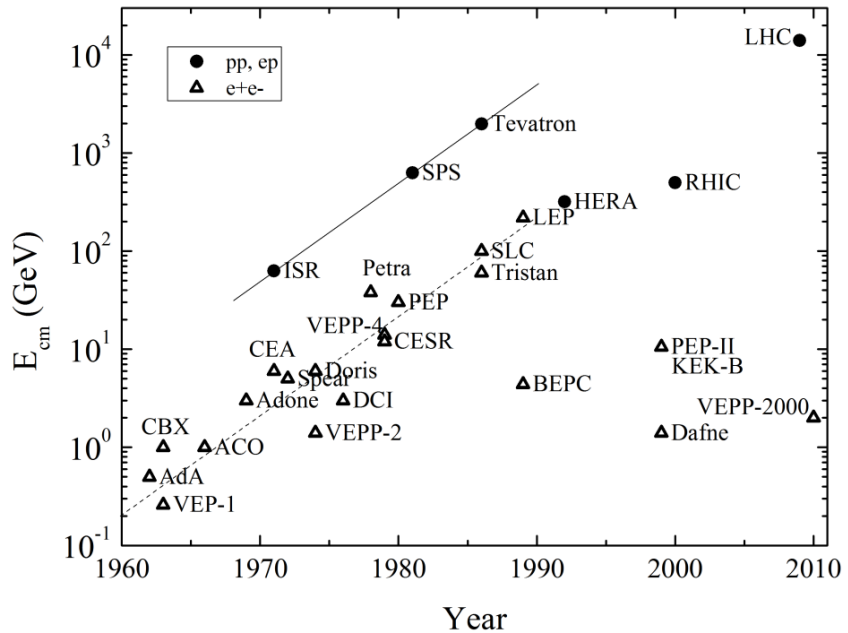


Figure 4.6: The historical progression of collider energies in time.

Table 4.4: LHC Running Parameters [68]

Parameter	Value	Remarks
Circumference (km)	26.7 km	100-150 m underground
Number of Dipoles	1232	Nb-Ti Cables
Length of Dipole	13.3 m	
Dipole Field Strength	8.4 T	Results from high beam energy
Operating Temperature	1.9 K	He cooled superconducting magnets
Current in Dipole Coils	13kA	Results from high magnetic field
Beam Intensity	0.5 A	
Beam Stored Energy	362 MJ	1MJ melts 2kg Cu
Magnet Stored Energy / octant	1100 MJ	

powerful particle collider of the world at a design instantaneous luminosity of 10^{34} $\text{cm}^{-2}\text{s}^{-1}$ and $\sqrt{s} = 13 \text{ TeV}$ (Figure 4.6). The previous highest energy collider, Tevatron, a proton anti-proton collider, operated at $\sqrt{s} = 1.96 \text{ TeV}$ and an upgraded instantaneous luminosity of $4 \times 10^{32} \text{ cm}^{-2}\text{s}^{-1}$.

The LHC consists of a series of super conducting magnets that steer two beams of protons about the circumference and focus them at collision points where the experiments are located. The bunches of protons in the LHC are bent into a circular trajectory by more than 1200 superconducting dipole magnets and are focused and maintained close to the ideal orbit around the ring by hundreds of superconducting quadrupole magnets. Thousands of corrector magnets around the ring allow the beam to be steered closer to the ideal orbit, make the focusing independent of the particle's energy variations within a bunch, and cancel the effects of higher order multipoles in the fields induced by small field imperfections in the main magnets. The radio frequency (RF) field in superconducting cavities is placed periodically around the ring and accelerates the protons from the injection energy of 450 GeV to the final operating energy, which is designed to be 7 TeV per beam. The RF field also causes the protons to be bunched, as only particles at or near a certain equilibrium phase on the RF wave will be accelerated stably. Special quadrupoles around each interaction

region focus the bunches down to a small transverse size, to increase the likelihood of a proton-proton collision each time two bunches pass through each other.

The instantaneous luminosity delivered by the large hadron collider can be determined from the following expression:

$$L = \frac{f}{\pi} \frac{N_p N_{p^c}}{n_b} \frac{\gamma}{\sqrt{\beta_x^* \beta_y^* E_x^* E_y^*}} \quad (4.1)$$

- f : revolution frequency of the beams.
- N_p the number of protons in the beam
- n_b the number of proton bunches
- $\beta_{x,y}^*$ the transverse wavelengths of the betatron oscillations
- $E_{x,y}^*$ the transverse emittance of the beams
- γ : relativistic factor

To increase luminosity and correspondingly the total amount of data taken in a fixed time interval, this parameterization tells us we want a high frequency of collisions, high proton density within the bunches, small oscillations transverse to the ideal path, and a small average spread in position momentum space. The small spread in phase space (low emittance) means the particles are confined to a small area and have roughly the same momentum. This result in a high probability of interaction.

4.2 Superconducting Solenoid

It is worth beginning this discussion around the central feature the rest of the detector is built, the 4 T superconducting solenoidal magnet. For scale, a typical refrigerator magnet is on the order of 10^{-2} T and the MRI magnets can range between 0.5-3.0 T.

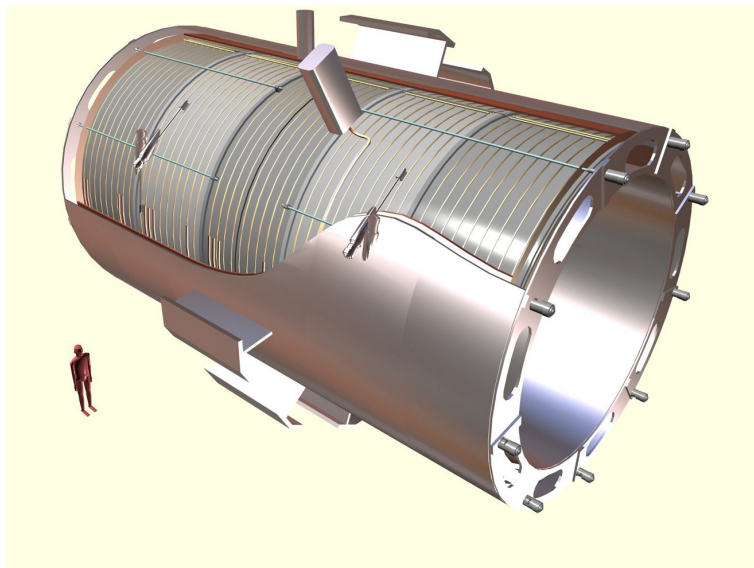


Figure 4.7: The CMS solenoid with a human for scale.

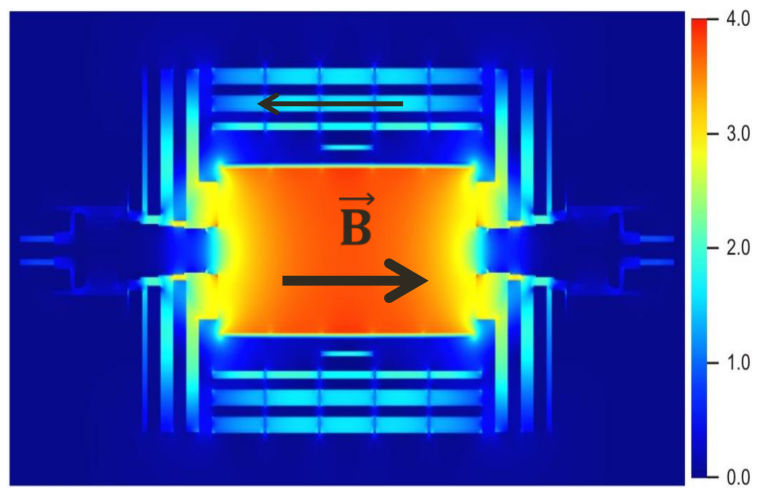


Figure 4.8: The CMS magnetic field in units of Tesla (T).

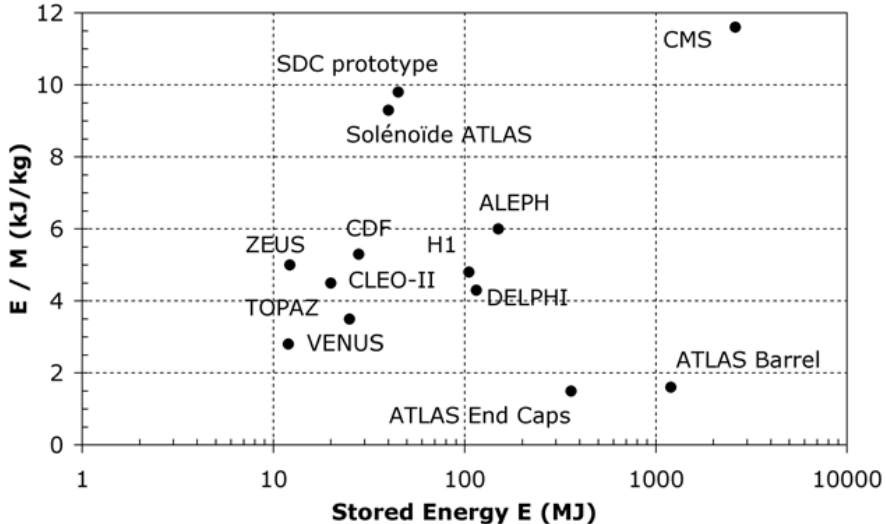


Figure 4.9: The relationship of E/M and E for various collider experiments.

The magnetic field is used to measure the momentum of charged particles by bending their trajectories. As the size of the bend is proportional to the field and inversely to the momentum of the particle, a stronger field is required to measure higher energy particles with precision.

The magnet is 6 meters in diameter with 12.5 meters in length (Figure 4.7). The magnetic field (Figure 4.8) is generated 2180 turns wound in four layers of Niobium Titanium conductors inside an aluminum cylinder carrying a nominal current of 20 kA. At the design field strength the solenoid stores magnetic field of 2.66 GJ, the largest stored energy of any magnet ever built. The energy to mass ratio is 11.6 kJ/kG a identifying feature in the historical context of detector magnets (Figure 4.9). The magnet is supplemented by a 10,000 ton iron return yoke which takes in the flux of the magnetic field from the solenoid improving uniformity in the field.

To operate in a superconducting state, the system is cooled to 4.5 K with a thermosiphon [30]. This process takes 3 days to achieve from room temperature. A thermosiphon is an indirect cooling method utilizing passive heat exchange where, rather than pumping the liquid helium, the flow is induced thermally (Figure 4.10).

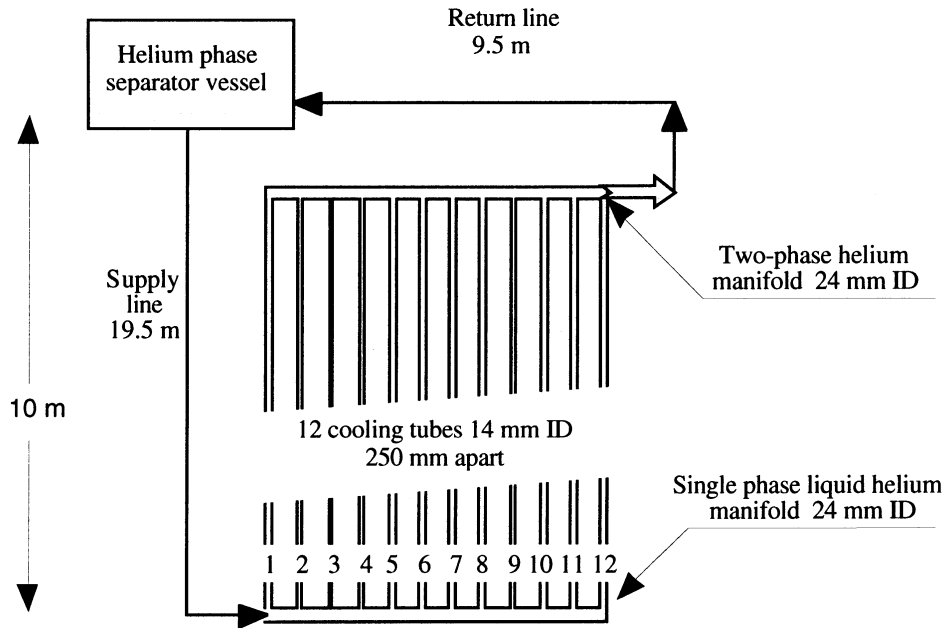


Figure 4.10: A sub circuit of the CMS thermosiphon

4.3 Electromagnetic Calorimeter (ECAL)

The electromagnetic calorimeter (ECAL) exists to measure the energy of electromagnetic showers of electrons and photons. For high energy electromagnetic objects above the mass threshold of pair production, $\gamma \rightarrow e^+e^-$, the interaction with matter occurs as an electromagnetic shower. In this shower, photons pair produce electron-positron pairs and electrons undergo bremsstrahlung radiation: $e^\pm \rightarrow \gamma e^\pm$. This processes continues until the individual particles in the shower cannot continue $1 \rightarrow 2$ processes and instead undergo multiplicity preserving interactions such as Compton scattering and ionization.

The detector material (for CMS a scintillating crystal) is characterized by the shower's Molière Radius, defined as the radius transverse to the incidence of a cylinder that containing 90% of the shower. For the CMS ECAL, crystals have approximately the Molière radius of approximately 2.2 cm. The material can further be characterized by its radiation length, the typical amount of matter the incident particle can traverse

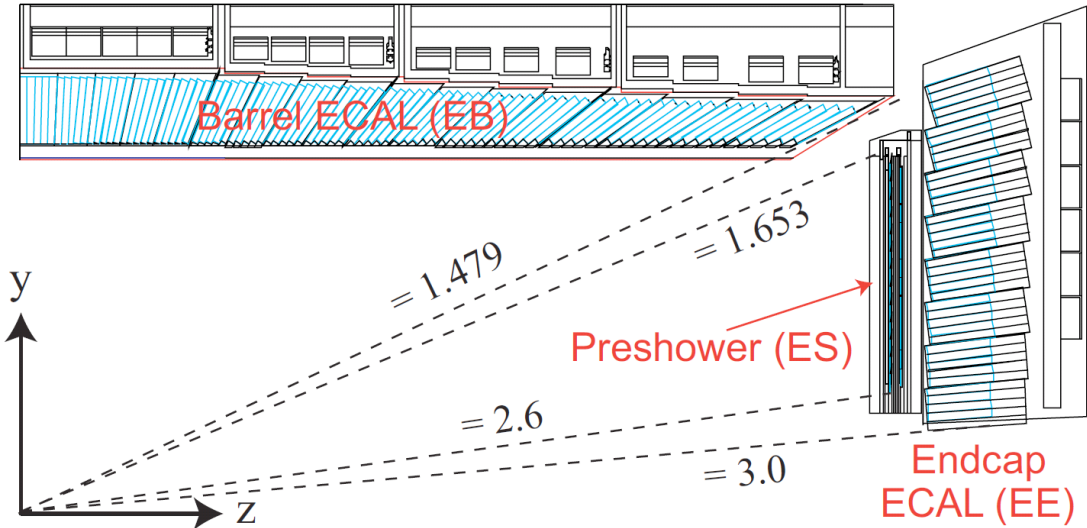


Figure 4.11: Kinematic coverage of the electromagnetic calorimeter (ECAL) barrel and endcap

before an interaction. The CMS crystals have a relatively short radiation length of 0.9 cm. Each crystal is approximately 25 radiation lengths = 23 cm.

The crystal energy resolution as a function of energy is characterized as:

$$\frac{\sigma(E)}{E} = \frac{S}{\sqrt{E}} \oplus \frac{N}{E} \oplus C \quad (4.2)$$

Here σ is the gaussian standard deviation of the energy measurement, the operator \oplus signifies addition in quadrature, S is the stochastic term, N is the electronic readout noise, and C is the constant term which does not scale with energy. The stochastic term S comes from the statistical nature of the photoelectric shower and the containment within the crystal. The readout term arises from the electronics noise in the preamplifier and digitization of the signal. The constant term C is caused by non uniformities between the many crystals and is ultimately dominated by the crystal to crystal inter calibration. As the first two terms scale inversely with energy, the constant term is dominant for high energy photons and electrons > 50 GeV . The

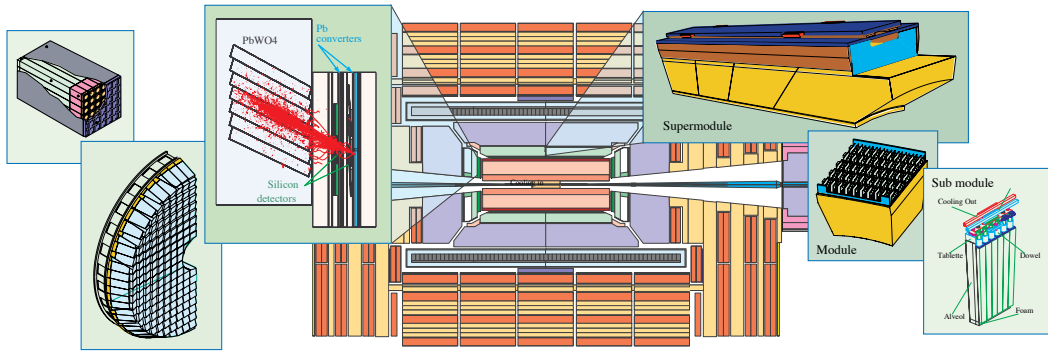


Figure 4.12: The CMS ECAL crystals as formed into sub modules, modules, supermodules and dees.



Figure 4.13: (left) The ECAL barrel installed within CMS. (right) A single dee of the ECAL endcap.

design energy resolution for high energy photons like those found in the discovery of the Higgs boson is $< 0.5\%$

The ECAL consists of 75,848 Lead Tungstate PbWO₄ scintillating crystals (Figure 4.12). The ECAL is separated into two sections: the endcaps and the barrel. The Barrel consists of 61200 $2 \times 2 \times 23$ cm crystals, separated into 36 supermodules, and is contained in $|\eta| < 1.48$. The endcaps are separated into 4 dees (Figure 4.13) of 3662 crystals with each crystal measuring $3 \times 3 \times 22$ cm. The 4 dees cover a pseudorapidity range between $1.48 < |\eta| < 3.0$. The endcaps are behind a preshower detector, composed of two lead absorbers interleaved with silicon detectors. The preshower

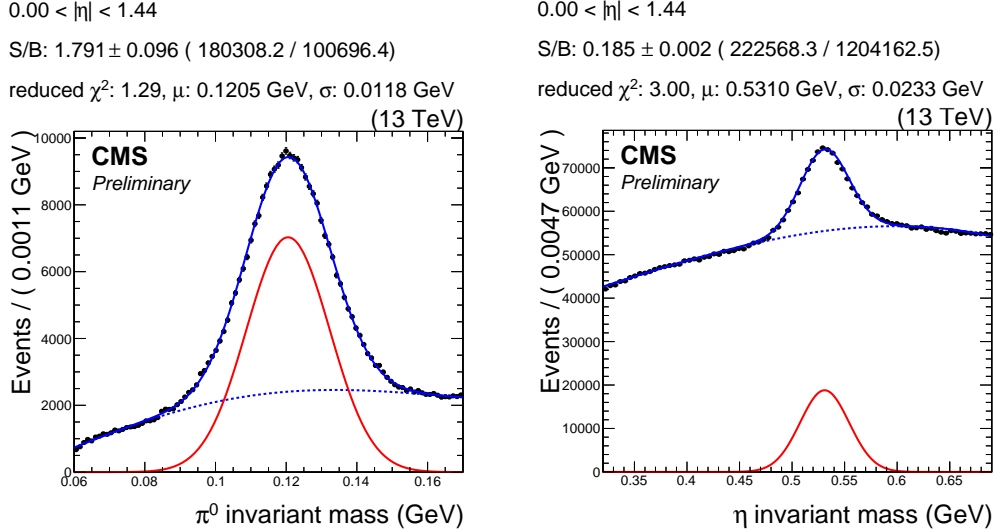


Figure 4.14: Calibration data for used for the pizero and eta calibration of the ECAL

covers the pseudorapidity range of $1.653 < |\eta| < 2.6$ with each silicon sensor covering a square area of $63 \text{ mm} \times 63 \text{ mm}$ divided into 32 strips. The preshower is designed to give significantly better spatial resolution than using the endcap alone to aid in the separating single photons and $\pi^0 \rightarrow \gamma\gamma$ decays used to calibrate the endcap. As the first layer is 2 radiation wavelengths thick, such that the majority of incident single photons will begin to shower before reaching the second layer. The conversion of the photons by the preshower assists in distinguishing directly produced photons from pairs of photons resulting from neutral pion decays.

The light in each crystal is collected as a current and amplified by avalanche photodiodes (APDs) in the barrel region and vacuum phototriodes (VPTs) in the endcap. This transition is necessary as the endcap region must be tolerant to much higher levels of radiation damage from softly scattered (low momentum transfer Q^2) interactions. The detector is calibrated with a method that reconstructs the mass of neutral pion and eta mesons to precisely calibrate the entire ECAL (Figure 4.14). The copious production of these particles in hadronic jets at the LHC allows us to perform this calibration rapidly, even at very low luminosity.

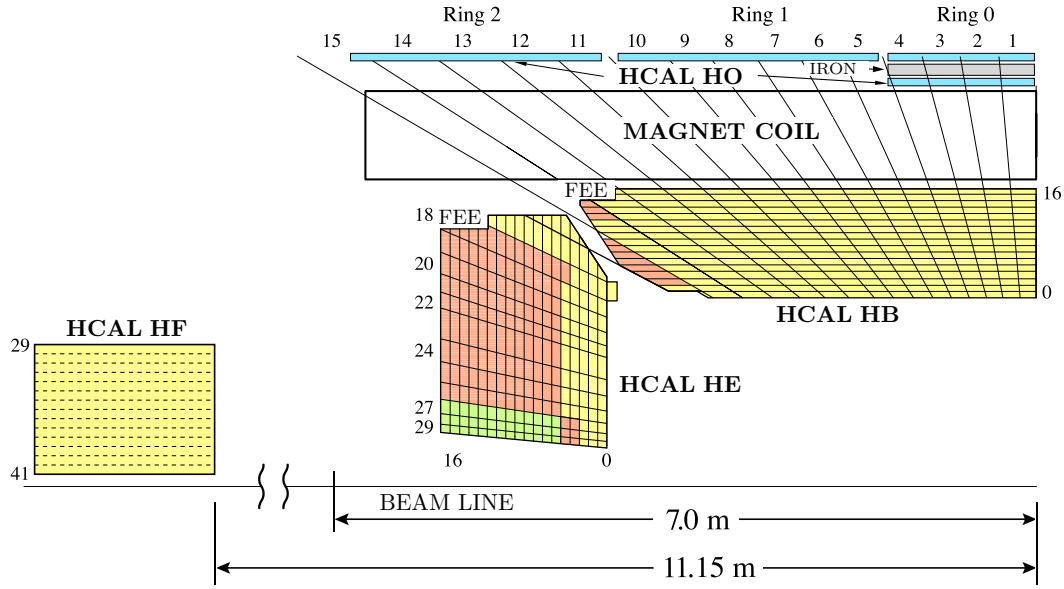


Figure 4.15: Kinematic acceptance of the CMS HCAL.

Under irradiation, the crystals undergo transparency changes due to the formation of color centers, which interestingly recover spontaneously when there is no radiation present. As the crystal transparency affects the energy measurement, the crystal transparency is continuously monitored by a laser monitoring system. The system takes advantage of a $3\ \mu\text{s}$ gap in the LHC bunch train to inject the pulses at a rate of 100 Hz. This rate allows for a measurement of every crystal to be made at least every 30 minutes. In the barrel, only laser pulses of known wavelength are injected through optical fibers. In the endcap, LEDs provide an additional wavelength.

4.4 Hadronic Calorimeter (HCAL)

Surrounding the ECAL. The Hadronic Calorimeter (HCAL) is hermetic (full coverage of interaction), non-compensating (asymmetric electromagnetic and hadronic energy response), sampling calorimeter (showering material differs from measurement mate-

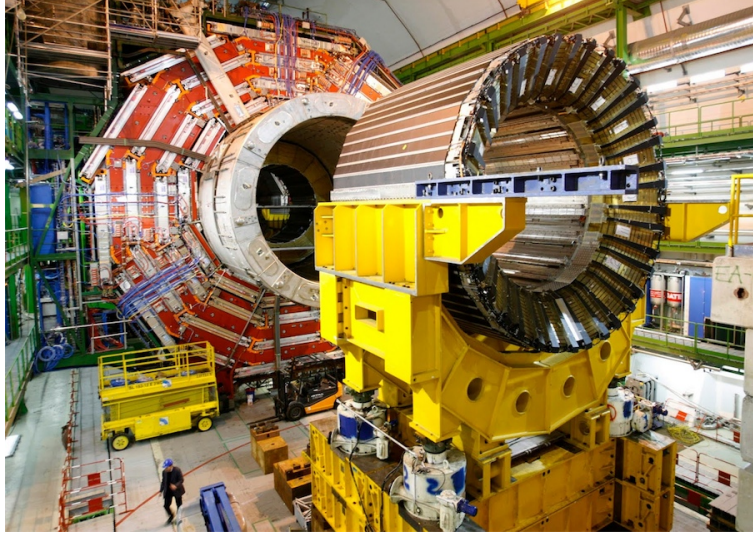


Figure 4.16: The CMS HCAL outside of the CMS detector.

rial) designed to measure the energy of neutral hadrons which would not deposit significant energy in the ECAL.

The HCAL consists of 9072 channels divided between four sections: the barrel (HB), the endcaps (HE), two forward calorimeters (HF) and an outer hadron calorimeter (HO). The barrel and endcap of the HCAL cover $|\eta| < 4$. The forward detectors extend the sub-detector's reach to $|\eta| = 5$. As the HCAL is radially limited by the design of the enclosing solenoid, the HO is built around the solenoid to measure any leaked energy from high momentum showers. The towers are segmented into towers that project into η, ϕ space with $\Delta\eta \times \Delta\phi = 0.087 \times 0.087$ for $|\eta| < 1.6$ and $\Delta\eta \times \Delta\phi = 0.17 \times 0.17$ for $|\eta| > 1.6$.

The HF sub-detector is a Cherenkov light detector using quartz fibers within 165 cm of steel absorber. Photomultiplier tubes (PMTs) connected to the fibers convert the detected light into an electronic signal. Cherenkov detectors utilize the characteristic electromagnetic “sonic boom” created by particles traveling faster than light can travel in a material. As the angle of emission and intensity of the radiation

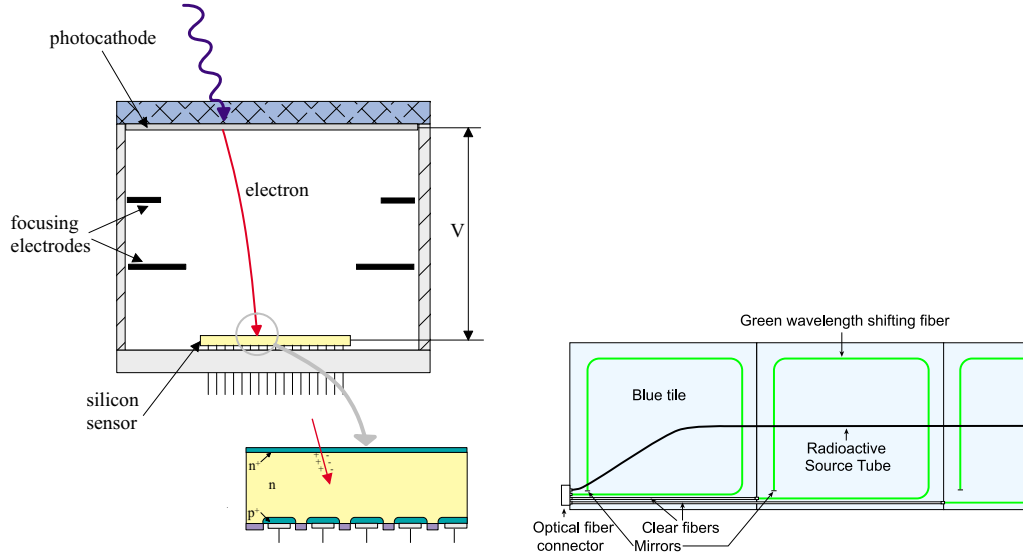


Figure 4.17: (left) A diagram of a typical HPD under a potential difference V [42].
 (right) 2 visible scintillator plates of 16 within a megatile [11].

depends on the velocity of the particle. For energetic particles $E > 1 \text{ GeV}$ the energy lost to the radiation is negligible [34].

Unlike electromagnetic showers, hadronic interaction cross sections are an order of magnitude smaller for the same material. To compensate cost effectively, hadronic calorimeters are constructed from dense materials such as copper, iron, lead, uranium, and tungsten [66]. In general, hadronic showers produce irregularly shaped deposits and varied particle content when compared to electromagnetic showers.

The HB/HE are constructed as alternating layers of brass absorber and plastic scintillator. The light is merged, wavelength shifted and measured by hybrid photodiodes (HPDs) with 17 channels per HPD. The HPD (Figure 4.17) functions by converting light into photoelectrons emitted at the photocathode and accelerated by a potential difference of 8-10 kV toward the silicon layer. The absorbed energy in the silicon sensor creates electron hole pairs which induce a detectable current. The light is wavelength shifted to avoid a loss of photons when piping light to the HPDs through a small cross sectional fiber.

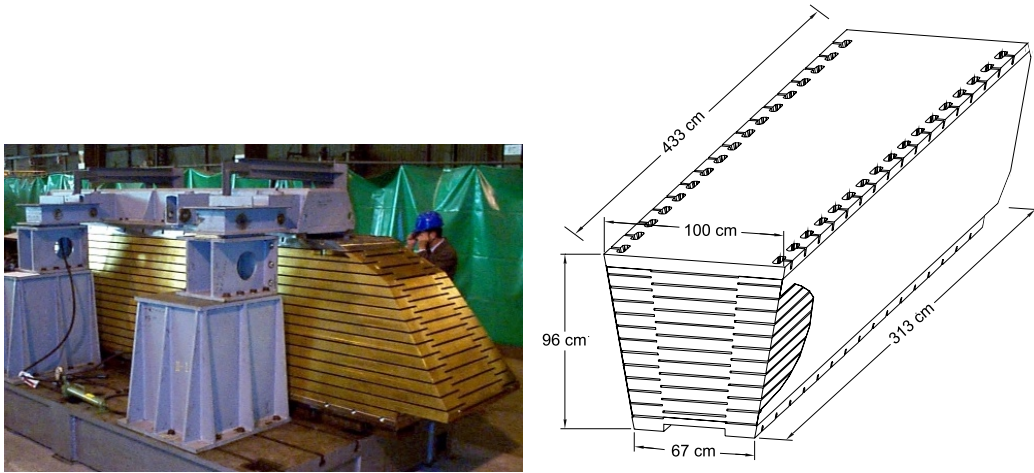


Figure 4.18: (left) A single wedge of the CMS HCAL barrel. (right) Scintillator trays (Figure 4.17) are inserted into slots at the end of the wedge [11].

Large deposits of energy reconstructed of hadronic energy in the HCAL are of particular interest to the study of long lived decays when the long-lived decay occurs inside of the HCAL calorimetry. Although not studied in this thesis, large signal to background discrimination can be found by requiring a calorimeter deposit to have no associated tracks and a large ratio of hadronic energy H/E . It is also of concern that the HCAL is known to have spurious noise that generally results in the mis-measurement of missing energy, and mimics the signature of long lived decay signatures. It is possible that using a coincidence of activity in the muon spectrometer could suppressed these events.

4.5 Tracking Layers

The CMS tracker's purpose is to reconstruct the trajectories (or simply “tracks”) of the charged particles copiously produced in hadron collisions. For a silicon strip detector, like that in CMS, the position measurements are derived from the ionization charge in the strips known as a charge cluster. As photons and electrons exhibit nearly identical signatures in the ECAL, the reconstruction of the track associated with

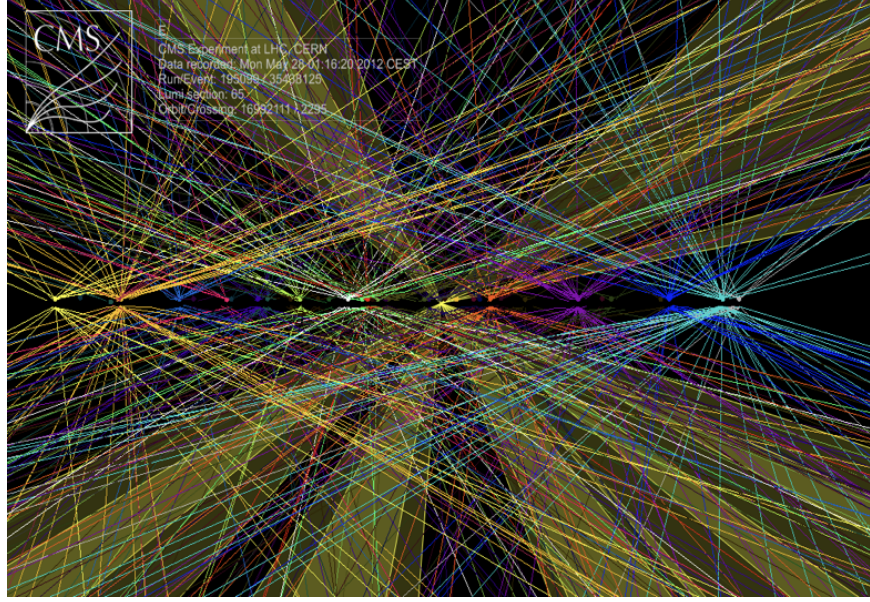


Figure 4.19: Pileup interactions during a single bunch crossing in data.

electron energy clusters is the main component of their particle identification. Using knowledge of the magnetic field along the trajectory with position measurements taken from multiple layers of silicon strips and pixels, the helical tracks are fit and kinematic parameters extracted.

By fitting trajectories to vertices, the tracker enables the reconstruction of the hard interaction position (Figure 4.19). As only one vertex is typically of interest, identifying background vertices and subtracting their contribution is of increasing importance with the increasing number of pile up interactions.

The CMS tracker is the world's largest all silicon detector with a sensitive area larger than 200 m^2 (Figure 4.22) [20]. The tracker consists of 10 layers in the barrel region: 4 inner barrel layers (TIB) and 6 outer barrel layers (TOB). The endcap is made up of 12 disks: 3 inner disks (TID) and 9 endcap disks (TEC). The CMS pixel detector (Figure 4.21) consists of three layers with radii of 5.3 cm, 7.2 cm and 11 cm and 2 disks on each side of the barrel at 34.6 and 46.6 cm from the either side of the interaction point.

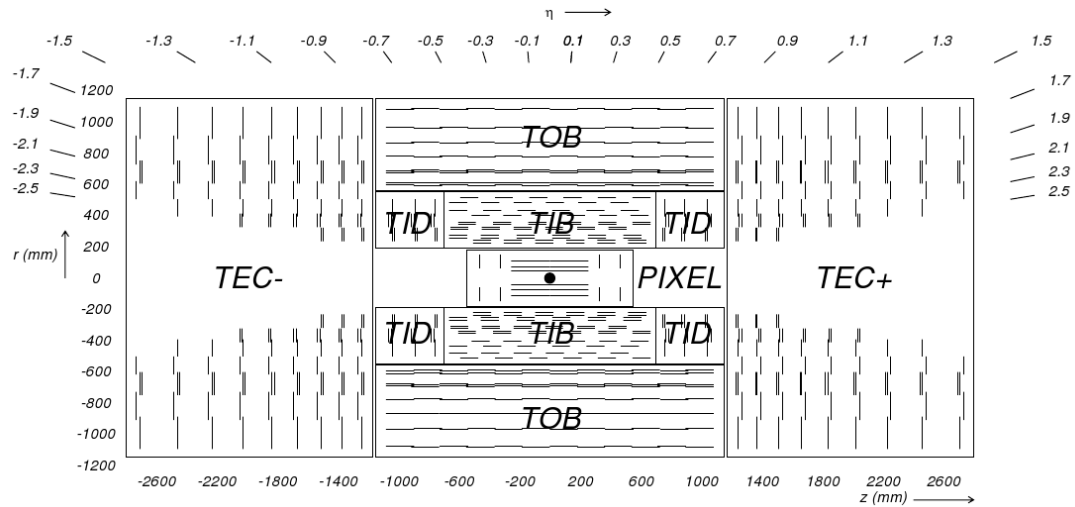


Figure 4.20: Kinematic acceptance of the CMS tracker.

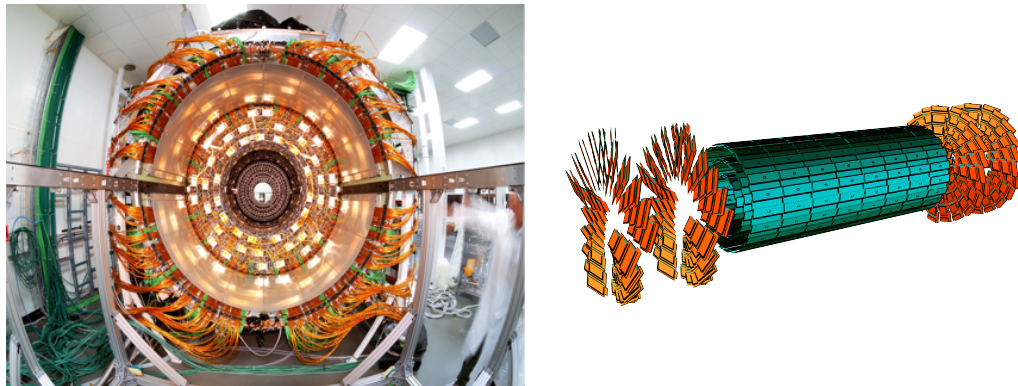


Figure 4.21: The two wheels and three layers of the CMS Pixel detector.

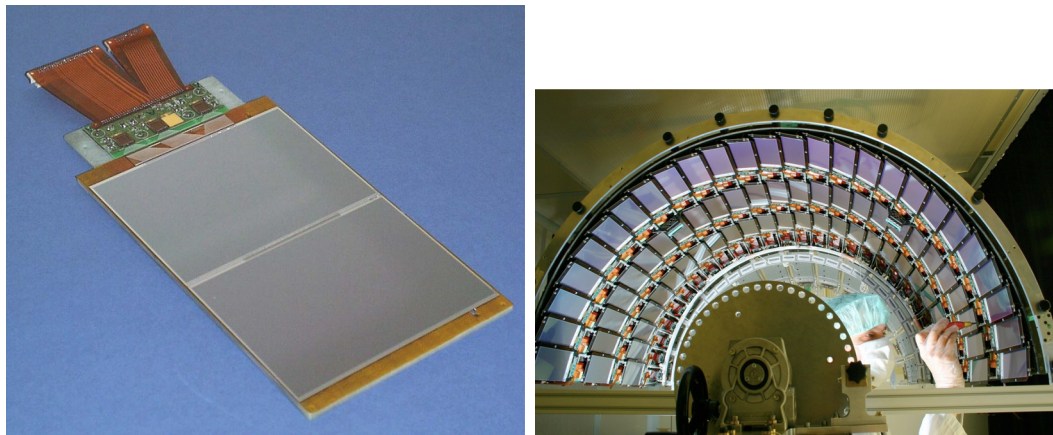


Figure 4.22: (left) A single CMS tracker module. (right) A tracker inner barrel module.

Track reconstruction resolution is affected by a series of kinematic dependent effects. Track reconstruction is degraded by interactions with the tracker material. With some finite probability as a function of the material density and thickness, the track will randomly scatter. The overall rate of this scattering degrades overall tracking resolution. High energy charged particles for which the detector volume and strength of the magnetic field do not permit the track to bend cause significant degradation of momentum resolution as well as charge sign determination. For low energy tracks ~ 500 MeV, the strong magnetic field deflects the charge particle into closed loops (loopers) within the tracker volume. As these tracks do not reach the calorimetry, they have no associated calorimeter deposit and are rarely considered in a non-specific analysis.

A track in a uniform magnetic field, like that of the CMS Solenoid are parameterized by 5 parameters:

- d_ρ : the distance of closest approach to the reference point
- ϕ_0 : azimuthal angle specifying the reference point to the helix center
- p_t^* : charged signed transverse momentum
- d_z : signed distance of the helix from the reference point in the z direction
- $\tan \lambda$: the slope of the track

using these parameters, the trajectory is parameterized in the turning angle ϕ :

$$\begin{aligned} x &= x_0 + d_\rho \cos \phi_0 + \alpha p_t^* (\cos \phi_0 - \cos(\phi_0 + \phi)) \\ y &= y_0 + d_\rho \sin \phi_0 + \alpha p_t^* (\sin \phi_0 - \sin(\phi_0 + \phi)) \\ z &= z_0 + d_z - \alpha p_t^* \tan \lambda \cdot \phi \end{aligned}$$

In the context of displaced tracks, it is important to know that tracks do not necessarily have the same reference point. For CMS, each individual track parameter is

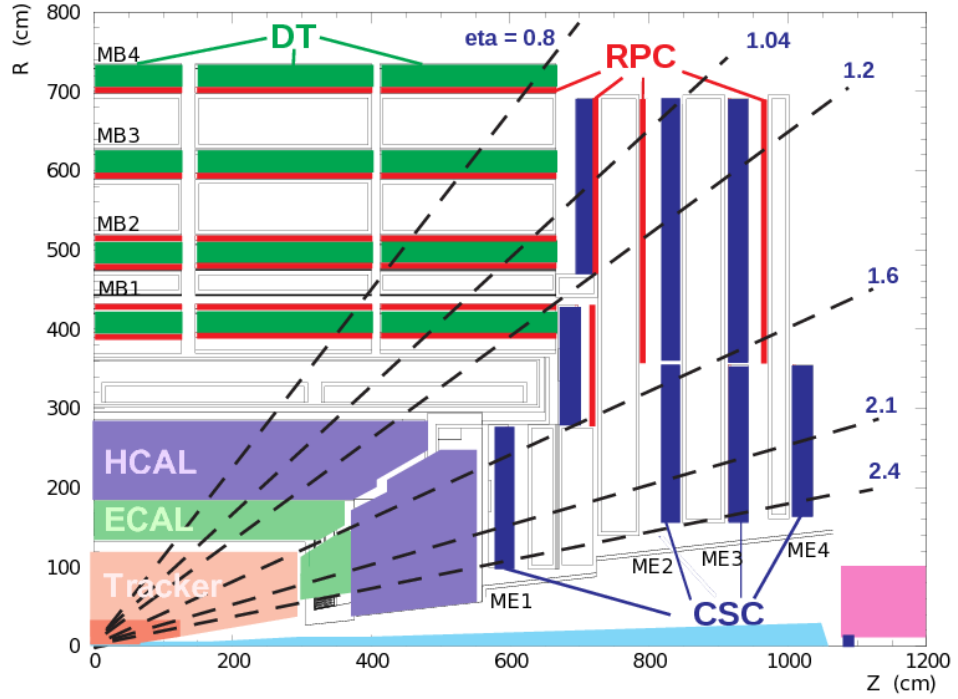


Figure 4.23: Kinematic acceptance of the CMS Muon system.

computed against a reference point determined by the the closest point of approach to the beam line. For prompt physics, this reference point coincides with the collision vertex used to compute the kinematic parameters for calorimeter jets. In contrast, when tracks are displaced, the reference point used for the track is not the same as the reference point for the calorimeter jet η and ϕ . This mis-match of coordinate systems affects the ultimate track and jet association.

4.6 Muon Spectrometer

The Compact Muon Solenoid's name is partly taken from the muon subsystem which is built to identify and measure the trajectories of muons. This thesis uses only calorimeter quantities and inner tracking with correspondingly no sensitivity to muons. This section is included only for completeness.

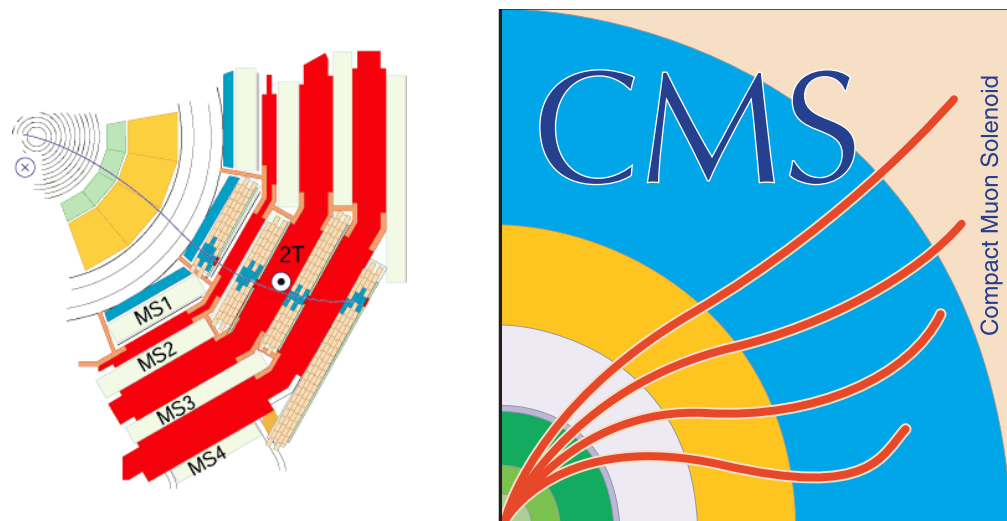


Figure 4.24: (left) A transverse slice of the muon detector. (right) The CMS logo depicting the change muon curvature outside of the solenoid.

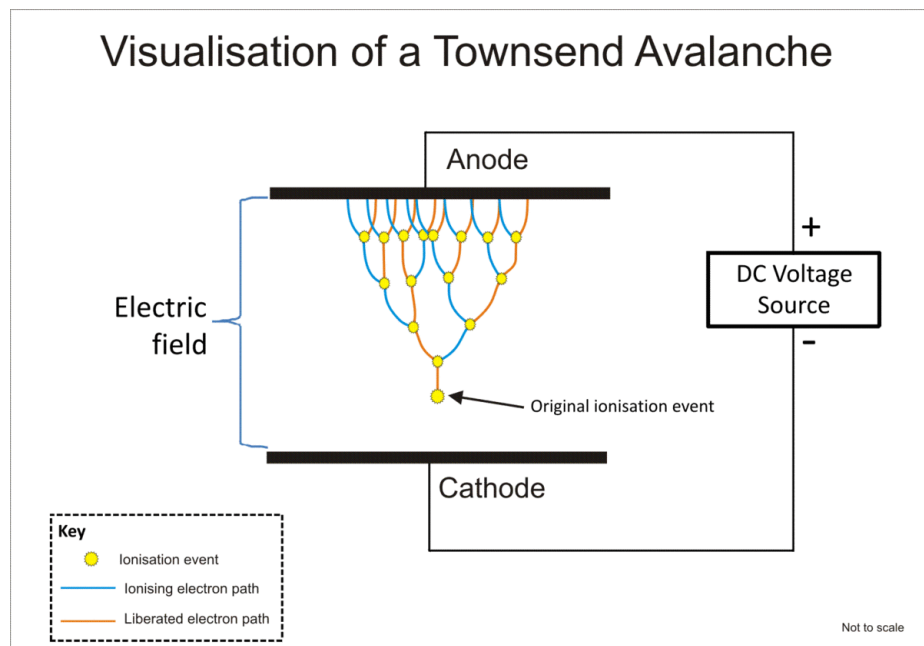


Figure 4.25: When a gaseous medium is ionized by the track of a muon, the resulting liberated electrons are accelerated in the electric field and collide with gas molecules. The result is an avalanche of electrons collected at the anode. The process is known as a Townsend Avalanche.

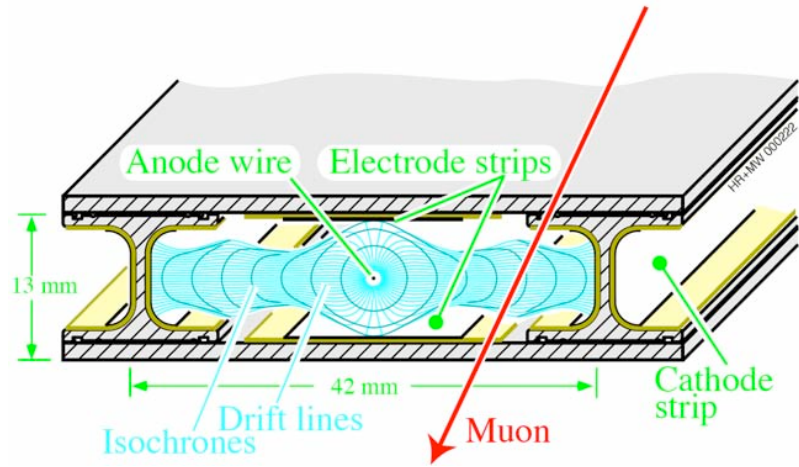


Figure 4.26: The drift tube design showing the drift lines, wire, and cathode strips.

The muon system consists of 3 separate detectors: drift tubes (DT's), resistive plate chambers (RPCs), and cathode strip chambers (CSCs). All three systems rely on the ionization of a gas medium caused by the charged muon's traversal through the detector. The detectors are multi-layered and sandwiched between layers of the iron return yoke (Figure 4.23). The iron layers aid in particle identification by stopping nearly all other particle activity before the final detector layer. As muons are very weakly interacting, they should be the only particles reaching the edge of the detector. When the magnetic field changes outside of the solenoid, muon tracks will change curvature in the muon system as depicted in the CMS logo (Figure 4.24). The second measurement made in the muon spectrometer improves the momentum resolution for energetic muons > 100 GeV, however lower momentum muons are dominated by a increase of multiple scattering from the additional detector material.

In the context of long-lived searches it is interesting that the muon has a lifetime of $\tau_0 = 2.2 \mu\text{s}$ or equivalently $c\tau_0 = 660 \text{ m}$. The dominant decay to an electron and two neutrinos is suppressed by requiring the muon decays off-shell through the much heavier W^\pm . This method of generating long-lived signatures mirrors the motivations of split supersymmetry where the gluinos are long-lived because they must decay

through much heavier squarks. If this were the end of the story we would expect $\approx 1\%$ of muon decays to occur before the final layer. However, a moderately energetic muon will experience time dilation $c\gamma\tau_0$ in the lab frame with $\gamma = E/m = (1 \text{ GeV})/105 \text{ MeV} \approx 10$. Accordingly, on detector length scales $O(10 \text{ m})$ energetic muons can be considered stable.

The drift tube system located in the barrel region covers $|\eta| < 1.2$ with 4 concentric rings (segmented in $r = 4.0, 4.9, 5.9, 7.0 \text{ m}$) referred to as “stations”. Five divisions are also made in the z direction referred to as “wheels” partitioned into 12 sectors of 30 degrees. The three inner cylinders have 60 chambers each and the outer cylinder has 70. Each chamber measures $3.0 \text{ m} \times 2.5 \text{ m}$. Each chamber is divided into 3 (or 2) super layers with 4 drift cells per layer (2 in ϕ , 2 in z). The drift cells use anode wires at voltage of $+3.6 \text{ kV}$, electrode strips at 1.8 kV and -1.2 kV cathode strips to detect the localized ionization showers from muon tracks (Figures 4.25 and 4.26). The full system includes 172,000 wires. The maximal drift path is 21 mm corresponding to a drift time of 380 ns in a gas mixture of 85% Argon and 15 % CO₂ [19].

A combination of CSCs and DTs are located in the endcap region. The CSCs are located between $0.9 < |\eta| < 2.4$ and the RPCs between $0.9 < |\eta| < 1.6$. There are 4 stations for each endcap. The CSCs are trapezoidal multi-wire proportional chambers comprised of 6 wire planes interleaved with 7 cathode panels. The chambers extend 1.7 (or 3.4) m in the radial direction covering 10 (or 20) degrees. Wires running in the ϕ direction define a tracks radial position. The ϕ coordinate along the wires is obtained by interpolating charges induced on the cathode strips.

All four DT layers and multiple CSC layers include RPCs , which have a coarse position resolution (order $\sim 1 \text{ cm}$) relative to the CSC and DT layers, but a much faster response time of 3 ns . This allows the RPC’s to identify the bunch crossing of a muon unambiguously as well as aide in triggering on muon events. Each layer of the RPC is built from two resistive plates separated by a gap of freon gas held at a

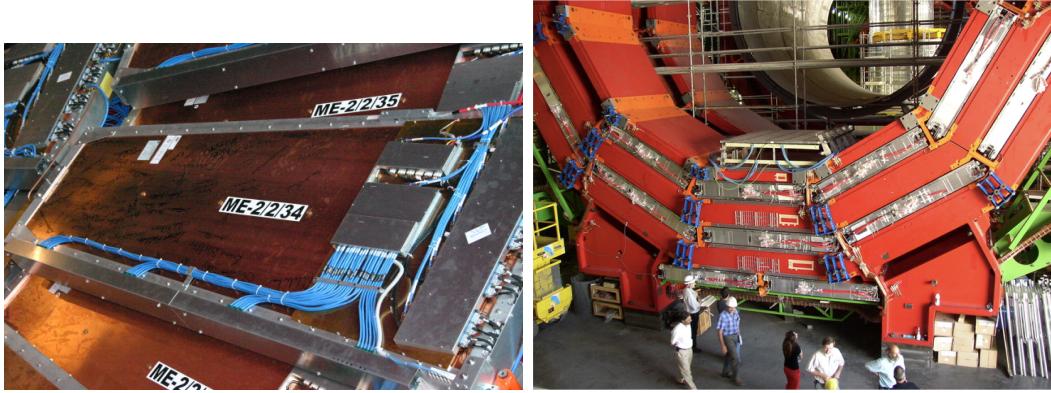


Figure 4.27: The Muon cathode strip chamber.

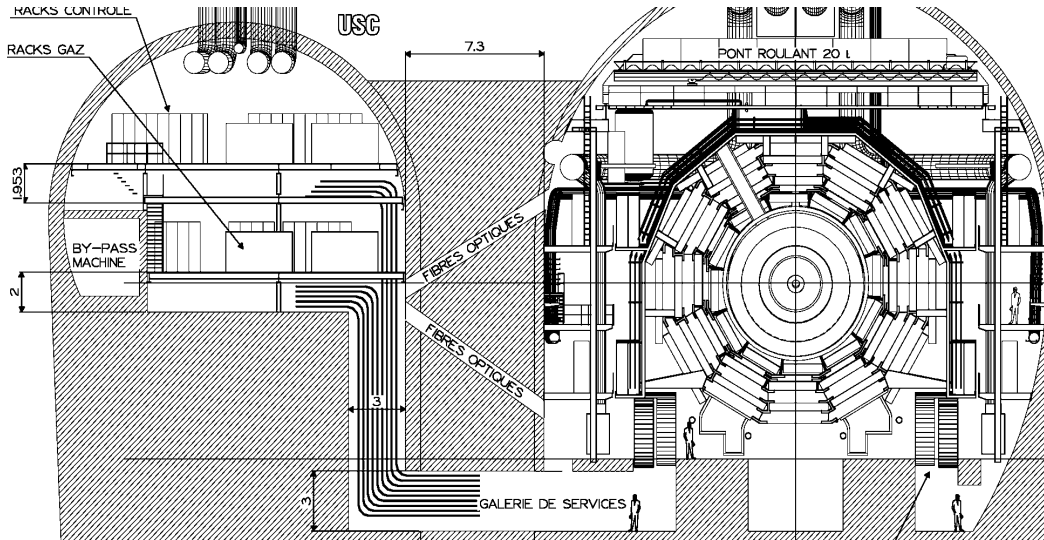


Figure 4.28: The location of the counting room relative to the experimental hall.

9.5 kV. Electrons knocked from the gas atoms cause an electron avalanche picked up by detector strip. The strip pattern gives a measure of momentum.

4.7 Trigger System

The CMS trigger system exists as a filter through which events are determined to be interesting or useful enough to be written to mass storage. The name comes from the nature of algorithms used to determine what to write down. If an event

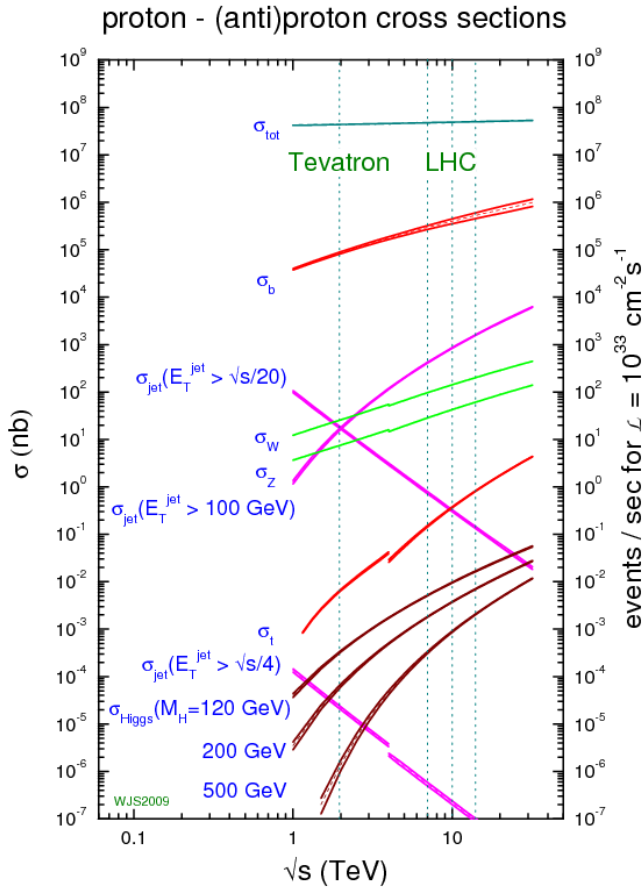


Figure 4.29: Common cross sections of proton collisions as a function of the center of mass energy \sqrt{s} .

passes any of the online algorithms, this “triggers” the collision to be written in its entirety regardless of the goals of the path in particular (albeit with some notable exceptions). It is both unnecessary and impractical to record every collision the LHC delivers. The low momentum transfer hadronic events contained in the vast majority of proton collisions is well understood from past experiments. Figure 4.29 shows typical physics processes for proton-proton scattering. Events such as the production of a b quark occur at $\approx 10^6$ Hz at a luminosity of $\mathcal{L} = 10^{33} \text{ cm}^{-2}$ whereas processes of interest, such as the production of the Higgs is much lower at $\approx 10^{-2}$ Hz.

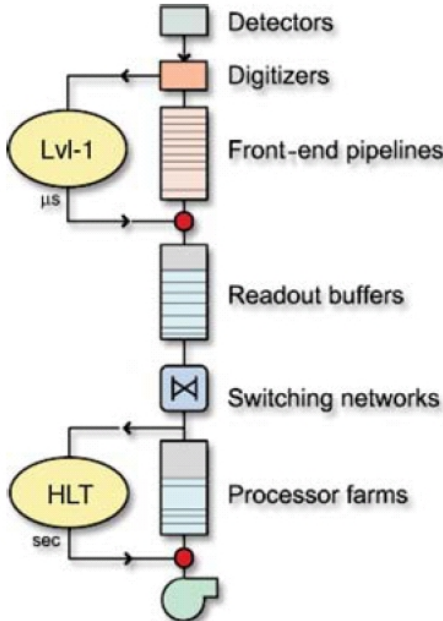


Figure 4.30: The L1 and HLT trigger processing chain [22].

The LHC has beam crossings at a rate of ≈ 40 MHz. The number of inelastic collisions per bunch cross crossing is given by the total inelastic cross section times the luminosity divided by the bunch collision rate. If every bunch is filled, this is respectively $8.5 \times 10^{-26} \text{ cm}^2 \times 10^{34} \text{ cm}^{-2} \text{ s}^{-1} / (40 \times 10^6 \text{ s}^{-1}) \approx 24$ interactions. The collisions are stored with an average file size $O(1 \text{ MB})$ in their unprocessed form in a format referred to as RAW. However the bandwidth for the combined constraints of acquisition rate, storage and processing, is limited to 10^3 Hz and equivalently 10^3 MB/s. The trigger must be able to select these events quickly while maximizing the physics collected by the experiment with limited bandwidth.

The CMS trigger system is designed to read events at the event crossing frequency and generate the factor 10^5 of rejection between the crossing frequency and the archival capacity. This factor is too large to achieve in a single step given the complexity of triggers and event reconstruction necessary to build fast algorithms. Therefore the task is split into two steps the Level 1 (L1) and High Level (HLT)

Trigger systems (Figure 4.30). The L1 system is a coarse study of an event designed to be fast and capable of analyzing every event at 40 MHz. The HLT provides the flexibility the L1 lacks permitting more elaborate event reconstruction.

The simplest criterion for interesting events are hard physics events with large high momentum transfer, q^2 , and correspondingly large transverse momentum. As the protons collide with effectively no transverse momentum, significant deposits of transverse energy (or even missing transverse momentum) is indicative of a hard physics process. The total transverse energy of an event falls off exponentially, so a simple way to reduce the rate of processed events is to raise the energy requirements of accepted events. However, given the increasing luminosity of the LHC the thresholds are encroaching upon Standard Model physics processes like single W production, where triggering on most $W \rightarrow e\nu$ events is reaching a kinematically limited regime.

Generally, analyses searching for new physics are categorized by their final state signature. Correspondingly, the triggers require loose particle identification on the particular objects such as the isolation and energy deposition. Requirements such as the angular separation, or the invariant mass of two objects is common as well. Once the event has passed the L1 and HLT Triggers, tighter and more computationally costly selection can be made offline where we are unrestricted by bandwidth limitations.

4.7.1 Level 1 (L1) Trigger

The L1 Trigger is built using custom hardware composed of field programmable gate arrays (FPGAs), application-specific integrated circuits (ASICs) and programmable look up tables (LUTs).

The trigger primitive generators (TPGs) are locally constructed from the energy deposits in the calorimeters or hits/ track-segments in the muon chambers. The regional reconstruction applies coarse pattern recognition to the primitives and com-

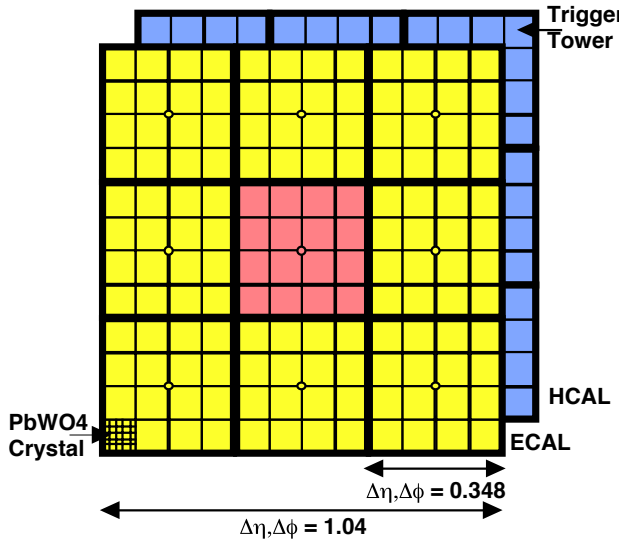


Figure 4.31: A representation of a jet as assembled from the ECAL and HCAL trigger primitives. [22]

bines them. Together the global calorimeter trigger (GCT) and global muon trigger (GMT) are processed at the global trigger (GT) to decide whether or not an event is kept. There is no inner tracking performed at this level (only muon specific tracking). Track building is time intensive and cannot, in its current state, be performed reliably at speeds comparable to the bunch crossing frequency. Future upgrades are planned to include tracking at L1, which would significantly aide in the detection of soft hadronic signatures with specific track topologies (eg. displaced signatures and VBF Standard Model Higgs production in decays to $b\bar{b}$).

4.7.2 High Level Trigger (HLT)

Algorithms at trigger stage are referred to as paths. The entire collection of paths is referred to as a trigger menu. As the physics goals of the experiment change and machine luminosity ramps, the menu must evolve and adjust the thresholds within a given menu. The HLT is a crucial component of CMS data taking, as new physics that is never stored is never discovered. Problems with the offline reconstruction can

Table 4.5: High Level Trigger filter farm configuration in 2015 [56]

Install Year:	2011	2012	2015
CPU	X5650	E6-2670	E6-2680v3
Architecture	Westmere	Sandy Bridge	Haswell
CPUs per board	2	2	2
Cores/CPU	6	8	12
RAM	24 GB	32 GB	64 GB
Clock Rate (w/Boost)	2.66 (3.06) GHz	2.60 (3.30) GHz	2.50 (3.30) GHz
Total Cores (Boards)	3456 (288)	4096 (256)	8640 (360)

be fixed at a later date by reprocessing the raw data, but problems with the online reconstruction will permanently bias the data collected.

The paths are configured as a series of reusable modules that either build some quantity/object (producers) or terminate the execution of the path based on some quantity (filters). The paradigm ensures, that a producer which creates, say, the sum of transverse energy in the detector, is processed exactly once despite being used by multiple paths. Ensuring that modules are reusable and reused greatly minimizes timing overhead of additional paths. Common sequences, such as unpacking the calorimeter energy, are utilized by nearly every trigger. CMS as an experiment excels from a monolithic approach to software, where the same software (known as CMSSW) is for analysis and data processing is used online.

The development, debugging, and testing of these menus is a large organizational effort that requires input from nearly every level of the experiment. Physics object groups (POGs): e/ γ , muons, jets, and b tagging group must build the online recommendations for object identification and validate their performance. Physics Groups (Higgs, Exotica, SUSY, ect.) must develop paths and justify the added physics value of the individual paths in terms of their sensitivity. The detector performance groups (DPGs) must provide calibrations for the online reconstruction that will differ from the offline reconstruction.

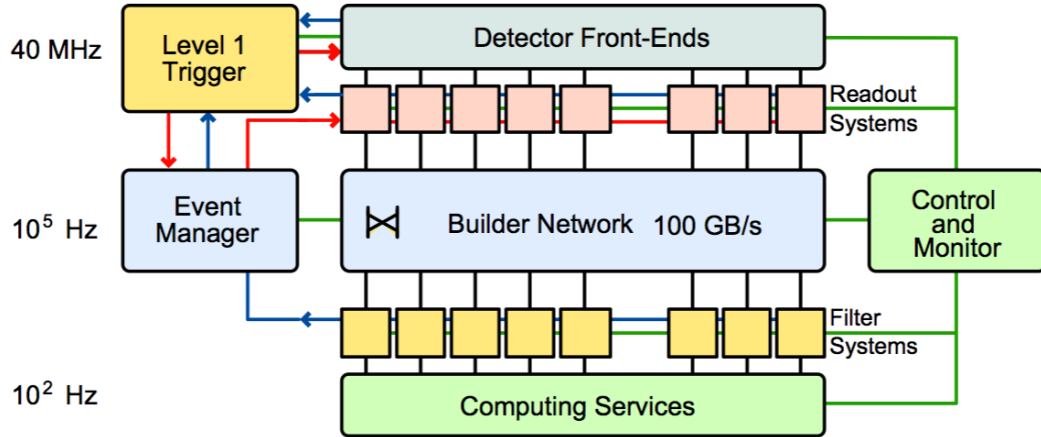


Figure 4.32: A diagrammatic representation of the level 1 and HLT trigger processing

Additionally, the DPGs must implement separate data streams, which save a much smaller event content, to calibrate the detector. For instance a separate data stream exists for collecting the copious production of π^0 and η^0 mesons which predominantly decay to two photons. The stream performs only the reconstruction of the ECAL and searches for low p_t clusters within an invariant mass window. Saving only the hits corresponding to these clusters reduces the event size from 1 MB to 2 kB allowing the stream to acquire events at a rate of 7 kHz while maintaining a small bandwidth. For comparison, the physics data stream writes at 1 kHz.

The CMS HLT System is built from a varied collection of commercially available CPUs comprising more than 16,000 cores in 2015 (Table 4.32).

Chapter 5

Studies of Displaced Jet Tagging Variables

5.1 Introduction

The identification of jets originating from b quarks (b -tagging) was originally developed and successfully utilized for the discovery of the top quark. Among other applications, b -tagging is now a tool for studying the Higgs and searching for BSM physics. Since its inception, b -tagging has evolved including the implementation of particle flow reconstruction, refined secondary vertex algorithms, and advanced multivariate techniques. This strength of this construction is that successive improvements in the b -tag object are shared by all users with minimal redundancy of effort.

The algorithms are publicly documented with corresponding working points and data/MC correction factors. Changes in methodology are integrated directly into the experiments software, allowing fast adoption of subsequent improvements. The object is then used interchangeably as part of a large toolkit of jets, leptons, taus, photons, and missing energy. This allows well established searches to improve existing sensitivity or interpret new final states not previously accessible with relative ease.

It was the principal goal of this analysis to build a track based displaced jet “object” similar to a b-tag that could capture the relevant behavior of displaced signatures while providing a maintainable tool for a variety of long-lived searches. Although long-lived particles will decay to objects for which there are well studied definitions, many of the principal assumptions and quality requirements are not suited for particles arriving at glancing angles. To avoid these quality criteria, the displaced jet tag is not built as a modification of existing objects, but from the global track collection and separately clustered calorimeter energy. The variables used in the tag definition then rely on the geometry of the tracks matched to clusters. It is also possible to identify long-lived decays using energy deposits with a large hadronic energy fraction and no associated tracks. These deposits can be indicative of long-lived decays occurring inside of the hadronic calorimeter.

The tag is designed to be sensitive to jets, electrons, and taus regardless of the source of the long-lived decay when at least one track can be reconstructed. The tag has diminished sensitivity for decays occurring below 1 mm, a region where prompt analyses have negligibly diminished sensitivity.

Past searches by the CMS and ATLAS experiment for long lived particles decaying to jets rely significantly on secondary vertexing of displaced tracks. As the ability to vertex the jet is dependent on the ability to reconstruct highly displaced tracks, the existence of a vertex, although offering good separation between signal and background is often the most inefficient selection criterion [44]. This is especially true at lifetimes on the scale of the detector or longer. Of particular concern is that current vertexing algorithms may not perform effectively for non-Standard Model jet vertices such as found in Emerging Jets [57].

Given the close analogy to b -tagging techniques, it is important to clarify where b -tagging algorithms are inefficient and where they can be extended.

For shorter lifetime regimes ($c\tau_0 < 1$ mm), b -tagging can still identify displaced jets, but leaves room for new techniques. Heavy long-lived resonances undergoing a 2 body decay will have significantly more momentum transverse to the flight direction of the long lived particle (when compared to a b decay). This angle is a powerful discriminant against background nuclear interactions and is correlated with the boost of the mother particle. Under the assumption that the angle is small, b -tagging uses only positively signed impact parameters for track identification. This corresponds to decays downstream of the flight path. Heavy particles produced nearly at rest will decay isotropically with impact parameters of negative sign.

For longer lifetimes, a transition occurs at distances larger than a few centimeters where new issues unaddressed by b -tagging arise. Although the b meson is displaced it is comparably straightforward to discern the primary vertex of the event. This allows b -tagging algorithms to more accurately calculate longitudinal quantities, such as 3D track impact parameters. For displaced jets, this is not the case and utilizing longitudinal quantities relative to a mis-identified primary vertex can yield poor performance. Pixel hit are explicitly required for tracks used in b -tag secondary vertexing, but displaced jets decays can occur outside the pixel layers. In addition, b -tagging algorithms include upper bounds on longitudinal and transverse impact parameters to limit contributions from nuclear interactions.

This section discusses in detail the preliminary studies leading up to the choice of variables used in the analysis tag definition. Comparisons are made between prompt and displaced signatures with and without pileup for a variety of variables, including correlations between the most effective quantities. The final three variables used in the tag definition are discussed in the next chapter detailing the analysis.

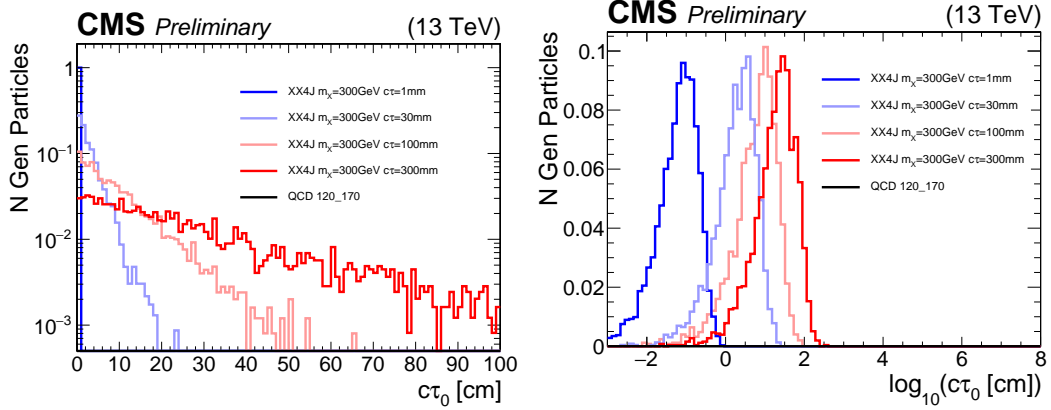


Figure 5.1: The proper lifetime of the XX4J samples. The samples are generated with exponential lifetime distributions $e^{-x/c\tau_0}$ which have mean $c\tau_0$ and exponential slope $1/c\tau_0$.

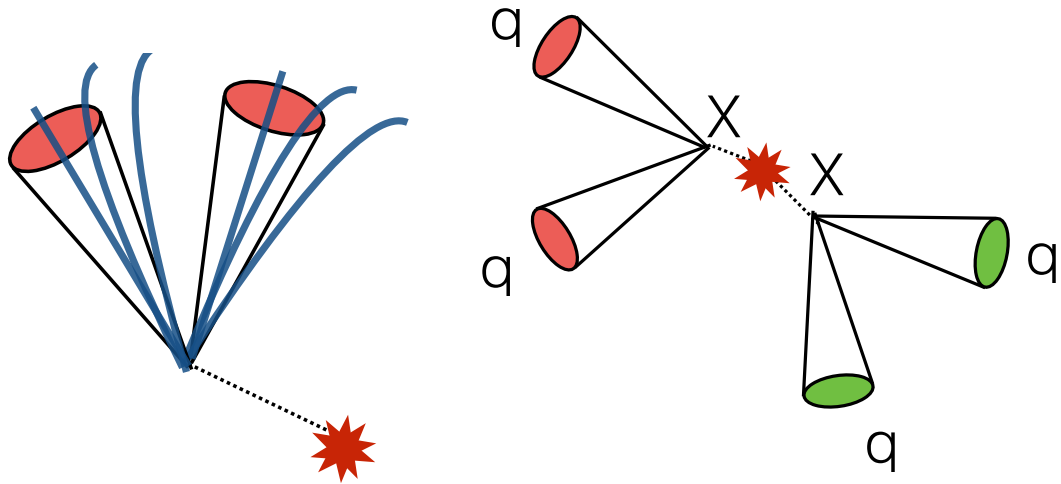


Figure 5.2: The topology of the two samples used in the study GUN (left) and XX4J (right)

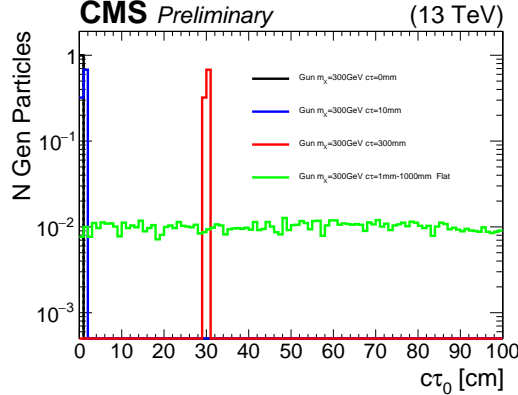


Figure 5.3: The proper lifetime of the GUN samples. The samples are generated with either flat, or delta function $\delta(c\tau_0 - c\tau'_0)$ lifetime distributions

5.2 Displaced Jet Samples

Two signal samples are used to study displaced identification which we will refer to as XX4J and GUN. Both samples are generated using Pythia 8 [64].

The XX4J sample consists of the direct pair production of two neutral X^0 's with finite lifetime. Each X^0 decays to u,d,s,c , and b pairs with equal probability. This sample is generated with a flat pileup distribution between 10 and 50 interactions from 25 ns bunch crossings. It is important to note these samples will contain prompt jets from pile up interactions as well as from initial state radiation. In this sample, variables for displaced jet identification generally have two distinct populations of jets. The samples are generated with varied lifetimes and masses (Figure 5.1). Each X^0 has an exponential lifetime distribution $e^{-x/c\tau_0}$ with mean $c\tau_0$.

The GUN sample is a single long-lived particle gun. This sample is generated by producing a single X^0 particle with flat kinematic distributions $50 < p_t < 500$ GeV and flat $-2.4 < \eta < 2.4$. The X^0 decays to a pair of d quarks with 100% branching fraction (or b quarks with 100% fraction when noted). The resonance is decayed within Pythia and passed directly to showering and hadronization bypassing all process level Pythia effects: initial state radiation, final state radiation, and beam

remnants. Furthermore, the event is reconstructed without pileup mixing. This sample is generated to have a sample of reconstructed tracks that originate from a displaced vertex without the complications of correctly associating the displaced tracks to calorimeter deposits. One important side effect of simulating without pileup is the lack of a reconstructed primary vertex. As the only vertex in the event is far from the luminous region of the beam, the primary vertex fitting fails to produce a vertex.

The proper lifetime distribution of the sample is chosen to be either a delta function $\delta(c\tau_0 - c\tau'_0)$ or flat between 1mm and 1000mm (Figure 5.3). Additionally two prompt GUN samples are built for comparison. One sample with a proper lifetime of 0 mm decaying to two b-quarks and one sample with lifetime 0mm decaying to two d-quarks. The decay length in the lab frame will differ by a factor $\gamma\beta$ from the proper lifetime.

5.3 Displaced Jet Tagging Variables

5.3.1 Impact Parameter Information

The tracks originating from a decay at a displaced vertex will have large impact parameters relative to the true primary vertex. The impact parameter is calculated by starting from the particle trajectory at the innermost measurement point and extrapolating backward in the helix. The minimum distance from the extrapolated track to the primary vertex gives the magnitude of the impact parameter. The vector pointing from the primary vertex to the point of minimum distance is \vec{IP} . The distance between the jet axis and the closest position on the track helix was also investigated (Figure 5.13), but was found to be less effective at separating the signal and background.

Impact parameter significance IP_{sig} is introduced to the account of the tracking resolution. The significance is the impact parameter divided by the error on the

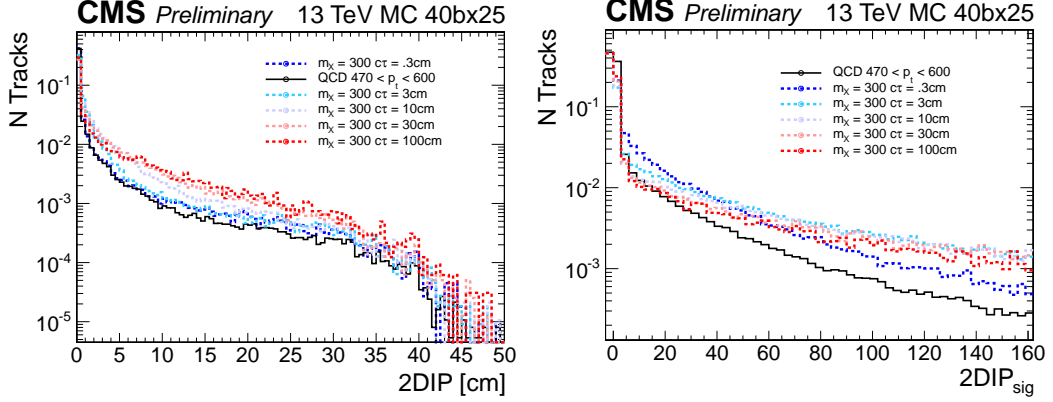


Figure 5.4: (left) The 2D impact parameter of tracks matched to calo jets matched to generator quarks with $\Delta R < 0.5$. (right) 2D impact parameter significance of the same tracks. All distributions are normalized to 1.

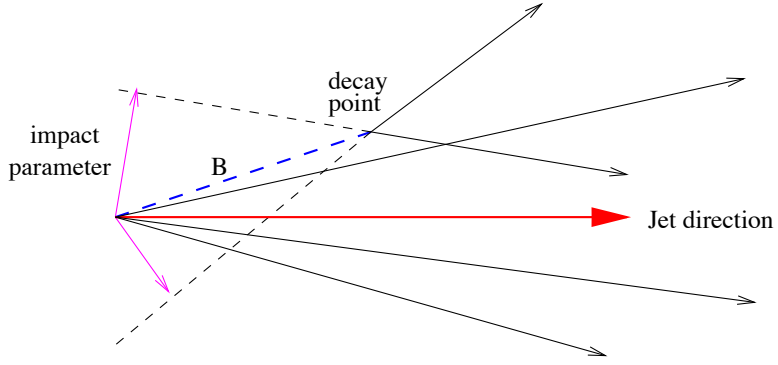


Figure 5.5: Diagram of a B hadron decay showing the mis-alignment of the jet direction and the decay vertex.

measurement. For decays within 10 mm using $IP_{\text{sig}}^{\text{2D}}$ gives improvements in signal background separation relative to the absolute impact parameter value Figure 5.7.

The sign of the impact parameter is given as the sign of the scalar product between \vec{IP} and the direction of the jet: $\vec{IP} \cdot \vec{j}$. For B meson decays, the impact parameter of displaced tracks will have positive sign, corresponding to the decay occurring down stream of the jet direction. In simulation is found that heavy long-lived decays will have large negative IP significance (Figure 5.6). Accordingly, the analysis opts to use un-signed IP significance to identify displaced jets. Restricting to only positive

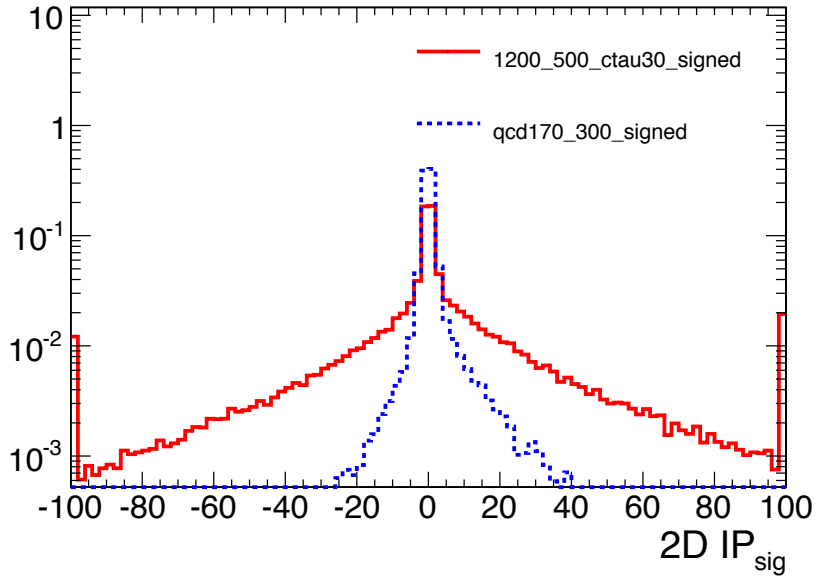


Figure 5.6: The comparison between the $IP_{\text{sig}}^{2\text{D}}$ of tracks within (i) QCD jets and (ii) the decay of a heavy Higgs $H^0 = 1200$ GeV decaying to two long lived X^0 with $m_{X^0} = 500$ GeV. The contribution of B mesons producing tracks with large positive $IP_{\text{sig}}^{2\text{D}}$ explains the asymmetry of the QCD distribution.

impact parameters, as is the standard in b -tagging, topologically restricts the analysis. Rather, the un-signed significance extends inclusivity.

It is important to note that as most GUN samples, excluding the prompt samples, do not have a reconstructed primary vertex, a fake primary vertex with a nominal error is introduced in the calculation. This biases the impact parameter significance relative to the XX4J.

Impact parameters are reconstructed with limited requirements on the tracks. No maximum longitudinal or transverse impact parameter is enforced. No requirement on the number of hits, pixel tracks, or track quality is required at this step. The tracks are required to have $p_t > 1$ GeV to remove tracks which would not reach the calorimeter face.

Variables leveraging the impact parameter information are derived from the distribution of impact parameter significances. Figure 5.8 demonstrates the improved

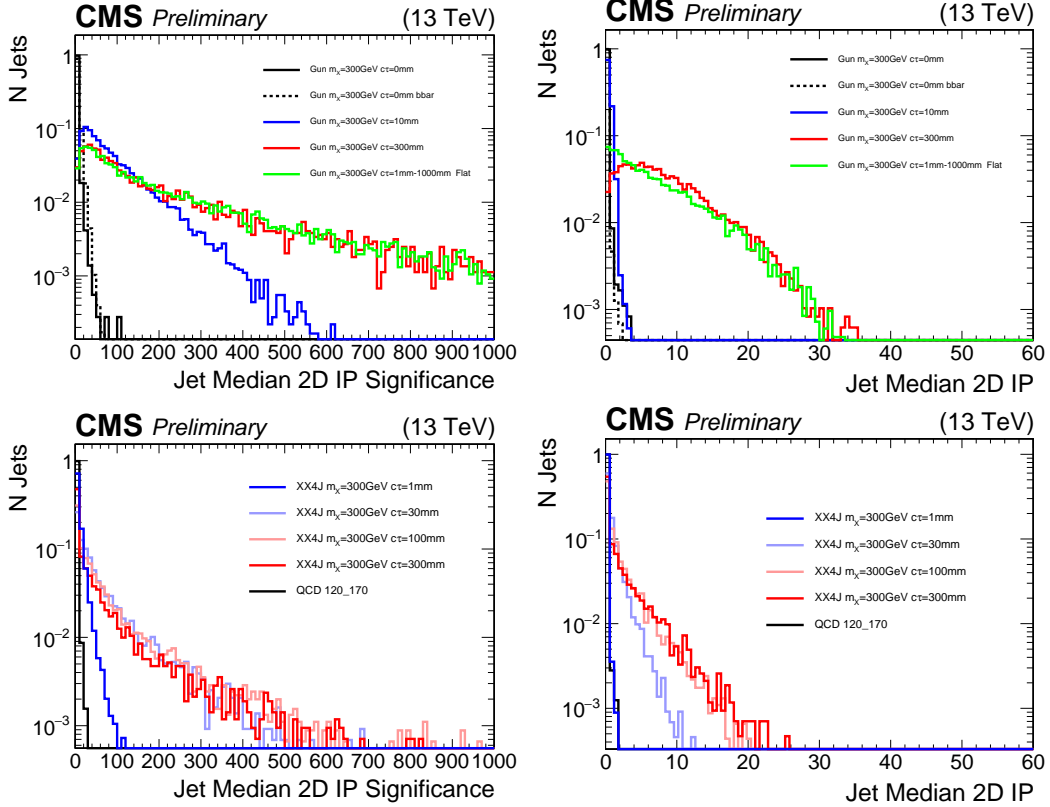


Figure 5.7: Unsigned 2D impact parameter for the XX4J and GUN samples

separation of median IP significance relative to the mean (Figure 5.8). As background QCD jets contain real displaced tracks (Table 2.7, 2.8), the mean calculation is sensitive to outlier tracks with large IP significance. For signal-like displaced jets, all tracks have large impact parameter preserving a high median value.

The tracks from displaced jets should not have significant contribution from tracks included in a primary vertex fit. For long lifetimes this reduces the reliability of selecting the correct primary vertex for the calculation of 3D impact parameters. Instead, the analysis opts to use exclusively transverse quantities that negligibly depend on the primary vertex selection when a beam-spot constraint is applied. Figure 5.9 shows the comparison between the 2D and 3D impact parameters. 3D distributions exhibit long tails where the wrong primary vertex was chosen.

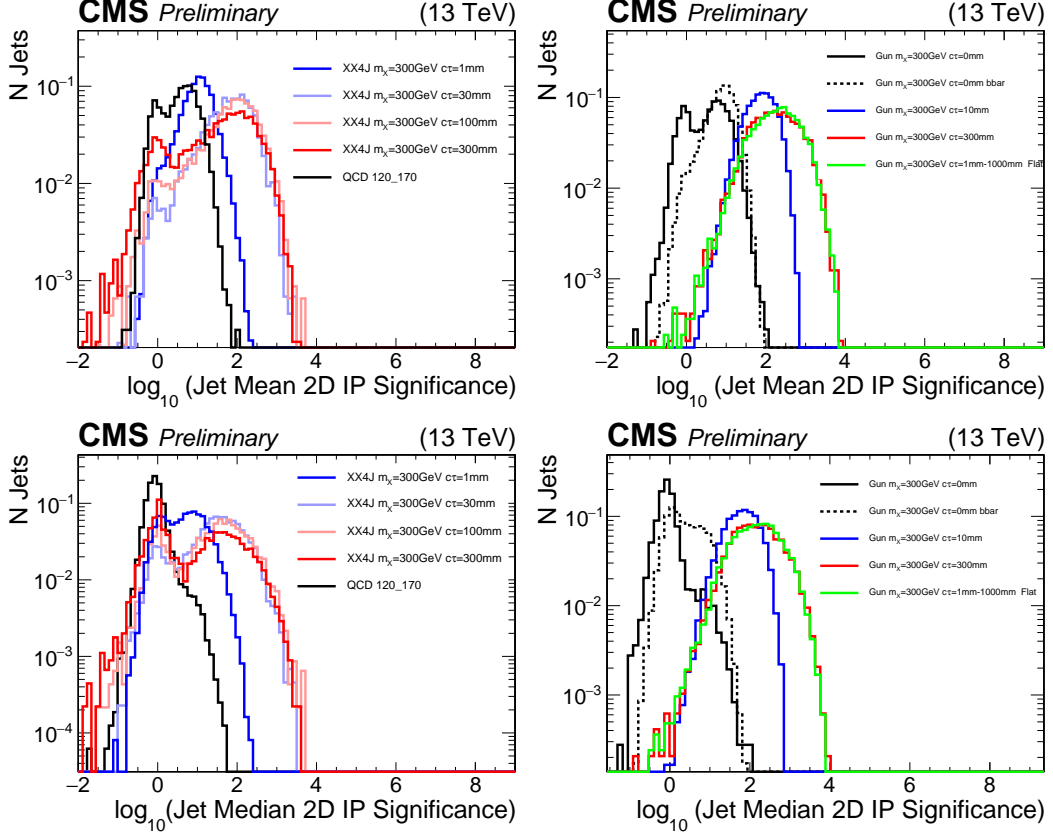


Figure 5.8: A comparison between using mean or median IP significance for the GUN and XX4J signal samples.

The choice is made to use report the value of impact parameter related variables on log scale. As impact parameter significance varies over many orders of magnitude (Figure 5.11), the variable transformation reveals structure not visible on linear scales. On log scale, two populations of tracks are clearly visible.

Jet Primary Vertex Fraction (α and β)

Decays that occur displaced from the primary vertex are unlikely to contain tracks included in the primary vertex fit when a beam spot constraint is included. On the other hand, QCD jets expect the majority of their tracks to be from either the true primary vertex or a pile up vertex. For a given jet $\alpha(PV)$ is calculated as the sum is taken over tracks matching in $\Delta R < 0.4$ between two collections of tracks: the tracks

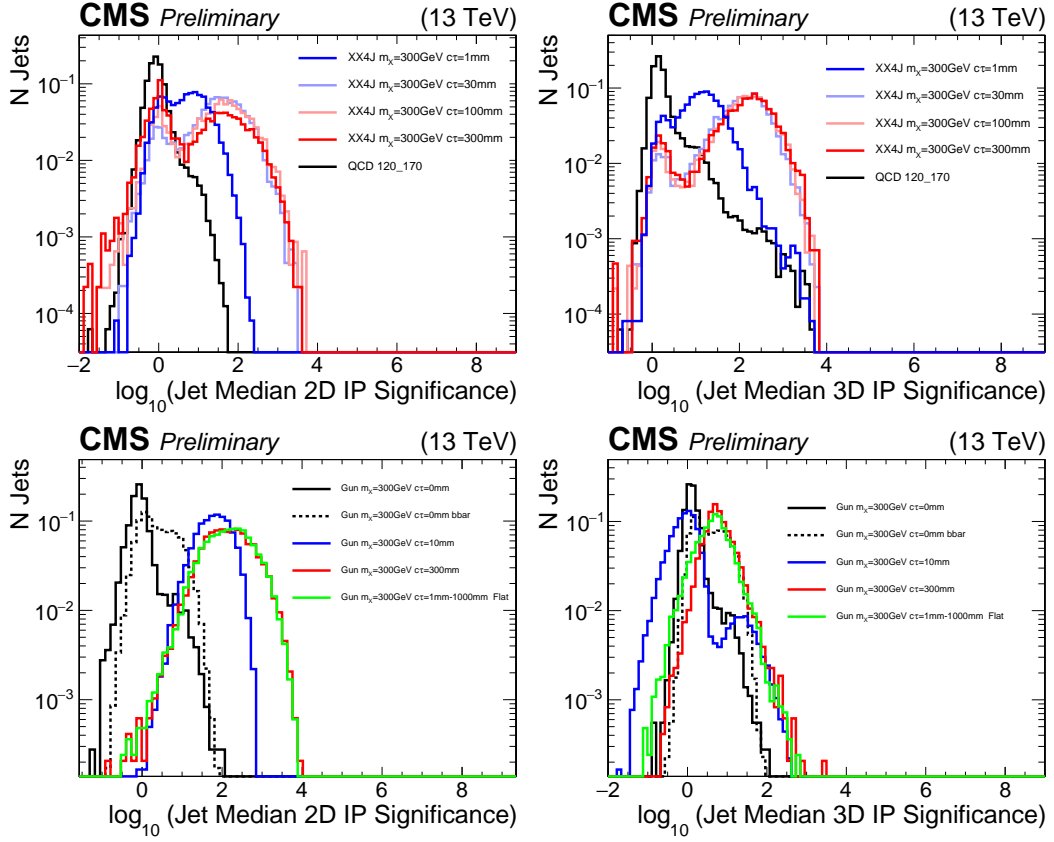


Figure 5.9: A comparison between the median IP significance in 2D vs 3D for the GUN and XX4J signal samples

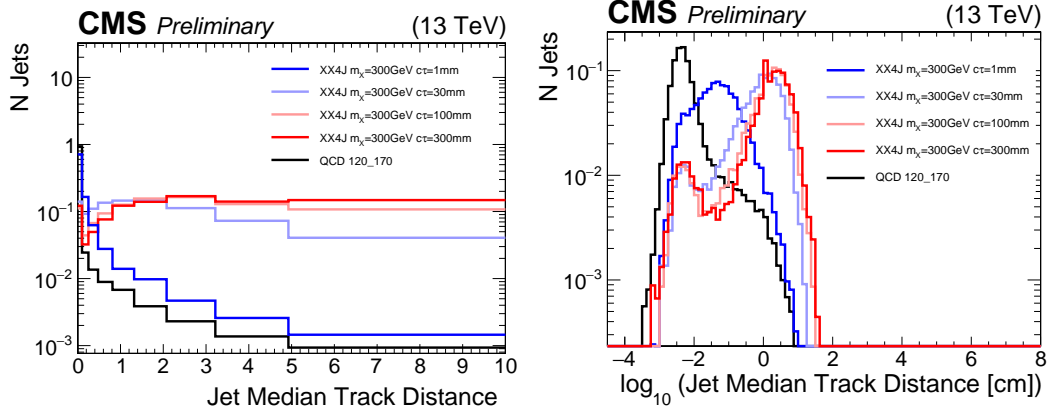


Figure 5.10: For each track in a jet the minimum distance between the track and the jet axis is computed. From this distribution the median is computed for each jet.

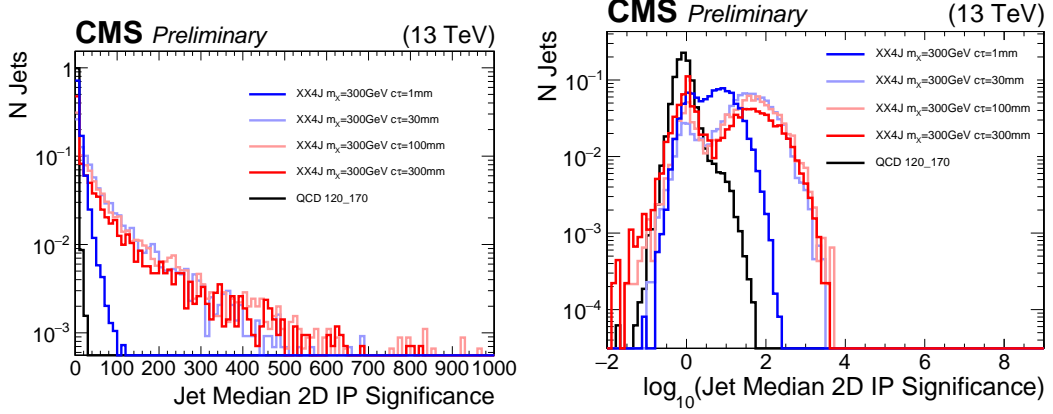


Figure 5.11: A comparison between log and linear scale variables. The log scale case shows the distinct population of significances related to pileup in the XX4J sample.

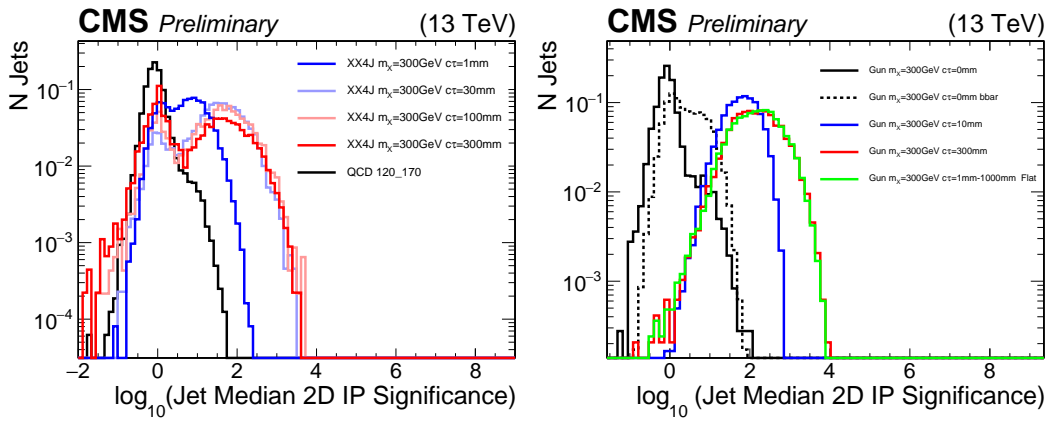


Figure 5.12: A comparison of the jet median 2D IP significance between the GUN and XX4J samples

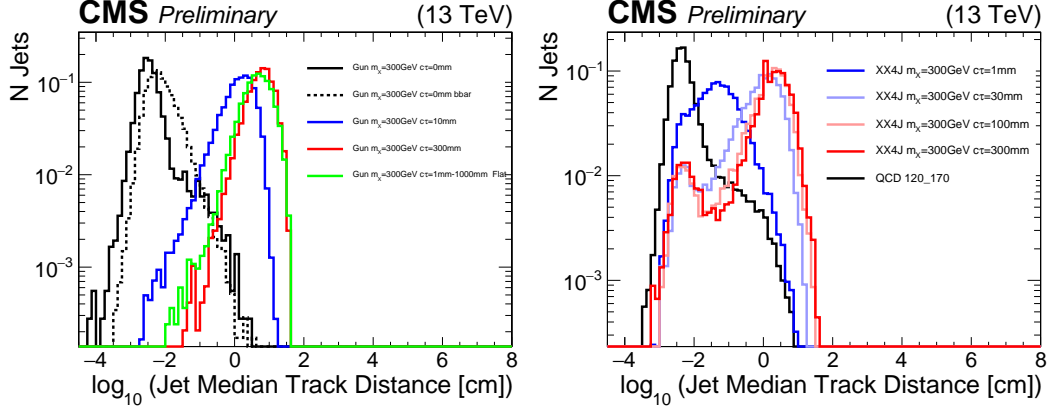


Figure 5.13: The closest distance between the jet axis and track for the GUN and XX4J samples

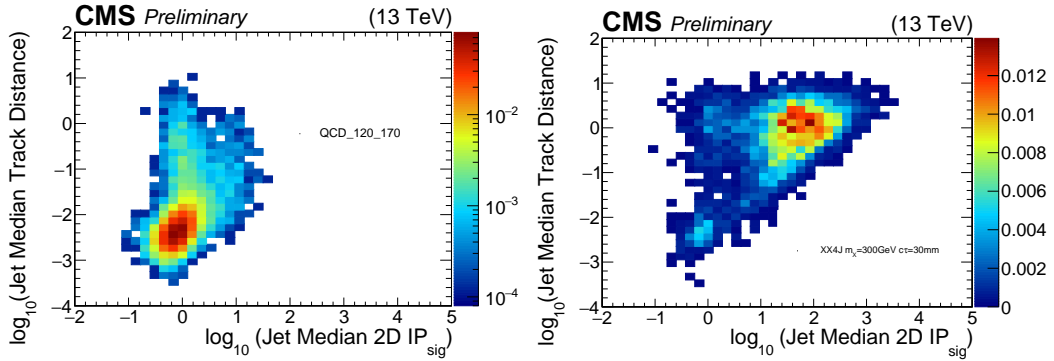


Figure 5.14: Correlations between the IP significance and the jet distance variables

in the specified primary vertex and tracks from the global track collection. The sum is restricted to tracks with $p_t > 1.0$ GeV.

$$\alpha_{\text{jet}}(\text{PV}) = \frac{\sum_{\text{tracks} \in \text{PV}} p_t^{\text{tracks}}}{\sum_{\text{tracks}} p_t^{\text{tracks}}} , \quad (5.1)$$

If the true PV is selected to calculate α , PU jets will have signal-like $\alpha = 0$. To avoid this, we define α_{\max} for each jet by individually selecting the primary vertex with the largest contribution to the sum. As the GUN samples typically have no reconstructed primary vertices (except in the prompt case), these plots are not shown.

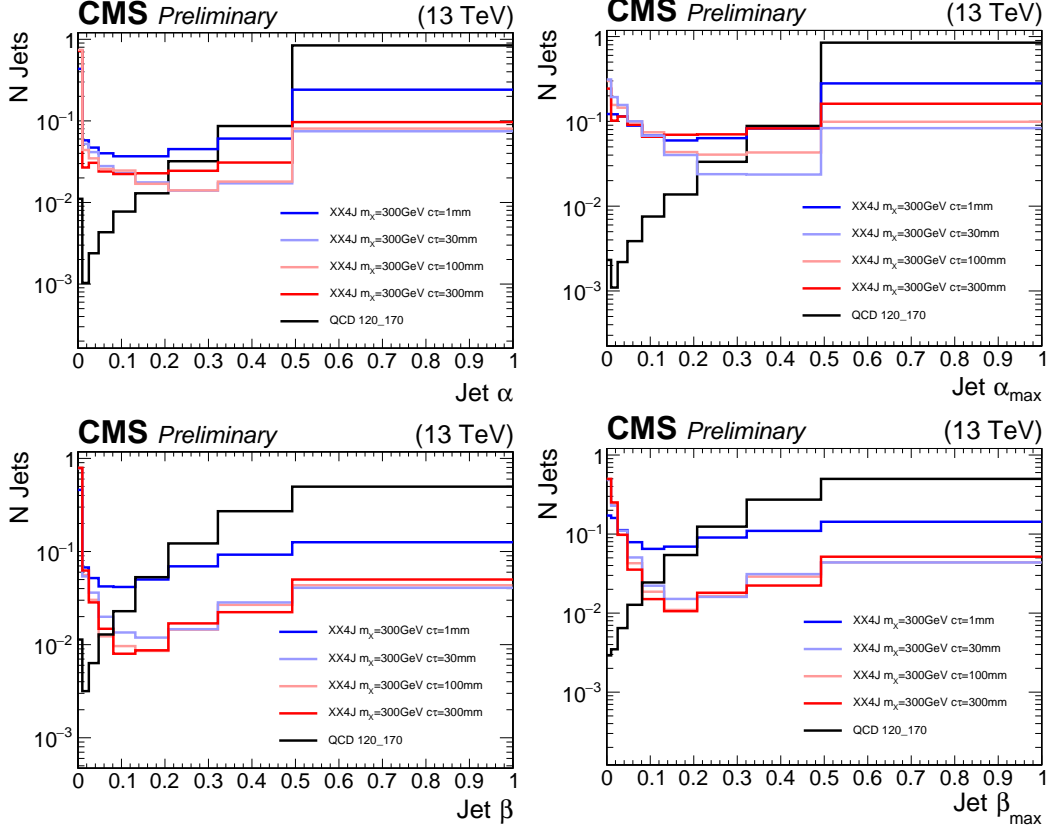


Figure 5.15: $\alpha, \alpha_{\max}, \beta, \beta_{\max}$ when varying the lifetime of the decaying X^0

A second jet variable $\beta(\text{PV})$ and β_{\max} are defined similarly:

$$\beta_{\text{jet}}(\text{PV}) = \frac{\sum_{\text{tracks} \in \text{PV}} p_t^{\text{tracks}}}{p_t^{\text{jet}}} , \quad (5.2)$$

A comparison of the four variables: $\alpha, \alpha_{\max}, \beta, \beta_{\max}$ is shown in Figure 5.15 by varying the lifetime of the sample. In Figure 5.16 the same comparison is made but varying the mass and leaving the lifetime fixed. Figure 5.17 shows α_{\max} has small correlation in background with the median 2D IP significance and β_{\max} less so. This is because α_{\max} is a function of the tracks matched to the jet, which are utilized in the median IP significance calculation.

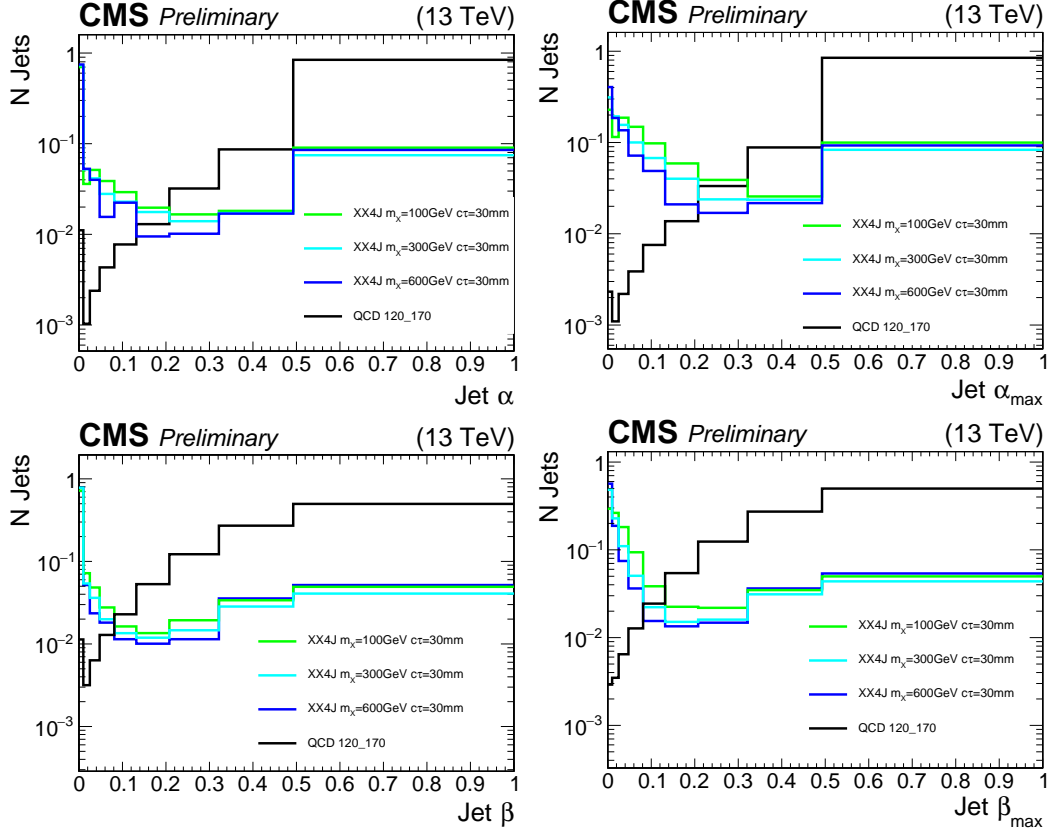


Figure 5.16: $\alpha, \alpha_{\max}, \beta, \beta_{\max}$ when varying the mass of the decaying X^0

5.3.2 Calo Jet Information

In the case which there are no tracks to identify the decay as displaced, we can utilize the high hadronic energy fraction of jets that occur from long-lived decays inside of the hadronic calorimeter. Figure 5.18 includes a generator level cut on the transverse decay distance of > 1 m to ensure that the decay occurs outside of the tracker.

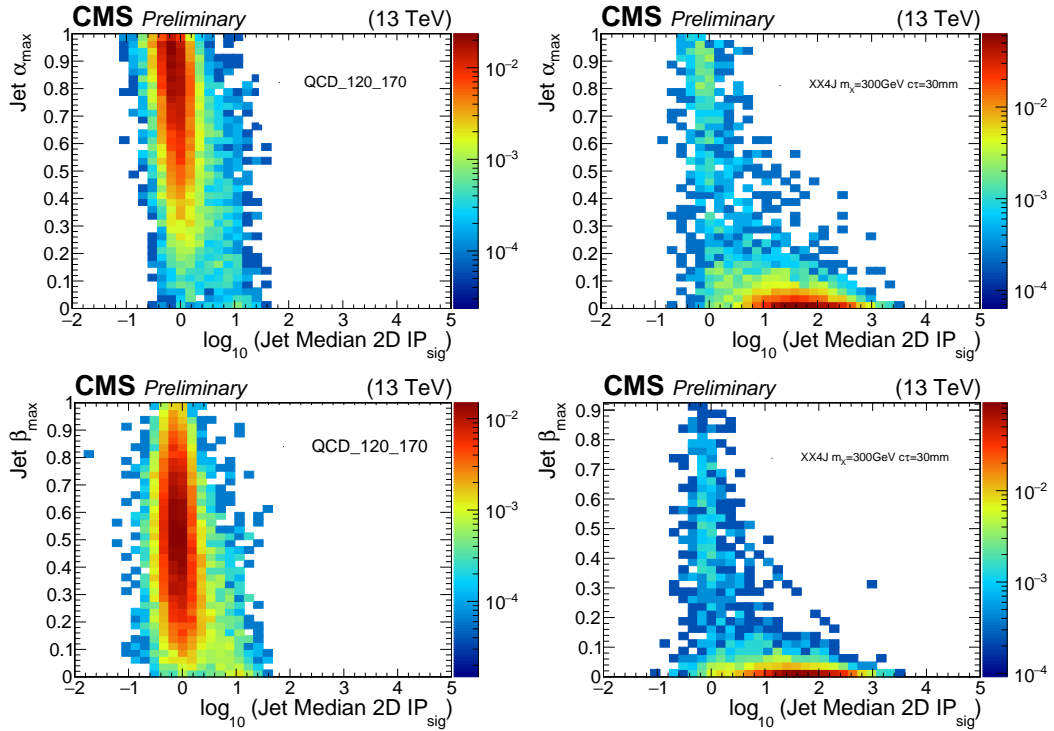


Figure 5.17: (left) The correlation between α_{\max} and β_{\max} and median 2D IP significance for QCD. (right) The same correlation plot for XX4J with $m_{X^0} = 300 \text{ GeV}$ and $c\tau_0 = 30 \text{ mm}$

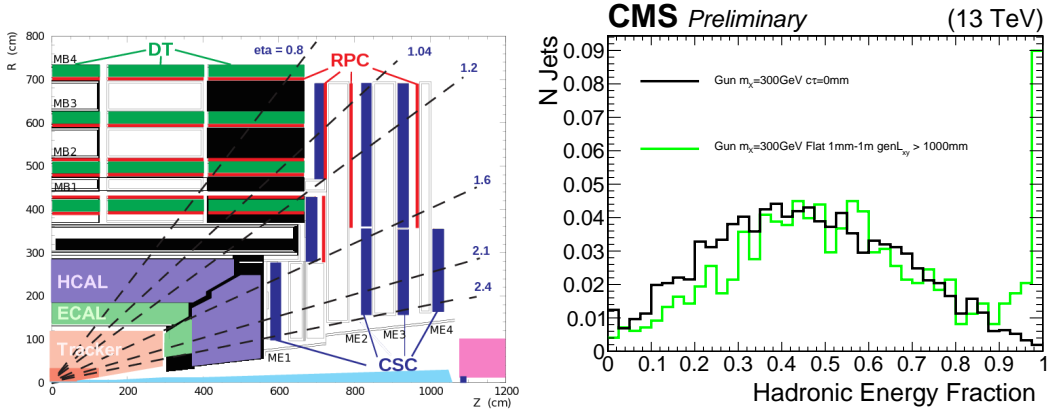


Figure 5.18: (left) A longitudinal slice of the CMS detector showing the transverse coverage of the tracking layers. (right) Hadronic fraction of jets in events with generator level requirement that the X^0 decay at a transverse distance $L_{xy} > 100 \text{ cm}$

Chapter 6

Displaced Jet Analysis

6.1 Introduction

The study of physics beyond the standard model (BSM) is one of the main objectives of the ATLAS and CMS experiments at the CERN LHC. With no signal observed so far, the ATLAS and CMS results put severe bounds on BSM theories.

The majority of these searches focus on prompt particles with lifetimes $c\tau_0 < 1\text{mm}$ and contain requirements on the physics objects that reject longer lived particle decays. This leaves open the possibility that light long-lived particles could exist and still remain undetected. In this study, we present an inclusive search for long-lived particles decaying to various combinations of jets and leptons. The analysis exploits the information originating from the CMS calorimeters to reconstruct jets and measure their energies. The information from reconstructed tracks, in particular the transverse impact parameters, is used to discriminate the displaced-jets signal from the background of ordinary multijet events. The analysis is performed on data collected with the CMS detector at a center-of-mass energy $\sqrt{s} = 13 \text{ TeV}$ in 2015. The data set corresponds to an integrated luminosity of 2.6 fb^{-1} . Results for similar

signatures have been reported by ATLAS [4, 3] and CMS [44], using data collected at $\sqrt{s} = 8$ TeV.

6.2 Datasets and simulated samples

Events are collected from two dedicated online selection algorithms, designed to identify events with displaced jets. The algorithms consider jets clustered from energy deposits in the calorimeters, using the FASTJET [18] implementation of the anti- k_t algorithm [17], with size parameter 0.4. Jets with transverse momentum $p_t < 60$ GeV or $|\eta| > 2.0$ are discarded. An inclusive trigger algorithm accepts events when the scalar sum of the jet p_t 's, H_T , is greater than 500 GeV and at least two jets with $|\eta| < 2.0$ and at most two prompt tracks are found. Tracks are classified as prompt if their transverse impact parameter relative to the beam line, IP^{2D} , is less than 1mm. Another trigger algorithm is used, which requires $H_T > 350$ GeV and asks that there be two displaced jets each having at least one track with transverse impact parameter $IP^{2D} > 5\sigma_{IP^{2D}}$, where $\sigma_{IP^{2D}}$ is the uncertainty on IP^{2D} . Samples with large H_T are used to study the performance of the online selection algorithms.

The main source of background events originates from multijet production. The properties of this background process are studied using a simulated multijet sample, generated with Pythia 8 [64]. The NNPDF 2.3 [12] parton distribution functions (PDFs) are used to model the parton momentum distribution inside the colliding protons. The event simulation includes the effect of multiple proton-proton collisions in the same bunch crossing and in bunch crossing nearby in time, referred to as pileup. Simulated samples are reweighted to match the pileup profile observed in data.

The analysis is interpreted with a set of benchmark signal models. The Jet-Jet model predicts pair-produced long-lived scalar neutral particles X^0 [62], each decaying to two light quarks u,d,s,c , and b with equal probability. The resonance mass m_{X^0} and

proper lifetime $c\tau_0$ are scanned between 50 and 1500 GeV and between 1 and 2000mm, respectively. The trigger efficiencies for a fixed $m_{X^0} = 300$ GeV and $c\tau_0 = 1, 30$, and 1000 mm are 30%, 81%, and 42% respectively. The trigger efficiencies for a fixed $c\tau_0 = 30$ mm and $m_X = 50, 100$, and 1000 GeV are 2%, 14%, and 92% respectively.

The B-Lepton model contains pair-produced long-lived top squarks in R-parity violating models of Supersymmetry [33]. Each top squark decays to one b quark and a lepton. The branching fractions of the decay to the three lepton flavors are equal. The resonance mass $m_{\tilde{t}}$ and proper lifetime $c\tau_0$ are scanned between 300 and 1000GeV and between 1 and 1000mm, respectively. The trigger efficiencies for a fixed mass $m_{\tilde{t}} = 300$ GeV and $c\tau_0 = 1, 30$, and 1000 mm are 15%, 41%, and 23% respectively. The trigger efficiencies for $m_{\tilde{t}} = 500, 700$, and 1000 GeV and fixed $c\tau_0 = 30$ mm are 64%, 71%, and 74% respectively.

These models are also investigated with modified branching fractions. The Light-Light model is the Jet-Jet model excluding decays to b quarks (equal decays to lighter quarks) and the B-Mu, B-Ele, and B-Tau models are derived from the B-Lepton model with 100% branching fraction to muons, electrons, and taus, respectively. Leptonic tau decays are included in the B-Tau interpretation. All signal samples are generated with Pythia, with the setup described above for the multijet sample.

6.3 Event selection

A signal is searched for by applying the selection described in section 6.4 and counting the number of tagged displaced jets, N_{tags} . In addition to the online and offline requirements described in section 6.2, the analysis signal region requires $N_{\text{tags}} \geq 2$. Efficiencies are reported for all interpreted models as a function of the lifetime with fixed mass (Table 6.1 and 6.2) as well as a function of mass with fixed lifetime (Table 6.3 and 6.4).

Table 6.1: Signal efficiencies (in %) for $m_{X^0} = m_{\tilde{t}} = 300$ GeV and varied $c\tau_0$ for the Jet-Jet and B-Lepton models. Selection requirements are cumulative from the first to the last row.

Jet-Jet				
m_{X^0} [GeV]	300	300	300	300
$c\tau_0$ [mm]	1	10	100	1000
≥ 2 tags	2.33 ± 0.15	39.49 ± 0.63	54.54 ± 0.74	14.58 ± 0.38
Trigger	2.16 ± 0.15	38.12 ± 0.62	39.32 ± 0.63	8.07 ± 0.28
Selection	2.09 ± 0.14	37.09 ± 0.61	36.53 ± 0.60	6.67 ± 0.26
≥ 3 tags	0.17 ± 0.04	14.14 ± 0.38	16.72 ± 0.41	1.36 ± 0.12
≥ 4 tags	0.01 ± 0.01	4.73 ± 0.22	4.71 ± 0.22	0.17 ± 0.04

B-Lepton				
$m_{\tilde{t}}$ [GeV]	300	300	300	300
$c\tau_0$ [mm]	1	10	100	1000
≥ 2 tags	0.45 ± 0.02	15.82 ± 0.13	31.52 ± 0.19	8.55 ± 0.10
Trigger	0.29 ± 0.02	11.45 ± 0.11	17.08 ± 0.14	3.22 ± 0.06
Selection	0.27 ± 0.02	9.91 ± 0.11	13.33 ± 0.12	2.08 ± 0.05
≥ 3 tags	0.02 ± 0.01	2.46 ± 0.05	3.81 ± 0.07	0.37 ± 0.02
≥ 4 tags	–	0.30 ± 0.02	0.48 ± 0.02	0.03 ± 0.01

The two classes of events: (i) events passing the inclusive trigger algorithm and with $H_T > 650$ GeV; (ii) events passing the exclusive trigger algorithm and with $H_T > 450$ GeV are treated as a single class.

6.4 An inclusive displaced-jet tagger

The basic requirement for the displaced jet tagging criteria is at least a single track with $p_t > 1$ GeV. Besides the requirements implicitly enforced on the iterative tracking in the global track collection collection (`generalTracks`), there are no further requirements. This includes total and pixel hit requirements. There are no energy composition requirements of the calorimeter deposit and no requirements of a reconstructed secondary vertex, both of which can exclude sensitivity to long-lived decays to electrons and single prong taus.

The three tagging variables utilize 2D quantities. By excluding the longitudinal dimension we prevent large overestimation of displacement due to primary vertex mis-identification. When the signal model in question has a lifetime small on the scale of the longitudinal spread of pile up, the primary vertex can still be accurately reconstructed. In contrast, for a decay in the lab frame of a few centimeters the probability of selecting the correct primary vertex can be highly model dependent. In fact, with beam spot constraints applied and no initial state radiation it is possible the primary vertex would not be reconstructed at all. This is the case for relatively light particles produced with lifetimes longer than the beamspot radius. By utilizing the beamspot constraint to compute primary vertex related quantities, we limit the transverse spread relative to the z direction to 10^{-3} cm. As the tag sensitivity drops at distances smaller than 1 mm, the effect of choosing the wrong PV is negligible.

In contrast to previous analyses, a fitted secondary vertex is not utilized in the tag definition. This decision is deliberate to maintain sensitivity to electrons and single track taus while maintaining a single definition. Previous analyses had sensitivity to single tracks by fitting a secondary vertex to pairs of jets. By not vertexing pairs of jets the displaced object allows for sensitivity to odd (non-even) multiplicities of displaced jets. For example, in the Jet-Jet interpretation there is sensitivity to 3 jets when the 4th is reconstructed outside of the tracker acceptance. These high multiplicity events, in the case of a discovery would have higher statistical significance.

The Primary Vertex Compatibility Variable α_{\max}

The variable α_{\max} characterizes the disassociation of the jet's tracks and all fitted primary vertices in an event. Jets decaying displaced from the primary vertex are unlikely to contain tracks included in the event's primary vertex fit. Background QCD jets, will contain a majority of tracks from either the true primary vertex or a pile up vertex. For a given jet $\alpha(PV)$ is calculated as the ratio of sums of p_t taken

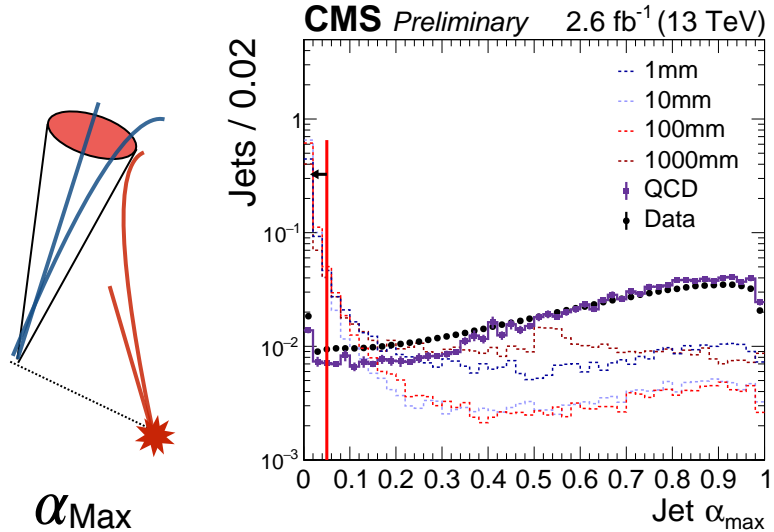


Figure 6.1: Diagram (left) and data/MC comparison (right) for the displaced jet tagging variable α_{\max} . The left distribution shows the data collected by the displaced jet triggers with kinematic cuts and H_T trigger matching thresholds applied. Signal samples are taken from Jet-Jet interpretation with no generator matching for the signal jets, fixed $m_{X^0} = 700$ GeV and varied proper lifetime $c\tau_0$ in the mother frame.

over tracks matching in $\Delta R < 0.4$ between two collections of tracks: the tracks in the specified primary vertex and tracks from the global collection. The sum is restricted to tracks with $p_t > 1.0$ GeV.

If a single PV is selected for all jets in the event, PU jets which are not from this vertex can have signal-like $\alpha \approx 0$. To avoid this, we define α_{\max} for each jet individually selecting the primary vertex with the largest contribution to the sum. The assumption is PU jets will have high α for at least one of the vertices. Many jets with $\alpha = 0$ have $\alpha_{\max} > 0$ as they originate from a sub-leading vertex in the vertex collection. As the variable is calculated relative to all primary vertices, there is no dependence on selecting a single vertex.

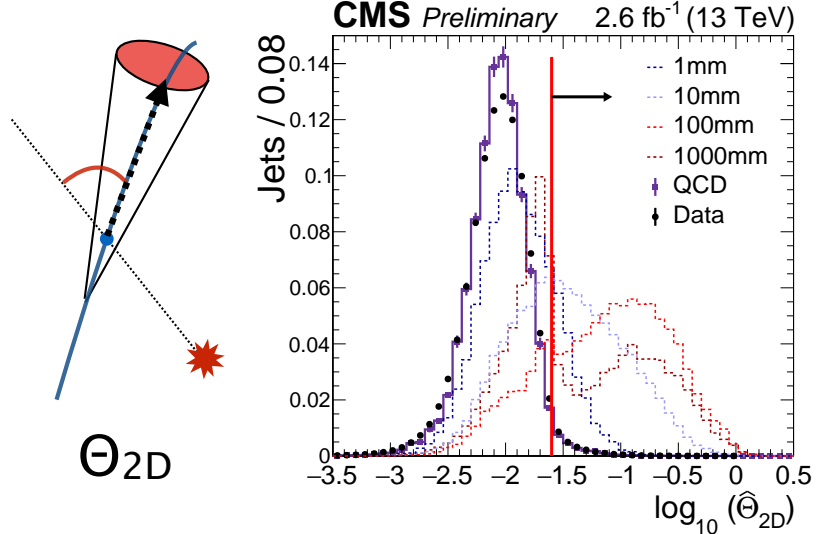


Figure 6.2: Diagram (left) and data/MC comparison (right) for the displaced jet tagging variable Θ_{2D} . The left distribution shows the quantities collected by the displaced jet triggers with kinematic cuts and H_T trigger matching thresholds applied. Signal samples are taken from Jet-Jet interpretation with no generator matching for the signal jets, fixed $m_{X^0} = 700$ GeV and varied proper lifetime $c\tau_0$ in the mother frame.

The 2D Angle $\hat{\Theta}_{2D}$

The variable Θ_{2D} is utilized to characterize the recoil angle of the tracks from the flight direction of the long lived particle. Θ_{2D} is defined as the angle between (i) the 2D ray extended from the primary vertex to the inner hit of the track and (ii) the track 2D momentum vector at the inner hit of the track extended from the inner hit.

The highest sum scalar p_t vertex is selected for all jets in the event.

As Standard Model QCD jets do contain long lived particles and tracks associated with conversions, a typical jet has a long tail in its distribution of Θ_{2D} . To minimize the effect of this tail, the median value (2D) is used, $\hat{\Theta}_{2D}$ (for the same reasons as it is used for IP_{sig}^{2D}). Additionally, as the range of Θ_{2D} spans many orders of magnitude near zero a logarithm is applied constraining typical QCD jet values of $-2.5 < \log(\hat{\Theta}_{2D}) < -1.5$.

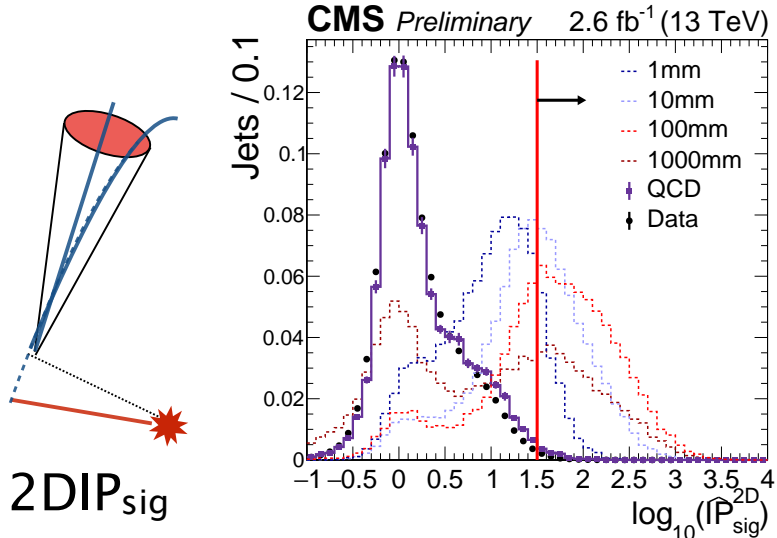


Figure 6.3: Diagram (left) and Data vs. Monte Carlo comparison (right) for the displaced jet tagging variable $IP_{\text{sig}}^{2\text{D}}$. The left distribution shows the quantities collected by the displaced jet triggers with kinematic cuts and H_T trigger matching thresholds applied. Signal samples are taken from Jet-Jet interpretation with no generator matching for the signal jets, fixed $m_{X^0} = 700$ GeV and varied proper lifetime $c\tau_0$ in the mother frame.

As mentioned previously, the smaller the boost of the particle, the more isotropic the decay angles. Thus, the decays of heavier long-lived particles yield larger values of $\Theta_{2\text{D}}$. When the lifetime of the particle is small near 1 mm it is more difficult to resolve this angle because the ray's extrapolation backward corresponds to a smaller and smaller distance from the primary vertex. Background jets capable of passing strict $\Theta_{2\text{D}}$ requirements typically consist of a single track.

Jet $\widehat{IP}_{\text{sig}}^{2\text{D}}$

Variables leveraging the impact parameter information for a given jet are derived from the distribution of impact parameter significances derived from the tracks matched to the jet. As background QCD jets contain a long tail from the presence of real displaced tracks with large IP significance, the median $IP_{\text{sig}}^{2\text{D}}$ is chosen: $\widehat{IP}_{\text{sig}}^{2\text{D}}$. For

jets originating from displaced decay, most tracks have a large impact parameter preserving a high median value.

6.4.1 Tagging Variable Cut Optimization

The requirements included in the baseline tag definition are determined through a scan of the relevant parameter space. The values of the tagging variables scanned can be found in Table 6.8. First, a scan is performed to determine the optimal selection relative to a figure of merit that is maximal labeled $fom_{\max}(x)$ for a given sample $x \in X$ where X is a pre-determined set of signal samples. We will refer to these samples as the training set. The figure of merit for a given sample $x \in X$ and selection $s_i \in S$ is computed as $fom(x, s_i) = \bar{N}(s_i, x)/\sqrt{\bar{N}(s_i, x) + \hat{N}_b(s_i)}$ where \bar{N} is the average number of jets tagged per event passing the event selection and \hat{N}_b is an estimate number of background events in the two tag bin. This estimation \hat{N}_b is calculated as the total number of jets tagged in data times the misidentification rate $\hat{N}_b(s_i) = N_{\text{jets-tagged}}^{\text{data}} \times \frac{N_{\text{jets-tagged}}^{\text{data}}}{N_{\text{jets}}^{\text{data}}}$. Once fom_{\max} is calculated for every sample and selection we choose the tagging requirements which minimize sum of the differences squared of the figure of merit $fom(s_i, x)$ relative to the maximal value fom_{\max} Eq. 6.1.

$$\chi^2(s_i) = \sum_{x \in X} \left(\frac{(fom(s_i, x) - fom_{\max}(x))^2}{fom_{\max}(x)} \right) \quad (6.1)$$

The training set is chosen as the set of all Jet-Jet samples $m_{X^0} = 50 \dots 1500$ GeV with $c\tau_0 = 1, 3$ mm. This set is chosen as it is the most difficult region for the analysis with the largest upper limit on the excluded cross-section.

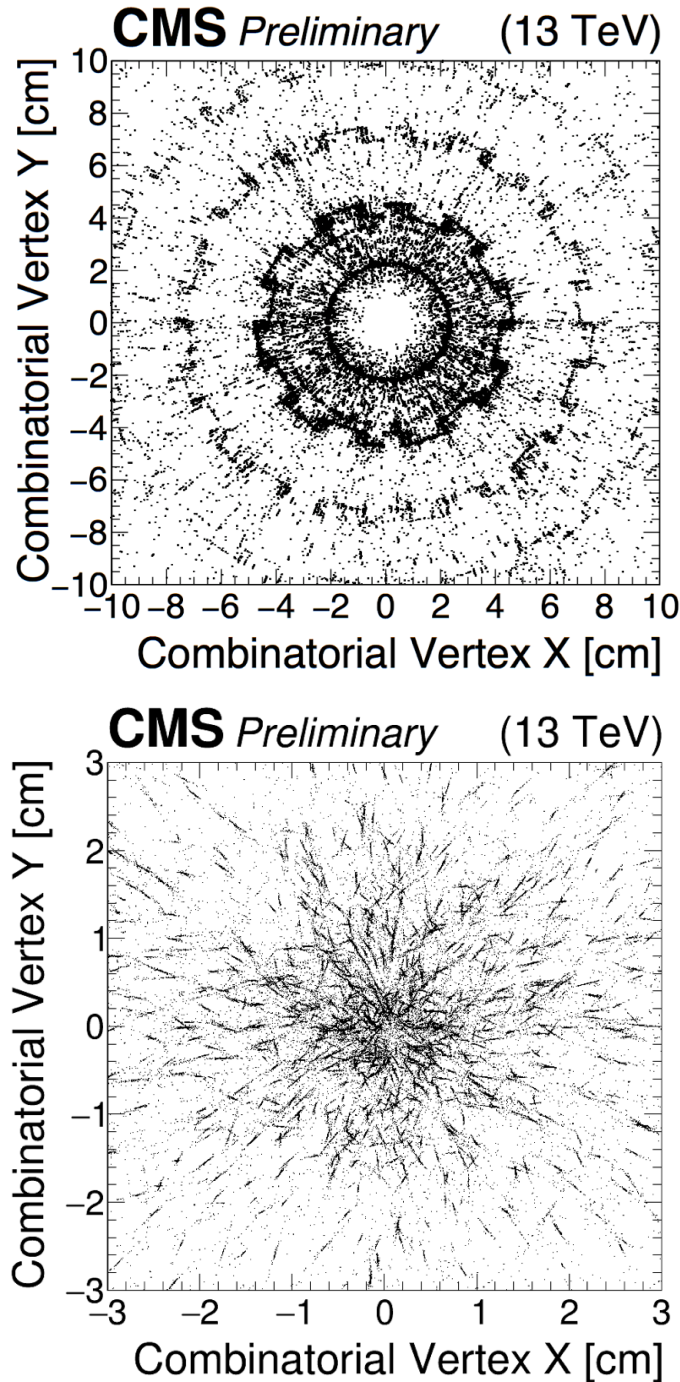


Figure 6.4: From the tracks associated with a calorimeter jet pairs of oppositely charged tracks are fit to a secondary vertex. These vertices are then overlayed from many events. The top figure shows these vertices in data. The bottom figure shows them for simulated signal. The simulated signal shows that including all combinatorial pairs of track vertices can produce clusters of vertices and distinct X patterns along the jet axes where the decay occurs.

6.5 Background prediction

As typical multijets contain only a sub dominant fraction of real displaced tracks, jets with a small multiplicity of tracks represent the dominant background. These tracks can occur from K Short or Lambdas decays, photon conversions, and/or from nuclear interactions with the detector material. Figure 6.4 shows vertices fit from pairs of oppositely charged displaced tracks overlaid from many events. The detector elements of the tracker as well as the beam pipe are clearly visible. As the tagging criteria utilize averages of all tracks matched to the jet, the likelihood of tagging a fake decreases exponentially with N_{tracks} .

Figure 6.5 shows the fraction of jets that are tagged as displaced jets in data as a function of the number of tracks associated with the jet, N_{tracks} . This function is the misidentification rate of tagging a prompt jet as displaced (up to possible signal contamination) and is interpreted as the probability $p(N_{\text{tracks}})$ of being tagged. This parameterization allows for a representative estimation, event by event, of the probability of tagging multiple fake displaced jets. That is to say, an event with two high track multiplicity jets is much less probable than two single track jets to have 2 fake displaced-jet tags.

To maintain the statistical independence of the events that are used to perform the prediction and the events in the signal region, the probabilities are measured in the full control sample of events with $N_{\text{tags}} \leq 1$, while the final signal region requires $N_{\text{tags}} \geq 2$. Additionally, this limits signal contamination in the probability measurement. The control sample of $N_{\text{tags}} = 1$ includes 1391 events.

The size of the bias introduced by only measuring the misidentification rate in events with $N_{\text{tags}} \leq 1$ is quantifiable. For the nominal tag, the size of the effect of removing these events on the predicted number of two tag events is negligible (0.4%) compared to the statistical uncertainty of the prediction.

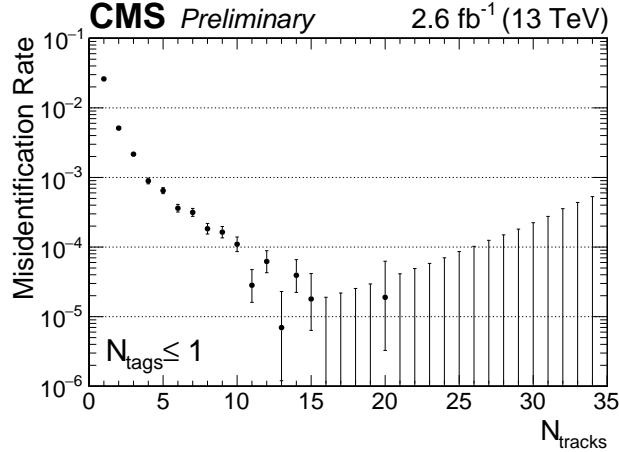


Figure 6.5: The fraction of jets passing the displaced-jet tagging criteria as a function of the number tracks associated with the jet N_{tracks} . The results are from data events with $N_{\text{tags}} \leq 1$ collected with the displaced-jet triggers and passing the offline selection criteria.

The mistagging rate is used to predict the probability for an event to have N_{tags} tagged jets, $P(N_{\text{tags}})$. For instance, for an event m with three jets j_1 , j_2 , and j_3 , there is one configuration with no tags, with a probability:

$$P^m(N_{\text{tags}} = 0) = (1 - p_1)(1 - p_2)(1 - p_3) ,$$

where $p_i = p(N_{\text{tracks}}(j_i))$. Similarly, there are three possibilities for this same event to have $N_{\text{tags}} = 1$:

$$P^m(N_{\text{tags}} = 1) = p_1(1 - p_2)(1 - p_3) + (1 - p_1)p_2(1 - p_3) + (1 - p_1)(1 - p_2)p_3 .$$

The probability of finding N_{tags} tags in the m event is:

$$P^m(N_{\text{tags}}) = \sum_{\text{jet-configs}} \prod_{i \in \text{tagged}} p_i \prod_{k \in \text{not-tagged}} (1 - p_k) . \quad (6.2)$$

Tagged jets enter the product as p_i and non-tagged jets enter as $(1-p_i)$. Equation (6.2) is used to compute the probability of observing N_{tags} , under the assumption that the sample does not contain any signal. The number of events expected for a given value of N_{tags} is then computed as

$$N_{\text{events}}(N_{\text{tags}}) = \sum_m P^m(N_{\text{tags}}) , \quad (6.3)$$

where m runs only over events with fewer than two tagged jets. The prediction is then compared to the observed N_{tags} multiplicity in events with two or more tagged jets, to assess the presence of a signal.

Let q_i be the misidentification rate corresponding to a jet with i tracks and N_{tracks} the maximum number of tracks for any jet in the analysis. The statistical error σ_{q_i} in the misidentification rate is propagated to an error on the number of tagged events with $N_{\text{tags}} = 1, 2, 3, \dots$

$$\begin{aligned} \sigma_{N_{\text{events}}(N_{\text{tags}})}^2 &= \sum_{i=1}^{N_{\text{tracks}}} \left(\frac{\partial N_{\text{events}}(N_{\text{tags}})}{\partial q_i} \sigma_{q_i} \right)^2 \\ &= \sum_{i=1}^{N_{\text{tracks}}} \left(\left(\sum_{m \in N_{\text{events}}} \frac{\partial P^m(N_{\text{tags}} = n)}{\partial q_i} \right) \sigma_{q_i} \right)^2 \end{aligned}$$

The probability is determined for each event for $N_{\text{tags}} \leq N_{\text{jets}}$. The predicted number of events with N_{tags} is calculated as the sum over all events.

We validate this procedure in the absence (background-only test) and presence (signal-injection test) of a signal, using simulated events.

The background-only test is performed predicting the tag multiplicity on the simulated multijet sample, taking as input the misidentification rate distribution. In order to populate the large- N_{tags} region of the distribution, a looser version of the displaced-jet tagger is employed in this test. The full sample of events passing the event selection is divided into multiple independent samples and the background pre-

diction validated. The predicted background of N_{tags} events in simulated multijet events is found to be consistent within statistical uncertainty.

6.5.1 Signal region removal correction

As the misidentification rate is determined from only events with 1 tag or less, there is a systematic underestimation of the background depending on the tag multiplicity of the order $r_{21} = N_{2\text{tags}}^{\text{events}} / N_{1\text{tag}}^{\text{events}}$. To see this, let us consider two predictions of the background distribution of 1 tag N_1^{pred} where the probability p that includes only events with 1 or less tag and $N_1^{\text{pred},\text{SR}}$ with probability p^{SR} that includes all events, and calculate their approximate relative difference:

$$\frac{N_1^{\text{pred}} - N_1^{\text{pred},\text{SR}}}{N_1^{\text{pred}}} = \frac{\sum p - \sum p^{\text{SR}}}{\sum p} = \frac{N^{\text{events}}(p - p^{\text{SR}})}{N^{\text{events}}p} = \frac{p - p^{\text{SR}}}{p}$$

where we have assumed a flat probability p and assume that $N_{2\text{-tag}}^{\text{events}} \ll N_{\text{events}}$ so that sums over all events are equivalent to sums over events with 1 or less tags. Now, let $p = N_1/N_{\text{jets}}$ and $p^{\text{SR}} = \sum_{n=1}^N (nN_n/N_{\text{jets}}) \approx (N_1 + 2N_2)/N_{\text{jets}}$. Where N_i is the number of events with i tagged jets and N_{jets} is the total number of jets passing the kinematic selection in the sample.

$$\frac{p - p^{\text{SR}}}{p} = -\frac{2N_2}{N_1} = -2r_{21}$$

Now consider the two tag prediction where we assume the dominant term in the configuration sum is p^2 :

$$\begin{aligned} \frac{N_2^{\text{pred}} - N_2^{\text{pred},\text{SR}}}{N_2^{\text{pred}}} &= \frac{\sum p^2 - \sum(p^{\text{SR}})^2}{\sum p^2} \\ &= -\frac{4N_2}{N_{\text{jets}}} \frac{N_{\text{jets}}}{N_1} - \frac{N_{\text{jets}}}{N_1^2} \left(\frac{2N_2}{N_{\text{jets}}} \right)^2 = -\frac{4N_2}{N_1} - \frac{4N_2^2}{N_1^2} = -4r_{21} - 4r_{21}^2 \end{aligned}$$

As we do not know the true number of 2 tag events before un-blinding we estimate the parameter $r_{21} \approx N_2^{\text{pred}}/N_1^{\text{pred}}$. We iteratively define:

$$r_{21}^{i+1} = \frac{N_2^{\text{pred}}(1 + 4r_{21}^i + 4(r_{21}^i)^2)}{N_1^{\text{pred}}(1 + 2r_{21}^i)}$$

where $r_{21}^0 = N_2^{\text{pred}}/N_1^{\text{pred}}$. As $i \rightarrow \infty$ the estimation quickly converges and the value r_{21}^∞ is used to correct N_2^{pred} .

The correction for the baseline tag is on the order of $4r_{21} < 1\%$ and negligible within the systematic on the 2 tag prediction for the baseline tag. However, for the loose tag the correction is $4r_{21} \approx 14\%$.

6.5.2 Tag probability cross validation

To test the bias of the background estimation a method of cross validation is utilized. For a given sample, N_{div} non-overlapping sub-samples are partitioned. For each sub-sample, a corresponding set of jet probabilities are computed as described in the previous section. For each set of jet probabilities, an $N_{\text{tags}}^{\text{pred}}$ prediction is made for the $N_{\text{div}} - 1$ remaining samples (which have no overlapping events). We will refer to the sample used for the prediction as the measurement sample. The result is $N_{\text{div}}(N_{\text{div}} - 1)$ pairs of probabilities and measurement samples. From each pair, in each bin of N_{tags} , we generate a distribution of pulls $(N_{\text{obs}} - N_{\text{pred}})/\sqrt{N_{\text{pred}}}$ for each N_{tags} bin. All events must pass the event selection. Due to limited statistics in the 2 tag bin for the baseline tag, the loose tag definition (Table 6.6) is used to generate pull distributions in the 2 tag bin.

We summarize the cross validation studies in the following figures:

- Figure 6.6: SR corrected and uncorrected 1 tag bin pulls for the loose tag definition in data collected by Displaced Jet Triggers.

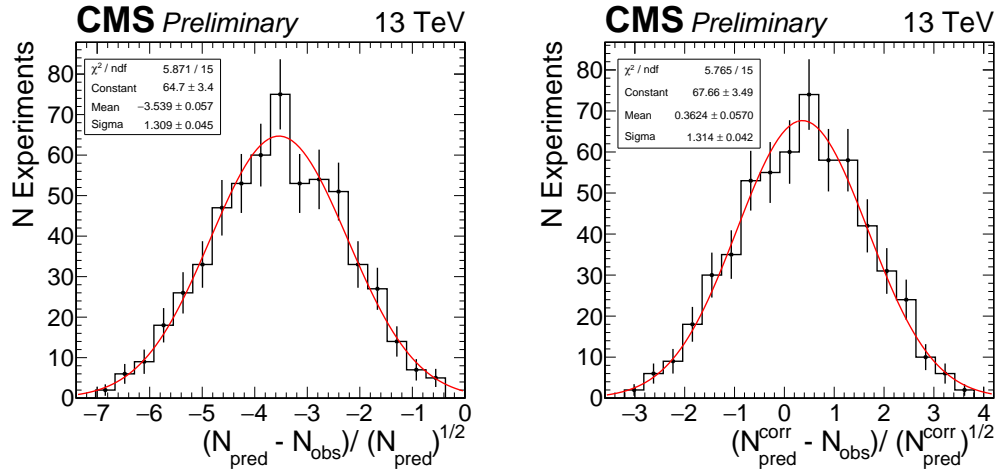


Figure 6.6: (left) Cross validation of the predicted of the number of loose tags in data collected by the displaced jet triggers. Pulls for the 1 tag bin with the loose tag. (right) Pulls for the 1 tag bin with the loose tag with the SR correction .

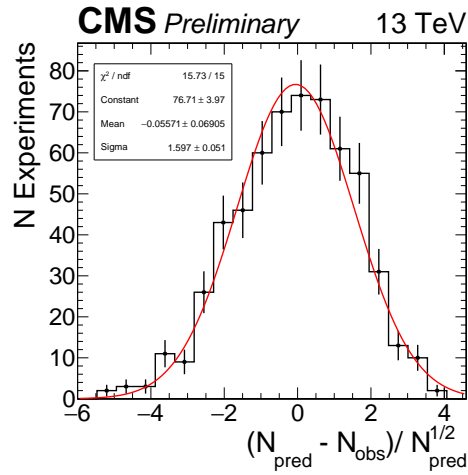


Figure 6.7: Cross validation of the predicted of the number of tags in data passing the displaced jet triggers. Pulls for the 1 tag bin with the baseline tag after the application of the signal removal correction $2r_{12} = 0.2\%$

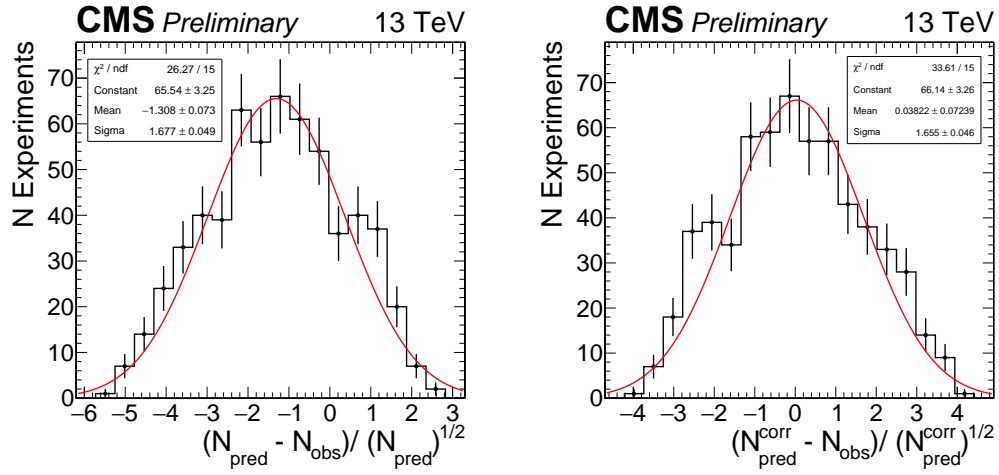


Figure 6.8: (left) Cross validation of the predicted of the number of loose tags in QCD events passing the displaced jet triggers. Pulls for the 1 tag bin with the loose tag. (right) The signal region removal corrected pulls.

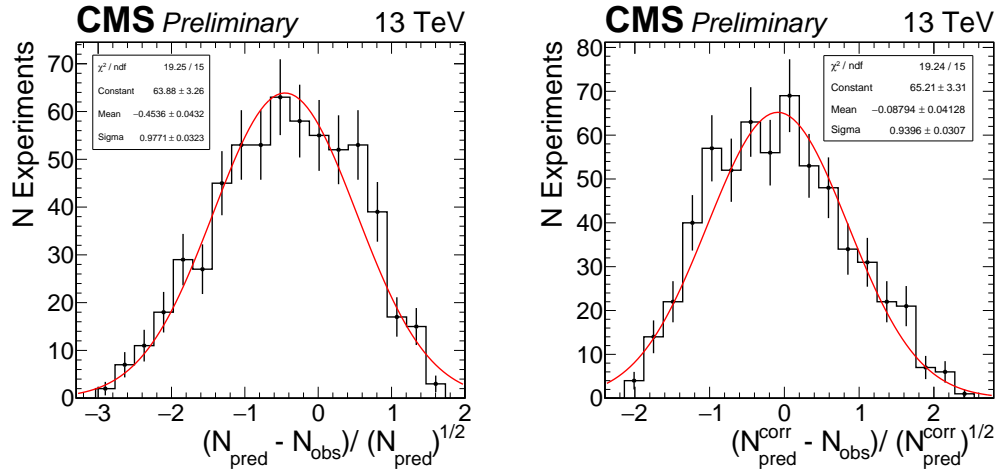


Figure 6.9: (left) Cross validation of the predicted of the number of loose tag in QCD events passing the displaced jet triggers. Pulls for the 2 tag bin with the loose tag uncorrected. (right) The same prediction corrected for the SR removal

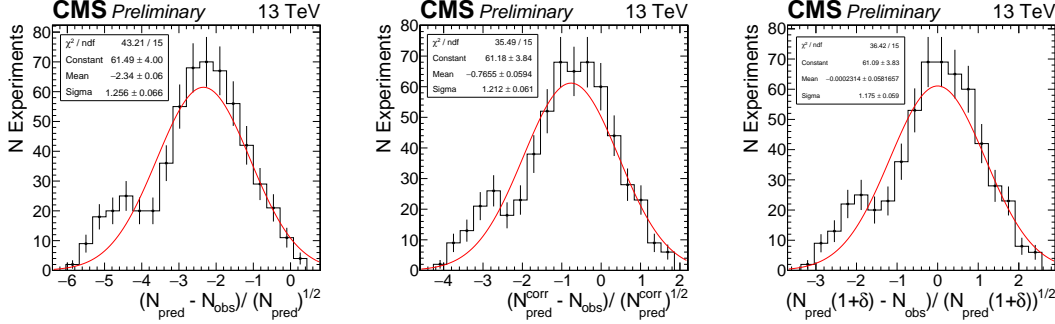


Figure 6.10: (left) Cross validation of the predicted of the number of baseline tags in data collected by the displaced jet triggers. Pulls for the 2 tag bin with the loose tag. (right) Pulls with the signal region removal correction applied (middle). The same signal region removal correction shifted by $\delta = 7.5\%$.

- Figure 6.8: 1 tag bin pulls for the loose tag definition in QCD events passing the Displaced Jet Triggers.
- Figure 6.9: 2 tag bin pulls for the loose tag definition in QCD events passing by Displaced Jet Triggers.
- Figure 6.10: SR corrected, uncorrected, and SR corrected $+\delta$ 2 tag bin pulls for the loose tag definition in data collected by Displaced Jet Triggers.

In data and QCD, the SR correction provides a significant improvement on the pull distributions with respect to the ideal parameters $\mu = 0$ and $\sigma = 1.0$. For the 1 tag prediction in data with the loose tag the central value changes from $\mu = 3.5$ (uncorrected) to $\mu = 0.36$ (corrected). For the signal region (2+ tags), the loose tag in data is within 7.5% of ideal μ and the QCD estimate is within error of $\mu = 0$ but has $\sigma = 1.6 > 1.0$.

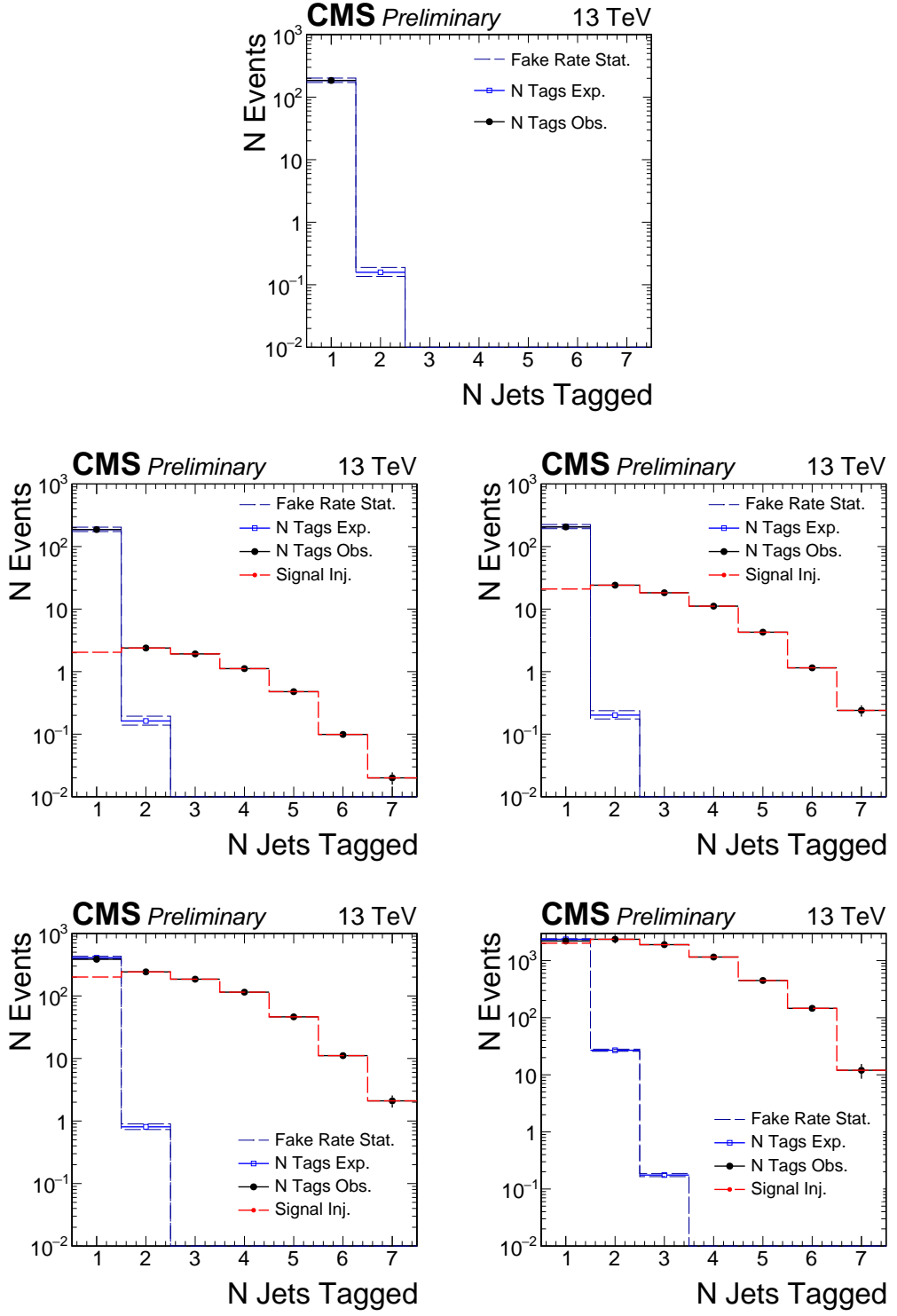


Figure 6.11: Signal Injection tests. The Jet-Jet signal sample used has fixed $m_{X^0} = 700$ GeV and $c\tau_0 = 10$ mm. The level of signal contamination is progressively varied between 10, 100, 1000, and 10000 events injected before any selection. The full event selection is applied and the baseline jet tag definition.

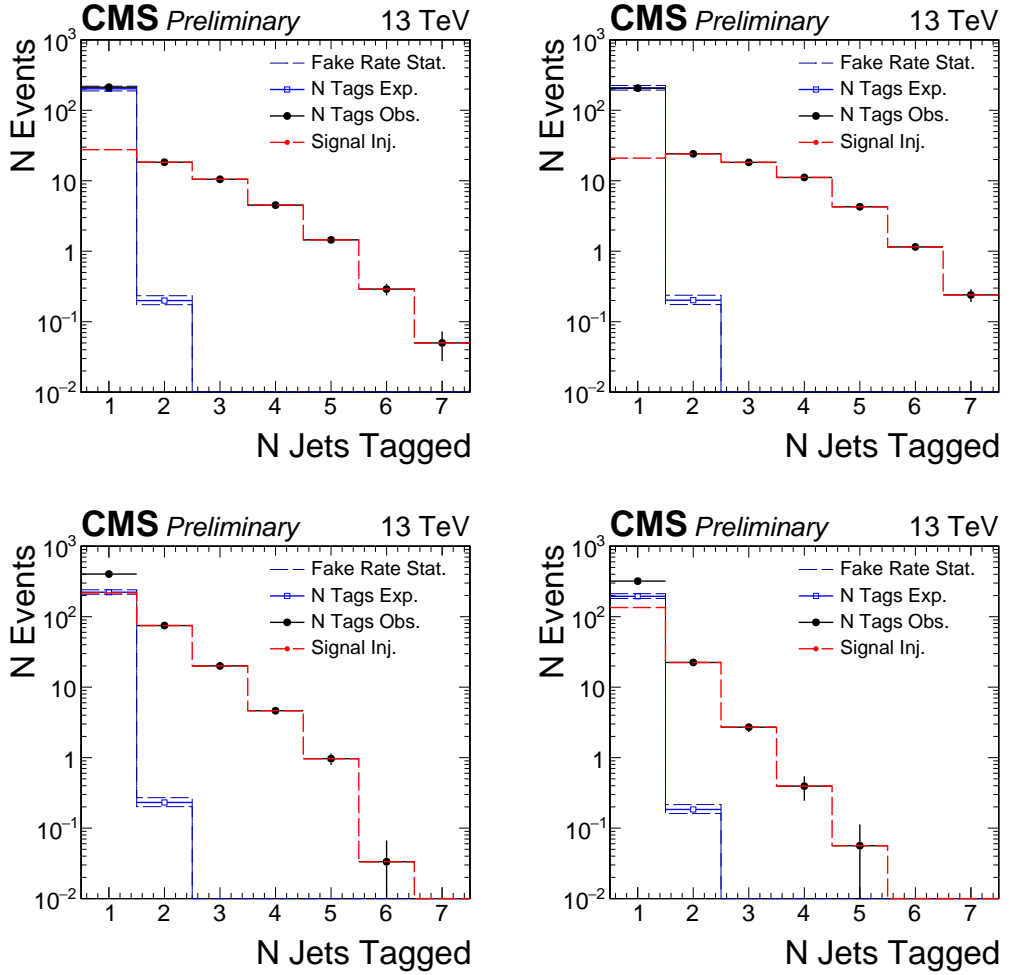


Figure 6.12: Signal Injection. The Jet-Jet signal sample is varied $m_{X^0} = 700$ GeV and $c\tau_0 = 1000$ mm (top left) $m_{X^0} = 700$ GeV and $c\tau_0 = 10$ mm (top right) $m_{X^0} = 100$ GeV and $c\tau_0 = 1000$ mm (bottom left) $m_{X^0} = 100$ GeV and $c\tau_0 = 10$ mm (bottom right). The level of signal contamination is fixed at 100 events for the $m_{X^0} = 700$ GeV and 1000 events for $m_{X^0} = 100$ GeV. The full event selection is applied and the baseline jet tag definition.

6.5.3 Signal injection tests

Injection with QCD

To test the response of the background prediction to the presence of signal contamination in the jet probabilities used for the $P(N_{\text{tags}})$ derivation, signal events are ‘injected’ into QCD Monte Carlo. The resulting predictions for varied masses, lifetimes, and sizes of contamination are shown in Fig. 6.11 and Fig. 6.12. The corresponding predictions, observed number of tags, and the deviation from expectation are summarized in Table 6.9 and Table 6.10. The goal of this exercise is to understand the quantity of signal contamination, as well as lifetime and mass, required to significantly alter the background prediction.

The resulting predictions are also reported normalized such that the total number of signal plus QCD events passing the event selection are equal to the number of events passing the event selection in the analysis in Table 6.11.

The change in the $N_{\text{tags}}^{\text{obs}}$ distribution to the presence of signal is on the order of the number of events with $N_{\text{tags}} > 2$ whereas the integrated shift in $P(N_{\text{tags}} \geq 2)$ is on the order of the shift induced in the $p(j)$ distribution. This shift is of the order the signal contamination. We can conclude the analysis will retain relative sensitivity as long as the signal contamination is relatively smaller than the QCD contribution in the fake rate calculation.

In summary, the background prediction is robust to a variety signal masses, lifetimes and sizes of contamination. In particular, the background is correctly determined within error in the 0 injection case and the bias to the background prediction due to the contamination is small relative to the number of signal events injected.

The following section explores the sensitivity to signal explicitly in a simplified scenario given the assumption that the jet probabilities accurately predict the background when there are no signal events present. This assumption is based on the

closure studies in the previous section and can be considered true within some closure systematic.

Explicit sensitivity in a simplified injection scenario

Consider a sample of N_{QCD} QCD events with a known fraction of jets that are tagged $f(j_i)$ as a function of some jet parameters j_i . For simplicity, assume events have exactly 2 jets. Also assume we have shown that the observation approximately determined $N_{\text{obs}}^{2\text{-tag}} = N_{\text{pred}}^{2\text{-tag}}$ when we interpret $f(j_i)$ as a conditional probability $p(j_i)$ such that:

$$N_{\text{obs}}^{2\text{-tag}} = N_{\text{pred}}^{2\text{-tag}} = \sum_i [p(j_1)p(j_2)]_i = N_{\text{QCD}} p^2$$

where we are using a flat probability p such that $p(j_1) = p(j_2) = p = n_{\text{tag}}/n_{\text{jets}} = n_{\text{fake}}/2N_{\text{events}}$. n_{tag} is the number of jets tagged, which in a QCD sample is exactly n_{fake} . Now, say we perform the signal injection test by injecting N_{sig} events with correspondingly $2N_{\text{sig}}$ signal jets. Let ϵ be the efficiency for a signal event to have 1 tag. Accordingly the probability will shift $p(j_i) \rightarrow \tilde{p}(j_i)$:

$$\tilde{p} = \frac{n_{\text{fake}} + n_{\text{true-tags}}}{2N_{\text{QCD}} + 2N_{\text{sig}}} = \frac{n_{\text{fake}} + \epsilon 2N_{\text{sig}}}{2N_{\text{QCD}} + 2N_{\text{sig}}}$$

Expanding in N_{sig} about 0 we obtain:

$$\begin{aligned} \tilde{p} &= \frac{n_{\text{fake}}}{2N_{\text{QCD}}} - \frac{N_{\text{sig}}n_{\text{fake}}}{2(N_{\text{QCD}})^2} + \epsilon \frac{2N_{\text{sig}}N_{\text{QCD}}}{2(N_{\text{QCD}})^2} \\ &= p - p \frac{N_{\text{sig}}}{N_{\text{QCD}}} + \frac{N_{\text{sig}}\epsilon}{N_{\text{QCD}}} \end{aligned}$$

Let $\Delta = N_{\text{sig}}/N_{\text{QCD}}$

$$\tilde{p} = p(1 - \Delta) + \Delta\epsilon$$

Note that as the signal contamination $\Delta \rightarrow 0$, we obtain the correct probability $\tilde{p} = p$.

Now we attempt to predict the number of events with 2 tags using \tilde{p} and splitting the sum over signal and QCD events.

$$\begin{aligned} N_{\text{pred}}^{\text{2-tag}} &= \sum_i \tilde{p}\tilde{p} \\ &= \sum_i (p(1 - \Delta) + \Delta\epsilon)^2 \\ &= \sum_i p^2 - p^2(2\Delta) + p^2\Delta^2 + 2p\Delta\epsilon - 2p\Delta^2\epsilon + \Delta^2\epsilon^2 \end{aligned}$$

We now split the events in the sum between QCD and Signal.

$$\begin{aligned} N_{\text{pred}}^{\text{2-tag}} &= \sum_i (\text{QCD}) + \sum_i (\text{Signal}) \\ \sum_i (\text{QCD}) &= N_{\text{QCD}}(p^2 - p^2(2\Delta) + p^2\Delta^2 + 2p\Delta\epsilon - 2p\Delta^2\epsilon + \Delta^2\epsilon^2) \\ &= N_{\text{obs}}^{\text{QCD}} - N_{\text{sig}}(p^2\Delta + \Delta\epsilon^2 - 2p^2 + 2p\epsilon - 2p\Delta\epsilon) \end{aligned}$$

where we have used the fact that $\Delta N_{\text{QCD}} = N_{\text{sig}}$ and $\sum_i p^2 = N_{\text{obs}}^{\text{QCD}}$:

$$\sum_i (\text{Signal}) = N_{\text{sig}}(p^2 - p^2(2\Delta) + p^2\Delta^2 + 2p\Delta\epsilon - 2p\Delta^2\epsilon + \Delta^2\epsilon^2)$$

We now evaluate the disagreement between observed and prediction by the variable S . Let $N_{\text{obs}}^{\text{2-tag}} = N_{\text{obs}}^{\text{sig}} + N_{\text{obs}}^{\text{QCD}}$. The sensitivity S , is a measure of how well we have predicted the background in the presence of signal. When $S = 1$ the prediction is exactly the background and the excess is exactly the number of signal events. When $S = 0$ the probabilities prediction has over estimated the background entirely

resulting in no disagreement between observed and predicted 2 tag events.

$$S = \frac{N_{\text{obs}}^{\text{2-tag}} - N_{\text{pred}}^{\text{2-tag}}}{N_{\text{sig}}} = 1 - (2p\epsilon + \Delta\epsilon^2) \\ - (p^2 + \Delta^2\epsilon^2 + 2p\Delta\epsilon - 2p^2 - 2p\Delta\epsilon) \\ - (p^2\Delta - 2p^2\Delta - 2p\Delta^2\epsilon) \\ - (p^2\Delta^2)$$

Terms are grouped by their order in $O(\Delta) + O(p)$. Consider the case when $\epsilon \approx 1$ (this is an approximation for readability as $\epsilon = 1$ would imply no 2 tag events) and for simplicity say $\Delta = p = x$.

$$S = 1 - 3x + 3x^3 - x^4$$

The analysis sensitivity to signal as a fraction of the signal present is at leading order $1 - 3x$. As the misidentification rate in the analysis is small $O(10^{-4})$, we conclude signal contamination will negligibly affect the sensitivity of the analysis.

6.6 Systematic uncertainties

6.6.1 Background systematic uncertainties

A background systematic uncertainty is quoted for the data-driven background prediction method. This uncertainty is estimated by repeating the background-prediction procedure on data with a looser version of the displaced-jet tagging algorithm as outlined in section 6.5. The background estimation uncertainty of 7.5% is the required adjustment to the prediction to remove the bias observed in the Gaussian fit. For three or more tags, the systematic uncertainty for the method is kept fixed.

The statistical uncertainty on the measured misidentification rate as a function of N_{tracks} is propagated to the predicted N_{tags} distribution as a systematic uncertainty. This systematic uncertainty is calculated for each tag multiplicity bin individually. The uncertainty for the 2 tag bin is $-12/+13\%$.

In summary, for the background prediction in the two tag bin, a 7.5% uncertainty is assigned to the background prediction method and $-12/+13\%$ uncertainty is assigned to the statistics of the misidentification rate.

6.6.2 Signal systematic uncertainties

A summary of the systematic uncertainties associated with the signal yields is given in Table 6.12. The uncertainty on the trigger emulation is measured by comparing the predicted efficiency for simulated multijet events and data collected by a loose H_T trigger. The observed difference at threshold (5%) is taken as an estimate of the uncertainty in the emulation of the online H_T requirement. Similarly, the uncertainty induced by the online versus offline jet acceptance is obtained from the shift in the trigger efficiency when the offline jet p_t requirement is increased from $p_t > 60 \text{ GeV}$ to $p_t > 80 \text{ GeV}$ (5%).

The systematic uncertainty on the luminosity is 2.7% [1].

The uncertainty arising from the PDFs for pair-produced masses in the range of 50–1500 GeV is found to be 1–6% (Figure 6.13). An ensemble of alternative PDF is sampled from the output of the NNPDF fit. Events are reweighted according to the ratio between these alternative PDF sets and the nominal ones. The distribution of the signal prediction for these PDF ensemble is used to quantify the uncertainty.

The systematic uncertainty on the modeling of the jet tagging variables in signal MC samples is estimated from the displaced track modeling in multi-jet events in data and MC. The mismodeling of the measured value of Θ_{2D} and IP_{sig}^{2D} for single tracks is propagated to the final tag distribution by varying the individual measured values

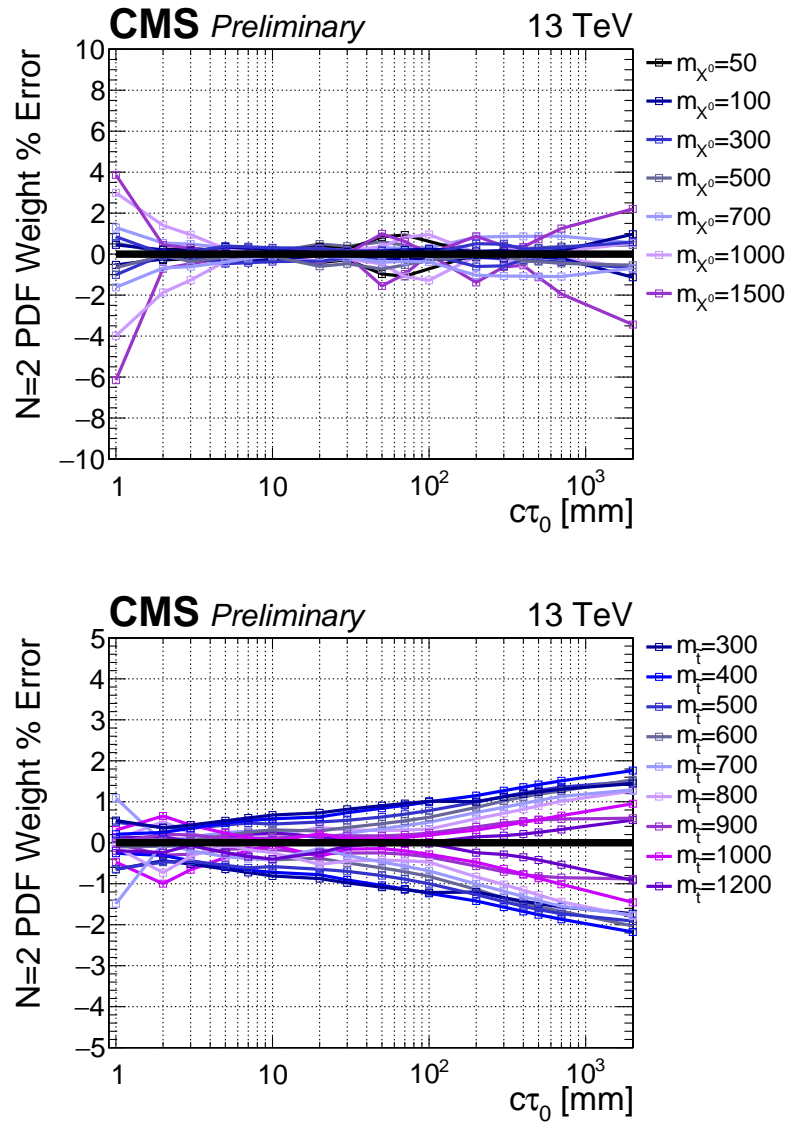


Figure 6.13: The PDF acceptance systematics in the Jet-Jet (left) and B-Lepton (right) signal model as a function of the mass m_{X^0} or $c\tau_0$ for the 2 tag bin. The systematic is reported two sided for the two tag bin in the analysis. The error to fluctuate up is in the upper half plane and the error to fluctuate down on the lower half plane.

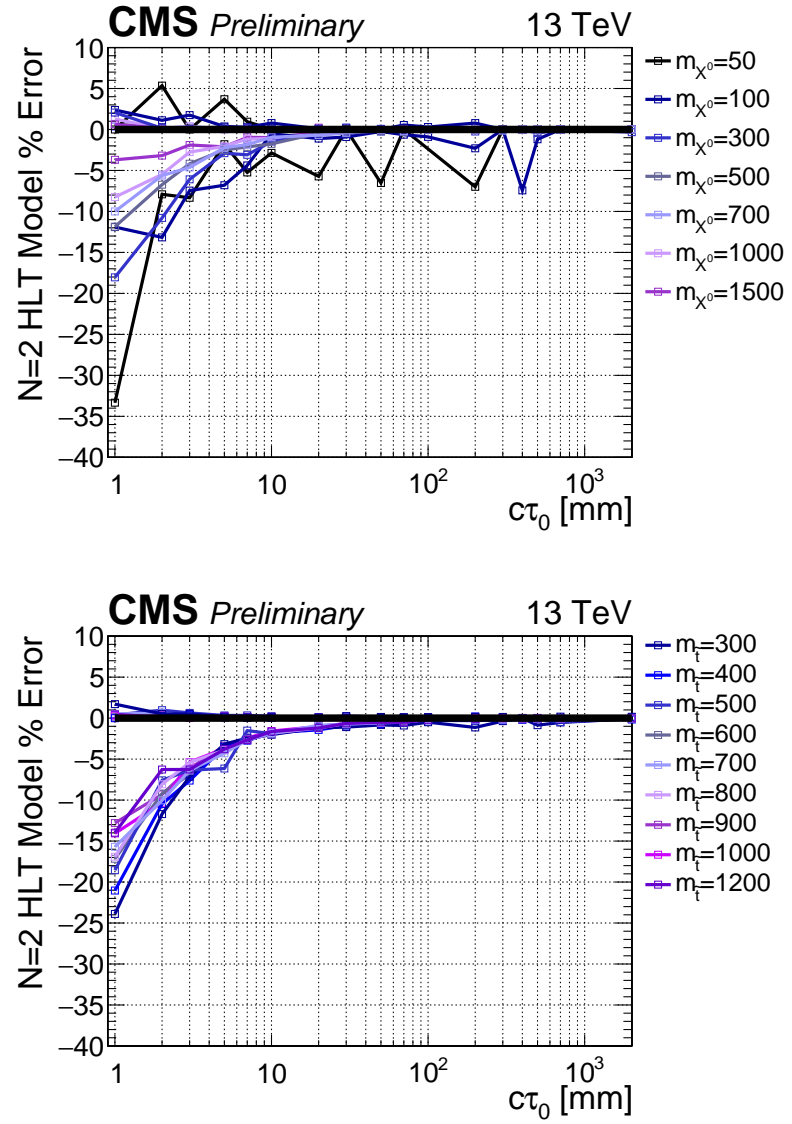


Figure 6.14: The onling tracking related systematics in the Jet-Jet (top) and B-Lepton (bottom) model as a function of $c\tau_0$. The online track IP_{2D} and IP_{sig}^{2D} modeling in the 2 tag bin.

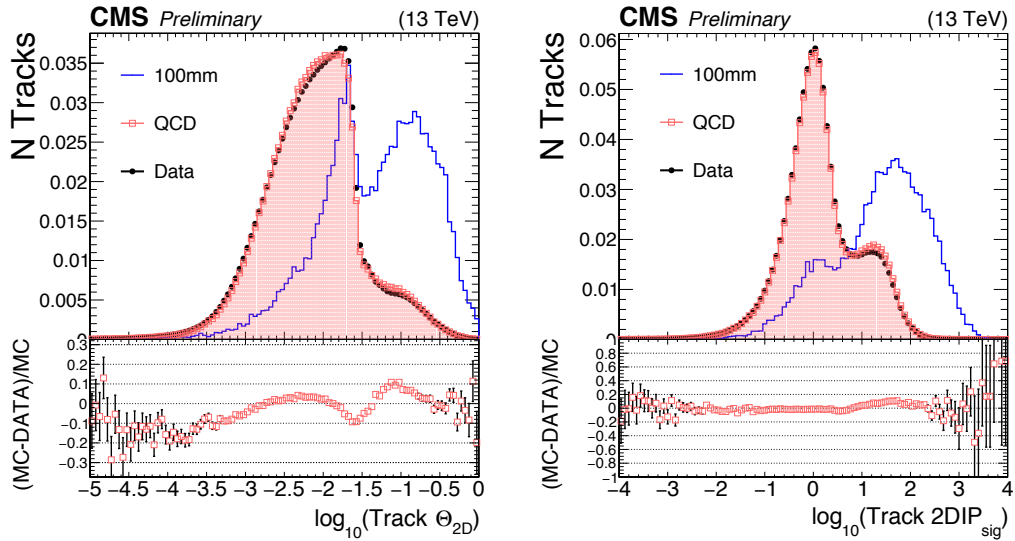


Figure 6.15: A comparison of the offline $\theta_{2\text{D}}$ and $IP_{\text{sig}}^{2\text{D}}$ for individual tracks associated to jets passing $p_{\text{t}} > 60 \text{ GeV}$ and $|\eta| < 2.0$ as collected by H_{T} control triggers.

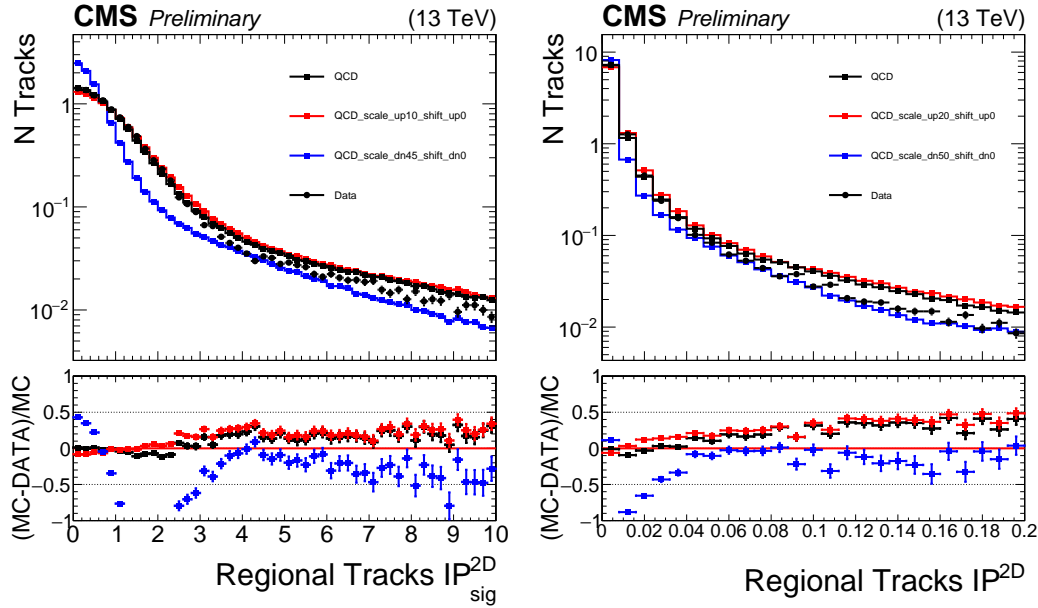


Figure 6.16: A comparison of the online $IP^{2\text{D}}$ and $IP_{\text{sig}}^{2\text{D}}$ for individual tracks associated to jets passing $p_{\text{t}} > 60 \text{ GeV}$ and $|\eta| < 2.0$ as collected by H_{T} control triggers. For each variable x the value is scaled as $x(1 \pm \Delta)$ with positive in red and the negative in blue. A re-scaling of $+10/-45$ and $+20/-50$ for $IP_{\text{sig}}^{2\text{D}}$ and $IP^{2\text{D}}$ respectively provide an envelope for the Data/MC differences.

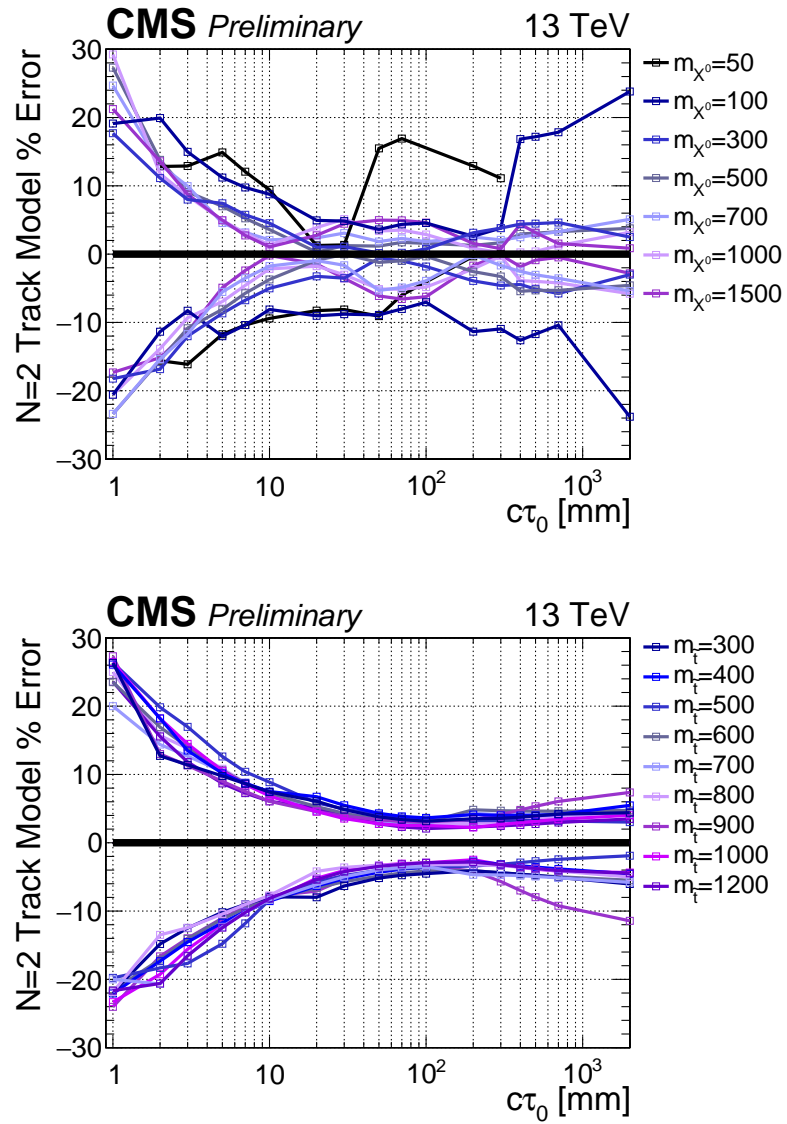


Figure 6.17: (top) Jet-Jet and (bottom) B-Lepton model as a function of $c\tau_0$. The displaced jet offline tagging variable systematic in the 2 tag bin. The systematic is reported two sided for the two tag bin in the analysis. The error to fluctuate up is in the upper half plane and the error to fluctuate down on the lower half plane.

in MC by the difference in the measured value relative to data (3–10%). The tagging variables are then re-calculated. The N_{tags} distribution is recalculated with the new values. The systematic uncertainty is assigned as the relative change in events, bin by bin in N_{tags} . For the two tag bin, this varies from 1 to 30% depending on the mass and lifetime (Figure 6.17). The mismodeling of α_{\max} is found to have a negligible effect on the signal efficiency as the requirement is relatively loose.

The systematic uncertainty on the modeling of the online tracking efficiency is obtained by studying the online regional track reconstruction in data and MC. The online values of IP^{2D} and IP_{sig}^{2D} are varied by the magnitude of the mismodeling found in events collected in control triggers (Figure 6.15). The new values are used to determine if the event would still pass at least one of the trigger paths and its associated offline H_T requirement. The N_{tags} distribution is recalculated with the values varied up and down. The relative change in the number of events per bin is taken as the systematic uncertainty. For the two tag bin, this uncertainty varies from 1 to 35% (Figure 6.14).

All signal systematic uncertainties are calculated individually for each model for all individual mass and lifetime points, and for each value of N_{tags} in the signal region.

6.7 Results and interpretation

The numerical values for the expected and observed yields are summarized in Table 6.13. The observed yields are found to be consistent with the predicted background, within the statistical and systematic uncertainties. No evidence for a signal at large values of N_{tags} is observed.

The single observed event with two tagged jets is shown in Figure 6.18 and Figure 6.19. The event has an $H_T = 951$ GeV. Both tagged jets have only one track. As jets

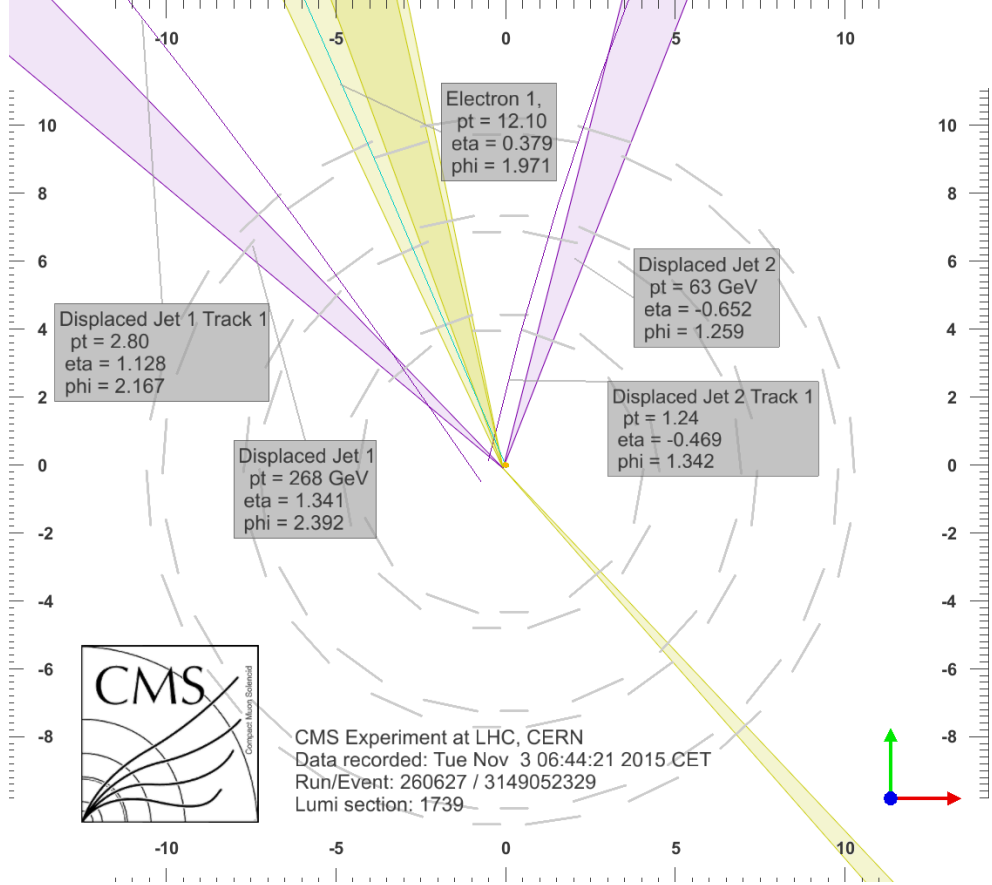


Figure 6.18: The candidate signal event with $N_{\text{tags}} = 2$ from a radial view. The two tagged jets and their corresponding tracks are highlighted in purple. Here one can see the three pixel layers.

with one associated track have the highest misidentification rate, this event would be typical of background events.

Exclusions for each model are obtained from the predicted and observed event yields in Table 6.13 and the signal efficiencies in Tables 6.3–6.4. All bounds are derived at 95% confidence-level (CL) according to the CL_s prescription [55, 43, 21] in the asymptotic approximation. For each limit derivation, we consider events with $N_{\text{tags}} \geq 2$ using independent bins for $N_{\text{tags}} = 2$ and $N_{\text{tags}} \geq 3$. Finer binning of the tag multiplicity for $N_{\text{tags}} > 3$ is found to have a negligible affect on the expected limits. Cross section upper limits are presented as a function of the mass and lifetime of the parent particle. The analysis sensitivity is maximal for $(10 < c\tau_0 < 1000)$ mm.

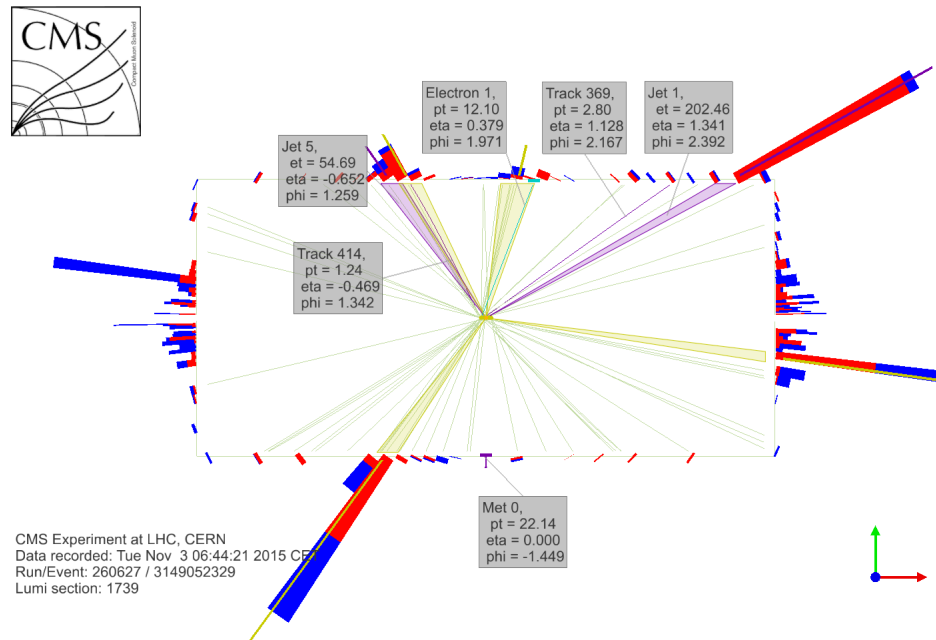
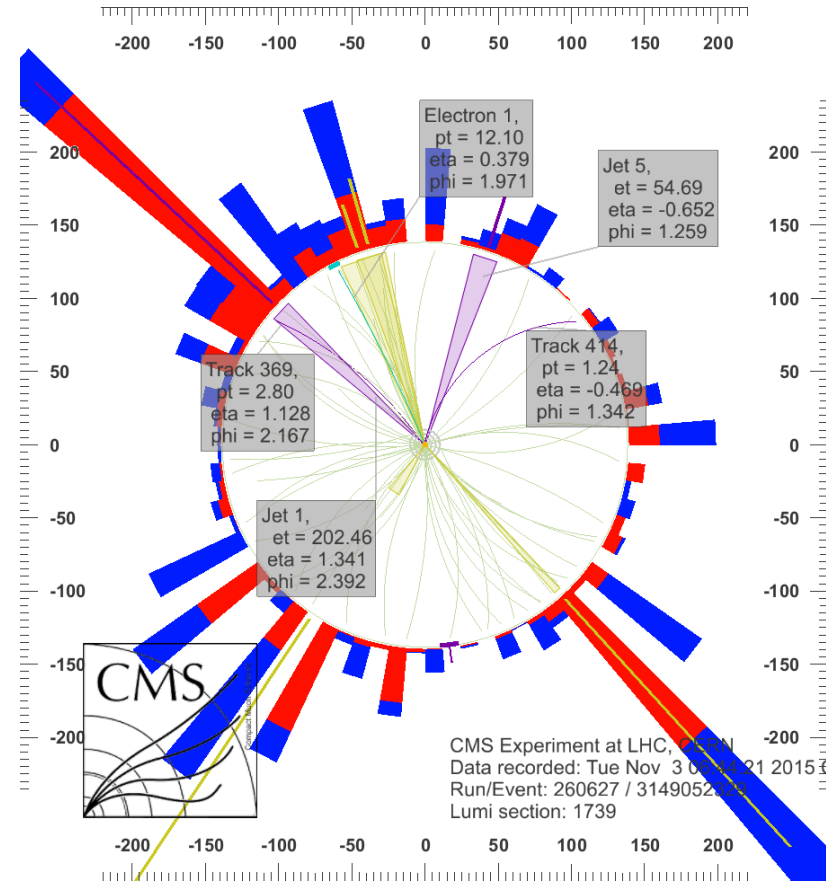


Figure 6.19: The candidate signal event with $N_{\text{tags}} = 2$ from a (top) radial (bottom) longitudinal view. The two tagged jets and their corresponding tracks are highlighted in purple.

Mass exclusion bounds at fixed lifetime are also derived, comparing the excluded cross section with the values predicted for the benchmark models described in section 6.2. In the case of SUSY models, the next-to-leading order (NLO) and next-to-leading-logs (NLL) $t\tilde{t}$ production cross section is used as reference, computed in the large-mass limit for all the other SUSY particles [13, 46, 47, 14, 15, 45].

Figures 6.20 and 6.21 show the excluded pair-production cross section for the Jet-Jet and Light-Light models, respectively. Cross sections as small as 1.2 fb are excluded for $c\tau_0 = 50\text{mm}$ for both models. Exclusion limits are also derived for resonances decaying to $b\ell$ final states, as shown in Fig. 6.22. The sensitivity is similar to what is observed for the Jet-Jet model, although less stringent as additional jets give higher efficiency than additional leptons from both the tagging and triggering perspectives. Cross sections larger than 2.5 fb are excluded at 95% CL, for $c\tau_0$ in the range 70–100 mm excluding a parent mass value of 1130 GeV.

Figures 6.23 and 6.24 show the exclusions on the B-Tau and B-Ele models, respectively. The two models have similar performance at high mass with slightly stronger limits for the B-Ele model at lower mass $m_{\tilde{t}} = 300$ GeV and lifetimes $c\tau_0 > 10\text{mm}$. The highest mass excluded in the B-Ele (B-Tau) model occurs at $m_{\tilde{t}} = 1145$ (1150) GeV and $c\tau_0 = 70$ (70)mm at an observed cross section upper limit of 2.3 (2.2) fb at 95% CL.

In contrast, Fig. 6.25 shows the exclusion for the B-Mu model. Since the analysis uses jets reconstructed from calorimetric deposits while the two muons have small or no associated calorimeter deposit, the signal reconstruction efficiency and displaced-jet multiplicity are smaller in this case. This results in a weaker exclusion bound. The highest mass excluded in the B-Mu model occurs at $m_{\tilde{t}} = 1085$ GeV and $c\tau_0 = 70\text{mm}$ at an observed cross section upper limit of 3.5 fb at 95% CL.

Table 6.2: Signal efficiencies (in %) for $m_{X^0} = m_{\tilde{t}} = 300$ GeV and varied $c\tau_0$ with modified branching ratios relative to the Jet-Jet and B-Lepton models. Selection requirements are cumulative from the first to the last row.

Light-Light				
m_{X^0} [GeV]	300	300	300	300
$c\tau_0$ [mm]	1	10	100	1000
≥ 2 tags	2.20 ± 0.19	40.49 ± 0.80	54.92 ± 0.93	14.55 ± 0.47
Trigger	2.04 ± 0.18	39.16 ± 0.78	39.63 ± 0.79	8.20 ± 0.36
Selection	2.03 ± 0.18	38.41 ± 0.77	36.99 ± 0.76	6.89 ± 0.33
≥ 3 tags	0.19 ± 0.05	14.77 ± 0.48	16.70 ± 0.51	1.48 ± 0.15
≥ 4 tags	–	5.11 ± 0.28	4.73 ± 0.27	0.22 ± 0.06
B-Ele				
$m_{\tilde{t}}$ [GeV]	300	300	300	300
$c\tau_0$ [mm]	1	10	100	1000
≥ 2 tags	0.81 ± 0.10	20.51 ± 0.47	39.01 ± 0.65	11.46 ± 0.35
Trigger	0.40 ± 0.07	14.68 ± 0.40	22.95 ± 0.50	5.15 ± 0.23
Selection	0.40 ± 0.07	13.92 ± 0.39	20.34 ± 0.47	3.58 ± 0.19
≥ 3 tags	0.04 ± 0.02	4.22 ± 0.21	7.21 ± 0.28	0.82 ± 0.09
≥ 4 tags	–	0.73 ± 0.09	1.19 ± 0.11	0.05 ± 0.02
B-Tau				
$m_{\tilde{t}}$ [GeV]	300	300	300	300
$c\tau_0$ [mm]	1	10	100	1000
≥ 2 tags	0.48 ± 0.07	18.40 ± 0.45	34.98 ± 0.61	9.31 ± 0.32
Trigger	0.44 ± 0.07	14.63 ± 0.40	20.20 ± 0.46	3.81 ± 0.20
Selection	0.41 ± 0.07	12.45 ± 0.37	15.50 ± 0.41	2.37 ± 0.16
≥ 3 tags	0.02 ± 0.02	3.23 ± 0.19	4.62 ± 0.22	0.44 ± 0.07
≥ 4 tags	–	0.53 ± 0.08	0.66 ± 0.09	0.02 ± 0.02
B-Mu				
$m_{\tilde{t}}$ [GeV]	300	300	300	300
$c\tau_0$ [mm]	1	10	100	1000
≥ 2 tags	0.13 ± 0.04	8.02 ± 0.29	20.09 ± 0.46	4.03 ± 0.21
Trigger	0.05 ± 0.02	3.97 ± 0.21	6.63 ± 0.26	0.88 ± 0.10
Selection	0.04 ± 0.02	2.92 ± 0.18	4.21 ± 0.21	0.49 ± 0.07
≥ 3 tags	–	0.23 ± 0.05	0.31 ± 0.06	0.03 ± 0.020
≥ 4 tags	–	0.01 ± 0.01	–	–

Table 6.3: Signal efficiencies (in %) for the Jet-Jet and B-Lepton models with $c\tau_0 = 30$ mm and varied mass. Selection requirements are cumulative from the first to the last row.

Jet-Jet						
m_{X^0} [GeV]	50	100	300	1000	1500	
$c\tau_0$ [mm]	30	30	30	30	30	
≥ 2 tags	2.71 ± 0.10	14.80 ± 0.22	54.24 ± 0.74	79.93 ± 0.89	82.55 ± 0.91	
Trigger	0.50 ± 0.04	5.39 ± 0.13	46.41 ± 0.68	74.05 ± 0.86	77.65 ± 0.88	
Selection	0.30 ± 0.03	3.70 ± 0.11	44.75 ± 0.67	73.99 ± 0.86	77.53 ± 0.88	
≥ 3 tags	0.05 ± 0.01	1.09 ± 0.10	20.87 ± 0.46	49.42 ± 0.70	55.28 ± 0.74	
≥ 4 tags	–	0.22 ± 0.03	6.81 ± 0.26	25.45 ± 0.50	32.26 ± 0.57	
B-Lepton						
$m_{\tilde{t}}$ [GeV]	300	600	800	1000		
$c\tau_0$ [mm]	30	30	30	30		
≥ 2 tags	31.52 ± 0.19	47.32 ± 0.23	52.53 ± 0.24	55.88 ± 0.35		
Trigger	17.08 ± 0.14	35.03 ± 0.20	40.40 ± 0.21	43.14 ± 0.30		
Selection	14.70 ± 0.13	32.34 ± 0.19	36.94 ± 0.20	39.26 ± 0.29		
≥ 3 tags	4.11 ± 0.07	10.76 ± 0.11	13.29 ± 0.12	15.00 ± 0.18		
≥ 4 tags	0.55 ± 0.03	1.83 ± 0.05	2.69 ± 0.05	3.09 ± 0.08		

Table 6.4: Signal efficiencies (in %) for $c\tau_0 = 30$ mm and varied mass with modified branching ratios relative to the Jet-Jet and B-Lepton models. Selection requirements are cumulative from the first to the last row.

Light-Light					
m_{X^0} [GeV]	50	100	300	1000	1500
$c\tau_0$ [mm]	30	30	30	30	30
≥ 2 tags	2.84 ± 0.12	15.56 ± 0.29	54.87 ± 0.92	80.52 ± 1.11	82.19 ± 1.14
Trigger	0.53 ± 0.05	5.70 ± 0.17	47.14 ± 0.85	74.85 ± 1.07	77.07 ± 1.10
Selection	0.33 ± 0.04	3.90 ± 0.14	45.68 ± 0.84	74.80 ± 1.07	76.96 ± 1.10
≥ 3 tags	0.05 ± 0.02	1.11 ± 0.08	21.77 ± 0.58	50.04 ± 0.88	55.36 ± 0.93
≥ 4 tags	–	0.23 ± 0.04	7.38 ± 0.34	25.80 ± 0.63	32.47 ± 0.71
B-Ele					
$m_{\tilde{t}}$ [GeV]	300	600	800	1000	
$c\tau_0$ [mm]	30	30	30	30	
≥ 2 tags	39.01 ± 0.65	53.70 ± 0.75	59.62 ± 0.78	62.42 ± 1.11	
Trigger	22.95 ± 0.50	38.07 ± 0.63	43.06 ± 0.66	45.21 ± 0.95	
Selection	21.59 ± 0.48	37.02 ± 0.62	39.47 ± 0.64	42.20 ± 0.92	
≥ 3 tags	7.86 ± 0.29	14.28 ± 0.38	17.37 ± 0.42	20.39 ± 0.64	
≥ 4 tags	1.37 ± 0.12	3.32 ± 0.19	4.34 ± 0.21	4.69 ± 0.31	
B-Tau					
$m_{\tilde{t}}$ [GeV]	300	600	800	1000	
$c\tau_0$ [mm]	30	30	30	30	
≥ 2 tags	34.98 ± 0.61	51.42 ± 0.73	57.20 ± 0.76	59.43 ± 1.07	
Trigger	20.20 ± 0.46	39.78 ± 0.64	45.46 ± 0.68	47.62 ± 0.96	
Selection	17.17 ± 0.43	37.47 ± 0.62	43.64 ± 0.67	44.26 ± 0.92	
≥ 3 tags	5.21 ± 0.24	13.29 ± 0.37	16.15 ± 0.40	19.13 ± 0.61	
≥ 4 tags	0.86 ± 0.10	3.09 ± 0.18	3.68 ± 0.19	4.48 ± 0.29	
B-Mu					
$m_{\tilde{t}}$ [GeV]	300	600	800	1000	
$c\tau_0$ [mm]	30	30	30	30	
≥ 2 tags	20.09 ± 0.46	35.46 ± 0.60	41.18 ± 0.64	43.13 ± 0.93	
Trigger	6.63 ± 0.26	24.73 ± 0.50	31.85 ± 0.56	34.10 ± 0.82	
Selection	5.25 ± 0.24	21.40 ± 0.47	27.42 ± 0.52	31.18 ± 0.79	
≥ 3 tags	0.34 ± 0.06	3.03 ± 0.18	5.28 ± 0.23	6.08 ± 0.35	
≥ 4 tags	–	0.12 ± 0.04	0.68 ± 0.08	0.68 ± 0.12	

Table 6.5: The baseline tag definition in terms of the three displaced jet tagging variables

Variable	$\log_{10}(x)$	Requirement	Linear Requirement
α_{\max}		N/A	< 5%
\widehat{IP}_{sig}^{2D}		> 1.5	> 31.6
$\widehat{\Theta}_{2D}$		> -1.6	> 0.025

Table 6.6: The loose tag definition in terms of the three displaced jet tagging variables.

Variable	$\log_{10}(x)$	Requirement	Linear Requirement
α_{\max}		N/A	< 50%
\widehat{IP}_{sig}^{2D}		> 0.43	> 2.71
$\widehat{\Theta}_{2D}$		> -1.70	> 0.02

Table 6.7: The integrated fake-rate is precisely N_{tagged}/N_{jets} for all jets passing the jet selection in events passing the event selection in data collected by the displaced jet triggers.

Working Point	Flat Fake-Rate / Probability
Loose Tag	2.5816%
Baseline Tag	0.0496%

Table 6.8: The values of the tagging variables included in the scan for selecting the baseline tag definition

Tagging Variable	Begin Scan	End Scan	Step Size	N Points
α_{\max}	0	0.5	0.05	11
$\log_{10}(\widehat{IP}_{sig}^{2D})$	0.0	2.5	0.1	26
$\log_{10}(\widehat{\Theta}_{2D})$	-2.5	-0.5	0.1	21

Table 6.9: The signal injection test using a fixed signal point $m_{X^0} = 700$ GeV and $c\tau_0 = 10\text{mm}$ with varied amount of injection. A summary of the 1,2,3, and 4 tag predictions as a function of the number of events injected (top). The two background systematic errors are listed separately as $\sigma_{method}, \sigma_{fake-rate}$. A summary of the observed number of tags (bottom).

Injection $\sigma \times \mathcal{L}$	1 Pred	2 Pred	3 Pred	4 Pred
0	$185^{+14,+17}_{-14,-13}$	$0.16^{+0.01,+0.03}_{-0.01,-0.02}$	—	—
10	$187^{+14,+17}_{-14,-13}$	$0.16^{+0.01,+0.03}_{-0.01,-0.02}$	—	—
100	$207^{+16,+18}_{-16,-14}$	$0.20^{+0.02,+0.04}_{-0.02,-0.03}$	—	—
1000	$408^{+31,+23}_{-31,-19}$	$0.81^{+0.06,+0.09}_{-0.06,-0.08}$	—	—
10000	$2366^{+177,+53}_{-177,-49}$	$26.95^{+2.02,+1.19}_{-2.02,-1.10}$	$0.18^{+0.01,+0.01}_{-0.01,-0.01}$	—
Injection $\sigma \times \mathcal{L}$	1 Obs	2 Obs	3 Obs	4 Obs
0	185	—	—	—
10	187	2	2	1
100	205	23	20	12
1000	386	237	188	116
10000	2260	2341	1976	1165

Table 6.10: Signal injection test with fixed number of injected events and varied $c\tau_0$ and m_{X^0} . A summary of the 1,2,3, and 4 tag predictions as a function of the number of events injected (top). The two background systematic errors are listed separately as $\sigma_{method}, \sigma_{fake-rate}$. A summary of the observed number of tags (bottom).

$\sigma \times \mathcal{L}$	m_{X^0} [GeV]	$c\tau_0$ [mm]	1 Pred	2 Pred	3+4 Pred
100	700	10	$207^{+16,+18}_{-16,-14}$	$0.20^{+0.02,+0.04}_{-0.02,-0.03}$	—
100	700	1000	$202^{+15,+18}_{-15,-14}$	$0.20^{+0.02,+0.03}_{-0.02,-0.03}$	—
1000	100	10	$222^{+17,+18}_{-17,-14}$	$0.23^{+0.02,+0.04}_{-0.02,-0.03}$	—
1000	100	1000	$195^{+15,+17}_{-15,-13}$	$0.18^{+0.01,+0.03}_{-0.01,-0.02}$	—
$\sigma \times \mathcal{L}$	Mass [GeV]	$c\tau_0$ [mm]	1 Obs	2 Obs	3+4 Obs
100	700	10	205	23	32
100	700	1000	211	18	12
1000	100	10	404	74	26
1000	100	1000	321	23	4

Table 6.11: A summary of the size of the signal injected in the signal injection test (top). A summary of signal region yields in the 2,3, and 4 nominal displaced jet tag bins (middle) and the observed number of tags (bottom), as a function of the size of the signal contamination, for a signal injection test using a fixed signal point $m_{X^0} = 700$ GeV and $c\tau_0 = 10$ mm with varied signal yields. The no signal case is included as a reference to the predicted values without contamination. The test is normalized such that the sum of signal and background events stays fixed at the observed number of events passing the analysis event selection. The contamination fraction corresponds to the hypothetical fraction of signal events contained within the events passing the event selection.

Contam. Fraction	Signal σ [fb]		
0	0		
0.01%	30		
0.10%	290		
1.04%	3000		
9.47%	28000		
Contamination %	2 tag pred	3 tag pred	4 tag pred
0	$1.34^{+0.25}_{-0.17}$	-	-
0.01%	$1.34^{+0.25}_{-0.17}$	-	-
0.10%	1.67 ± 0.33	-	-
1.04%	$6.71^{+0.91}_{-0.82}$	-	-
9.47%	205.38 ± 15.21	1.37 ± 0.08	-
Contamination %	2 tag obs	3 tag obs	4 tag obs
0.00%	0	0	0
0.01%	19	16	10
0.10%	179	159	93
1.04%	1914	1520	943
9.47%	17632	14883	8775

Table 6.12: Summary of the systematic uncertainties. When the uncertainty depends on the specific features of the models (mass, lifetime and decay mode of the long-lived particle) a range is quoted, which refers to the computed uncertainty for $N_{\text{tags}} = 2$ events.

Signal systematic uncertainty	Effect on yield
H_T trigger inefficiency	5.0%
Jet p_t trigger inefficiency	5.0%
Trigger online tracking modeling	1.0–35.0%
Luminosity	2.7%
Acceptance due to PDF	1.0–6.0%
Displaced-jet tag variable modeling	1.0–30.0%

Table 6.13: The predicted and observed number of events as a function of N_{tags} . The prediction is based on the mistagging probability derived from events with fewer than two tags. The full event selection is applied. The quoted uncertainty corresponds to the total background systematic uncertainty.

N_{tags}	Expected	Observed
2	$1.09^{+0.16}_{-0.15}$	1
≥ 3	$(4.9 \pm 1.0) \times 10^{-4}$	0

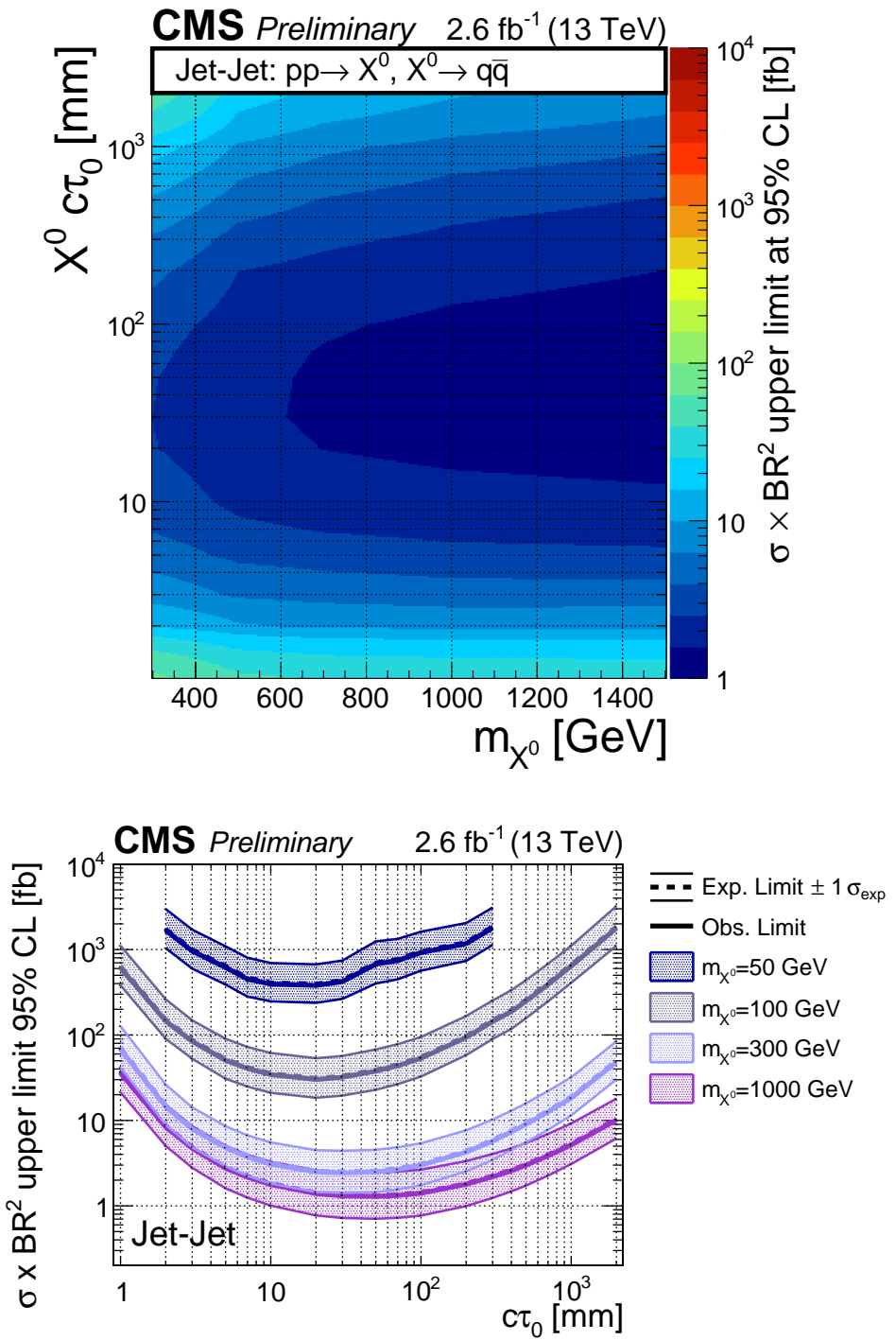


Figure 6.20: The excluded cross section at 95% CL for the Jet-Jet model as a function of the mass and lifetime of the parent particle X^0 (top) and as a function of the lifetime for four values of the mass (bottom).

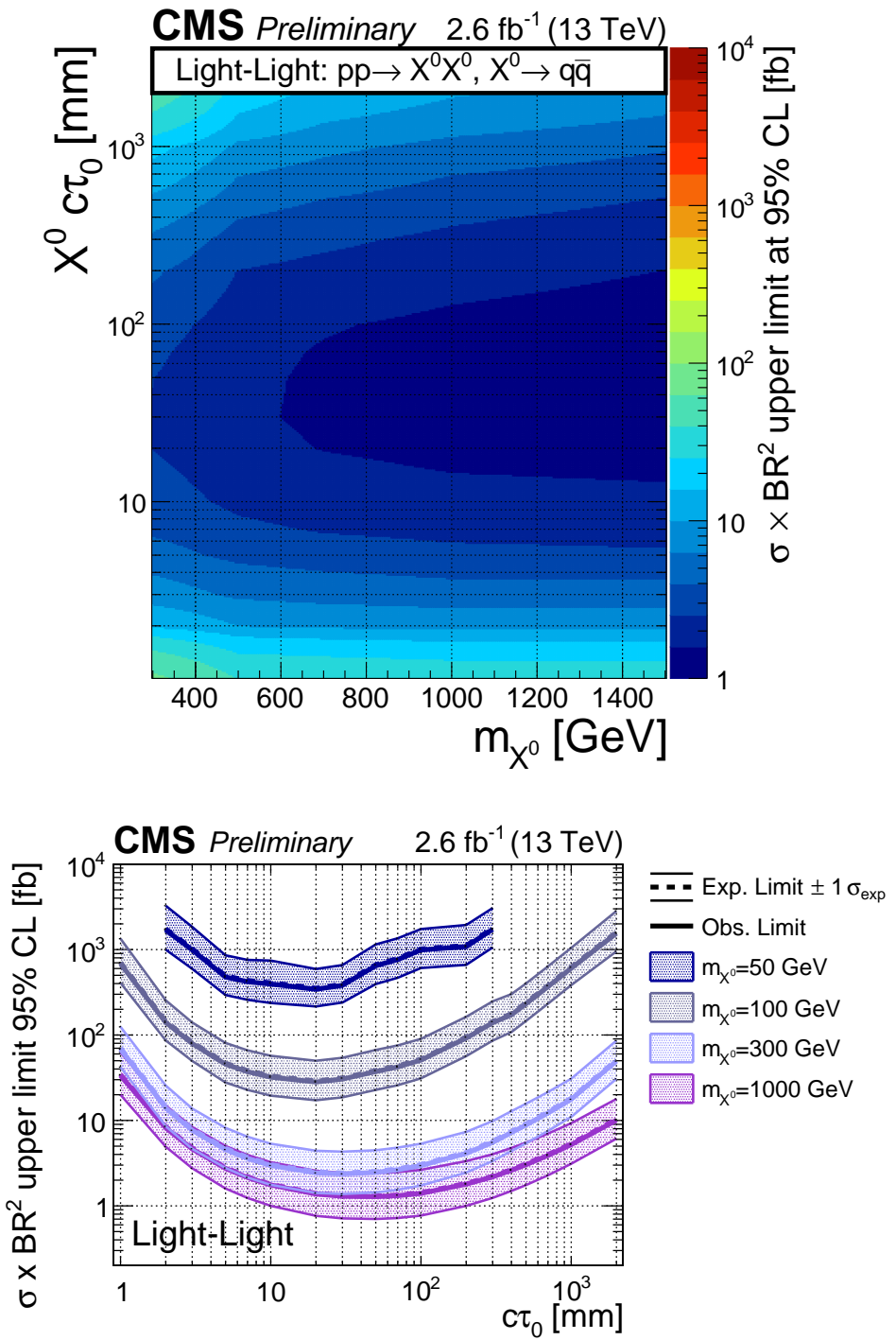


Figure 6.21: The excluded cross section at 95% CL for the Light-Light model as a function of the mass and lifetime of the parent particle X⁰ (top) and as a function of the lifetime for four values of the mass (bottom).

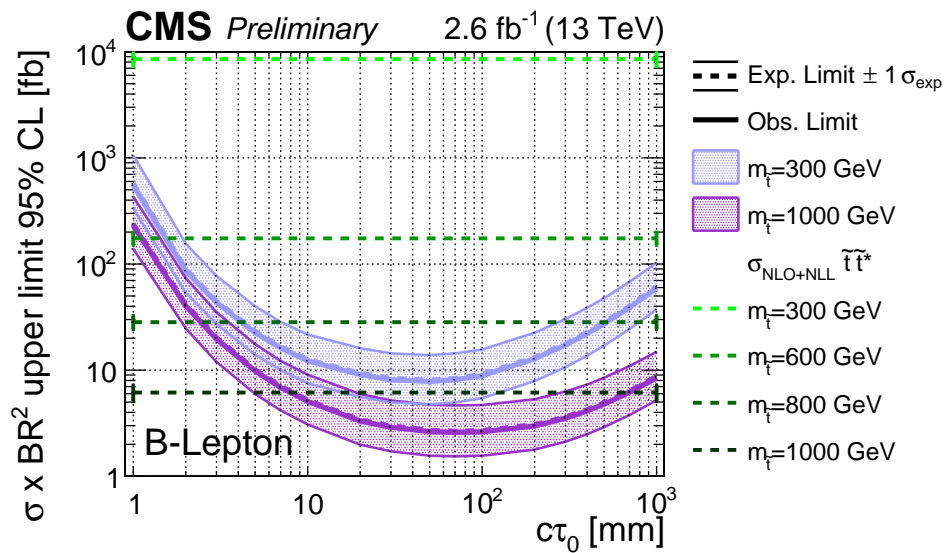
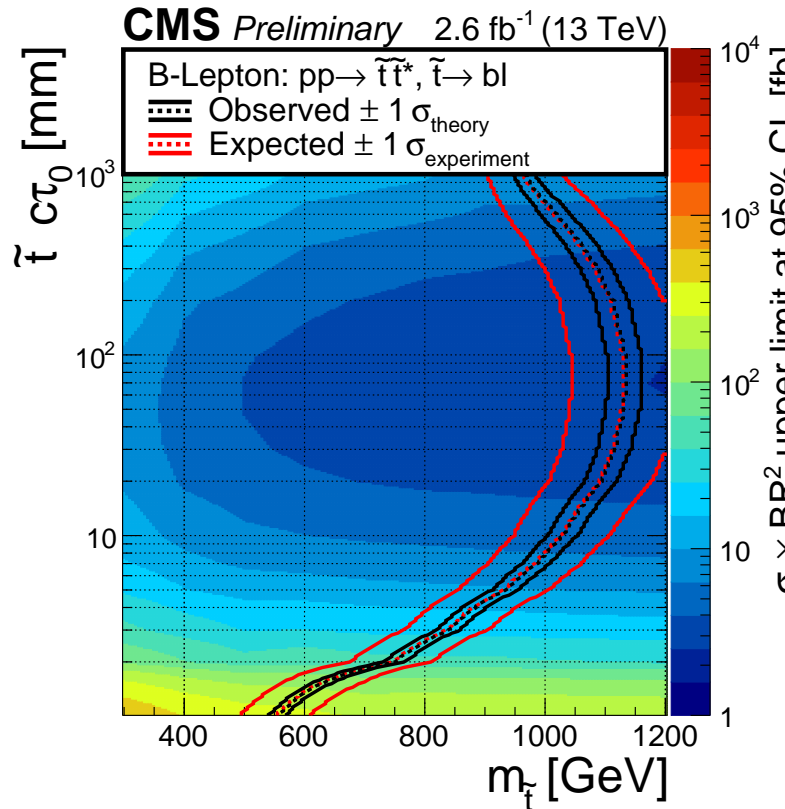


Figure 6.22: The excluded cross section at 95% CL for the B-Lepton model as a function of the mass and lifetime of the parent particle \tilde{t} (top) and as a function of the lifetime for two values of the mass (bottom). The bottom plot also shows the expected upper limits with one standard deviation uncertainties.

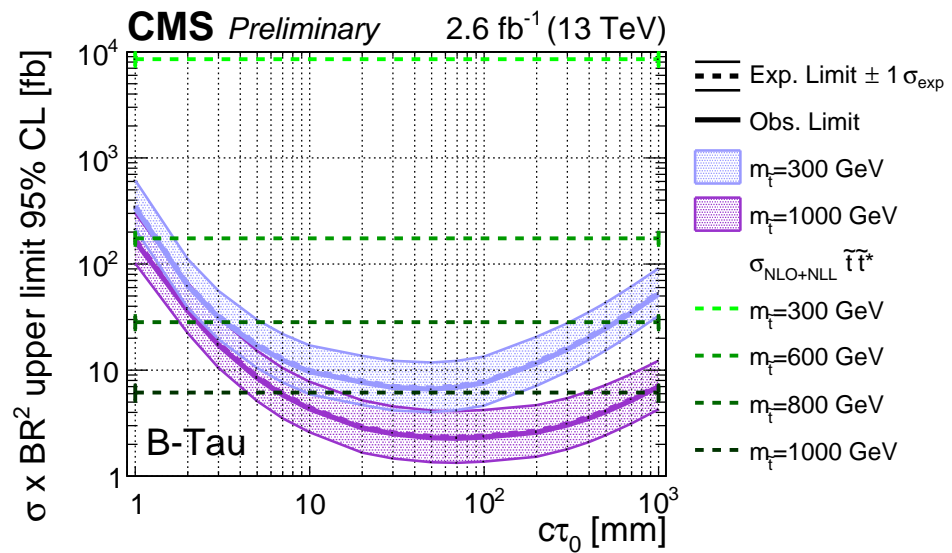
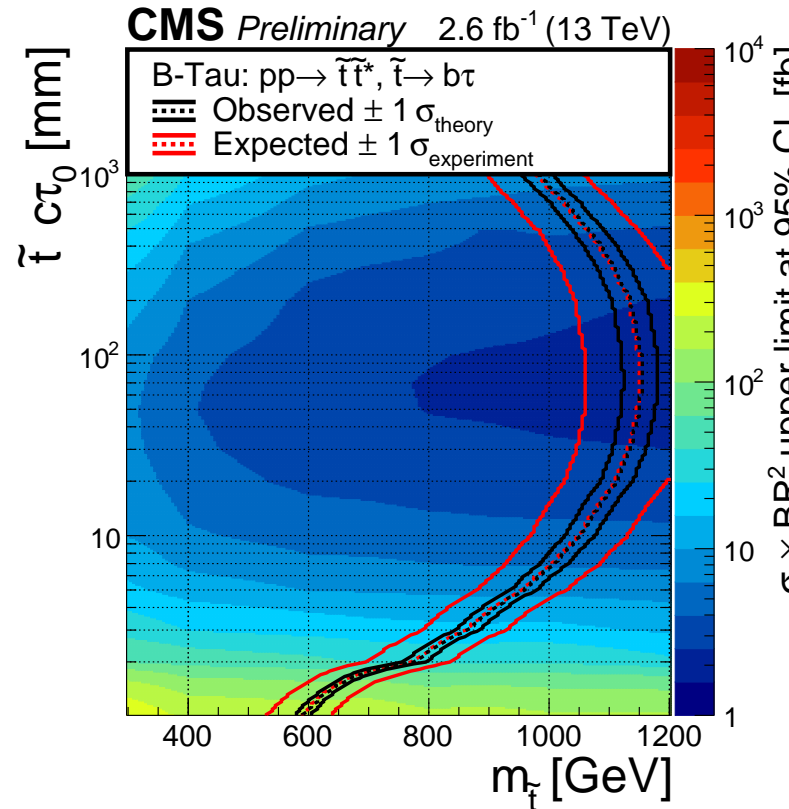


Figure 6.23: The excluded cross section at 95% CL for the B-Tau model as a function of the mass and lifetime of the parent particle \tilde{t} (top) and as a function of the lifetime for two values of the mass (bottom). The bottom plot also shows the expected upper limits with one standard deviation uncertainties.

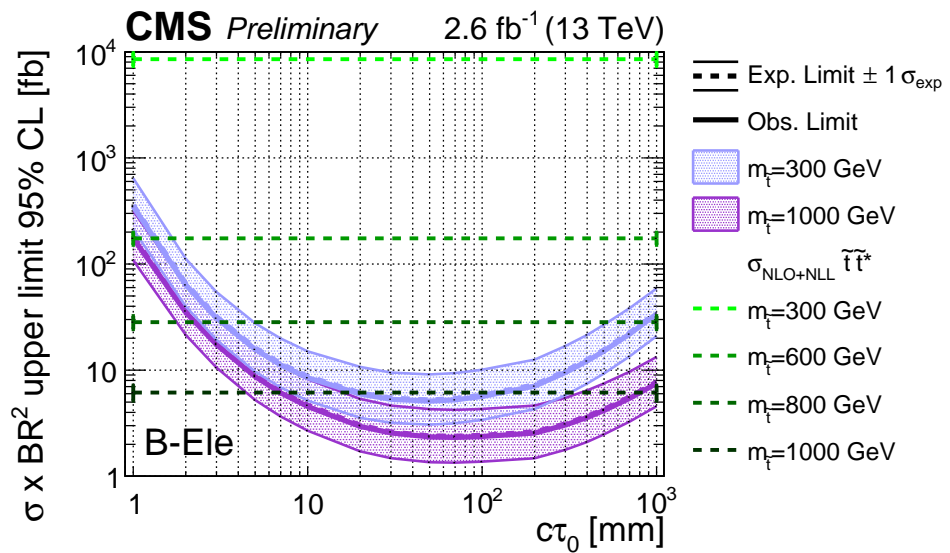
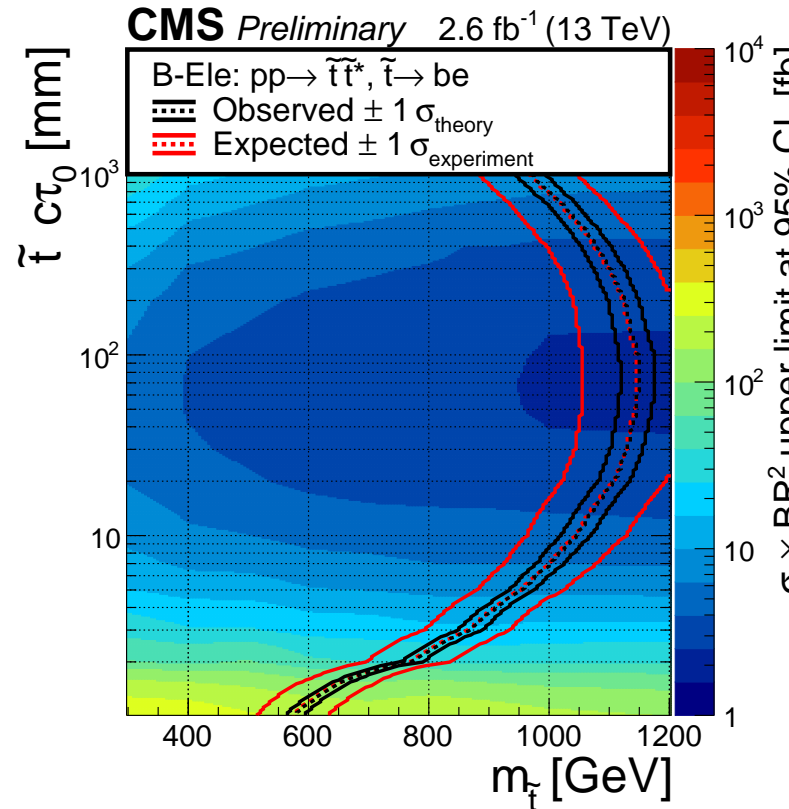


Figure 6.24: The excluded cross section at 95% CL for the B-Ele model as a function of the mass and lifetime of the parent particle \tilde{t} (top) and as a function of the lifetime for two values of the mass (bottom). The bottom plot also shows the expected upper limits with one standard deviation uncertainties.

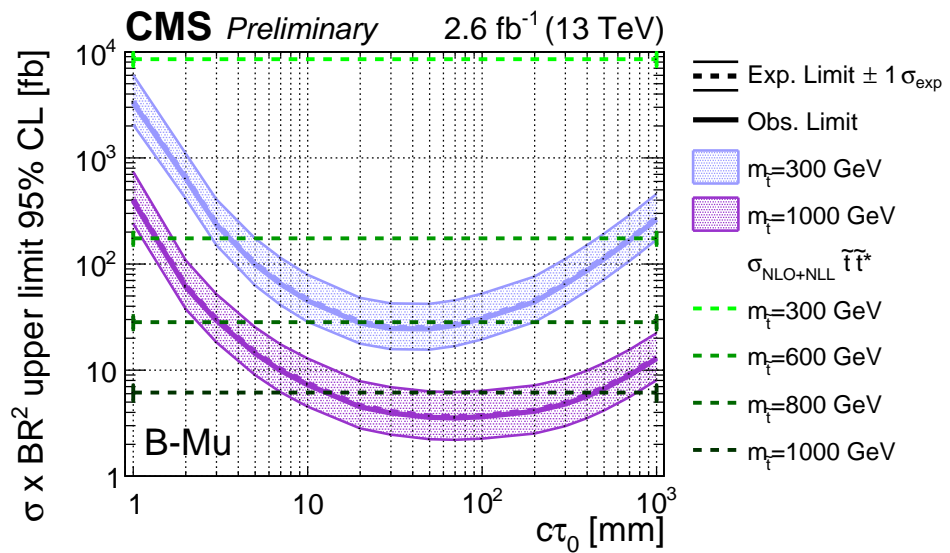
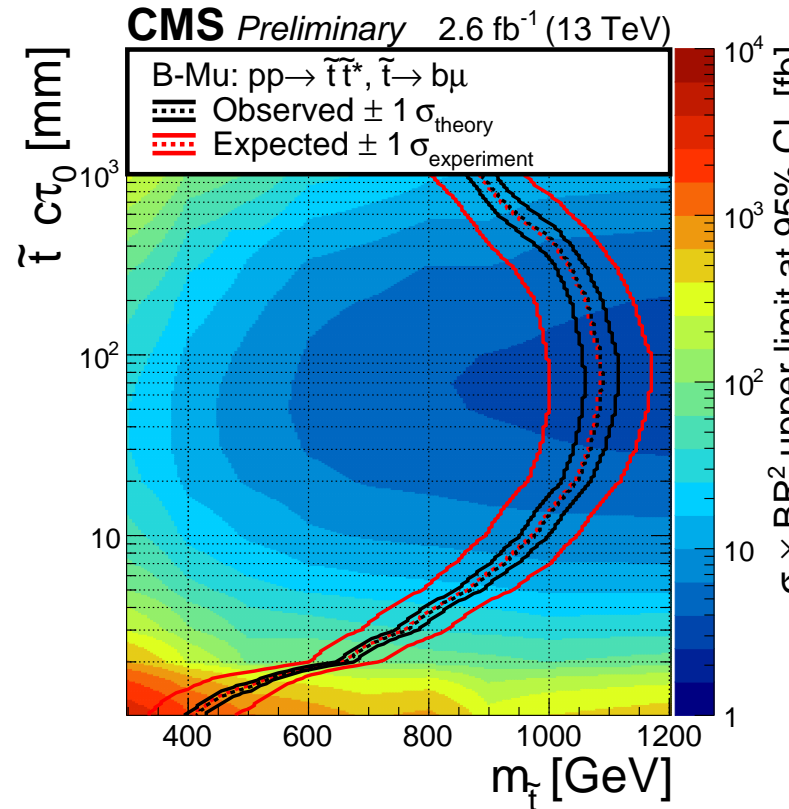


Figure 6.25: The excluded cross section at 95% CL for the B-Mu model as a function of the mass and lifetime of the parent particle \tilde{t} (top) and as a function of the lifetime for two values of the mass (bottom). The bottom plot also shows the expected upper limits with one standard deviation uncertainties.

Chapter 7

Conclusions

A search for long-lived particles was performed with data corresponding to an integrated luminosity of 2.6 fb^{-1} collected at a center-of-mass energy of 13 TeV by the CMS experiment in 2015. This is the first search made for long-lived decays to jet final states in 13 TeV data and the first search to demonstrate explicit sensitivity to long-lived decays to tau leptons. The analysis utilized two customized topological trigger algorithms and an offline displaced-jet tagging algorithm, with the multiplicity of displaced jets used to search for the presence of a signal. As no excess above the predicted background is found, upper limits are set at 95% confidence level on the production cross section for resonances decaying to two jets or to a lepton and b quark. The limits are calculated as a function of the mass and proper lifetime of the long-lived particles. For the Jet-Jet (B-Lepton) decay mode, cross sections larger than 1.2 fb (2.5 fb) are excluded for proper lifetimes of 50 mm (70-100 mm). The cross section limits are also translated into mass exclusion bounds, using a calculation of the top squark production cross section as a reference. Pair-produced long-lived R-parity violating top squarks lighter than 550-1130 GeV are excluded, depending on their lifetime and decay mode. This mass exclusion bound is currently the most stringent bound available for top squark proper lifetimes greater than 3 mm.

Bibliography

- [1] CMS Luminosity Measurement for the 2015 Data Taking Period. Technical Report CMS-PAS-LUM-15-001, CERN, Geneva, 2016. URL <https://cds.cern.ch/record/2138682>.
- [2] Inclusive search for new particles decaying to displaced jets at $\sqrt{s} = 13$ TeV. Technical Report CMS-PAS-EXO-16-003, CERN, Geneva, 2017. URL <http://cds.cern.ch/record/2256654>.
- [3] Georges Aad et al. Search for massive, long-lived particles using multitrack displaced vertices or displaced lepton pairs in pp collisions at $\sqrt{s} = 8$ TeV with the ATLAS detector. *Phys. Rev. D*, 92:072004, 2015. doi: 10.1103/PhysRevD.92.072004.
- [4] Georges Aad et al. Search for long-lived, weakly interacting particles that decay to displaced hadronic jets in proton-proton collisions at $\sqrt{s} = 8$ TeV with the atlas detector. *Phys. Rev. D*, 92:012010, 2015. doi: 10.1103/PhysRevD.92.012010.
- [5] Bo Andersson, G. Gustafson, G. Ingelman, and T. Sjostrand. Parton Fragmentation and String Dynamics. *Phys. Rept.*, 97:31–145, 1983. doi: 10.1016/0370-1573(83)90080-7.
- [6] Jamie Antonelli. Searches for long-lived particles at cms. Apsen 2017, 2017. URL <https://indico.cern.ch/event/550030/contributions/2417789/>.
- [7] T. Aoyama, M. Hayakawa, T. Kinoshita, and M. Nio. Revised value of the eighth-order QED contribution to the anomalous magnetic moment of the electron. *Phys. Rev.*, D77:053012, 2008. doi: 10.1103/PhysRevD.77.053012.
- [8] N. Arkani-Hamed, S. Dimopoulos, G. F. Giudice, and A. Romanino. Aspects of split supersymmetry. *Nucl. Phys.*, B709:3–46, 2005. doi: 10.1016/j.nuclphysb.2004.12.026.
- [9] Nima Arkani-Hamed and Savas Dimopoulos. Supersymmetric unification without low energy supersymmetry and signatures for fine-tuning at the LHC. *JHEP*, 06:073, 2005. doi: 10.1088/1126-6708/2005/06/073.
- [10] Nima Arkani-Hamed, Arpit Gupta, David E. Kaplan, Neal Weiner, and Tom Zorawski. Simply Unnatural Supersymmetry. 2012.

- [11] G. Baiatian et al. Design, Performance, and Calibration of CMS Hadron-Barrel Calorimeter Wedges. 2007.
- [12] R. et al Ball. Parton distributions with LHC data. *Nucl. Phys. B*, 867:244, 2013. doi: 10.1016/j.nuclphysb.2012.10.003.
- [13] W. Beenakker, R. Höpker, M. Spira, and P. M. Zerwas. Squark and gluino production at hadron colliders. *Nucl. Phys. B*, 492:51, 1997. doi: 10.1016/S0550-3213(97)80027-2.
- [14] W. Beenakker, S. Brensing, M. Krämer, A. Kulesza, E. Laenen, and I. Niessen. Soft-gluon resummation for squark and gluino hadroproduction. *JHEP*, 12:041, 2009. doi: 10.1088/1126-6708/2009/12/041.
- [15] W. Beenakker, S. Brensing, M. Krämer, A. Kulesza, E. Laenen, L. Motyka, and I. Niessen. Squark and gluino hadroproduction. *Int. J. Mod. Phys. A*, 26:2637, 2011. doi: 10.1142/S0217751X11053560.
- [16] Andy Buckley et al. General-purpose event generators for LHC physics. *Phys. Rept.*, 504:145–233, 2011. doi: 10.1016/j.physrep.2011.03.005.
- [17] Matteo Cacciari, Gavin P. Salam, and Gregory Soyez. The anti- k_t jet clustering algorithm. *JHEP*, 04:063, 2008. doi: 10.1088/1126-6708/2008/04/063.
- [18] Matteo Cacciari, Gavin P. Salam, and Gregory Soyez. Fastjet user manual. *Eur. Phys. J. C*, 72, 2012. doi: 10.1140/epjc/s10052-012-1896-2.
- [19] S. Chatrchyan et al. The CMS Experiment at the CERN LHC. *JINST*, 3:S08004, 2008. doi: 10.1088/1748-0221/3/08/S08004.
- [20] Serguei Chatrchyan et al. Description and performance of track and primary-vertex reconstruction with the CMS tracker. *JINST*, 9:P10009, 2014. doi: 10.1088/1748-0221/9/10/P10009.
- [21] CMS and ATLAS Collaborations. Procedure for the lhc higgs boson search combination in summer 2011. CMS-NOTE-2011-005, 2011.
- [22] The CMS Collaboration. Cms tridas project : Technical design report, volume 1: The trigger systems. Technical report, 2000. URL <https://cds.cern.ch/record/706847>.
- [23] CERN Finance Committee. Future arrangements for the calculation of the scale of Member State contributions and implementation scheme . URL <https://indico.cern.ch/event/75003/contributions/1246494/attachments/1048068/1493947/fc-e-5383-dec.pdf>.
- [24] CERN Finance Committee. 2015 Budget Scale of Contributions. . URL <https://cds.cern.ch/record/1711110/files/fc-e-5827-CERN3118.pdf>.

- [25] CERN Communications. Experiments. URL <https://home.cern/about/experiments>.
- [26] Nathaniel Craig, Andrey Katz, Matt Strassler, and Raman Sundrum. Naturalness in the Dark at the LHC. *JHEP*, 07:105, 2015. doi: 10.1007/JHEP07(2015)105.
- [27] Yanou Cui and Brian Shuve. Probing Baryogenesis with Displaced Vertices at the LHC. *JHEP*, 02:049, 2015. doi: 10.1007/JHEP02(2015)049.
- [28] Meike de With. *Signals of minimal Gauge-Mediated Supersymmetry Breaking in ATLAS*. PhD thesis, Universiteit Van Amsterdam, 2011.
- [29] R. Keith Ellis, W. James Stirling, and B. R. Webber. QCD and collider physics. *Camb. Monogr. Part. Phys. Nucl. Phys. Cosmol.*, 8:1–435, 1996.
- [30] P. Fazilleau, D. Campi, B. Cure, A. Herve, F. Kircher, C. Lesmond, and G. Maire. Analysis and Design of the CMS Magnet Quench Protection. *IEEE Trans. Appl. Supercond.*, 16(2):1643201, 2006. doi: 10.1109/TASC.2006.873267.
- [31] R. P. Feynman. Space - time approach to quantum electrodynamics. *Phys. Rev.*, 76:769–789, 1949. doi: 10.1103/PhysRev.76.769.
- [32] G. F. Giudice and A. Romanino. Split supersymmetry. *Nucl. Phys.*, B699:65–89, 2004. doi: 10.1016/j.nuclphysb.2004.11.048, 10.1016/j.nuclphysb.2004.08.001. [Erratum: Nucl. Phys.B706,487(2005)].
- [33] P. Graham, D. Kaplan, S. Rajendran, and P. Sarawat. Displaced supersymmetry. *Journal of High Energy Physics*, 149, 2012. doi: 10.1007/JHEP07(2012)149.
- [34] D. Green. The physics of particle detectors. *Camb. Monogr. Part. Phys. Nucl. Phys. Cosmol.*, 12:1–361, 2000.
- [35] Tao Han, Zongguo Si, Kathryn M. Zurek, and Matthew J. Strassler. Phenomenology of hidden valleys at hadron colliders. *JHEP*, 07:008, 2008. doi: 10.1088/1126-6708/2008/07/008.
- [36] D. Hanneke, S. Fogwell, and G. Gabrielse. New Measurement of the Electron Magnetic Moment and the Fine Structure Constant. *Phys. Rev. Lett.*, 100:120801, 2008. doi: 10.1103/PhysRevLett.100.120801.
- [37] JoAnne L. Hewett, Ben Lillie, Manuel Masip, and Thomas G. Rizzo. Signatures of long-lived gluinos in split supersymmetry. *JHEP*, 09:070, 2004. doi: 10.1088/1126-6708/2004/09/070.
- [38] Diego M. Hofman and Juan Maldacena. Conformal collider physics: Energy and charge correlations. *JHEP*, 05:012, 2008. doi: 10.1088/1126-6708/2008/05/012.

- [39] Wouter Hulsbergen. Search for long-lived particles at the LHC. Interpretation in different models. Moriond Electroweak, 2017. URL <https://indico.in2p3.fr/event/13763/session/6/#20170321>.
- [40] S. Jadach, Z. Was, R. Decker, and Johann H. Kuhn. The tau decay library TAUOLA: Version 2.4. *Comput. Phys. Commun.*, 76:361–380, 1993. doi: 10.1016/0010-4655(93)90061-G.
- [41] H. F. Jones. *Groups, representations and physics*. 1990.
- [42] C. Joram. Large area hybrid photodiodes. *Nucl. Phys. Proc. Suppl.*, 78:407–415, 1999. doi: 10.1016/S0920-5632(99)00578-2.
- [43] Thomas Junk. Confidence level computation for combining searches with small statistics. *Nucl. Instrum. Meth. A*, 434:435, 1999. doi: 10.1016/S0168-9002(99)00498-2.
- [44] Vardan Khachatryan et al. Search for Long-Lived Neutral Particles Decaying to Quark-Antiquark Pairs in Proton-Proton Collisions at $\sqrt{s} = 8$ TeV. *Phys. Rev. D*, 91:012007, 2015. doi: 10.1103/PhysRevD.91.012007.
- [45] M. Krämer, A. Kulesza, R. van der Leeuw, M. Mangano, S. Padhi, T. Plehn, and X. Portell. Supersymmetry production cross sections in pp collisions at $\sqrt{s} = 7$ TeV. 2012.
- [46] A. Kulesza and L. Motyka. Threshold resummation for squark-antisquark and gluino-pair production at the LHC. *Phys. Rev. Lett.*, 102:111802, 2009. doi: 10.1103/PhysRevLett.102.111802.
- [47] A. Kulesza and L. Motyka. Soft gluon resummation for the production of gluino-gluino and squark-antisquark pairs at the LHC. *Phys. Rev. D*, 80:095004, 2009. doi: 10.1103/PhysRevD.80.095004.
- [48] CERN Laboratory. Budget overview, 2016. URL <https://press.cern/facts-and-figures/budget-overview>.
- [49] Paul Langacker. *The standard model and beyond*. 2010. URL http://www.taylorandfrancis.com/shopping_cart/search/search.asp?search=978-1-4200-7906-7.
- [50] D. J. Lange. The EvtGen particle decay simulation package. *Nucl. Instrum. Meth.*, A462:152–155, 2001. doi: 10.1016/S0168-9002(01)00089-4.
- [51] Y. Nambu. The Confinement of Quarks. *Sci. Am.*, 235N5:48–70, 1976. doi: 10.1038/scientificamerican1176-48.
- [52] C. Patrignani et al. Review of Particle Physics. *Chin. Phys.*, C40(10):100001, 2016. doi: 10.1088/1674-1137/40/10/100001.

- [53] Michael E. Peskin and Daniel V. Schroeder. *An Introduction to quantum field theory*. 1995. ISBN 9780201503975, 0201503972. URL <http://www.slac.stanford.edu/spires/find/books/www?cl=QC174.45%3AP4>.
- [54] Fernando Quevedo, Sven Krippendorf, and Oliver Schlotterer. Cambridge Lectures on Supersymmetry and Extra Dimensions. 2010.
- [55] A. L. Read. Presentation of search results: the CL_s technique. *J. Phys. G*, 28: 2693, 2002. doi: 10.1088/0954-3899/28/10/313.
- [56] Clint Richardson. CMS High Level Trigger Timing Measurements. *J. Phys. Conf. Ser.*, 664(8):082045, 2015. doi: 10.1088/1742-6596/664/8/082045.
- [57] Pedro Schwaller, Daniel Stolarski, and Andreas Weiler. Emerging Jets. *JHEP*, 05:059, 2015. doi: 10.1007/JHEP05(2015)059.
- [58] R. Shankar. *Principles of Quantum Mechanics*. Springer, 1994.
- [59] Torbjorn Sjostrand, Stephen Mrenna, and Peter Z. Skands. PYTHIA 6.4 Physics and Manual. *JHEP*, 05:026, 2006. doi: 10.1088/1126-6708/2006/05/026.
- [60] American Physical Society. Women in Physics Statistics. URL <https://www.aps.org/programs/women/resources/statistics.cfm>.
- [61] M. Srednicki. *Quantum field theory*. Cambridge University Press, 2007. ISBN 9780521864497, 9780511267208.
- [62] M. Strassler and Zurek K. Discovering the higgs through highly displaced vertices. *Phys. Lett. B*, 263, 2008. doi: 10.1016/j.physletb.2008.02.008.
- [63] V. V. Sudakov. Vertex parts at very high-energies in quantum electrodynamics. *Sov. Phys. JETP*, 3:65–71, 1956. [Zh. Eksp. Teor. Fiz.30,87(1956)].
- [64] T. Sjöstrand, Stephen Mrenna, and Peter Z. Skands. A brief introduction to PYTHIA 8.1. *Comput. Phys. Commun.*, 178:852, 2008. doi: 10.1016/j.cpc.2008.01.036.
- [65] D. Tong. *Quantum Field Theory: University of Cambridge Part III Mathematical Tripos*. 2006. URL <http://www.damtp.cam.ac.uk/user/tong/qft.html>.
- [66] Christopher G. Tully. *Elementary particle physics in a nutshell*. 2011.
- [67] A. Tuna. *Evidence for Decays of the Higgs Boson to Tau Leptons at ATLAS*. PhD thesis, University of Pennsylvania, 2015.
- [68] Frank Zimmerman. Lhc: The machine, 2012. URL <http://www-conf.slac.stanford.edu/ssi/2012/Presentations/Zimmermann.pdf>.